

University of Windsor

Scholarship at UWindor

Electronic Theses and Dissertations

Theses, Dissertations, and Major Papers

1-1-2007

Microstructure characterization and micro- and nanoscale mechanical behaviour of magnesium-aluminum and magnesium-aluminum-calcium alloys.

Lihong Han
University of Windsor

Follow this and additional works at: <https://scholar.uwindsor.ca/etd>

Recommended Citation

Han, Lihong, "Microstructure characterization and micro- and nanoscale mechanical behaviour of magnesium-aluminum and magnesium-aluminum-calcium alloys." (2007). *Electronic Theses and Dissertations*. 7221.

<https://scholar.uwindsor.ca/etd/7221>

This online database contains the full-text of PhD dissertations and Masters' theses of University of Windsor students from 1954 forward. These documents are made available for personal study and research purposes only, in accordance with the Canadian Copyright Act and the Creative Commons license—CC BY-NC-ND (Attribution, Non-Commercial, No Derivative Works). Under this license, works must always be attributed to the copyright holder (original author), cannot be used for any commercial purposes, and may not be altered. Any other use would require the permission of the copyright holder. Students may inquire about withdrawing their dissertation and/or thesis from this database. For additional inquiries, please contact the repository administrator via email (scholarship@uwindsor.ca) or by telephone at 519-253-3000ext. 3208.

**MICROSTRUCTURE CHARACTERIZATION AND MICRO-AND
NANO-SCALE MECHANICAL BEHAVIOUR OF Mg-Al
AND Mg-Al-Ca ALLOYS**

By

Lihong Han

A Dissertation
Submitted to the Faculty of Graduate Studies
through Mechanical, Automotive & Materials Engineering
in Partial Fulfillment of the Requirements for
the Degree of Doctor of Philosophy at the
University of Windsor

Windsor, Ontario, Canada

2007

© 2007 Lihong Han



Library and
Archives Canada

Bibliothèque et
Archives Canada

Published Heritage
Branch

Direction du
Patrimoine de l'édition

395 Wellington Street
Ottawa ON K1A 0N4
Canada

395, rue Wellington
Ottawa ON K1A 0N4
Canada

Your file *Votre référence*
ISBN: 978-0-494-42374-5
Our file *Notre référence*
ISBN: 978-0-494-42374-5

NOTICE:

The author has granted a non-exclusive license allowing Library and Archives Canada to reproduce, publish, archive, preserve, conserve, communicate to the public by telecommunication or on the Internet, loan, distribute and sell theses worldwide, for commercial or non-commercial purposes, in microform, paper, electronic and/or any other formats.

The author retains copyright ownership and moral rights in this thesis. Neither the thesis nor substantial extracts from it may be printed or otherwise reproduced without the author's permission.

AVIS:

L'auteur a accordé une licence non exclusive permettant à la Bibliothèque et Archives Canada de reproduire, publier, archiver, sauvegarder, conserver, transmettre au public par télécommunication ou par l'Internet, prêter, distribuer et vendre des thèses partout dans le monde, à des fins commerciales ou autres, sur support microforme, papier, électronique et/ou autres formats.

L'auteur conserve la propriété du droit d'auteur et des droits moraux qui protègent cette thèse. Ni la thèse ni des extraits substantiels de celle-ci ne doivent être imprimés ou autrement reproduits sans son autorisation.

In compliance with the Canadian Privacy Act some supporting forms may have been removed from this thesis.

Conformément à la loi canadienne sur la protection de la vie privée, quelques formulaires secondaires ont été enlevés de cette thèse.

While these forms may be included in the document page count, their removal does not represent any loss of content from the thesis.

Bien que ces formulaires aient inclus dans la pagination, il n'y aura aucun contenu manquant.


Canada

ABSTRACT

The application in the automotive industry of the as-cast AM50 alloy (Mg-5.0 wt.%Al-0.3 wt.%Mn) has been limited by its low creep resistance at elevated temperatures. Permanent mold cast (PM) Mg-Al-Ca alloys with calcium additions (0 ~ 2.0 wt.%) were investigated in this study due to their potential for improving the high temperature creep strength.

The microstructures of the die cast (DC) or PM AM50 alloys consisted of an intergranular β -Mg₁₇Al₁₂ phase surrounded by a region of Al-rich eutectic α -Mg phase, sometimes with attached Al₈Mn₅ particles. In this study, significant grain refinement was observed in the PM Mg-Al-Ca alloys with Ca addition to the AM50 alloy. The grain refining effect was confirmed by quantitative image analysis through measurement of the secondary dendrite arm spacing (SDAS). The intergranular phases in Mg-Al-Ca alloys with 0.5 or 1.0 wt.% Ca were β -Mg₁₇Al₁₂ and (Al, Mg)₂Ca phases. As the Ca addition was increased to 1.5 wt.% Ca, the β -Mg₁₇Al₁₂ phase was completely replaced by a (Al, Mg)₂Ca phase.

Differential scanning calorimetry (DSC) results showed that the (Al, Mg)₂Ca phase was thermally more stable than the β -Mg₁₇Al₁₂ phase, which contributed to the better creep strength of the Mg-Al-Ca alloys. The change in heating/cooling rates played an important role in the redistribution of alloying elements and the dissolution or precipitation of the eutectic phases in the as-cast Mg alloys during DSC runs.

The micro-and nano-scale hardness and composite modulus of the PM Mg-Al-Ca alloys increased with increasing Ca content, and the indentation size effect (ISE) was also observed in the as-cast Mg-Al and Mg-Al-Ca alloys. PM AC52 alloy (Mg-5.0wt.%Al-2.0wt.%Ca) was a much more creep resistant alloy than other Mg-Al-Ca alloys with lower

Ca contents because of the higher solute content in the primary α -Mg in the as-cast state and also because of the presence of nano precipitates within the primary α -Mg. The size and volume fraction of the precipitates and the solute content within the primary α -Mg of the AC52 alloys were related to the different solidification rates, which directly influence the nano indentation creep strength of the alloys.

DEDICATION

To My parents and
My Family
Wen Qin
Leo Lang Han

ACKNOWLEDGEMENTS

I would like to thank my advisors Dr. Derek O. Northwood and Dr. Henry Hu for their constant encouragement, advice, suggestion, patience, interest and involvement in this project. I appreciate, in particular, their assistance with the review and writing of the papers published resulting from this thesis.

I would also like to thank Dr. X. Nie of University of Windsor and Dr. R. Klassen of University of Western Ontario for giving me the opportunity to use their indentation equipment. Thanks also go to Dr. N. Li of Research and Advanced Engineering of Ford Motor Company for his industrial support. The technical assistance of Mr. Patrick Seguin, Mr. John Robinson, and Mr. Bruce Durfy, University of Windsor, was appreciated. Support from the Natural Science and Engineering Research Council of Canada and Ontario Graduate Scholarship in Science and Technology for this project are gratefully appreciated.

I am grateful to my fellow students, Mrs, Linlin Wang, Mr. Fang Yu, Mr. Mohsen Masoumi, Mr. Peng Zhang, Mr. Robert Shang, Mr. Shuping Wang, University of Windsor, and Dr. Haiping Sun of University of Michigan for their friendship and support. Finally, I wish to express my heartfelt thanks to my wife Wen Qin and my son Leo Lang Han for their constant support, great patience and encouragement, and thoughtful understanding during the entire course of this work.

TABLE OF CONTENTS

ABSTRACT	iii
DEDICATION	v
ACKNOWLEDGEMENTS	vi
LIST OF TABLES	xii
LIST OF FIGURES	xiv
LIST OF ABBREVIATIONS, SYMBOLS, NOMENCLATURE	xxiii
1. INTRODUCTION	1
2. LITERATURE REVIEW	4
2.1 Magnesium casting alloys.....	4
2.1.1 Alloying magnesium alloys.....	4
2.1.2 Mechanical properties of die cast Mg-Al alloys.....	6
2.1.3 Mg-Al alloy systems.....	7
2.1.3.1 Mg-Al-Zn alloys.....	7
2.1.3.2 Mg-Al-Mn alloys.....	9
2.1.3.3 Creep resistant Mg alloys.....	11
2.1.4 Grain refinement of magnesium alloys by zirconium.....	17
2.1.5 Die casting and permanent mould casting.....	18
2.2 Indentation testing.....	20
2.2.1 Introduction.....	20
2.2.2 Indenter geometry and geometric similarity.....	21
2.2.2.1 Indenter shapes and sizes.....	21
2.2.2.2 Geometric similarity.....	21
2.2.3 Measurement of mechanical properties.....	22
2.2.3.1 Hardness and elastic modulus.....	22

2.2.3.2	Yield strength.....	29
2.2.3.3	Creep.....	30
2.2.3.4	Dynamic mechanical properties.....	31
2.2.4	Factors affecting indentation test data.....	32
2.2.4.1	Contact depth, “sinking-in” and “piling-up” phenomena.....	33
2.2.4.2	Indentation size effect.....	34
2.3	Calorimetric analysis.....	36
2.3.1	Introduction.....	36
2.3.2	Experimental aspects of calorimetry.....	36
2.3.2.1	Isothermal calorimetric analysis.....	36
2.3.2.2	Differential scanning calorimetry.....	37
2.3.2.3	Sample preparation.....	38
2.3.2.4	Baseline correction in calorimetry.....	39
2.3.3	Modelling of thermally activated reactions.....	40
2.3.3.1	Introduction.....	40
2.3.3.2	Single state variable approaches.....	41
2.3.3.3	Equivalent time, state variable, and temperature integral.....	42
2.3.3.4	Activation energy determination.....	45
2.3.5	Applications of thermal analysis for Mg based alloys.....	46
3.	EXPERIMENTAL PROCEDURES.....	50
3.1	Experimental material.....	50
3.1.1	Die casting.....	50
3.1.2	Permanent mold casting.....	51
3.1.3	High Temperature Observation Unit.....	53
3.2	Heat treatment.....	53
3.3	Indentation testing.....	54
3.3.1	Microindentation testing.....	54
3.3.2	Nanoindentation testing.....	55

3.4 DSC analysis.....	56
3.5 Microstructural analysis.....	57
3.5.1 Optical and SEM analysis.....	57
3.5.2 TEM analysis.....	59
4. RESULTS AND DISCUSSION OF MICROSTRUCTURE OF DIE CAST AM50 ALLOY.....	60
4.1 Microstructure of DC AM50 alloy.....	60
4.1.1 Optical and SEM micrographs.....	60
4.1.2 TEM micrographs.....	65
4.2 Distribution of secondary dendrite arm spacing.....	77
4.3 Distribution of eutectic phases.....	80
4.4 Summary.....	82
5. RESULTS AND DISCUSSION OF MICROSTRUCTURES OF PERMANENT MOLD CAST Mg-Al AND Mg-Al-Ca ALLOYS.....	84
5.1 As-cast microstructures of Mg-Al alloy.....	84
5.2 As-cast microstructures of Mg-Al-Ca alloys.....	87
5.3 Effects of cooling rates on the microstructure of the PM AC52 alloy.....	105
5.3.1 Thermal analysis.....	105
5.3.2 SDAS and volume fraction of eutectic.....	110
5.3.3 Phase transformations during permanent mold casting of the AC52 alloy	118
5.4 Heat treatment of PM Mg-Al and Mg-Al-Ca alloys.....	123
5.4.1 Solution treatment.....	124
5.4.2 Aging without solution treatment.....	128
5.4.3 Aging after solution treatment.....	132
5.5 Summary.....	138
6. RESULTS AND DISCUSSION OF DSC ANALYSIS	141
6.1 DSC analysis	141
6.1.1 DSC runs of the DC AM50 alloy.....	141

6.1.2	DSC runs of the PM AC series alloys.....	143
6.1.3	DSC runs of the PM AC52 alloy.....	145
6.1.3.1	DSC runs with heating.....	145
6.1.3.2	DSC runs with cooling after heating.....	148
6.2	Microstructural development during DSC runs.....	152
6.2.1	Effect of heating rate on the microstructure in the PM AM50 alloy.....	152
6.2.2	Variation of the microstructure in the AC series alloys after a DSC run...	154
6.2.3	Effect of heating rate on the microstructure of the PM AC52 alloy.....	157
6.2.4	Effect of cooling rate after heating on microstructure of the PM AC52 alloy.....	161
6.3	Calorimetric kinetics of as-cast Mg-Al and Mg-Al-Ca alloys.....	164
6.3.1	Peaks on DSC traces of as-cast Mg-Al alloy.....	164
6.3.2	Peaks on DSC traces of as-cast Mg-Al-Ca alloys.....	167
6.3.3	Microstructural evolution during homogenization.....	169
6.3.4	Microstructural evolution on cooling.....	169
6.4	Summary.....	171
7.	RESULTS AND DISCUSSION OF MICRO-AND NANO-INDENTATION STUDIES.....	174
7.1	Measurement of hardness and modulus.....	174
7.1.1	Vickers microhardness of DC AM50 alloy.....	174
7.1.2	Vickers microhardness of the PM Mg-Al and Mg-Al-Ca alloys.....	176
7.1.3	Nanoindentation and composite modulus.....	179
7.1.4	Continuous hardness and composite modulus.....	183
7.1.4.1	Experimental and calculated results.....	183
7.1.4.2	Correlation analysis.....	188
7.1.5	Hardness behavior of as-cast Mg-Al and Mg-Al-Ca alloys.....	191
7.1.6	Correlation of hardness and yield strength.....	197
7.2	Indentation size effect.....	199
7.3	Nanoindentation creep.....	204
7.3.1	Constitutive equation of indentation creep.....	204

7.3.2 Nanoindentation creep results.....	205
7.3.3 Nanoindentation creep behavior and mechanisms.....	212
7.4 Summary.....	217
8. CONCLUSIONS.....	219
9. SUGGESTIONS FOR FUTURE WORK	225
10. STATEMENT OF ORIGINALITY.....	226
REFERENCES	227
PUBLICATIONS RESULTING FROM THIS WORK.....	250
VITA AUCTORIS	251

LIST OF TABLES

Table 2.1 Binary magnesium alloy systems [11].....	5
Table 2.2 Typical room temperature mechanical properties of die cast Mg-Al alloys[15-18] 6	6
Table 2.3 Tensile properties as a function of the aluminum content in AM type alloys[35] 10	10
Table 2.4 Mechanical properties of Mg-Al-Ca and AE42 alloys [53-55, 59].....	15
Table 2.5 A set of alternate reaction models applied to describe the reaction kinetics in heterogeneous solid state systems [133, 134].....	42
Table 3.1 Chemical composition of DC AM50 alloy (wt.).....	50
Table 3.2 Die casting process parameters.....	51
Table 3.3 Chemical compositions of the permanent mold cast alloys (wt.).....	52
Table 5.1 SDAS and the volume fraction of eutectic phase measured in the Mg-Al-Ca series alloys.....	89
Table 5.2 Cooling curve parameters obtained at different cooling rates.....	106
Table 5.3 Average secondary dendrite arm spacing of the as-cast Mg-Al-Ca alloys.....	112
Table 5.4 Average volume fraction of (Al, Mg) ₂ Ca phase in the PM AC52 alloy.....	115
Table 6.1 DSC results measured at different heating rates for the DC AM50 alloy.....	142
Table 6.2 DSC results of the PM AC series alloys obtained at a heating rate of 30 °C/min.....	145
Table 6.3 DSC results of the PM AC52 alloy obtained at different heating rates.....	146
Table 6.4 DSC results of the PM AC52 alloy obtained at different cooling rates after heating.....	151
Table 6.5 Average Al content (wt.%) in the matrix of the AM50 alloy after DSC runs.	153
Table 7.1 Regression coefficient (R^2) and the constants (a and b) of the $S-h$ lines for the as-cast Mg alloys.....	188

Table 7.2	Calculated n values and correlation coefficients for as-cast Mg alloys.....	201
Table 7.3	Summary of fitting parameters for the micro- and nano-scale regimes.....	202
Table 7.4	Creep parameters obtained for the as-cast AC51 and AC52 alloys (cast at 30 °C/s) at applied loads of 1, 5 and 8 mN.....	211
Table 7.5	Creep parameters obtained for the as-cast AC52 alloys (cast at 0.5 ~ 30 °C/s) at an applied load of 5 mN.....	212

LIST OF FIGURES

Fig. 2.1 Mg-Al binary phase diagram[19].....	8
Fig. 2.2 (a) Schematic diagram of indenter and specimen surface geometry at full load and full unload for a conical indenter. (b) Load versus displacement for elastic-plastic loading followed by elastic unloading [75].....	23
Fig. 3.1 Schematic illustration showing DC AM50 coupons with the thicknesses of 2, 6 and 10 mm.....	50
Fig. 3.2 Permanent copper molds: (a) disk mold and (b) tube molds	52
Fig. 3.3 ULVAC-Riko High Temperature Observation Unit.....	53
Fig. 3.4 Hysitron Ubi [®] 1 Nanomechanical Test Instrument.....	55
Fig. 3.5 Differential Scanning Calorimetry - Thermogravimetric Analyzer (DSC-TGA Q600).....	56
Fig. 3.6 Buehler Optical Image Analyzer Model 2002.....	57
Fig. 3.7 Scanning Electron Microscope (JEOL Model JSM-5800LV).....	58
Fig. 3.8 JEOL 2010 Transmission Electron Microscope with an Energy Dispersive X-ray Spectrometer (EDS).....	59
Fig. 4.1 Optical microstructures of DC AM50 alloys: (a) the skin of 2 mm sample, (b) the center of 2 mm sample, (c) the skin of 6 mm sample, (d) the center of 6 mm sample, (e) the skin of 10 mm sample and (f) the center of 10 mm sample.....	61
Fig. 4.2 SEM micrographs of the microstructures in DC AM50 alloys: (a) the skin of 2 mm sample, (b) the center of 2 mm sample, (c) the center of 6 mm sample, and (d) the center of 10 mm sample	62
Fig. 4.3 (a) SEM micrograph and (b) the EDS line scans in the 2 mm DC AM50 alloy...	63
Fig. 4.4 EDS results for the 2mm DC AM50 alloy: (a) SEM micrograph, and elemental maps from the same region for (b) Mg, (c) Al and (d) Mn.....	65

Fig. 4.5	Typical EDS spectra of: (a) β -Mg ₁₇ Al ₁₂ and (b) Al ₈ Mn ₅ phases in the 2mm DC AM50 alloy.....	66
Fig. 4.6	Typical TEM image of (a) β -Mg ₁₇ Al ₁₂ in the 2 mm DC AM50 alloy, (b) selected area diffraction pattern from β -Mg ₁₇ Al ₁₂ phase with dark contrast, and (c) indexing of diffraction pattern in (b).....	68
Fig. 4.7	Typical TEM image of (a) β -Mg ₁₇ Al ₁₂ in the 2 mm DC AM50 alloy and (b) selected area diffraction pattern from β -Mg ₁₇ Al ₁₂ phase with dark contrast.....	69
Fig. 4.8	(a) TEM image and (b) EDS result of nano Mg ₁₇ Al ₁₂ particles in the 2 mm DC AM50 alloy.....	69
Fig. 4.9	(a) Typical TEM image of Al ₈ Mn ₅ in die cast AM50 alloy with a 2 mm thickness, (b) selected area diffraction pattern from Al ₈ Mn ₅ phase with dark contrast, and (c) indexing of diffraction pattern in (b).....	71
Fig. 4.10	(a) Typical TEM image of Al ₈ Mn ₅ in the 2 mm DC AM50 alloy, and selected area diffraction patterns from (b) the whole Al ₈ Mn ₅ phase with dark contrast, and (c) star location, (d) square location, and (e) circle location.....	72
Fig. 4.11	(a) TEM image and (b) EDS result of finer Al ₈ Mn ₅ particles in the 2 mm thick DC AM50 alloy.....	73
Fig. 4.12	Morphology of twin structure formed during solidification for the 2 mm DC AM50 alloy: (a) SEM and (b) TEM images	74
Fig. 4.13	TEM micrographs of grain and dislocation network in the 2 mm DC AM50 alloy. (a) grain boundaries, (b) arranged dislocations, (c) stacking fault and (d) tangled dislocations and precipitates	76
Fig. 4.14	Distribution of the SDAS across the DC AM50 castings with section thicknesses of (a) 2 mm, (b) 6 mm and (c) 10mm.....	78
Fig. 4.15	Histograms showing the distribution of the SDAS in the skin regions of the castings with section thicknesses of: (a) 2 and (b)10 mm.....	79
Fig. 4.16	Distribution of volume fraction of eutectic phase throughout the DC AM50 castings with section thicknesses of (a) 2 mm, (b) 6 mm and (c) 10 mm.....	81

Fig. 5.1 SEM micrographs of the PM AM50 alloy in: (a) skin region and (b) central region.....	84
Fig. 5.2 (a) SEM micrograph and (b) EDS line scans in the PM AM50 alloy.....	86
Fig. 5.3 EDS results for the PM AM50 alloy: (a) SEM micrograph, and elemental maps from the same region for (b) Mg, (c) Al and (d) Mn.....	87
Fig. 5.4 SEM micrographs of the PM Mg-Al-Ca alloys with different Ca contents (wt.%): (a) 0.5, (b) 1.0, (c) 1.5, and (d) 2.0.....	88
Fig. 5.5 Effect of Ca content on: (a) the SDAS and (b) the volume fraction of eutectic phase in the PM Mg-Al-Ca alloys.....	90
Fig. 5.6 Microstructure in the center of the Mg-Al-Ca alloys with the content of Ca (wt.%): (a) 0.5, (b) 1.0, (c) 1.5 and (d) 2.0.....	92
Fig. 5.7 EDS results for the PM AC51 alloy: (a) SEM micrograph, (b) EDS line scans, and elemental maps from the same region for (c) Mg, (d) Al, (e) Ca and (f) Mn....	93
Fig. 5.8 TEM BF images of: (a) $(Al, Mg)_2Ca$ at triangular grain boundary, (b) $(Al, Mg)_2Ca$ at grain boundary, (c) Al_8Mn_5 and (d) $Mg_{17}Al_{12}$ in the PM AC51 alloy.....	94
Fig. 5.9 Typical EDS spectra of $(Al, Mg)_2Ca$ phase phases in the PM AC52 alloy.....	95
Fig. 5.10 (a) Typical TEM image of $(Al, Mg)_2Ca$ in PM AC52 alloy, (b) selected area diffraction pattern from $(Al, Mg)_2Ca$ phase with dark contrast, and (c) indexing of diffraction pattern in (b).....	96
Fig. 5.11 (a) Typical TEM image of $(Al, Mg)_2Ca$ in PM AC52 alloy, (b) selected area diffraction pattern from $(Al, Mg)_2Ca$ phase with dark contrast, and (c) indexing of diffraction pattern in (b).....	98
Fig. 5.12 (a) SEM micrograph, (b) total EDS line scans from the same region, and individual line scan: (c) Mg, (d) Al, (e) Ca and (f) Mn in the PM AC52 alloy	99
Fig. 5.13 EDS results for the PM AC52 alloy: (a) SEM micrograph, and elemental maps from the same region for (b) Mg, (c) Al, (d) Ca and (e) Mn.....	100

Fig. 5.14 HREM image of the $(Al, Mg)_2Ca$ phase along the [012] zone axis in the PM AC52 alloy.....	101
Fig. 5.15 TEM image of nano-scale Al_8Mn_5 particle in the PM AC52 alloy.....	101
Fig. 5.16 Twin structures in SEM images of: (a) AC505, (b) AC51, (c) AC515, (d) AC52 alloys, and in (e) and (f) TEM images of AC52 alloy	103
Fig. 5.17 HREM images along the [011] zone axis in the PM AC52 alloy. Nanostrain fields are surrounded by squares in (a); Dash line denotes twin boundary in (b).....	104
Fig. 5.18 Cooling curves obtained during solidification of the alloys cast at (a) $0.5 \sim 65^\circ C/s$ and (b) $T-t$ and dT/dt curves at $0.5^\circ C/s$ (T : temperature, t : time).....	107
Fig. 5.19 Cooling curves in: (a) the primary and (b) the eutectic regions of the AC52 alloys cast at lower cooling rates from 0.5 to $1.2^\circ C/s$ (T : temperature, t : time).....	108
Fig. 5.20 SEM micrographs of the microstructural evolution with cooling rates for: (a) $65.0^\circ C/s$, (b) $30.0^\circ C/s$, (c) $20.0^\circ C/s$, (d) $9.2^\circ C/s$, (e) $3.0^\circ C/s$ and (f) $0.5^\circ C/s$	111
Fig. 5.21 Variation of the SDAS with cooling rate for all the tested AC52 alloys on logarithmic scale.....	113
Fig. 5.22 SEM micrograph of the microstructure in: (a) the skin and (b) the center of the AC52 alloy cast at $30^\circ C/s$	114
Fig. 5.23 Variation of the volume fraction of the secondary eutectic phase with cooling rates for all the tested AC52 alloys.....	115
Fig. 5.24 SEM micrograph of the microstructure in the AC52 alloy recast at 1 and $12.5^\circ C/s$ with HTOU.....	117
Fig. 5.25 SEM micrographs showing the microstructural evolution with cooling rates for: (a) $30^\circ C/s$, (b) $9.2^\circ C/s$ and (c) $0.5^\circ C/s$	120
Fig. 5.26 TEM bright field micrograph of dispersed eutectic phases in the AC52 alloy cast at $30^\circ C/s$	122
Fig. 5.27 Variation of the Vickers hardness of the solution treated (T4) AM50 and AC51 alloys at $420^\circ C$, and AC52 alloy at $520^\circ C$ against solution time.....	125

Fig. 5.28 Microstructures of: (a) AM50 and (b) AC51 alloys solution treated at 420 °C for 2 h, (c) and (d) AC52 alloy solution treated at 520 °C for 2 h and 24 h, respectively.....	126
Fig. 5.29 Relationship between solution time (<i>h</i>) and the volume fraction (%) of the eutectic phase during the early stage of the solution treatment (T4) at 420 °C for the AM50 alloy and 520 °C for the AC52 alloy	128
Fig. 5.30 Age-hardening curves for the Mg-Al and Mg-Al-Ca alloys aged at 200 °C without solution treatment.....	129
Fig. 5.31 Effect of aging at 200 °C for 2 and 10 h on microstructures of the AC505 and AC51 alloys without solution treatment: (a) 2 h (AC505), (b) 10 h (AC505), (c) 2 h (AC51) and (d) 10 h (AC51).....	130
Fig. 5.32 Effect of aging at 200 °C for 2 and 10 h on microstructure of the AC515 and AC52 alloys without solution treatment: (a) 2 h (AC515), (b) 10 h (AC515), (c) 2 h (AC52) and (d) 10 h (AC52).....	131
Fig. 5.33 Age-hardening curves for the Mg-Al and Mg-Al-Ca alloys aged at different temperatures for 100 h after solution treatment for 2 h at 420 °C and 520 °C, respectively.....	132
Fig. 5.34 Effect of aging at different temperatures: (a) 120 °C, (b) 150 °C, (c) 200 °C, (d) 250 °C, (e) 300 °C and (d) 350 °C for 100 h on microstructures of the AC52 alloy solution treated at 520 °C for 2 h	134
Fig. 5.35 Age-hardening curves for the Mg-Al and Mg-Al-Ca alloys aged at 200 °C and 250 °C for different times after solution treatment for 2 h at 420 °C and 520 °C, respectively	135
Fig. 5.36 Effect of aging at 200 °C for given times: (a) 2 h, (b) 24 h, (c) 100 h, and (d) 1000 h on microstructure of the AM50 alloy solution treated at 420 °C.....	136
Fig. 5.37 Effect of aging at 200 °C for given times: (a) 2 h, (b) 24 h, (c) 100 h, and (d) 1000 h on microstructure of the AC51 alloy solution treated at 420 °C.....	137
Fig. 5.38 Effect of aging at 250 °C for given times: (a) 2 h, (b) 10 h, (c) 24 h, and (d) 100 h on microstructure of the AC52 alloy solution treated at 520 °C.....	140

Fig. 6.1	DSC traces of the DC AM50 alloy obtained at different heating rates ($^{\circ}\text{C}/\text{min}$)	142
Fig. 6.2	A plot of $\ln T_p^2/V$ and $1/T_p$ for determining activation energies of the dissolution of the secondary phases.....	143
Fig. 6.3	DSC traces of the PM AC series alloys: (a) AC505, (b) AC51, (c) AC515 and (d) AC52 obtained at a heating rate of $30\text{ }^{\circ}\text{C}/\text{min}$	144
Fig. 6.4	DSC traces of the PM AC 52 alloy obtained at different heating rates.....	146
Fig. 6.5	Effect of heating rate on the dissolution time of the secondary phase in the PM AC52 alloy during the DSC runs.....	147
Fig. 6.6	Variation of dissolution time with heating rate for the PM AC52 alloy.....	147
Fig. 6.7	A plot of $\ln T_p^2/V$ and $1/T_p$ for determining activation energies of the dissolution of the secondary phases in the PM AC52 alloy.....	148
Fig. 6.8	DSC traces for the PM AC 52 alloy run at a heating rate ($30\text{ }^{\circ}\text{C}/\text{min}$) /different cooling rates ($^{\circ}\text{C}/\text{min}$): (a) 5, (b) 10, (c) 20 and (d) 30.....	151
Fig. 6.9	(a) SEM image and typical EDS spectra from the main constituents of: (b) primary α -Mg solid solution, (c) Al_8Mn_5 and (d) β - $\text{Mg}_{17}\text{Al}_{12}$ in the AM50 after DSC runs.....	153
Fig. 6.10	Microstructural evolution in the AC series alloys: (a) AC505, (b) AC51, (c) AC515 and (d) AC52 after DSC run at a heating rate of $30\text{ }^{\circ}\text{C}/\text{min}$ followed by air quenching.....	156
Fig. 6.11	Higher magnification of the microstructures in: (a) the AC505 and (b) AC52 alloys after DSC run at a heating rate of $30\text{ }^{\circ}\text{C}/\text{min}$ followed by air quenching.....	156
Fig. 6.12	Effect of Ca content on grain size in the AC series alloys after DSC run at a heating rate of $30\text{ }^{\circ}\text{C}/\text{min}$ followed by air quenching.....	157
Fig. 6.13	Optical micrographs of the microstructures in the AC52 alloy after DSC run at heating rates ($^{\circ}\text{C}/\text{min}$): (a) 10, (b) 30 and (c) 50.....	159
Fig. 6.14	Variation of grain size with heating rate for the AC52 alloy after DSC run....	160

Fig. 6.15 SEM micrographs of the microstructures in the AC52 alloy after DSC run at heating rates ($^{\circ}\text{C}/\text{min}$): (a) 10 and (b) 40.....	160
Fig. 6.16 Variation of the microstructure of the AC52 alloy with cooling rates ($^{\circ}\text{C}/\text{min}$): (a) 5, (b) 10, (c) 20 and (d) 30 after heating at $30\text{ }^{\circ}\text{C}/\text{min}$ to $580\text{ }^{\circ}\text{C}$	161
Fig. 6.17 High magnification of the microstructure of the AC52 alloy obtained at cooling rates ($^{\circ}\text{C}/\text{min}$): (a) 5, (b) 20 and (c) 50 (air quenched) after heating at $30\text{ }^{\circ}\text{C}/\text{min}$ to $580\text{ }^{\circ}\text{C}$	162
Fig. 6.18 Effect of cooling rate after heating on grain size of the AC52 alloy.....	163
Fig. 7.1 Hardness profiles across casting thickness for the DC AM50 alloy with the thicknesses of: (a) 2mm, (b) 6 mm, and (c) 10 mm	175
Fig. 7.2 Average measured hardness across the casting thickness for the three tested DC AM50 alloys with different section thicknesses.....	176
Fig. 7.3 Hardness profiles across the casting thickness of 7 mm for: (a) the PM AM50 alloy and (b) the PM AC52 alloy.....	177
Fig. 7.4 Average measured hardness values in the skin and central regions for the five PM Mg-Al and Mg-Al-Ca alloys.....	178
Fig. 7.5 Average hardness values across the casting thickness and the hardness difference between the skin and central regions for the five PM Mg-Al and Mg-Al-Ca alloys.....	178
Fig. 7.6 Projected contact area functions, A , with and without tip shape corrections.....	180
Fig. 7.7 Typical load-unload curves for the indentation within the primary α -Mg grains for the as-cast Mg alloys using a Berkovich indenter with a maximum load of 8 mN: (a) ten individual locations on AC52 alloy, (b) five homologous load-unload curves, and (c) averaged load curves for these five Mg alloys.....	181
Fig. 7.8 Variations of: (a) nanohardness and (b) composite modulus with Ca content in Mg-Al base alloy.....	182

Fig. 7.9 Typical averaged load-unload curves for the indentation within the primary α -Mg grains for the as-cast Mg alloys using a Berkovich indenter with a maximum load of 8 mN.....	184
Fig. 7.10 Contact stiffness vs. penetration depth curves for the as-cast Mg alloys at room temperature.....	185
Fig. 7.11 Experimental and calculated hardness values vs. penetration depth curves for as-cast Mg alloys at room temperature.	186
Fig. 7.12 Experimental and calculated composite modulus values vs. penetration depth for as-cast Mg alloys at room temperature.....	187
Fig. 7.13 Calculated indentation results for the as-cast Mg alloys with a load of 8 mN: (a) hardness vs. penetration depth, and (b) composite modulus vs. penetration depth.....	190
Fig. 7.14 (a) Optical image of residual indent left by micro Vickers indenter and (b) SPM image of residual indent left by nano Berkovich indenter on the polished surface of the as-cast Mg-Al and Mg-Al-Ca alloys	191
Fig. 7.15 Vickers hardness values as a function of the yield strength of DC AM50 alloy	198
Fig. 7.16 Hardness size effect in the as-cast DC AM50, PM AM50, PM AC51 and PM AC52 alloys on the micro- and nano-scales.....	199
Fig. 7.17 Dependence of the hardness on the indentation displacement for the as-cast Mg alloys on the logarithmic scale.....	200
Fig. 7.18 H^2 vs. $1/h$ for the as-cast Mg alloys.....	203
Fig. 7.19 Changes of the experimentally measured penetration depth h , the indenter velocity \dot{h} , and average equivalent stress $\bar{\sigma}$ of the PM AC52 alloy with time at a load of 5 mN and at room temperature.....	206
Fig. 7.20 Indentation creep curves for: (a) the AC51 and AC52 alloys (cast at 30 °C/s) at applied loads of 1, 5, 8 mN, and (b) the as-cast AC52 series alloys (cast at different cooling rates) at an applied load of 5 mN at room temperature.....	207

Fig. 7.21 Relationship between the indentation velocity and penetration depth on logarithmic scales for: (a) the as-cast AC51 and AC52 alloys at loads of 1, 5 and 8 mN, and (b) the as-cast AC52 series alloys at a load of 5 mN at room temperature..... 208

Fig. 7.22 Indentation strain rate vs. normalized average equivalent stress ($\bar{\sigma} / E$) curves on a logarithmic scale for: (a) the as-cast AC51 and AC52 alloys at a load of 1 mN, and (b) the as-cast AM52 series alloys at a load of 5 mN at room temperature 209

Fig. 7.23 Variation of average Al and Ca contents with cooling rate in the primary α -Mg grains of the as-cast AC52 series alloys..... 213

LIST OF ABBREVIATIONS, SYMBOLS, NOMENCLATURE

AC	Mg-Al-Ca
AFM	Atomic force microscopy
BF	Bright field
CR	Cooling rate
CSM	Continuous stiffness measurement
DC	High pressure die cast
DIC	Differential isothermal calorimetry
DSC	Differential scanning calorimetry
DTA	Differential thermal analysis
EDS	Energy dispersive X-ray
FCC	Face centered cubic
GND	Geometrically necessary dislocations
HCP	Hexagonal close packed
HREM	High resolution electron microscopy
HTOU	High temperature observation unit
HV	Vickers hardness
ISE	Indentation size effect
KAS	Kissinger–Akahira–Sunose
MSG	Mechanism-based strain
OM	Optical microscopy
PM	Permanent mold cast
RE	Rare earth elements
SADP	Selected area diffraction pattern
SDAS	Second dendrite arm space
SEM	Scanning electron microscopy
SGP	Strain gradient plasticity
SPM	Scanning probe microscopy
SSD	Statistically stored dislocations gradient

T4	Solution heat treated
T6	Solution heat treated and aged
TCM	Tian–Calvet microcalorimeter
TEM	Transmission electron microscopy
TG	Thermogravimetry
TYS	Tensile yield strength
UTS	Ultimate tensile strength
VF	Volume fraction of eutectic
XRD	X-ray diffraction
Zn	Zinc

Symbols

a	Constant; Radius of the circle of contact
A	The projected contact area
b	Constant; Magnitude of the Burgers vector
B	Constant
C_0	Equilibrium solute content
C	A constraint factor; Mean solute content
d	Grain size
E	Elastic modulus; Activation energy
ΔG^*	Energy barrier
\dot{h}	Indenter velocity
h	Penetration depth
H	Hardness
L	Average dislocation spacing
n	Stress exponent for creep; Meyer exponent
m	Constant; Meyer exponent
q	Grain size exponent
P	Indentation load
ΔQ	Heat of reaction

Q	Activation energy
R	Gas constant; Indenter radius
R^2	Regression coefficient
S	Contact stiffness
t	Time
T	Temperature
V	Heating rate
Y	Yield strength
θ	Face angle of an indenter
α	Cone semi-angle; Transformed fraction
β	A geometrical correction term; The angle of a cone
ε	Intercept correction factor
ω	State variable
$\Delta\theta$	Undercooling
λ	Second dendrite arm space
δ	Elastic distortion
$\bar{\sigma}$	Average equivalent stress
ρ	Mobile dislocation density
\bar{v}	Average dislocation velocity

Superscripts

e	Eutectic reaction
p	Primary phase of solidification

Subscripts

$Grow$	Growth
$Nucl$	Nucleation
Min	Eutectic plateau

CHAPTER 1

INTRODUCTION

Magnesium alloys are attractive for application in the automotive, aerospace and other industries [1]. The low density of magnesium, only two thirds that of aluminum and less than one quarter that of iron, leads to relatively high specific stiffnesses and specific strengths for magnesium alloys. As a result, the use of Mg alloys in the automotive industry continues to grow in response to legislative requirements to reduce the weight of vehicles by substituting heavy ferrous structures with light Mg alloy components.

Some large structural components, such as steering wheels, transmission housings and engine blocks, can now be successfully obtained by substituting magnesium alloys for these components [2, 3]. Some of these components, which have complex shapes, can be cast by permanent mold casting, and particularly by high-pressure die casting, which achieves a near-net-shape component in one manufacturing step and allows rapid production rates. Because of its low heat content per unit volume, magnesium is particularly suitable for high-pressure die casting.

Conventional magnesium casting alloys have been based essentially on the Mg-Al system, with additions of Zn, Mn and, in some cases, Si. As an example, the commercial structural AZ91 alloys (Mg-9.0wt.%Al-1.0wt.%Zn), which have good castability, mechanical properties and corrosion resistance, are widely used in the automotive industry. However, due to the rapid degradation of the mechanical properties at elevated temperatures, especially the creep resistance, applications of these alloys are limited to specific components, which operate at temperatures below 150 °C [1]. Although the high temperature mechanical properties can be improved by adding Si to the Mg-Al base alloys, e.g. alloy AS21 (Mg-

2.0wt.%Al-1.0wt.%Si), the castability of the alloy deteriorates [4]. Previous work shows that an improvement in microstructure and mechanical properties, including creep resistance, can be achieved by the addition of rare earth elements to Mg alloys [5]. However, the cost of these alloys is somewhat higher than for conventional magnesium alloys. Therefore, the purpose of this study was to develop relatively low-cost as-cast magnesium alloys with sufficient elevated temperature strength. Ca is a relatively inexpensive alloying element, and the addition of Ca to Mg-Al alloys, such as AM50, can significantly modify and refine the as-cast microstructure of the alloys [6], reduce the oxidation during melting, and significantly improve the mechanical properties at room or elevated temperatures [7, 8]. While a large amount of room and high temperature macro-mechanical property data had been reported for the as-cast AM50 and Mg-Al-Ca alloys, there are little information relating the microstructure to local mechanical properties. A comprehensive understanding of the relationships between alloying additions, microstructure and the micro- and nano-mechanical properties for these Mg alloys need to be developed.

This study, therefore, focuses on understanding the solidification process and the evolution of the microstructure in Mg-Al and Mg-Al-Ca cast alloys after solidification and heat treatment. The relationships that exist between the microstructure and the micro- and nano-mechanical properties of die cast Mg-Al and permanent mold cast Mg-Al-Ca alloys have been studied using micro- and nano-indentation systems at room temperature. Important microstructural changes during DSC run have also been investigated in order to correlate the microstructural evolution and phase transformation with calorimetric kinetics.

The structure of this dissertation consists of eight chapters. Chapter 1 has provided a general background of as-cast Mg alloys, and the objective of this thesis. Chapter 2 is the

literature review, which overviews the composition, microstructure and mechanical properties of as cast AZ, AM, AS, and AE alloys (In the ASTM designation Mg alloys are identified by these alloying elements: A - aluminum; E - rare earths; M - manganese; S - silicon; Z - zinc). A review of important kinetic transformation changes that occur during DSC runs and the application of indentation technique in studying the local mechanical properties of materials is also included in Chapter 2. The experimental procedures used in the present study are described in Chapter 3. Chapter 4 reports the results on the effect of section thickness on the microstructure of high pressure die cast AM50 alloy. The microstructure of permanent mold cast AM50 alloy and the effect of calcium content on the refinement of permanent mold cast Mg-Al-Ca alloys are summarized in Chapter 5. The results of the kinetic transformations, which occur in Mg-Al and Mg-Al-Ca alloys during DSC runs, are reported in Chapter 6. In Chapter 7, indentation-testing results are presented. Chapter 8 summarizes the overall work, and Chapter 9 provides suggestions for future work.

CHAPTER 2

LITERATURE REVIEW

2.1 Magnesium casting alloys

With a density of two-thirds that of aluminum and only slightly higher than that of fiber-reinforced plastic, combined with excellent mechanical and physical properties as well as processability and recyclability, magnesium alloys are the obvious choice for light-weight designs. Because of their good castability, magnesium alloy castings can be produced by nearly all of the conventional casting methods including sand, investment, permanent and pressure die casting [9].

Cast magnesium alloys may be divided into two major groups: the zirconium-free alloys which mainly include Mg-Al and Mg-Al-Zn systems and the zirconium containing casting alloys with RE, Ag and Y as the primary additions. The strengthening mechanisms of magnesium alloys include grain refinement, solid solution strengthening, precipitation and dispersion hardening [9, 10].

2.1.1 Alloying magnesium alloys

Like most other metals, magnesium is rarely used in its pure form. Alloying is used to improve virtually all properties of magnesium for both wrought and cast products. Magnesium has a hexagonal lattice structure and has an atomic diameter that allows for solid solubility with a wide range of elements. Apart from cadmium, most binary alloys including magnesium form eutectic or peritectic systems [10]. The principal goal of alloying is to make specific improvements to the alloy's properties. Table 2.1 summarizes the characteristics of solid solutions and precipitates of binary magnesium alloy systems [11].

Table 2.1 Binary magnesium alloy systems [11]

System	Max. Solubility		Phase	Melting Point (°C)	System	Max. Solubility		Phase	Melting Point (°C)
	wt.%	at.%				wt.%	at.%		
Mg-Al	12.7	11.6	Mg ₁₇ Al ₁₂	402	Mg-Sm	5.8	0.99	Mg _{6.2} Sm	--
Mg-Ca	0.95	0.58	Mg ₂ Ca	714	Mg-Gd	23.5	4.53	Mg ₆ Gd	640
Mg-Sc	25.9	15.9	MgSc	--	Mg-Tb	24.0	4.57	Mg ₂₄ Tb ₅	--
Mg-Mn	2.2	1.0	Mn	1245	Mg-Dy	25.8	4.83	Mg ₂₄ Dy ₅	610
Mg-Zn	8.4	3.3	MgZn	347	Mg-Ho	28.0	5.44	Mg ₂₄ Ho ₅	610
Mg-Ga	8.5	3.1	Mg ₅ Ga ₂	456	Mg-Er	32.7	6.56	Mg ₂₄ Er ₅	620
Mg-Y	12.0	3.6	Mg ₂₄ Y ₅	620	Mg-Tm	31.8	6.26	Mg ₂₄ Tm ₅	645
Mg-Zr	3.6	0.99	Zr	1855	Mg-Yb	3.3	0.48	Mg ₂ Yb	718
Mg-Ag	15.5	4.0	Mg ₃ Ag	492	Mg-Lu	41.0	8.80	Mg ₂₄ Lu ₅	--
Mg-In	53.2	19.4	Mg ₃ In	484	Mg-Hg	3.0	0.4	Mg ₃ Hg	508
Mg-Sn	14.85	3.45	Mg ₂ Sn	770	Mg-Tl	60.5	15.4	Mg ₅ Tl ₂	413
Mg-Ce	0.74	0.13	Mg ₁₂ Ce	611	Mg-Pb	41.7	7.75	Mg ₂ Pb	538
Mg-Pr	1.7	0.31	Mg ₁₂ Pr	585	Mg-Bi	8.85	1.12	Mg ₃ Bi ₂	821
Mg-Nd	3.6	0.63	Mg ₄₁ Nd ₅	560	Mg-Th	5.0	0.49	Mg ₂₃ Th ₆	772

The most common alloying elements are aluminum, zinc, silicon, manganese, zirconium, yttrium, rare earth elements and calcium. Copper, nickel, and iron are considered harmful impurities that need to be controlled properly to insure the quality of magnesium alloys [10,12]. An aluminum addition to magnesium alloys improves the fluidity of molten magnesium alloys, making magnesium-aluminum alloys prime candidates for die casting. In Mg-Al-Zn alloys, an increase in aluminum content increases the yield strength but decreases the ductility [13]. A hard eutectic β -Mg₁₇Al₁₂ phase is formed by aluminum with magnesium, which contributes to both hardness and brittleness/ductility of as-cast Mg-Al alloys. The supersaturated solid solution produced by rapid solidification enables solid solution strengthening to play a significant role in determining the strength of all the die cast Mg-Al

alloys. Manganese is used primarily to enhance corrosion resistance. Silicon can improve creep resistance by forming Mg_2Si precipitates. Silicon may have a detrimental effect on the corrosion properties [9]. Zinc also improves fluidity and castability, but hot cracking and microporosity can be caused by high additions of zinc. Zinc strengthens the alloys by solid solution and precipitation strengthening [10, 12]. Zirconium is used in aluminum or manganese free magnesium alloys to provide improved room temperature and elevated temperature mechanical properties through grain refinement. Zirconium also reduces the tendency towards microporosity [10, 14]. Yttrium is used to improve high temperature creep resistance through age hardening and corrosion resistance. Rare earth additions including cerium, lanthanum, neodymium, gadolinium, and praseodymium can improve high temperature strength, and creep resistance, and reduce casting porosity [10], but they also result in susceptibility to oxidation problems during melting and casting. The addition of calcium has the potential to improve the creep resistance of Mg-Al based alloys due to the replacement of the $Mg_{17}Al_{12}$ phase by more stable Laves phases [7].

2.1.2 Mechanical properties of die cast Mg-Al alloys

Table 2.2 is a summary of typical mechanical properties of die cast Mg-Al alloys at room temperature [15-18].

Table 2.2 Typical room temperature mechanical properties of die cast Mg-Al alloys [15-18] *

Alloy	AZ91	AM60	AM50	AM20	AS41	AS21	AE42
Tensile Yield Stress (TYS), MPa	148	123	116	94	130	120	130
Elongation, %	6.6	12	14	16	10	12	13
Ultimate Tensile Stress (UTS), MPa	248	247	237	206	240	230	237

* The data in Table 2.2 are mean values obtained from 6 mm round tensile test bars cast in a cold chamber machine with a gauge length of 50 mm.

Although its ductility is the lowest, the AZ91 alloy has superior room temperature mechanical properties compared to all the other alloys included in Table 2.2. The AM series alloys exhibit an increased ductility compared to AZ91 while showing a decrease in yield strength and UTS. AM20 has higher elongation than AM60 as a result of the decrease in Al content. AS21 has been reported to have a yield stress of 120 MPa and a UTS of 230 MPa in Table 2.2 [15]. The tensile properties of AS21 are slightly lower than reported values for AS41 which is consistent with a decrease in room temperature strength with decreasing aluminum content [16, 17]. The ductility of die cast AS21 is clearly higher than that of AZ91. AS21 had the best combination of castability, room temperature mechanical properties and high temperature stress relaxation properties for applications in transmission housings with service temperatures reaching 150 °C [18]. Both the yield strength and the UTS of AE42 are close to those of AS41 and lower than those of AZ91. However, AE42 exhibits improved ductility over AS41 and AZ91, and its ductility compares well to that of AM50 or AM60.

2.1.3 Mg-Al alloy systems

2.1.3.1 Mg-Al-Zn alloys

The Mg-Al binary system is the origin of the most commonly used magnesium casting alloys. Alloys in the Mg-Al system are used in more than 95% of all magnesium castings and Mg-Al alloys, with or without zinc, such as AZ91 (Mg-9Al-1Zn-0.2Mn, wt.%) and AM60 (Mg-6Al-0.2Mn, wt.%) and AM50 (Mg-5Al-0.3Mn, wt.%) are the principal die casting magnesium alloys for room temperature applications [16]. Fig. 2.1 shows the Mg-Al binary phase diagram [19].

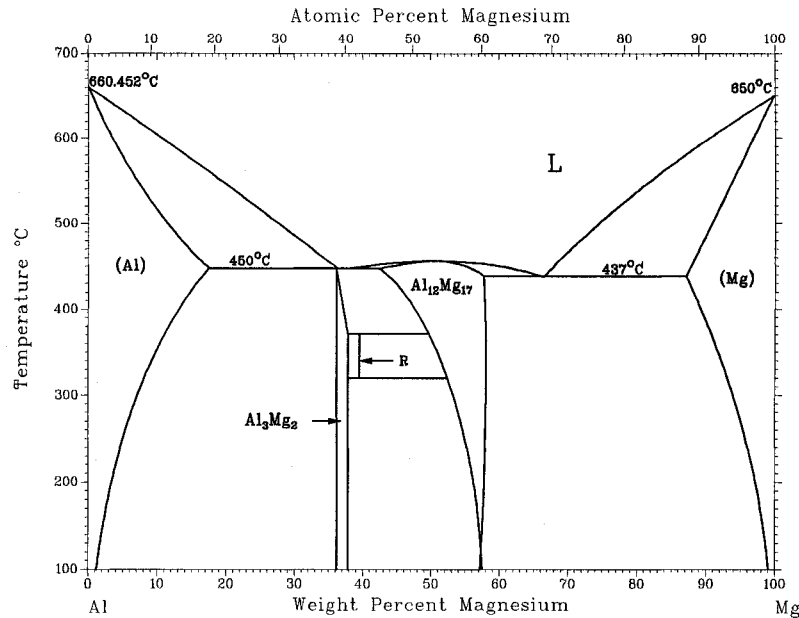


Fig. 2.1 Mg-Al binary phase diagram [19].

The maximum solubility of Al in Mg ranges from about 2.1wt.% at 25 °C to 12.7 wt.% at the eutectic temperature of 437 °C. Under equilibrium solidification conditions, the composition of aluminum should be higher than 12.7 wt.% before any eutectic β -Mg₁₇Al₁₂ phases appear in the microstructure. However, based on experimental investigations on the microstructure of the as-cast Mg alloys, the die cast Mg-Al alloys solidify under the non-equilibrium conditions. Usually, two distinct phases are observed in the microstructure of gravity or die cast AZ91 alloys [20-22], which are the primary α -Mg phase in a dendritic form along with interdendritic eutectic phases of α -Mg and β -Mg₁₇Al₁₂. A discontinuous β -Mg₁₇Al₁₂ phase is often observed in the microstructure of AZ91 cast at slow cooling rates [23]. A small amount of a ternary phase containing zinc, with a much lower melting point than the β -Mg₁₇Al₁₂, has also been observed in AZ91 [24]. It has also been suggested that the composition of the β -Mg₁₇Al₁₂ in AZ91 differs slightly from that present in Mg-Al alloys without zinc such that the composition of this eutectic phase in AZ91 is better represented by

$Mg_{17}(Al, Zn)_{12}$ [25]. Phases containing manganese are also present throughout the microstructure of AZ91 alloys [25, 26].

The β - $Mg_{17}Al_{12}$ phase that is present in the microstructure of as-cast AZ91 readily softens at elevated temperatures, which results in a weakening of the grain boundaries [27, 28]. It has been suggested that this is the principal reason for the poor creep properties of AZ91 and the other Mg-Al alloys [27, 29, 30].

AZ91B (Mg-9Al-0.7Zn-0.2Mn, wt.%) is the most commonly used die cast magnesium alloy. It exhibits good ductility and a moderately high yield strength at temperatures up to ~ 120 °C. AZ91A, which has a lower allowable copper content than AZ91B, is used when a higher corrosion resistance is required. AZ91C is used in pressure-tight sand and permanent mould castings, and has a high tensile strength and moderate yield strength [31]. The high purity AZ91D alloy is produced with the following impurity limits: wt.%Fe<0.005, wt.%Ni<0.001, wt.%Cu<0.015.

2.1.3.2 Mg-Al-Mn alloys

AM50 and AM60 alloys have good ductility and energy absorbing properties combined with good strength and castability. Typical uses are automotive seat frames, steering wheels, instrument panels, brackets and fans. AM20 is an alloy recognized for its ductility and impact strength. Typical uses are automotive safety parts where the highest possible ductility is required.

The presence of primary α -Mg and eutectic phases in the as-cast AM alloys is analogous to the non-equilibrium solidification principles discussed for the case of AZ91 [21, 32]. All the AM alloys have a smaller volume fraction of eutectic than AZ91. The amount of eutectic is related to the amount of aluminum in the alloy, with higher aluminum levels

resulting in more eutectic such that an AM20 alloy contains a smaller amount of eutectic than an AM60 alloy. AM20 probably contains a higher volume fraction of Mn intermetallics than AZ91 and AM60 since the solubility of manganese in the melt decreases with increasing aluminum content [26].

Typical stress-strain curves for die cast magnesium based alloys at room temperature [16, 33, 34] show that, at low aluminium contents, the alloys have a tendency to form a yield point and that the work hardening rate is decreased. The effect of the aluminium content on the tensile properties of AM type alloys at room temperature is shown in Table 2.3 [35]. These results show that there are relatively small changes in tensile properties by reducing the aluminium content below 6%. The ultimate tensile strength, tensile yield strength and fracture elongations do not change more than 10-20% when going from 6% Al down to 2% Al. Increasing the aluminium content from 6 to 8% increases the ultimate tensile strength and tensile yield strength values by about 3% and 21% respectively, along with decreasing the fracture elongation value by almost 70%.

Table 2.3 Tensile properties as a function of the aluminum content in AM type alloys [35] *.

AM series alloys	wt.% Al	UTS (MPa)	TYS (MPa)	Elongation (%)
AM20	2.0	217(±3)	99(±7)	18.8(±2.0)
AM48	4.8	229(±12)	116(±3)	15.2(±1.7)
AM53	5.3	249(±6)	123(±3)	16.0(±1.3)
AM58	5.8	253(±8)	125(±5)	16.1(±1.4)
AM64	6.4	250(±12)	131(±6)	14.3(±2.9)
AM69	6.9	248(±14)	132(±5)	12.8(±2.5)
AM75	7.5	258(±10)	151(±9)	8.7(±1.8)
AM80	8.0	245(±7)	159(±18)	5.4(±1.6)

*Room temperature values. Standard deviation values in parentheses.

For AM-type alloys, aluminium is the element that has the largest effect on aging properties. The amount of Al determines the formation of the binary β -phase $Mg_{17}Al_{12}$. A number of researchers [36-40] have reported up to 40 % reduction in fracture elongation values, up to 6~11 % increase in UTS, and 17~20 % increase in TYS for alloys containing from 4.5 to 6.5 % Al after aging up to 2,000 hours at temperatures of 110 ~ 125 °C.

2.1.3.3 Creep resistant Mg alloys

Factors influencing creep resistance: solute atoms can influence the creep strength of the matrix through the pinning of dislocations by “the solute atmosphere”. The presence of the solute atoms surrounding the matrix dislocations means that a greater stress is required to either move the dislocation away from its solute atmosphere, or to drag the atmosphere along with the dislocation [41-43]. This type of solid solution hardening is best achieved through the use of a solute differing markedly in atomic size and valency from the parent metal. This is because dislocations attract solute atoms which are either larger or smaller than the solvent atoms and also because the rearrangement of the conduction electrons around the dislocation attracts solute atoms of a different valency. In both cases, this results in segregation of solute atoms to the dislocation and the creation of a ‘solute atmosphere’ and a corresponding resistance to dislocation motion. Additionally, solute atoms may also affect the creep resistance of an alloy by influencing the stacking fault energy of the matrix and by the development of long range order in solid solutions [41].

Grain boundaries play an important role in elevated temperature deformation. Sliding of grain boundaries during elevated temperature deformation occurs as both a deformation mode in itself as well as enabling subsequent matrix deformation by relieving the stresses within grains. In both cases, the addition of solute elements results in the presence of second

phase particles which pin the grain boundaries is an essential design feature of creep resistant alloys [44]. The contribution of grain boundary deformation to the overall creep extension is also believed to increase as the grain size decreases [45, 46].

The presence of second phase particles is considered essential to produce a high level of creep resistance [47]. These particles could be present in the form of precipitates within the matrix, and/or as a dispersion at the grain boundaries. A sufficient volume fraction of finely dispersed particles can inhibit creep, irrespective of whether diffusion or dislocation creep processes are dominant [41]. Particle size, distribution and volume fraction of the second phase all affect the creep resistance and therefore it is necessary to maintain particle stability in both size and composition during exposure to elevated temperatures. In general, the thermal stabilities of intermetallics are proportional to their melting points: the higher the melting point, the higher the thermal stability. If intermetallics with a low melting point, such as $Mg_{17}Al_{12}$, dissolve at elevated temperatures, creep properties deteriorate.

As a consequence, the composition design of creep resistant Mg-Al alloys is based on the following principles:

- addition of alloying elements to decrease the diffusivity of atoms;
- suppression of the formation of the $Mg_{17}Al_{12}$ phase;
- precipitation of thermally stable second phases at grain boundaries; and
- introduction of dispersed small particles to pin dislocations.

Mg-Al-Si-Mn alloys: AS41 and AS21 are the two alloys that have been commercialized in the AS system. In 1969, Volkswagen used the die cast magnesium alloy AS41 (Mg-4.3Al-1.0Si-0.35Mn, wt.%) in a number of automobile parts such as the crank case and transmission housing [27]. Die cast AS41 has improved creep strength relative to

AZ91 and AM60 [15]. It is well established that AS21 is more creep resistant than AZ91 and AM60 alloys [13, 17, 26, 29] and slightly less creep resistant than the AE42 alloy [13, 27, 48]. In response to the requirement of increased load and temperature for the cast crank case component, alloy AS21 was developed and adopted by Volkswagen in 1971, when AS41 failed requirements due to creep. The AS21 alloy has significantly better creep strength than AS41.

As mentioned in Section 2.1.3.2, decreasing the aluminum content generally decreases the fluidity of Mg alloys and decreases the room temperature strength. As a result, AS41 has a slightly poorer castability than its predecessor AZ81. The loss of castability that results from a reduction in the aluminum level is somewhat compensated for by the addition of silicon which improves castability. Despite this, the lower aluminum content makes AS21 more difficult to cast [13, 49]. AS alloys also contain small amounts of manganese (~0.2 wt.%) at levels similar to AZ and AM alloys to improve corrosion resistance [26].

The low solid solubility of silicon of around 0.0003 at% at room temperature is a notable characteristic of the Mg-Si system [50]. The addition of silicon to die cast Mg-Al alloy introduces the high melting point Mg_2Si phase to the microstructure which, as a result of the die casting process, is finely dispersed. It is widely acknowledged that Mg_2Si is the only stable compound present in the microstructure of AS alloys [21, 32, 39]. Sakinnen [21] noted that the microstructure of AS41 also contained some eutectic β - $Mg_{17}Al_{12}$ and attributed the improved creep properties of AS 21 over AS41 to the reduction in the amount of eutectic β that resulted from the decrease in aluminum level. The positive effect of 1.0 wt.%Si on the creep properties of die cast Mg-Al alloys is well documented with AS21 showing a substantial improvement over the AM20 alloy [17, 26]. The effect of further additions of

silicon to die cast Mg-Al-Si-Mn alloys is not well established. However, it would be reasonable to expect that this may have detrimental effect on the ductility of the alloy due to an increased volume fraction of the brittle Mg_2Si phase.

Mg-Al-Ca alloys: The Mg-Al-Ca ternary system is one of the most important systems for further alloy development because Ca is a promising elemental addition for the following reasons:

- the addition of Ca significantly improves the high temperature strength and creep resistance [51-53];
- further improvement is possible with quaternary additions [53-55]; and
- it has a low density and a low cost.

Calcium can be introduced as a Mg-Ca master alloy. 15, 20 and 30% Ca master alloys are commercially available. Recommended addition temperatures for these master alloys depend on the Ca content and range from 680 - 720 °C.

In the grain boundary region of Mg-Al-Ca alloys, Mg_2Ca and/or Al_2Ca phases are reported to form during final eutectic reaction with the α -Mg phase. Mg_2Ca and Al_2Ca are Laves phases with hexagonal C14 and cubic C15 crystal structures, respectively. For an overall alloy composition of Mg-5.0wt.%Al-3.0wt.%Ca, the eutectic compounds have been variously reported to be Al_2Ca [6], Mg_2Ca [56], $(Mg, Al)_2Ca$ with hexagonal structure [7, 8], a mixture of these three phases [57] and a eutectic compound with the dihexagonal C36 structure [8]. The Ca containing compounds have stability at high temperatures, contributing to increased creep resistance, while also suppressing the formation of β - $Mg_{17}Al_{12}$ phase.

Ninomiya et al [58] reported that when the Ca/Al mass ratio was more than about 0.8, the compounds in Mg-Al-Ca series alloys identified by X-ray diffraction were Mg_2Ca and

Al₂Ca, but when the ratio was less than about 0.8, the compound was only Al₂Ca. Additionally, it was found that when the Ca/Al mass ratio was more than about 0.8, the hardness of Mg-Al-Ca series alloys became considerably higher than that of Mg-Al binary alloys.

The AXJ series alloys have been developed by modifying AC53 (Mg-5Al-3Ca, wt.%) with small Sr and Si additions [53-55, 59]. Table 2.4 summarizes the tensile yield stress, the total creep extension, and creep strength for Mg-Al-Ca series alloys in comparison with AE42 magnesium alloy. The results showed that AC52 and AC53 alloys exhibited 48-66% higher creep strength and 40-67% reduction in total creep extension than AE42 alloy. The addition of 0.03-0.15% Sr to AC53 alloy further improved the creep resistance of the Mg-Al-Ca alloys. Also, it was found that AC52 had slightly better creep resistance than AC53.

Table 2.4 Mechanical properties of Mg-Al-Ca and AE42 alloys [53-55, 59] *

Alloy	TYS (MPa)	Total Creep Extension (%)	Creep Strength (MPa)
AC52	160	0.06	75
AC53	186	0.09	74
AC53+0.3Si+0.1Sr	179	0.07	83
AC53+0.03Sr	186	0.08	-
AC53+0.07Sr	190	0.06	-
AC53+0.15Sr	-	0.08	83
AE42	107	0.12	50

* The tensile creep tests were performed at 175 °C with 70 MPa. Creep strength is the stress to produce 0.1% creep extension in 100 hours at 175 °C.

Mg-Al-Misch Metal (MM) alloys: Foerster [17, 60] reported that die cast AE21 containing 2% Al and 1% misch metal offers improved creep resistance over Mg-Al-Si alloys, and misch metal becomes more effective than silicon as the aluminum content is decreased. The strength and castability of Mg-Al-MM alloys can generally be improved by increasing the Al content, but this is at the expense of their creep strength. A compromise between the properties can be obtained by increasing both the Al and misch metal contents. AE42, for example, is inferior to AE21 in creep resistance by about 10-38 °C, but the loss in creep resistance and the higher cost of the greater rare earth content can be offset by an improvement in castability. Videm [61] concluded that the corrosion behavior of AE42 is superior to other Mg-Al alloys because of the low solid solubility of iron in the rare earth containing alloy.

The main intermetallic compound, Al_4MM (thermally-stable during solution treatment even at temperature as high as 500 °C), was found to form preferentially along grain boundaries in the AE42 alloy, and these phases have a well branched shape extending across a number of neighbouring grains [5, 18, 62, 63]. However, other RE containing phases have been noted in the microstructure of die cast AE42 including compounds containing manganese [18]. No eutectic β - $Mg_{17}Al_{12}$ is observed in AE42 [18, 21]. However significant segregation of Al (containing 4-7 at.%) in the matrix has been noted [18]. The presence of β - $Mg_{17}Al_{12}$ has been observed in die cast AE alloys which contain higher amounts of aluminum such as AE61 and AE91, which contain 6 and 9 wt.% Al respectively, indicating the formation of substantial amount of eutectics during the non-equilibrium solidification of these alloys. This results in regions of α -Mg, which are significantly enriched in solute Al, adjacent to these β phase particles in the as-cast microstructure [5, 63].

Foerster [17, 60] suggested that the excellent properties of AE21 at high temperatures can be attributed to the rapid solidification during the die casting process. The rate of solidification of AE21 during die casting is high enough to prevent extensive formation of the equilibrium Al-MM compound and sufficient misch metal is retained in solution to provide excellent high temperature properties.

2.1.4 Grain refinement of magnesium alloys by zirconium

As a potential grain refiner, Zirconium (Zr) can be added in magnesium alloys which contain zinc, rare earths, thorium, calcium, or a combination of these elements. However, Zr cannot be added in magnesium alloys containing Al, Mn, Si, Fe, Ni, Co, Sn and Sb [22], because stable compounds will form between zirconium and these elements. A very fine grained microstructure is obtained through adding low addition levels of soluble Zr (~0.04%) in magnesium alloys [64], and the maximum solubility of Zr in molten magnesium is approximately 0.6%. The addition of Zr in magnesium alloys can readily cause a decrease in the average grain size by 80% or more for normal cooling rates.

Sauerwald [65] reported that only dissolved Zr in the liquid magnesium is effective in grain refinement, while insoluble Zr, such as undissolved Zr particles, was believed to be irrelevant to grain refinement, despite both α -zirconium and magnesium having the same type of crystal structure and nearly identical lattice parameters. However, it was shown by Tamura et al [66] that undissolved Zr particles actually act as the grain refiner of magnesium alloys. Recent work [67] has confirmed the beneficial role of undissolved Zr particles in grain refinement and showed that grain refinement of magnesium alloys by Zr is dictated by both soluble and insoluble zirconium. Thus, an ideal Zr alloying process is to obtain both high soluble and high total Zr at the time of pouring.

However, zirconium can serve as a powerful grain refiner of magnesium only if the molten metal is saturated with soluble Zr at high temperature range of 750-800 °C. This leads to strong oxidation of the molten metal and loss of magnesium and expensive alloying elements such as Y, Gd, Dy, Yb, Nd etc. In addition, the existing technology of alloy preparation is based on single batch process with the use of small crucibles up to 300-400 kg. The process efficiency is relatively low due to the need to retain a significant amount of heel in the crucible in order to prevent the entrapment of settled inclusions and excessive Zr compounds in the castings. Thus, the preparation process and the use of expensive alloying elements results in relatively high cost of commercial gravity casting alloys both in ingot form and in final castings. Therefore, those alloys are mainly designated for the production of high performance complex castings, which are used in the aerospace industry and for luxury and racing vehicles. In such applications, the performance is of prime importance, while cost is regarded as a secondary factor [68].

2.1.5 Die casting and permanent mould casting

Magnesium alloys can be cast into products by die casting and permanent mould casting. Different alloys may be specified for the different processes. In cases where the same alloy is used with different casting processes, it is important to note that the properties of the finished castings depend on the fabrication method.

By far the most prevalent casting method is high-pressure die casting. During die casting, the mould, which is clamped together by hydraulic forces, is rapidly filled (5-100 ms) by forcing molten metal under pressure into permanent steel dies through a narrow gate. The metal solidifies with a high cooling rate, resulting in a fine-grained material. Die casting can produce shapes more complex than that produced by other metal forming process, and

castings with thinner walls. Greater length/thickness ratios, and the greater dimensional accuracies also can be produced by die casting. This method is the quickest and the most economical production process from raw material to finished product. The casting size is limited and the casting weight is normally less than 4.5 kg. The facilities for die casting are relatively expensive. There are two dominant types of die casting machines, horizontal cold-chamber and hot-chamber machines. The principal difference between the two machines is the way molten metal is fed to the machine. Whereas hot-chamber machines are fed by means of a piston pump submerged in the casting pot, cold-chamber machines rely on metering the liquid metal into the slot sleeve. Hot-chamber machines are therefore typically operated at lower casting temperatures than cold-chamber machines for small components, such as laptop and cell phone cases [69].

The permanent mold casting process is the production of castings by pouring molten metal into permanent metal molds under gravity pressure. Castings produced in permanent molds have finer grain structure and better strength properties than those cast from similar alloys in sand casting. Major savings through reduced machining costs are often obtainable because the castings have better dimensional uniformity, machining allowances are smaller, and holes may be accurately located and dimensioned with metal cores. In addition, a smooth surface finish is achieved right out of the mold, therefore, eliminating some secondary polishing operations. Permanent metal molds have a production life up to 120,000 or more castings. Generally the process is employed for larger, heavier section castings with low porosity level where large quantities are desired [70].

2.2 Indentation testing

2.2.1 Introduction

The indentation test for assessment of the penetration resistance of materials was developed over a hundred years ago and is widely used by the industry for material assessment and quality control. In such a test, an indenter is pressed into the surface under a fixed load and the depth of penetration or the area of the resultant impression can be used as a measure of the resistance of the material to damage. This is often characterized in terms of the indentation hardness which is given by the load divided by the area of the impression. The initial quantified test using a hardened steel ball indenter was developed by Brinell as a means of characterizing the variability of the steel [71], but a range of standard hardness tests have subsequently been developed which use indenters of different geometry, e.g. Vickers, Berkovich, Knoop and Rockwell tests [72, 73]. In conventional indentation tests, the area of contact is calculated from direct measurements of the dimensions of the residual impression left in the specimen surface upon the removal of load. However, in microindentation with low load, especially in nanoindentation tests, the size of the residual impression is of the order of microns and too small to be conveniently measured directly. In the last thirty years continuously recording indentation techniques have been developed [74] and are widely used to probe mechanical properties of materials at shallow contact depths. These instruments allow precise control of either the load or displacement during the test and can be performed with applied forces as low as a few micronewtons making indentations with depths in the nano range. Thus, it is customary to determine the contact area between the indenter and the specimen by directly measuring the depth of penetration of the indenter into the specimen surface.

In addition to measurements of hardness and Young's modulus of elasticity, static indentation tests have been used for measurements of a wide variety of material properties such as elastic-plastic deformation behaviour [75], flow stress [76], scratch resistance and film-substrate adhesion [77], residual stresses [78], creep [79-82], stress relaxation [83], fracture toughness and brittleness [84], and fatigue [85].

2.2.2 Indenter geometry and geometric similarity

2.2.2.1 Indenter shapes and sizes

Indenters of different geometry, such as spherical indenters and pointed indenters (Vickers, Knoop or Berkovich), with various sizes are available for indentation measurements. It is more convenient to make a three-sided than a four-sided sharp pyramidal diamond tip, because of the fact that three intersecting polished planes converge naturally to a single apex, while merging four planes at one point requires much more skill. Furthermore, although technologies exist for making hardened steel ball bearings, making very small size perfectly spherical diamond balls is nontrivial and would require expensive techniques such as ion milling using focused ion beams. Aside from these practical considerations, certain shapes of indenters possess the desirable property of self-similarity in indentation tests.

2.2.2.2 Geometric similarity

With an ideally sharp pyramidal or conical indenter, the ratio of the length of the diagonal or radius of circle of contact to the depth of the indentation remains constant for increasing indenter load. Indentation of this type has the property of "geometrical similarity." For geometrically similar indentations, it is not possible to set the scale of an indentation without some external reference. The significance of this is that the strain within the material is a constant, independent of the load applied to the indenter. For a spherical indenter, if the

indentation strain, a/R (a is the radius of the circle of contact and R the indenter radius), is maintained constant, then so is the mean contact pressure, and the indentations are geometrically similar.

The principle of geometrical similarity is widely used in hardness measurements. For example, owing to geometrical similarity, hardness measurements made using a diamond pyramid indenter are expected to yield a value for hardness that is independent of the load. For spherical indenters, the same value of mean contact pressure may be obtained with different sized indenters and different loads as long as a/R is the same in each case.

2.2.3 Measurements of mechanical properties

2.2.3.1 Hardness and elastic modulus

The two mechanical properties most frequently measured using indentation techniques are the hardness, H , and the elastic modulus, E . The most commonly used analysis method for obtaining hardness and modulus was developed by Oliver and Pharr [75]

Fig. 2.2 shows a typical load-penetration depth curve and the deformation pattern of an elastic-plastic sample during and after indentation.

Indentation hardness is defined as the indentation load divided by the projected contact area of the indentation. From the load-penetration depth curve, hardness can be obtained at the peak load as:

$$H = \frac{P_{\max}}{A} = \frac{P_{\max}}{24.5h_p^2} \quad (2-1)$$

where A is the projected contact area.

The elastic modulus of the indented sample can be inferred from the initial unloading contact stiffness, $S = dP / dh$, i.e. the slope of the initial portion of the unloading curve. The composite modulus of the system can be determined from the slope of the initial unloading [86]:

$$E^* = \frac{1}{2\beta} \frac{\sqrt{\pi}}{\sqrt{A}} \frac{dP}{dh} = \frac{1}{2\beta} \frac{\sqrt{\pi}}{\sqrt{A}} S \quad (2-2)$$

where $\beta = 1.034$ is a geometrical correction term to be applied for a Berkovich indenter [87] and accounts for the non-axisymmetric nature of the triangular pyramid geometry. The composite modulus is given:

$$\frac{1}{E^*} = \frac{1-\nu_s^2}{E_s} + \frac{1-\nu_i^2}{E_i} \quad (2-3)$$

where E_s and ν_s are elastic modulus and Poisson's ratio of the sample, and E_i and ν_i are elastic modulus and Poisson's ratio of the indenter.

To calculate hardness, H , and elastic composite modulus, E^* , from Eqs. (2-1) and (2-2), respectively, the contact stiffness (S) and the projected contact area (A) need to be determined from the load-penetration depth curve. Here, the method of the analysis of load-penetration curve for Berkovich indenter is presented in detail.

The Berkovich indenter has a face angle of $\theta = 65.27^\circ$. For a Berkovich indenter, the relationship between the projected area, A , of the indentation and the contact depth, h_p , beneath the contact area:

$$A = 3\sqrt{3}h_p^2 \tan^2 65.3 = 24.5h_p^2 \quad (2-4)$$

Once h_p is found, then the projected area of contact is thus calculated and the hardness is computed from Eq. (2-1).

It is convenient to examine the details of the method with reference to an axis-symmetric cone rather than the actual non-symmetric pyramidal indenter. It should be noted that a cone semi-angle of $\alpha_i = 70.3^\circ$ gives the same area to depth ratio as a triangular Berkovich indenter and is calculated from (It is convenient to regard the pyramidal geometry of a Berkovich indenter as an axis-symmetric cone for the purposes of analysis. The equivalent cone semi-angle α_i is calculated from):

$$\tan \alpha_i = \left(\frac{3\sqrt{3} \tan^2 65.3}{\pi} \right)^{1/2} \quad (2-5)$$

Upon unloading, the contact response is elastic and the relationship between the load, P , and the depth of elastic penetration, h_e , for a cone is given by [88]:

$$P = \frac{2E^*}{\pi} h_e^2 \tan \alpha' \quad (2-6)$$

where α' is the combined angle of the indenter and the residual impression, E^* is the composite modulus of the specimen and the indenter, and h_e is the difference in the depth of penetration at full load and the depth of the residual impression at full unload. The relatively large value of α' means that any effect of radial displacements predicted by the elastic contact equations can be ignored. The normal displacement h of points on the surface beneath the indenter is a function of the radial distance r from the axis of symmetry and is given by:

$$h = \left(\frac{\pi}{2} - \frac{r}{a} \right) a \cot \alpha' \quad (r \leq a) \quad (2-7)$$

As shown in Fig. 2.2, as the indenter is unloaded, the tip of the indenter (at $r = 0$) moves through a distance h_e and the edge of the circle of contact with the specimen surface

(at $r = a$) moves through a distance h_a . Making use of Eq. (2-7), at load P_t , the displacement h_e and h_a are given by:

$$h_e = \frac{\pi}{2} a \cot \alpha' \quad (2-8)$$

$$h_a = \left(\frac{\pi}{2} - 1 \right) a \cot \alpha' \quad (2-9)$$

and hence:

$$h_a = \left(\frac{\pi - 2}{\pi} \right) h_e \quad (2-10)$$

and also

$$h_t = h_p + h_a \quad (2-11)$$

Now, from Fig.2.2 (b), the maximum penetration depth, h_t , is given by:

$$h_t = h_p + h_a = h_p + \frac{\pi - 2}{\pi} h_e \quad (2-12)$$

From Eq. (2-6), the slope of the elastic unloading is given by:

$$\frac{dP}{dh} = 2E^* \frac{2}{\pi} h_e \tan \alpha' \quad (2-13)$$

Substituting back into Eq.(2-6), the load, P , can be determined by:

$$P = \frac{1}{2} \frac{dP}{dh} h_e \quad (2-14)$$

Substituting Eq.(2-14) into Eq.(2-10) and letting $P = P_{\max}$ and $S = dP/dh$, h_a is expressed:

$$h_a = \left[\frac{2(\pi - 2)}{\pi} \right] \frac{P_{\max}}{S} \quad (2-15)$$

h_p can now be found from Eq. (2-12), which leads to the projected area of contact A and hence the hardness H . The square-bracketed term depends on the indenter and is given the

symbol ε and in Eq. (2-15) is termed an “intercept correction factor” which is 0.72 for a cone as shown above, or 0.75 for a sphere and unity for a cylindrical punch. Oliver and Pharr [75] found experimental results on standard specimens indicated $\varepsilon = 0.75$ better accounts for the material behaviour and they suggest that the results from the inevitable tip rounding of a real indenter. There has been some formal justification for this choice of value for based upon the nature of the elastic recovery of the specimen material [89]. Thus,

$$h_p = h_t - 0.75 \frac{P_{\max}}{S} \quad (2-16)$$

Also, it was found [75] that the unloading curve is usually not linear, and should be described by a power law:

$$P = B(h - h_r)^m \quad (2-17)$$

where B and m are empirically determined fitting parameters. The unloading stiffness, S , is obtained by differentiating Eq. (2-17) at the maximum penetration depth, $h = h_{\max}$:

$$S = \left(\frac{dP}{dh} \right)_{h=h_{\max}} = Bm(h_{\max} - h_r)^{m-1} \quad (2-18)$$

The indentation tests are commonly used to measure surface mechanical properties of bulk materials. Oliver and Pharr [75] reported hardness and elastic moduli for six bulk materials including three materials used as a substrate for the construction of magnetic rigid disks and single crystal silicon. The data showed that indentation size has very little effect on the hardness values. In the case of aluminum and tungsten, there is a modest increase in hardness at low loads, which could be due to surface-localized cold work resulting from polishing. The moduli remain more or less constant over the entire range of load. The hardness value of single crystal silicon (110) is found to be about 11.5 GPa at a peak

indentation depth of 750 nm. This value is slightly higher than the macrohardness value of silicon of 9-10 GPa [90]. Using the atomic force microscope, Bhushan and Koinkar [91] and Bhushan et al. [82] investigated the hardness of single crystal silicon at an ultralow normal load and a corresponding residual indentation depth of 2.5 nm and reported a value of 13.5 GPa.

An increase in hardness at low indentation depths may result from contributions of the surface films. At small volumes, there is a low probability of encountering material defects. Furthermore, at small volumes, there is an increase in the stress necessary to operate dislocation sources [92]. According to the strain gradient plasticity theory advanced by Fleck et al. [93], the large strain gradients inherent in small indentations lead to the accumulation of the geometrically necessary dislocations that cause enhanced hardening. These are some of the plausible explanations for the increase in hardness at smaller volumes.

The nanoindenter is ideal for measurement of mechanical properties of thin films and composite structures. A number of investigators have reported the hardness of composite structures with thin films on a substrate [94, 95].

It is widely accepted that to measure the true hardness of the films, the indentation depth should not exceed 10% of the film thickness [68]. Based on a finite element analysis of the indentation of thin films of various thicknesses, Bhushan [96] concludes that true hardness of the films can be obtained if the indentation depth does not exceed about 30% of the film thickness.

2.2.3.2 Yield strength

Although hardness is the most often used quantity in the indentation test, it is not a basic material property. Its value depends on elasticity, ductility, and strain hardening of the material, and partly on the type of indenter and test conditions. As a consequence, it is often used only for qualitative evaluation of a material or for ranking of individual materials following various surface or heat treatments. A more useful quantity, characterizing inelastic behavior of a material, is the yield stress. This is a basic property, which can be used for determination of the mechanism of plastic deformation as well as for prediction of limit values of residual stresses or even of fracture behavior. Based on slip-line field solution for indentation in rigid-plastic solids by a frictionless rigid wedge and experimental observations of indentation in metals with elastic-perfectly plastic behavior, Tabor [72] has shown that the hardness can be related to the yield stress of the material in uniaxial compression, Y , by a simple expression:

$$H = CY \quad (2-19)$$

where C is a constraint factor (for soft metals, $C = 3$). Generally, the depth of penetration and contact area depend on plastic as well as elastic properties. This may be characterized by the ratio of elastic modulus to yield strength, E/Y , or to hardness, E/H . The process of indentation is predominantly controlled by plastic properties if the yield stress is much lower than the elastic modulus, $Y \ll E$. From the experimental and theoretical studies [97], the sufficient conditions is $E/H > 40$ (approximately), only for this case may the value $C = 3$ be used. For $E/H < 40$, the constraint factor C is smaller.

Johnson [97] proposed the following semi-empirical relationship between hardness, elastic modulus and yield stress with respect to the indenter geometry:

$$\frac{H}{Y} = \frac{2}{3} \left[2 + \ln \left(\frac{1}{3} \frac{E}{Y} \tan \beta \right) \right] \quad (2-20)$$

The agreement of equation of (2-20) with experimental data is good [20] but it can further be improved if a more general expression is used:

$$\frac{H}{Y} = A + B \ln \left(\frac{1}{3} \frac{E}{Y} \tan \beta \right) \quad (2-21)$$

Eqs. (2-20) and (2-21) are valid for pyramidal as well as spherical indenters. In the former case, β is the angle of a cone that would displace the same volume for the same depth of indentation. For Vickers and Berkovich indenters, $\beta = 19.7^\circ$.

$$5.76 < E/H < 38.6 \quad (2-22)$$

As it follows from the conditions $1 < H/Y < 3$ and $A = 1.25$, $B = 2/3$, $\beta = 19.7^\circ$.

2.2.3.3 Creep

Most materials including ceramics and even diamond are found to creep at temperatures well below half their melting point, even at room temperature. Indentation measurements have long been applied to the study of the strain-rate and temperature effects on the deformation behavior of materials. The analysis of creep is more complex than the analysis of creep data obtained using a conventional technique. Because of the shape of the tip, the indentation stress acting on the sample decreases with time as the contact area increases. Indentation creep is influenced by a large number of variables such as the plastic deformation properties of the material, diffusion constants, normal load of indenter, duration of the indentation, and the test temperature. Earlier experimental work was done primarily by measuring hardness as a function of time and temperature [98]. Later, instrumented indentation techniques, where load, displacement, and time could be controlled or monitored,

were developed to determine the creep properties of bulk materials. An example is the impression creep test using a cylindrical flat punch for examining metals and polymers [79, 99]. With the advent of nanoindentation, measurements of strain rate and temperature effects in thin films and nanostructured materials become possible [86, 100]. These measurements are important for a number of industrial applications, including interconnects for electronic devices, materials for lead-free solder joints, and metals exhibiting superplasticity for low cost forming of complex parts, as well as for fundamental understanding of deformation mechanisms at small length scales. Several types of indentation experiments have been proposed to gain insight into the strain-rate dependent properties of materials using self-similar indenters. Examples include the use of constant loading rate, \dot{P} ; constant displacement rate, \dot{h} ; or the keeping of parameters such as \dot{h}/h or \dot{P}/P constant. The “indentation strain rate” is usually defined as \dot{h}/h [86]. The strain-rate dependence of a measured property, such as hardness, is then expressed in terms of \dot{h}/h . This definition allows quantitative comparison between conventional creep or relaxation tests and indentation creep tests. It has been found that the creep exponent obtained from these macro- and micro-tests are comparable for metals [86] and ceramics [100] where the power-law creep model applies. A number of theoretical and numerical studies of indentation in strain-rate dependent solids have also appeared recently in the literature [101, 102].

2.2.3.4 Dynamic mechanical properties

Oliver and Pharr [75] introduced a dynamic indentation technique called continuous stiffness measurement (CSM), which offers a direct measure of dynamic contact stiffness during the loading portion of an indentation test, and, being somewhat insensitive to thermal drift, allows accurate observation of small volume deformation. Its applications are the study

of hardness, Young's modulus, creep and fatigue of graded materials and multilayered structures as a function of displacement [103]. The CSM technique has been used to perform nanoscale indentation creep testing [103]. Compared to conventional tensile creep tests, CSM indentation creep experiments are particularly useful as they simulate creep resulting from asperity contact.

2.2.4 Factors affecting indentation test data

It is usual to measure the load and depth of penetration directly during loading and unloading of the indenter in the indentation test to determine the projected area of contact for the purpose of calculating hardness and elastic modulus. In practice, various errors are associated with this procedure. The factors, which cause the errors, include: thermal drift [104], initial penetration depth [105], instrument compliance [106], indenter geometry [106], surface roughness [107], tip rounding [108], residual stresses [109], piling-up and sinking-in [110-113], and indentation size effect [114-120]. The most serious ones of these are indentation size effect and phenomena of piling-up and sinking in.

In an indentation testing, the geometry of the indenter is not ideal. To account for the non-ideal geometry of the indenter used in any practical test, it is necessary to apply a correction factor for the Eq. (2-4) to determine the real contact area at a given depth. The correction factor can be found from independent measurements of indenter geometry using either an AFM or SEM [106]. The measured real area is then plotted against the plastic depth determined from the measured depths. Regression analysis of the appropriate order may then provide an analytical function that gives the actual projected area for a given depth. This function is commonly called the "area function" for the particular indenter being

characterized. The area correction can be expressed as a mathematical function of the depth in a variety of forms, one popular expression being:

$$A = C_1 h_p^2 + C_2 h_p + C_3 h_p^{1/2} + C_4 h_p^{1/4} + \dots \quad (2-23)$$

2.2.4.1 Contact depth, “sinking-in” and “piling-up” phenomena

In an indentation into an elastic material, the surface of the specimen is typically drawn inwards and downwards underneath the indenter and sink-in occurs. When the contact involves plastic deformation, the material may either sink-in or pile-up around the indenter. In the fully plastic regime, the behaviour is seen to be dependent on the ratio of E/Y and the strain-hardening exponent of the material. It was found [110] that pile-up is most pronounced for non-strain-hardening materials with a high value of E/Y . Sink-in is more pronounced for strain-hardening or non-strain-hardening materials with a low value of E/Y .

Finite element analysis of contact in which pile-up occurs has demonstrated that the true contact area can be significantly greater than that calculated from the measured depth of penetration and the assumed elastic unloading response [110]. The existence of pile-up and sink-in can have a detrimental effect on the determination of the area function of the indenter if the specimen used for determination of the area function behaves differently to that of the eventual specimen to be tested.

Randall and Julia-Schmutz [111] compared the results for mechanical properties obtained from load-displacement curves on gold, titanium, and aluminum-coated silicon wafers with observed features of the residual impression obtained with an AFM. They found that for hard-coated specimens, the indenter load appears to be supported by a combination of elastic flexure and internal stresses of the coating resulting from plastic yielding of the substrate. For soft-coated systems, the indenter cuts through the softer surface layer causing

it to be squeezed outwards. The effect on the computed mechanical properties was found to be dependent upon the mode of deformation observed using AFM imaging.

McElhaney et al [112] describe a procedure for accounting for the effects of pile-up and sink-in based upon measurements of the contact stiffness and SEM pictures of the residual impressions from large indentations. This information provides a correction factor that quantifies the degree of pile-up and/or sink-in, and this factor can be applied to contact depths too small to be readily imaged thus providing a procedure for the determination of the area correction function for the indenter.

Bolshakov and Pharr [110] found that the results of finite element analysis showed that the ratio of the residual depth to the total depth is a useful parameter for predicting the constraint factor and the extent of pile-up during indentation in bulk materials for a given strain-hardening exponent. Finite element results [113] indicate that the dependence of the true contact area on the ratio of the slope of the loading curve to the slope of the unloading curve as a result of pile-up or sink-in if the strain-hardening characteristics of the specimen are known.

2.2.4.2 Indentation size effect

In a homogeneous isotropic material, one expects to measure only one value of hardness and modulus, yet, for a variety of reasons, experimental results often result in a variation of hardness and/or modulus with indentation depth. The indentation size effect (ISE) is considered as a phenomenon, in which an increase of hardness with decreasing indentation size (or load) for an indentation depth range typically less than about 10 μm . For a long time, the ISE was considered as a possible artefact caused by measurement errors or procedures of surface preparation. However, studies on the ISE were renewed and stimulated

by high accuracy depth-sensing micro- and nanoindentation [114] and scanning probe techniques [115] and fulfilling the requirements of the similarity of the indentation shapes and surface topography. Since the discovery of the ISE, many mechanisms have been offered for its explanation. ISE has been related to a surface effect [116], strain gradient effects [117], structural non-uniformity of the deformed volume [118], the change in the contribution of the elastic and plastic deformation at the indentation [119], and friction between the indenter and the sample [120]. The variety of proposed mechanisms emphasizes the rather complicated nature of the ISE. Most of the mechanisms developed are based on the suggestion of the dislocation nature of the ISE. Therefore, one could expect the manifestation of the ISE in crystalline solids, particularly in single crystals.

2.3 Calorimetric analysis

2.3.1 Introduction

Calorimetry is a thermal analysis method that measures the change in properties of substance under a controlled temperature program. Two particularly important reasons for performing kinetic studies to quantify the rate of a reaction are: (1) To predict the rate of reaction for any set of conditions by parameterizing the reaction rate as a function of state variables such as temperature, pressure, and concentration, and (2) To investigate the reaction mechanisms. The signals measured in thermal analysis include heat flows, temperature changes, mass, evolved gasses, length changes, elastic modulus, and many other properties that characterise properties or reactions of interest [121].

The most common techniques employed to study kinetics of thermally activated reactions are thermogravimetry (TG), differential thermal analysis (DTA), and differential scanning calorimetry (DSC). The TG technique measures mass loss from a sample due to gas formation as a function of time and/or temperature during a specified heating program. DTA measures the temperature difference between the sample and a reference material when both are subjected to the same heat flux. DSC measures the power required to keep the sample and a reference material at the same temperature throughout a specified temperature program.

2.3.2 Experimental aspects of calorimetry

The kinetics of thermally stimulated reactions is normally studied under the conditions of isothermal calorimetry and/or nonisothermal calorimetry.

2.3.2.1 Isothermal calorimetric analysis

Isothermal calorimetry can be performed with differential isothermal calorimetry (DIC), which uses the differential signal between a sample and a reference, and standard

isothermal calorimetry without using a reference. DIC can be carried out either with a standard power compensation DSC in the isothermal mode or in a much larger calorimeter with the high sensitivity, generally referred to as the Tian–Calvet microcalorimeter (TCM) [122].

A major problem of the isothermal experiment is that certain time is required to reach the desired temperature. During this period of nonisothermal heating, the sample undergoes some transformations that possibly affect the results of the following kinetic analysis. The situation is especially aggravated by the fact that, under isothermal conditions, a typical solid-state process has its maximum reaction rate at the beginning of the transformation.

2.3.2.2 Differential scanning calorimetry

Both DTA and DSC are concerned with the measurement of heat evolved from a substance during heating or cooling. The main distinction between DTA and DSC is that the equipment can be calibrated such that the heat evolution from the sample can be measured quantitatively in DSC, while this is often not possible for DTA [123]. There are two types of DSC: the heat flux DSC and the power compensation DSC [124]. For power compensation DSC, the signal is related to the differential heat provided to keep the sample and the reference to the same temperature. For heat flux DSC, the signal derives directly from the difference of temperature between the sample and the reference, and in that sense a heat flux DSC is similar to a DTA. For the heat flux DSC, the heat flux measurement has to be calibrated by performing calibration runs with standards that display a reaction for which the heat evolution is well known [125]. DSC, which has the characteristics of speed, convenience, accuracy and versatility, is probably the most popular of all such techniques according to the number of publications on thermal analysis techniques.

The advantages of nonisothermal calorimetry experiments are well known, but these temperature scanning methods have their own particular drawbacks and associated difficulties. On the experimental side, temperature inhomogeneities in the apparatus or in the sample can upset the specified controlled sample conditions. Further, analysis of nonisothermal experiments is generally more complicated than isothermal experiments, particularly because the changing temperature influences reaction rates. This added complexity in the past has made some researchers adopt a very cautious and often dismissive attitude towards the analysis of thermally activated reactions using nonisothermal methods. However, after more than four decades of research into the analysis of non-isothermal analysis methods, a large amount of knowledge has been gathered, and it has become increasingly clear that linear heating rate experiments, such as DSC, can be analyzed to reliably characterise many details of reactions. This, however, can be a daunting task as the amount of publications on the theory of analysis of thermal analysis data, and linear heating rate experiments in particular, is vast and very diverse in nature.

2.3.2.3 Sample preparation

Usually it is simple to prepare samples for the study of isothermal and nonisothermal calorimetry. The samples in the form of powder or ribbons can be put directly in a crucible. For bulk material, suitably sized samples can be readily punched from thin plate or cut from machined cylinders. The sample in isothermal calorimetry using a Tian–Calvet type instrument is either a cylinder which nearly fills the cavity in the calorimeter [126] or a batch of 10–20 disc-shaped samples with spacers to keep them apart, which is preferred for the tests with high and homogeneous cooling/quenching rates [127]. In DSC, the smaller sample generally is a single disc of about 0.5–2 mm thickness and 5-8 mm diameter [128].

In most calorimetric studies, the effects of sample preparation on the data are not a concern. However, it is well known that punching, grinding, machining and cutting all introduce deformation, and this influences precipitation by providing sites for heterogeneous nucleation, and by annihilating quenched-in excess vacancies [129,130]. Additionally, treatments on samples at relatively high temperatures can cause oxidation, or other surface reactions, and might cause loss of alloying elements to the atmosphere or to the reaction products formed in a surface reaction. For calorimetry samples, the thickness of the sample determines to a large extent the relative importance of the surface reactions, and also surface roughness can play a part.

2.3.2.4 Baseline correction in calorimetry

Although modern calorimeters are reliable instruments that can achieve remarkably high accuracies in measurements of heat evolution, negative effects always occur. The negative effects are often induced by disturbances from the outside of the measuring cell causing transients in heat flows within the zones where heat evolution from the sample and reference are measured. DSC in scanning mode has an initial transient period in which measurements are unreliable because in the very first phase of the experiment the heating rate accelerates from zero to the desired heating rate. During accelerating heating, the heat flow is variable, which depends on sample, pan and initial equipment temperature, and measured heat flows are not suited for analysis. In practice, this initial stage lasting approximately from 20 s to 1 min is generally disregarded. The duration of this transient is dependent on the thermal mass of the sample and oven, with the large ovens having a large transient. Power compensation DSCs in general have a lower thermal mass in the heated parts as compared to heat flux DSCs. Due to the reduced thermal mass in the oven section, power compensation

DSCs have the advantage of a short transient. In DSCs with a large furnace, mass transients of around 1 min can occur. At a heating rate of 100 K/min, this would result in a transient stretching over a range of 100 K. Thus, these transients limit the heating rate that can be used [131].

Unless the heat flows of reactions are significantly larger than the variability in the baseline, a correction for the temperature and time dependence of the baseline needs to be carried out. The standard procedure is to perform a DSC run with either empty inert pans, or an inert substance as sample and reference. Such a baseline run should be performed at the heating rate that is used for the actual experiment with a real sample, and is carried out just before or after the actual experiment with a real sample. In the post-analysis, the heat flow measured in the baseline run is subtracted from the heat flow in the experiment on the real sample [125].

2.3.3 Modelling of thermally activated reactions

2.3.3.1 Introduction

In many cases, calorimetry data obtained for metals have been analysed in a purely qualitative manner, i.e. by relating the presence of endothermic or exothermic effects to particular reactions without attempting to obtain quantitative information on these reactions or the mechanisms involved. Quantitative analysis is more often performed for isothermal experiments as compared to linear heating experiments. This is related to the availability of isothermal models, which are mathematically simpler than their non-isothermal equivalents. The type of modelling of thermally activated reactions that has been used in conjunction with calorimetry, or that can be applied to calorimetry, is of a broad and diverse nature. Modelling

approaches can mostly be classified as one of three types: (1) generic analysis models, (2) simplified physically based models, and (3) simulations.

A general objective of the modelling of thermally activated reactions by generic analysis methods and physically based methods is the derivation of a complete description of the progress of a reaction that is valid for any thermal treatment, be it isothermal, by linear heating or any other non-isothermal treatment. In the case of physically based methods, an additional aim is to be able to use the analysis to understand processes involved in the reaction.

2.3.3.2 Single state variable approaches

The most popular way of dealing with the complexity of thermally activated reactions is through the assumption that the transformation rate ($d\alpha/dt$) during a reaction is the product of two functions, one depending solely on the temperature T and the other depending solely on the fraction transformed α [132]:

$$\frac{d\alpha}{dt} = f(\alpha)k(T) \quad (2-24)$$

The temperature dependent function is generally assumed to follow an Arrhenius type dependency:

$$k = k_0 \exp\left(-\frac{E}{RT}\right) \quad (2-25)$$

where E is the activation energy of the reaction. Thus, to describe the progress of the reaction at all temperatures and for all temperature-time programs, the function $f(\alpha)$, and the constants k_0 and E need to be determined. A range of standard functions which represent particular idealised reaction models have been proposed [133,134] (See Table 2.5). Through selection

of specific $f(\alpha)$, the formalism described by the above two equations describes specific types of reaction kinetics.

Table 2.5 A set of alternate reaction models applied to describe the reaction kinetics in heterogeneous solid state systems [133, 134]

Reaction model		$f(\alpha)$
1	Power law	$4\alpha^{3/4}$
2	Power law	$3\alpha^{2/3}$
3	Power law	$2\alpha^{1/2}$
4	Power law	$2/3\alpha^{-1/2}$
5	One-dimensional diffusion	$1/2\alpha^{-1}$
6	Mampel (first order)	$1 - \alpha$
7	Avrami-Erofeev	$4(1 - \alpha)[- \ln(1 - \alpha)]^{3/4}$
8	Avrami-Erofeev	$3(1 - \alpha)[- \ln(1 - \alpha)]^{2/3}$
9	Avrami-Erofeev	$2(1 - \alpha)[- \ln(1 - \alpha)]^{1/2}$
10	Three-dimensional diffusion	$2(1 - \alpha)^{2/3} (1 - (1 - \alpha)^{1/3})^{-1}$
11	Contracting sphere	$3(1 - \alpha)^{2/3}$
12	Contracting cylinder	$2(1 - \alpha)^{1/2}$
13	Second order	$(1 - \alpha)^2$

2.3.3.3 Equivalent time, state variable, and temperature integral

The equivalent time concept refers to a method designed to describe any non-isothermal treatment with temperature path $T(t)$ by a single variable termed the equivalent time. It thus allows comparison of the progress of a reaction when samples are exposed to different temperature paths $T(t)$, e.g. compare the progress of a reaction under linear heating

conditions with the progress during isothermal annealing. The equivalent time approach is valid if the progress of a reaction can be described by a single state variable.

In the state variable approach, it is considered that the fraction transformed is a unique function of a state variable ω . If there is one single temperature dependent process operating, ω is given by:

$$\omega = \int_{t=0}^{t_e} k dt \quad (2-26)$$

For isothermal reactions at T_{iso} it simply follows:

$$\omega = kt_e \quad (2-27)$$

The state variable approach is justified in the case that Eq. (2-24) is valid. In this case, the above equation can be integrated:

$$\int_{\alpha=0}^{\alpha_e} \frac{d\alpha}{f(\alpha)} = \int_0^{t_e} k(T) dt \quad (2-28)$$

and, as the left-hand side of this equation is a unique function of the fraction transformed, a state variable can be defined as:

$$\omega = \int_{\alpha=0}^{\alpha_e} \frac{d\alpha}{f(\alpha)} \quad (2-29)$$

One result from these equations is the derivation of the equivalent time, which is defined as the time at temperature T_{iso} needed to complete the same amount of the reaction during a non-isothermal treatment. Considering that in many cases k can be assumed to be an Arrhenius expression, the equivalent time is given as:

$$t_{eq} = \int_{\alpha=0}^{\alpha_e} \exp\left(-\frac{E}{RT(t)}\right) dt \left[\exp\left(-\frac{E}{RT_{iso}}\right) \right]^{-1} \quad (2-30)$$

For linear heating, we can derive:

$$\int_{t=0}^{t_e} \exp\left(-\frac{E}{RT(t)}\right) dt = \frac{E}{RV} \int_{y=y_f}^{\infty} \frac{\exp(-y)}{y^2} dy \quad (2-31)$$

where $y = E/RT$, $y_f = E/RT_e$ (T_e being the temperature reached during the linear heating), and V is the heating rate. Thus, to obtain the equivalent time for linear heating, we need to calculate the integral:

$$\int_{y=y_f}^{\infty} \frac{\exp(-y)}{y^2} dy = p(y_f) \quad (2-32)$$

This integral $p(y)$ is termed as the temperature integral or Arrhenius integral.

A range of approximations of the temperature integral $p(y)$ have been suggested in the literature. All the known approximations will lose accuracy for small values of y (typically for y below 10-15) and some lose accuracy for large values of y (typically y exceeding 100). In a previous work [135], it was shown that the range of y values that in practice occur is limited for various reasons. It was concluded that only the range $9 < y < 100$ is of practical significance, while the overwhelming majority of reactions in fact occur for $15 < y < 60$. The temperature integral can be calculated using expansions of the integral in an infinite series, of which several forms have been proposed [136], and a range of approximations in the form of a finite number of terms have been proposed in the literature [135,136]. From this group of methods, the approximation for which the deviation reduces to zero in the limit of very large values of y is the approximation by Murray and White [137]:

$$p(y) \cong \frac{\exp(-y)}{y^2} \quad (2-33)$$

The approximation in Eq. (2-33) has been used to this end, and leads to [138]:

$$t_{eq} \cong \frac{T_f}{V} \frac{RT_f}{E} \exp\left(-\frac{E}{RT_f}\right) \left[\exp\left(-\frac{E}{RT_{iso}}\right) \right]^{-1} \quad (2-34)$$

The above expressions for equivalent time can be used in many problems where the progress of a reaction during linear heating needs to be compared with the progress during isothermal aging (or linear heating at a different heating rate).

2.3.3.4 Activation energy determination

Activation energy for the overall reaction generally is related to activation energy for the physical process that determines the rate of the reaction. Hence the objective of activation energy analysis is to permit a better understanding of the mechanisms of the thermally activated reaction. For linear heating experiments, activation energies of reactions can be derived from a set of experiments performed at different heating rates [138-140].

For activation energy analysis using isoconversion methods, and Eqs. (2-24) and (2-25), it follows immediately that for transformation studies by performing experiments at constant temperature T_i , E can be obtained from the well known relation:

$$\ln t_f = \frac{E}{RT_i} + C_1 \quad (2-35)$$

where t_f is the time needed to reach a certain fraction transformed, and C_1 is a constant which depends on the reaction stage and on the kinetic model. Thus, E can be obtained from two or more experiments at different values of T_i .

The equivalent stage (also called the constant or fixed stage) may be defined as the stage at which a fixed amount is transformed, or at which a fixed fraction of the total amount is transformed. Isoconversion methods includes the Kissinger method [137], the Kissinger–Akahira–Sunose method [141], the Flynn–Wall–Ozawa method [138], and several methods that were devised more recently [138]. These methods have been termed type B isoconversion methods [136]. The approximation of the temperature integral, which is key to

these methods, is here illustrated by considering the derivation of the Kissinger–Akahira–Sunose (KAS) method. In this derivation, Eq. (2-25) is inserted in Eq. (2-24) and this is integrated by separation of variables:

$$\int_0^\alpha \frac{d\alpha}{f(\alpha)} = \frac{k_0}{V} \int_0^{T_f} \exp\left(-\frac{E}{RT}\right) dT = \frac{k_0 E}{VR} \int_{y_f}^\infty \frac{\exp(-y)}{y^2} dy \quad (2-36)$$

where T_f is the temperature at an equivalent (fixed) state of transformation, and V is the heating rate. Using the Murray and White [142] approximation for $p(y)$ (Eq. (2-33)) yields:

$$\ln \int_0^\alpha \frac{d\alpha}{f(\alpha)} = \ln \frac{k_0 E}{R} + \ln \frac{1}{Vy_f^2} - y_f \quad (2-37)$$

At constant fraction transformed α , this leads to:

$$\ln \frac{V}{T_f^2} = -\frac{E}{RT_f} + C_2 \quad (2-38)$$

where C_2 is parameter that are independent of T and V . According to Eq. (2-38), plots of $\ln(V/T_f^2)$ versus $1/T_f$ should result in straight lines, the slope of the straight lines being equal to E/R .

2.3.5 Applications of thermal analysis for Mg based alloys

DSC experiments by themselves cannot identify the phases involved in the reactions. Other techniques, such as transmission electron microscopy (TEM) with selected area diffraction (SAD) and/or chemical analysis, for instance, by electron dispersive X-ray spectroscopy (EDS), and X-ray diffraction, should be used to identify these phases. Several of these studies have been reported [143-145]. In order to identify the phase changes, samples are heated to different conditions that correspond to the start, middle and end of the thermal effect, and then are rapidly quenched after heat treatment in this procedure.

DSC is a very valuable and efficient technique to analyze a number of reactions that occur in Mg based alloys, which include homogenisation and solution treatment [146-148], precipitation [149, 150], solidification [151-153], melting and incipient melting [154], and phase equilibria [155, 156].

Zheng et al [146] reported that the peak temperature of the $Mg_{17}Al_{12}$ dissolution in the SiCw/AZ91 magnesium matrix composite is higher than that in the monolithic alloy, which means that the precipitation kinetics is accelerated, and the stability of the precipitates is enhanced by the addition of SiC whisker.

In digital DSC studies on as-cast and T6 treatment and water quenched samples of WE43 (Mg-4.2wt.%Y-3.1wt.%E) and Elektron 21 (Mg-4.0wt.%E-3.1wt.%Zr) Mg alloys [149], it was observed that small and extended exothermic effects were found in all the samples at 150 °C, which corresponds to the formation of the metastable phases having different shapes and compositions. Also, large endothermic effects due to the dissolution of the same phases were evident in the range 200-300 °C, and an exothermal precipitation reaction at about 380 °C, which is due to the transformation of the metastable phase into the equilibrium phase.

An illustration of an application of isochronal DSC to a relatively simple binary Mg based alloy, is the study of solidification in an Mg - (1.7-8.3 at.%) Y alloy by Sommer et al [151]. The DSC curves for rapid solidification reveal three exothermic and two endothermic thermal effects. The activation energy for microstructural evolution in this temperature regime drops drastically at concentrations of more than 5.5 at.% Y.

In Mg alloys, which contain intermetallic phases, the melting of the Mg-rich phase is often preceded by melting of one or more of those minority phases, and this type of melting

is often termed 'incipient melting'. An illustration of the application to more complex alloys are the studies by Jardim et al [154] on melting in melt-spun Mg-Ca-Zn alloys. The large DSC peaks indicated that they were related to the onset of alloy melting and not to the precipitate dissolution. The measured melting onsets for the three Mg alloys MCZ-1, MCZ-2 and MCZ-3, which decrease with Zn content, were 412, 398 and 377 °C, respectively.

Additionally, DSC is an important tool for obtaining phase equilibria of liquid and solids, and such measurements can be used in verification of the predicted phase diagrams. The thermodynamic description of Mg-Al-Zn system has been reported by Liang et al. [155] and Ohno et al [156]. The good agreement between the experimental and calculated results strongly supports the reliability of the thermodynamic description. Based on thermodynamic calculation, it is clarified that a signal observed in thermal analysis, which was interpreted as the end of solidification in the literature, is related to the start of the monovariant eutectic reaction $L + (Mg) + \gamma\text{-Mg}_{17}\text{Al}_{12}$ under non-equilibrium condition, and the solidification process ends at lower temperature.

2.4 Summary

Based on the literature review, the addition of Ca in the Mg-Al alloy can significantly improve the high temperature strength and creep resistance of the relatively low-cost Mg-Al-Ca alloys by forming the stable Mg_2Ca and/or Al_2Ca Laves phases or $(\text{Al}, \text{Mg})_2\text{Ca}$ phase along the grain boundaries during the solidification. However, there have been no studies on the effect of solidification rates and calcium additions on the microstructural characteristics of the PM Mg-Al-Ca alloys. Also, there is little documentation regarding the relationship between the microstructural evolution after heat treatment and the micro-mechanical properties of the PM Mg-Al-Ca alloys.

Although the macro creep resistance of the Mg-Al-Ca alloys at elevated temperatures is recently reported [51-59], there are no publications describing the local creep behaviour of the PM Mg-Al-Ca alloys. The Mg-Al and Mg-Al-Ca alloys cast by die casting or permanent mold casting have the obvious chill effect (microstructural gradient), i.e. the fine structure in the skin of the casting, and the relatively coarse structure in the center of the casting. For this reason, micro- and nano-indentation systems are particular favoured for studying the local mechanical properties in a small volume of the as-cast Mg alloys having microstructural gradients, while the traditional methods, e.g. tensile test, are only applicable to the evaluation of the mechanical behaviour of bulk materials. Additionally, the contact area of the micro- and nano-indentation tests can be conveniently determined by measuring the penetration depth into the sample surface.

The industrial production of Mg alloys often involves a number of processing stages including casting, homogenization, preheat, hot rolling, solutionizing and ageing. Precipitation and dissolution of second phase particles occur during each of these processing steps and have a major influence on the microstructural evolution in subsequent stages. Therefore, to understand the origins of the microstructure of the final product, it is necessary to understand these interactions. Moreover, precipitation during intermediate processing steps usually occurs under non-isothermal conditions. The technique of Differential Scanning Calorimetry (DSC) is suitable for the detailed study of the kinetics of these phase transformations of the as-cast Mg alloys. However, there is very little detailed information relating the microstructure and the phase transformation to the kinetics of the as-cast Mg alloys.

CHAPTER 3

EXPERIMENTAL PROCEDURES

3.1 Experimental material

3.1.1 Die casting

AM50 flat rectangular coupons of 125mm×27mm with different thicknesses of 2, 6 and 10 mm were die cast in a 700 ton cold chamber horizontal high pressure die casting machine. The chemical composition of die cast AM50 alloy (DC AM50) is given in Table 3.1. Table 3.2 summarizes the die casting process parameters. A schematic illustration of die casting coupons with the thicknesses of 2, 6 and 10 mm is shown in Fig. 3.1.

Table 3.1 Chemical composition of DC AM50 alloy (wt.%)

Alloy	Al	Mn	Ca	Si	Other	Mg
DCAM50	4.92	0.294	0.0	0.013	<0.01	Balance

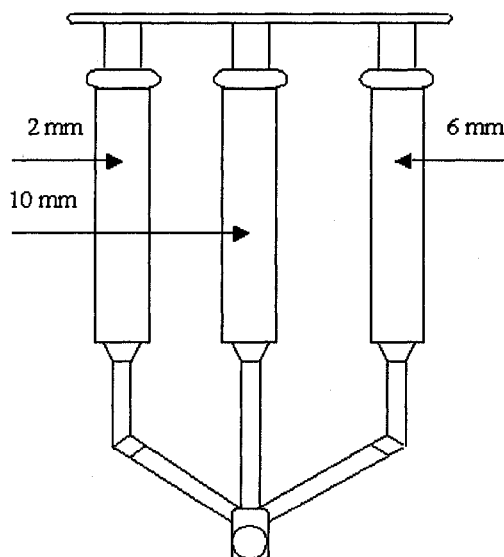


Fig. 3.1 Schematic illustration showing DC AM50 coupons with thicknesses of 2, 6 and 10 mm.

Table 3.2 Die casting process parameters

Plunger tip diameter	57.15 mm
Sleeve length	482.6 mm
Metal temperature	677 °C
Fill time	0.025 s
Oil temperature	66 °C
Cycle time	25 s
Die temperature	200 °C

3.1.2 Permanent mold casting

The Magnesium alloy designated as AM50 was selected as the base alloy in this study, and was provided by the Ford Motor Company. A master alloy of magnesium-calcium (70Mg-30 Ca, wt.%) produced by Timminco Metals was used to produce the desired alloys with different calcium contents (PM Mg-Al-Ca alloys). Raw materials were supplied in cast ingot bars. Small pieces cut from AM50 casting ingots were melted in a mild steel crucible which is inside a Lindberg/Blue M CF56822C Crucible furnace (Lindberg/Blue M Thermo Electron Corporation, Asheville, North Carolina, USA). To protect the melt from any excessive oxidation or possible burning, a protective gas (Sulfur Hexafluoride SF₆ 0.5% + Carbon Dioxide CO₂) was used during both melting and casting. When the temperature of the molten liquid metal was close to 760 °C, which was measured by a digital thermometer Omega HH509, the molten metal was poured from the crucible into the cavity of permanent copper molds (Fig. 3.2). First, AM50 alloy with calcium addition varying from 0.0 to 2.0 wt.% were cast using copper disk mold, as shown in Fig. 3.2(a). Then, to investigate the effects of cooling rates on the microstructure and mechanical properties of the alloy with 2 wt.% Ca addition, fast cooling rates (20 ~ 65 °C/s) were achieved by using copper disk mold

(Fig. 3.2(a)), while slow cooling rates ($0.5 \sim 9.2 \text{ }^{\circ}\text{C/s}$) were obtained by using a series of short copper tubes with diameters from 25 to 50 mm (Fig. 3.2(b)). Before pouring, the copper tubes or mold were preheated to $200 \sim 300 \text{ }^{\circ}\text{C}$. The casting produced by a copper disk mold was a flat circular disk 7 mm in thickness and 44 mm in diameter. Measurement of cooling rates was made by placing a thermocouple KTSS-116U-24 (Omega Engineering Inc., Stamford, Connecticut, USA) at the center or edge of the castings. Specimens for microstructural characterization were cut from castings at a location close to the tip of the thermocouple. The results of the chemical analysis of the specimens cut from the casting with different calcium contents are summarized in Table 3.3.

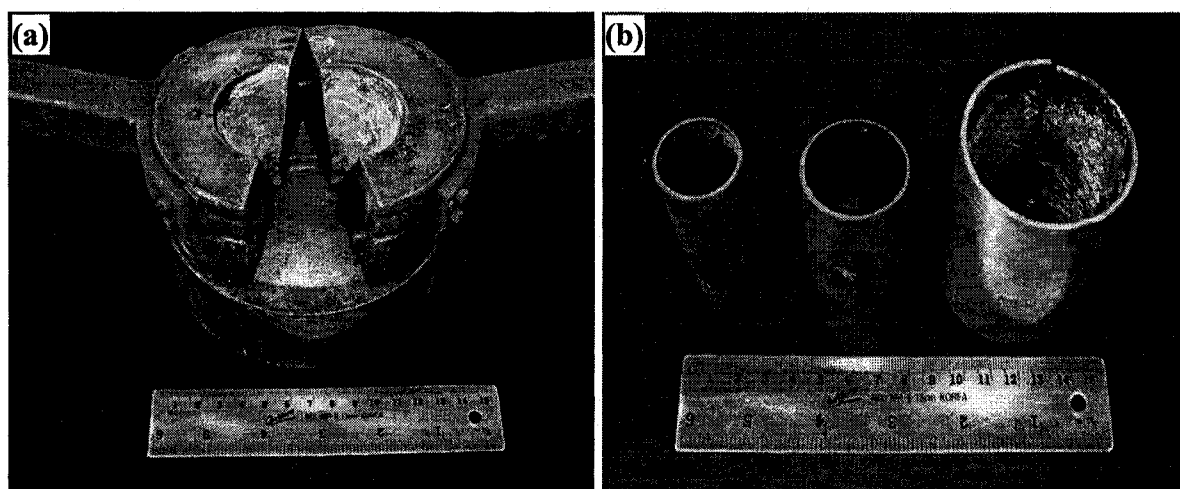


Fig. 3.2 Permanent copper molds: (a) disk mold and (b) tube molds

Table 3.3 Chemical compositions of the permanent mold cast alloys (wt.%)

Mg Alloy	Designation	Al	Ca	Mn	Zn	Fe	Si	Mg
Mg-5.0Al-0.0Ca	PM AM50	4.93	0.0	0.296	0.0023	0.0026	0.0164	Balance
Mg-5.0Al-0.5Ca	PM AC505	4.78	0.514	0.295	0.0025	0.0020	0.0178	Balance
Mg-5.0Al-1.0Ca	PM AC51	4.87	0.966	0.289	0.0027	0.0036	0.0175	Balance
Mg-5.0Al-1.5Ca	PM AC515	5.15	1.451	0.295	0.0025	0.0044	0.0204	Balance
Mg-5.0Al-2.0Ca	PM AC52	4.89	1.966	0.278	0.0024	0.0033	0.0170	Balance

3.1.3 High Temperature Observation Unit

In order to characterize the microstructures under different solidification conditions from using copper molds, the PM AC52 alloy was recast at cooling rates of 1 °C/s and 12.5 °C/s in a High Temperature Observation Unit (HTOU) made by ULVAC-Riko Inc (Fig. 3.3). The HTOU can accurately control the cooling rate of specimens that were put in the cylindrical alumina crucible (4mm inner diameter, 3mm height). Extra-high-purity argon gas was bled into the upper cavity of HTOU to prevent oxidation. The temperature of the crucible can be controlled to within $\pm 1\text{K}$ with a thermocouple welded to the platinum container that held the alumina crucible.

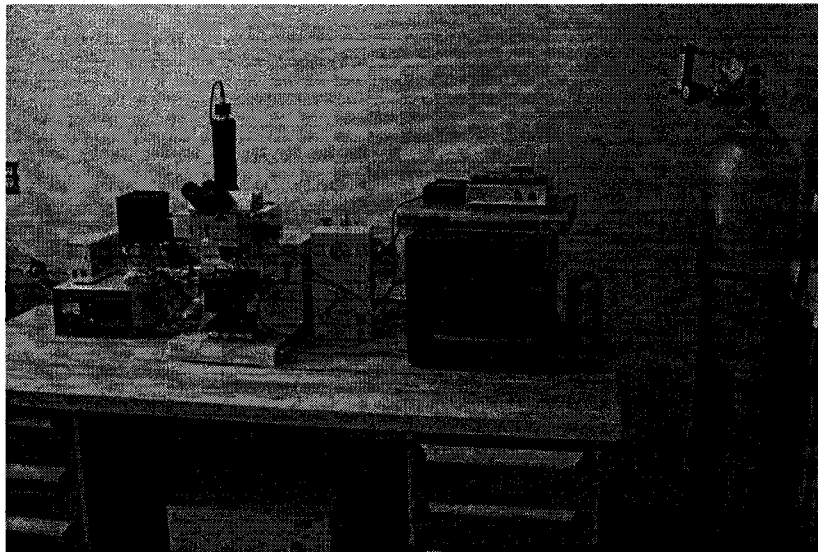


Fig. 3.3 ULVAC-Riko high temperature observation unit.

3.2 Heat treatment

A number of permanent mold cast Mg alloys were heat-treated. Based on the DSC results in Chapter 6, heat treatments (T4) were performed for various times (0.5 ~ 24 h) at 420 °C for PM AM50 and AC51 alloys and at 520 °C for AC52 alloy followed by water

quenching to investigate the evolution of the microhardness and the volume fraction of eutectic during the early stage of the solution treatment. Based on the above results, PM AM50, AC505 and AC51 alloys were finally solution heat treated at 420 °C for 2 h, and at 520 °C for 2 h for PM AC515 and AC52 alloys followed by water quenching. Specimens of all the tested alloys, with and without solution treatment, were age hardened for various times (2-1000 h) at 200 °C for PM AM50, PM AC505 and PM AC51 alloys and at 250 °C for PM AC515 and PM AC52 alloys, and also at 150, 200, 250, 300 and 350 °C for alloys PM AC51 and AC52 alloys for 100 h. In order to avoid burning or severe oxidation, the specimens of the alloys to be solution treated at 520 °C were sealed in a vacuum in pyrex capsules, and other specimens were embedded in Al₂O₃ powder during solution treatment at 420 °C and at temperatures lower than 420 °C during aging.

3.3 Indentation testing

Because both microindentation and nanoindentation test results were very sensitive to the surface quality of specimens at low load, specimens were first polished with the 1 μm and then 0.05 μm alumina polishing suspensions before indentation testing.

3.3.1 Microindentation testing

The Vickers microhardness measurements were performed at room temperature using a Buehler microhardness tester. The indenter was kept at the maximum load for 12 s for all measurements, and the measured hardness is the average value of 10 individual indents made on the surface of each sample. Initially, an indentation load of 200 g was used to measure the microhardness of all die cast and permanent mold cast Mg alloys for understanding: (a) the effect of the microstructures through the DC AM50 castings on the microhardness, (b) the

effect of Ca content on the microhardness of the PM Mg-Al-Ca alloys, and (c) the effect of heat treatment process on the microhardness of the PM Mg-Al-Ca alloys. Then, in an effort to determine the relationship between the loads and the microhardness, the PM Mg-Al-Ca alloys were measured with the loads varying from 10 to 200 g.

3.3.2 Nanoindentation testing



Fig. 3.4 Hysitron Ubi[®]1 nanomechanical test instrument

The nano-indentation tests were performed on a Hysitron Ubi[®]1 Nanomechanical Test Instrument with a Berkovich indenter at room temperature (Fig. 3.4). This instrument is computer controlled and is capable of performing multiple load-unload indentation tests with continuous acquisition of the indentation load and depth. There is a program in the instrument, which can be set up to carry out indentations along a straight line, a circle or a rectangle. Such an equipment allows applying loads varying from 10 to 8000 μN and

recording penetration depths as a function of applied loads with high load resolution (1nN) and high displacement resolution (0.04 nm). Ten indentations were made on each specimen for hardness and creep tests, which were precisely carried out within primary α -Mg grains under the control of a Scanning Probe Microscope (SPM) of the Ubi[®]1 Instrument.

3.4 DSC analysis

The thermal analysis was carried out using a Differential Scanning Calorimetry-Thermogravimetric Analyzer (DSC-TGA Q600) manufactured by TA Instrument, as shown in Fig. 3.5.



Fig. 3.5 Differential scanning calorimetry-thermogravimetric analyzer (DSC-TGA Q600).

An argon flow rate of 100mL/min was used to prevent sample from contamination of the measurement beams and from the oxidation during and after DSC runs. The DSC tests

were run at heating/cooling rates of 2 ~ 50°C/min over the temperature range of 50 to 580 °C. After heating, nitrogen-cooling was used for all runs. Before each DSC run, the SDT Q600 TA Instrument was calibrated for TGA weight, DTA baseline, temperature and DSC heat flow. Samples to be analyzed were put in an alumina cup on the sample beam, while an empty alumina cup was put on the reference beam. Right before or after each DSC run, a baseline run was required by running a separate test with two clean, empty alumina cups on the sample and reference beams. The DSC trace was then corrected by subtracting the baseline.

3.5 Microstructural analysis

3.5.1 Optical and SEM analysis

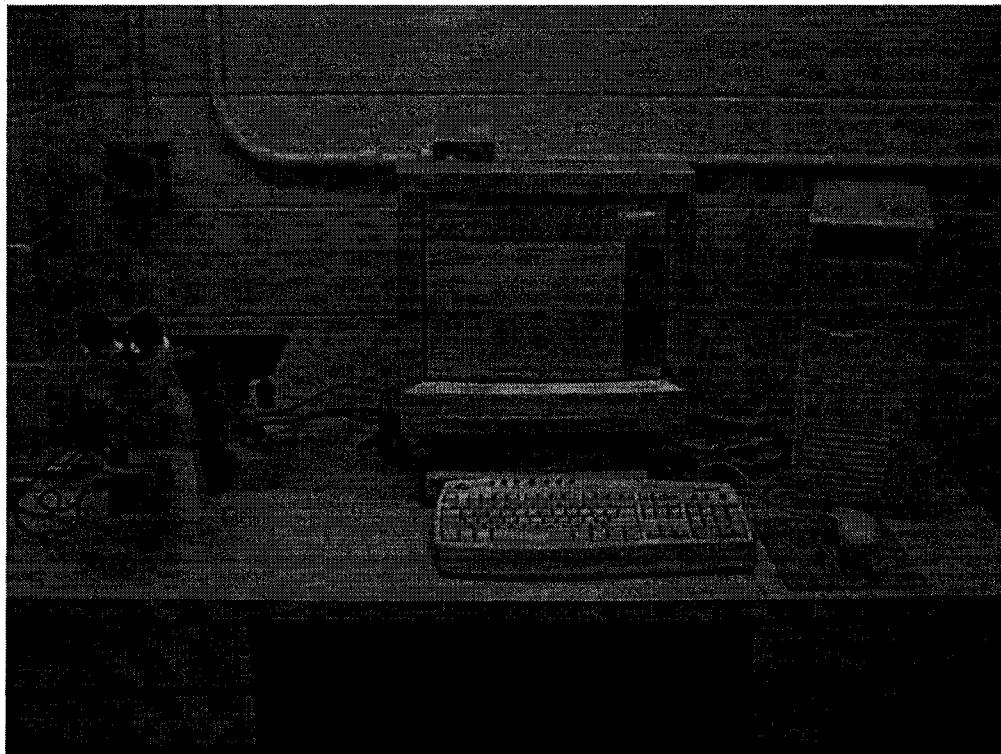


Fig. 3.6 Buehler optical image analyzer model 2002.

For optical and SEM microscopy, specimens were mounted and then ground with CARBIMET abrasive papers. The specimens were polished with 1.0 μm and 0.05 μm alumina polishing suspensions after grinding. Then specimens were chemically etched in a Glycol etchant (75 ml ethylene glycol, 1ml HNO_3 , 25 ml H_2O) for 5 ~ 20 seconds at room temperature. Specimens for SEM investigation were coated with either gold or carbon before inserting into the microscope.

Quantitative metallography was undertaken using a Buehler Optical Image Analyzer Model 2002 (Fig. 3.6). The secondary dendrite arm spacing (SDAS) was measured by the linear intersect method, and the volume fraction of the secondary phases in the specimens was measured by a point counting method. The morphological characterization of the specimens were undertaken with a JEOL JSM-5800LV scanning electron microscope (SEM) equipped with an energy dispersive X-ray spectrometer (EDS) at 15kV (Fig. 3.7).

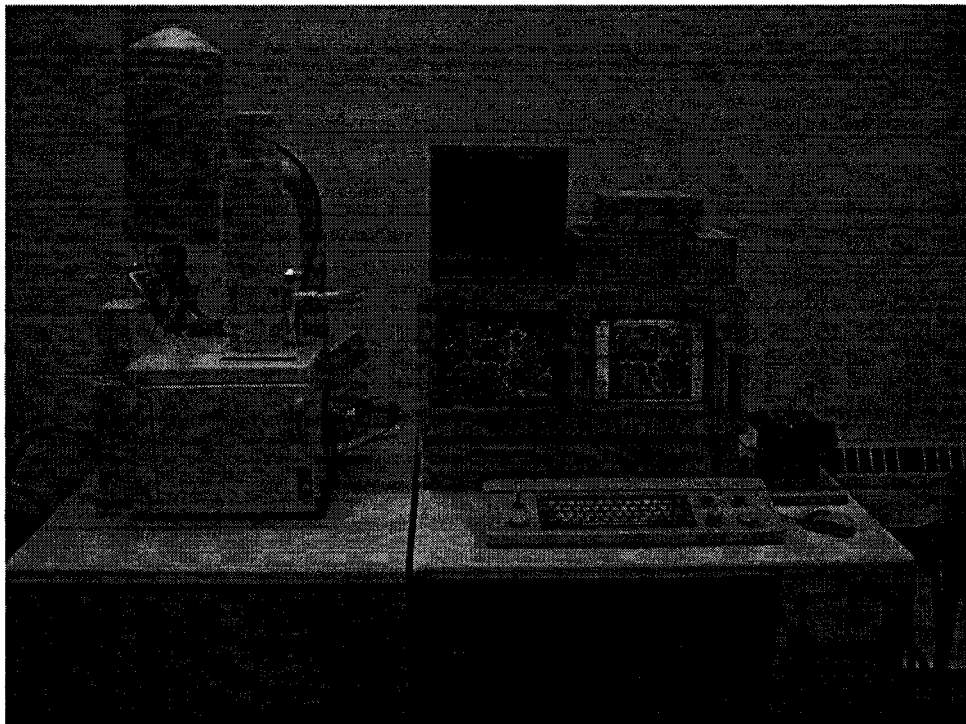


Fig. 3.7 Scanning electron microscope (JEOL Model JSM-5800LV).

3.5.2 TEM

Thin sections for transmission electron microscopy (TEM) analysis were ground with CARBIMET abrasive papers to thin foils with a thickness of $\sim 20 \mu\text{m}$. The thin foils were further thinned by ion beam milling with an incidence angle of $3 \sim 5^\circ$ for about 1 hour. TEM investigations were undertaken with a JEOL 2010 transmission electron microscope (TEM) equipped with an energy dispersive X-ray spectrometer (EDS) at an operating volt of 200 keV, as shown in Fig. 3.8. Two-beam conditions were used to observe the contrast caused by the coherent strain at the interfaces between precipitates and matrix. Selected area electron diffraction (SAED) combined with centered dark field imaging was used to identify the various phases.

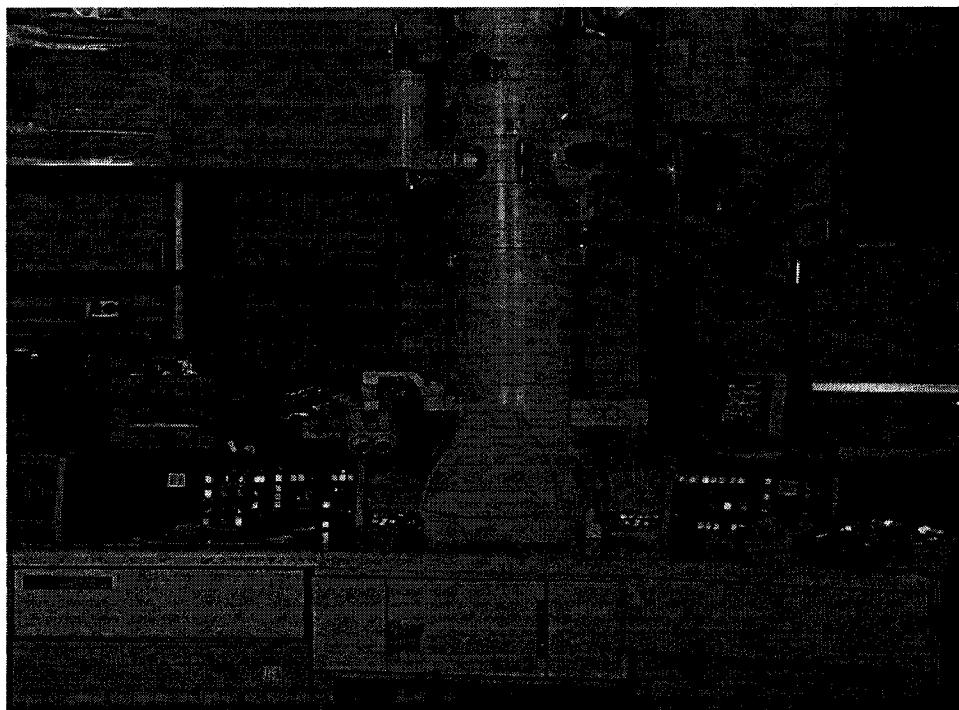


Fig. 3.8 JEOL 2010 transmission electron microscope with an energy dispersive X-ray spectrometer (EDS).

CHAPTER 4

RESULTS AND DISCUSSION OF MICROSTRUCTURE OF DC AM50 ALLOY

4.1 Microstructure of DC AM50 alloy

4.1.1 Optical and SEM micrographs

For high pressure die casting, steel dies for the casting of magnesium alloys cool faster when the back of the dies are cooled by oil, and heat can be quickly extracted from the casting through the metal-mold interface. Therefore, the high pressure die casting process invariably leads to a “skin effect”, where the microstructure of the casting near the free surfaces differs significantly from that in the interior, i.e. liquid metal close to the metal-mold interface first solidifies to form a fine grain microstructure, as shown in Figs. 4.1(a), (c) and (e). As the solidification process proceeds, the rate of heat transfer from the interior to the exterior decreases gradually so that a relatively coarse grain structure subsequently forms in the interior of casting, as shown in Figure 4.1(b), (d) and (f). Zhou [157] reported that a higher percentage of porosity, which is in the form of “bands”, is observed in the central regions of the same DC AM50 alloys as used in this study, while the skin regions are relatively free of porosity. The banded defects observed in die cast AM50 alloys are caused by shear deformation of the semi-solid mush entering the die cavity [157]. It was found that the bands include aluminum-rich segregation, porosity or a combination of both. The amount and degree of localization of porosity formed is dependent on the alloy composition and the casting conditions.

Skin Area

Center Area

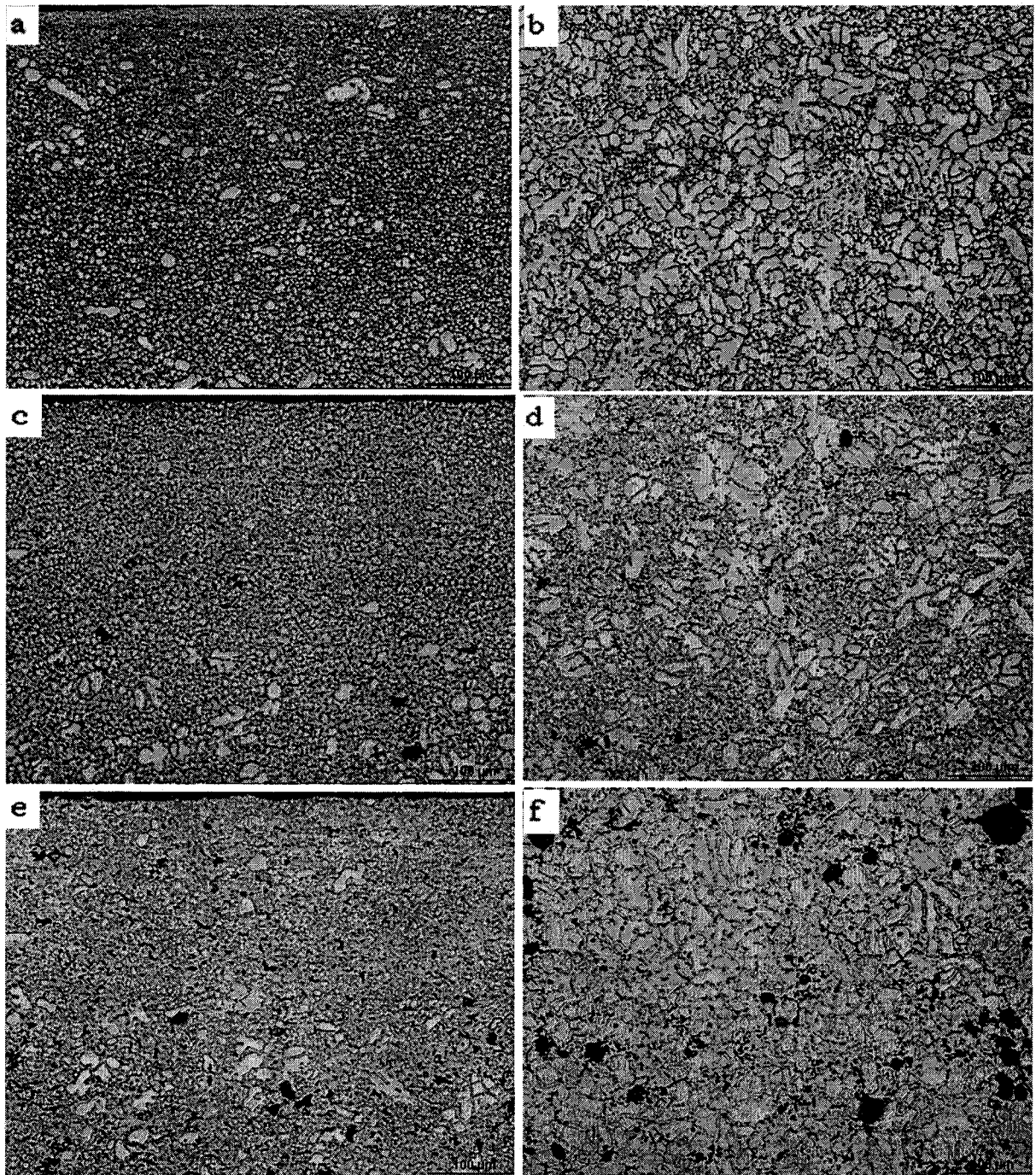


Fig.4.1 Optical microstructures of DC AM50 alloys: (a) the skin of 2 mm sample, (b) the center of 2 mm sample, (c) the skin of 6 mm sample, (d) the center of 6 mm sample, (e) the skin of 10 mm sample and (f) the center of 10 mm sample.

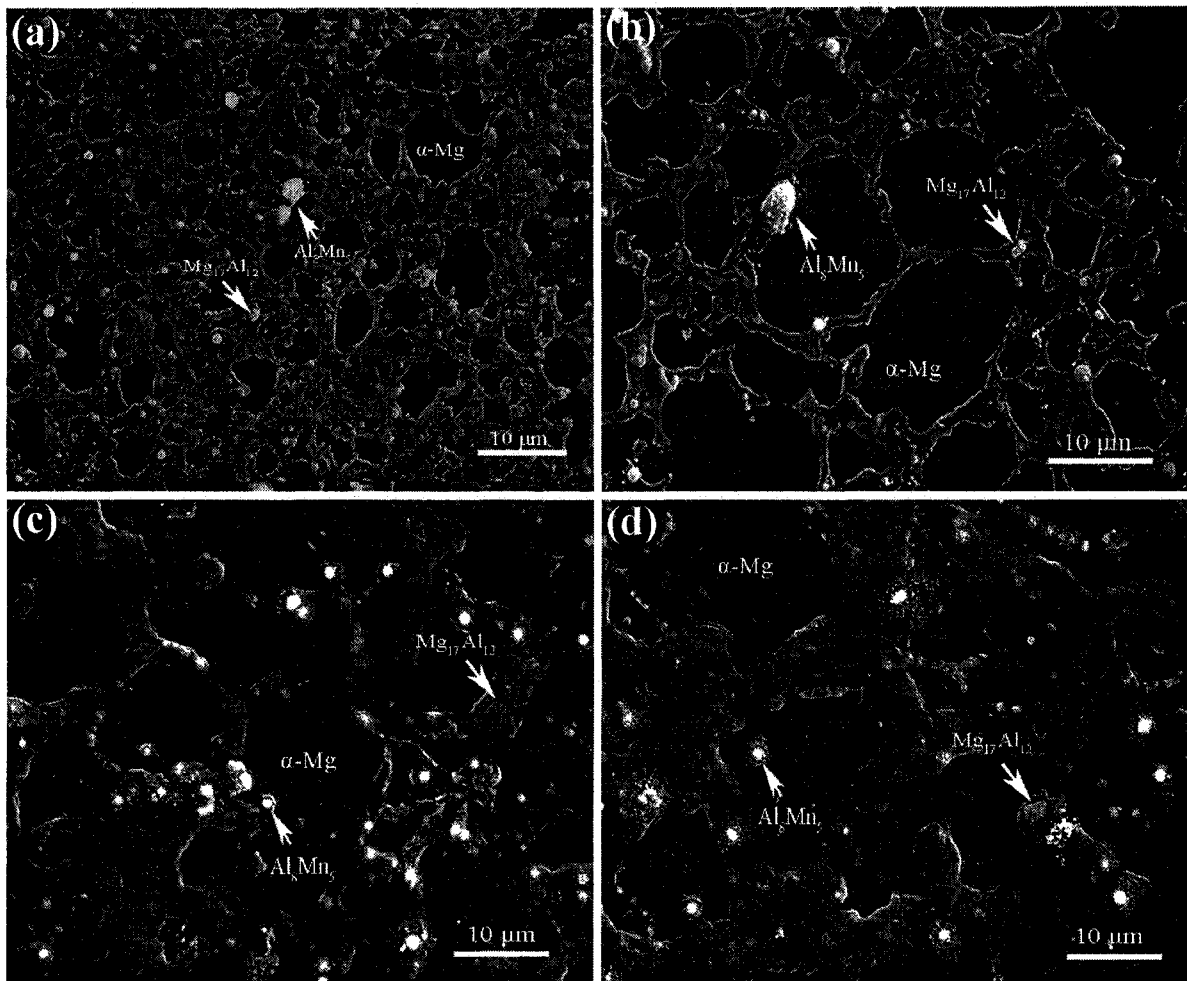


Fig. 4.2 SEM micrographs of the microstructures in DC AM50 alloys: (a) the skin of 2 mm sample, (b) the center of 2 mm sample, (c) the center of 6 mm sample and (d) the center of 10 mm sample.

The primary features of the microstructures of DC AM50 alloys are shown at a higher magnification in the SEM micrographs (Fig. 4.2). The microstructure consists of primary α -Mg solid solution and particles of the β - $Mg_{17}Al_{12}$ phase with bright contrast, which are common to other Mg-Al alloys. With the addition of Mn, Al_8Mn_5 particles, which exhibit the brightest contrast, have been found in the DC AM50 alloys either in the primary α -Mg grain or along the grain boundary with β - $Mg_{17}Al_{12}$ phase. However, the amount of Al_8Mn_5

particles is low. The regions with gray contrast surrounding the intermetallic phase is due to the different etching characteristics of the Al-rich α -Mg (higher in Al content) that formed last during the solidification sequence. The eutectic is divorced, and therefore the β -Mg₁₇Al₁₂ phase appears as discrete particles surrounded by the Al-rich α -Mg halo that is richer in Al than the primary α -Mg.

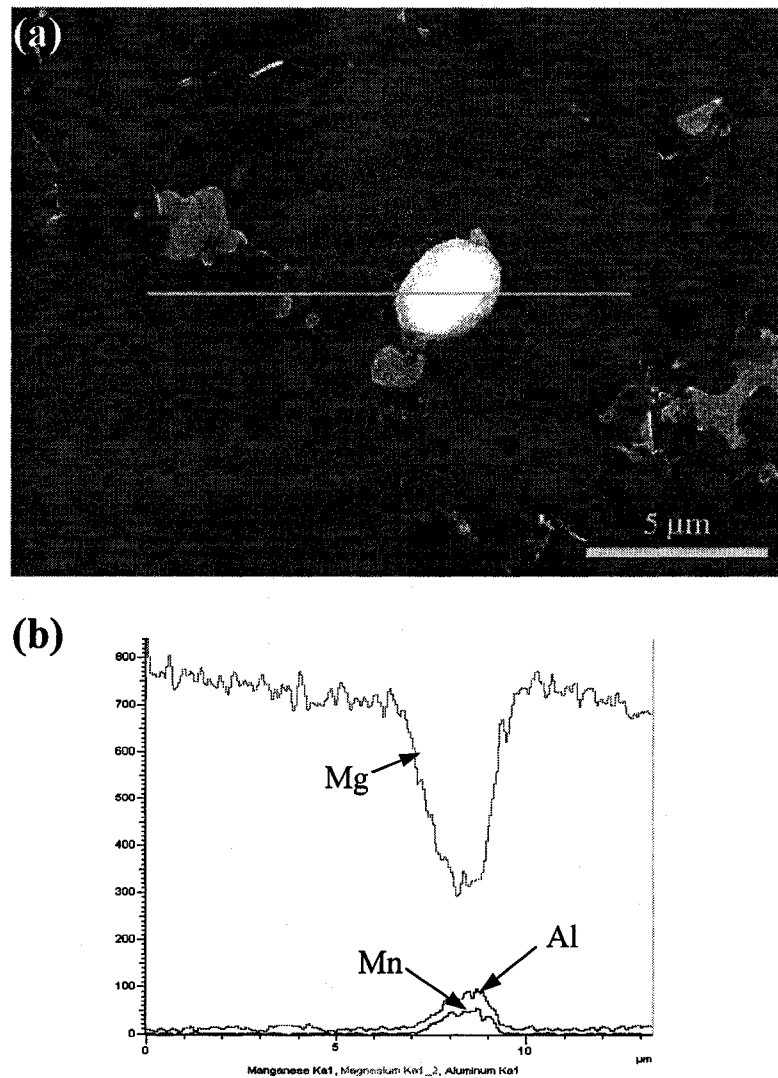


Fig. 4.3 (a) SEM micrograph and (b) the EDS line scans in the 2 mm DC AM50 alloy.

Fig. 4.3 presents SEM micrograph and the EDS line scan result at one location and shows the compositional variation across a Al_8Mn_5 particle (Fig. 4.3(a)) near the grain boundaries. It can be seen that the concentration of both Mg and Al inside the primary α -Mg grains are constant, and that a sharp increase in Al content is found when the probe crosses the Al_8Mn_5 particles, demonstrating that the phase contains Al. A sharp decrease in Mg content and a sharp increase in Mn content are also observed when the probe crosses the Al_8Mn_5 particles. When the probe crosses the Al-rich eutectic α -Mg that surrounds the β - $\text{Mg}_{17}\text{Al}_{12}$ or Al_8Mn_5 phases, the Mg content appears constant while Al content has a smooth increase. This indicates local microsegregation due to a coring effect. Czerwinski *et al.* [158] detected an obvious increase in Al concentration when the electron probe beam moved from the center towards the primary α -Mg grain boundary, indicating coring. Dargusch and Dunlop [159] also found similar micro-segregation in their DC AZ91D alloy.

Fig. 4.4 shows a SEM micrograph and elemental maps for the 2mm DC AM50 alloy from the same region. Using the Mg, Al and Mn X-ray maps of the same field shown in Fig. 4.4(a), the β - $\text{Mg}_{17}\text{Al}_{12}$ phases and the Al_8Mn_5 phases (marked by arrows) can be identified. Also, the network of the Al-rich regions surrounding the β - $\text{Mg}_{17}\text{Al}_{12}$ phases are distributed along the grain boundaries.

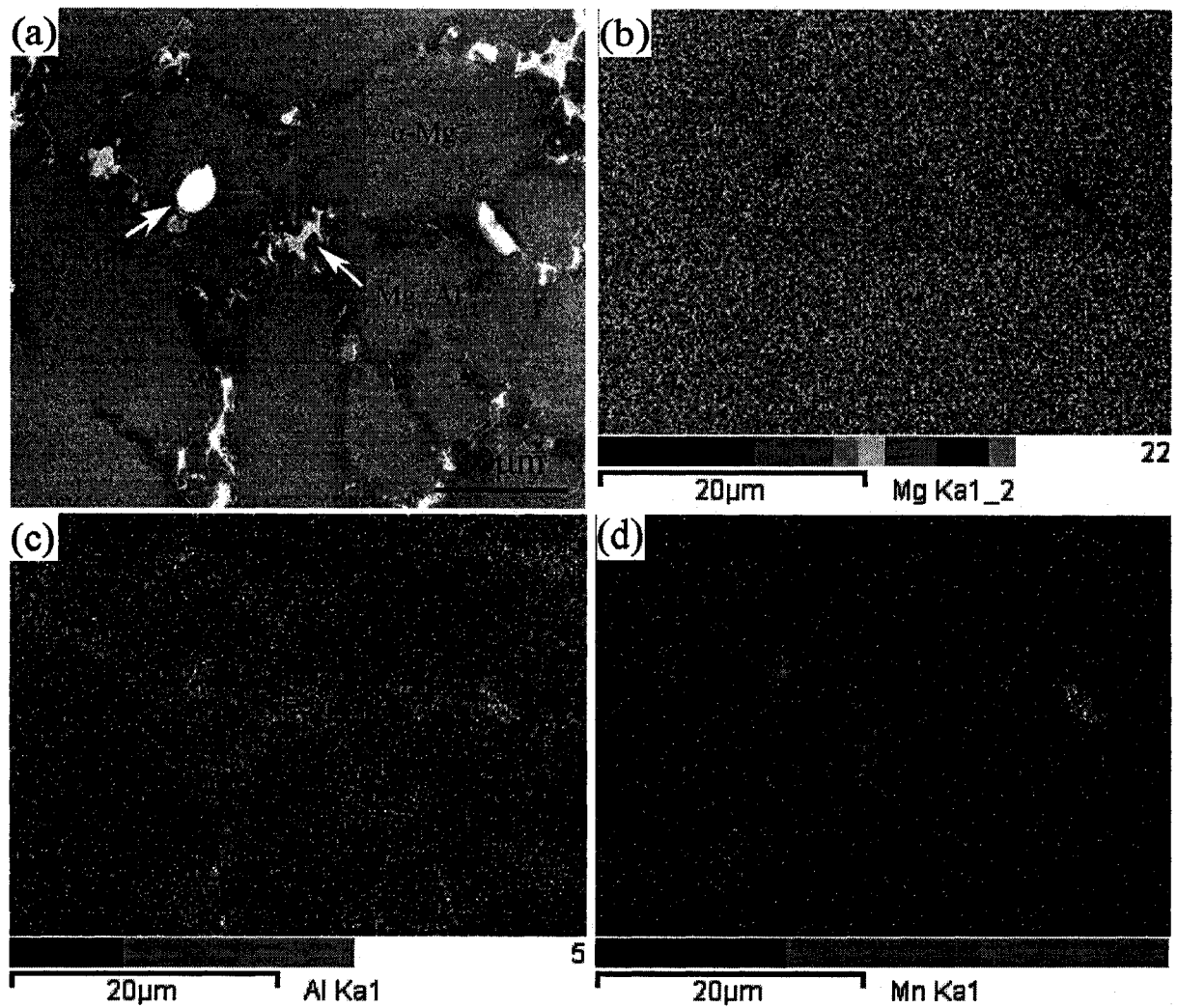
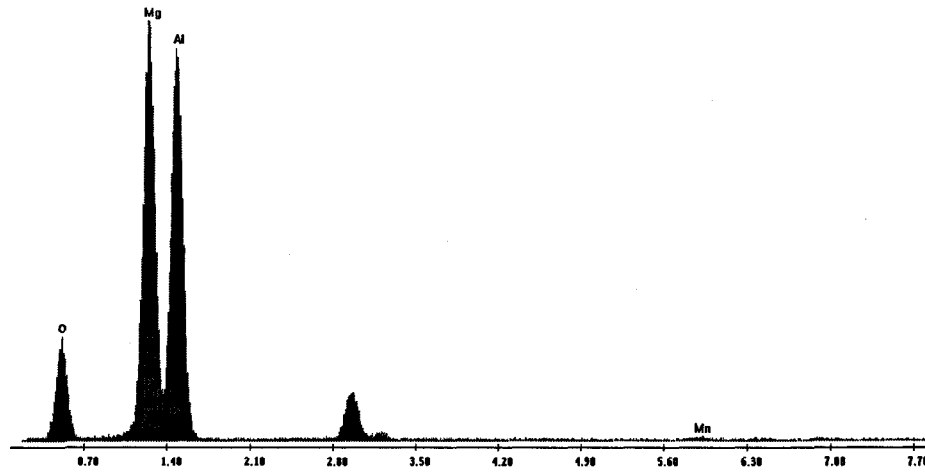


Fig. 4.4 EDS results for the 2mm DC AM50 alloy: (a) SEM micrograph, and elemental maps from the same region for (b) Mg, (c) Al and (d) Mn.

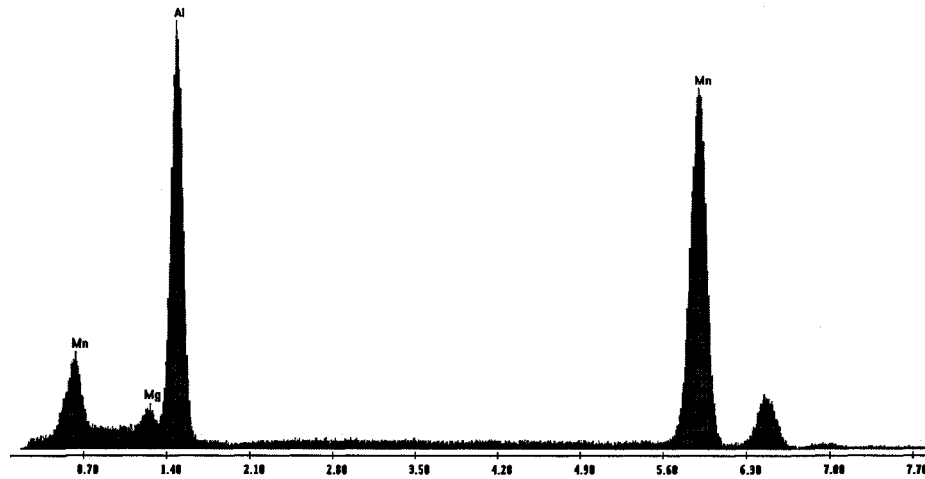
4.1.2 TEM micrographs

Analysis by SEM/EDS indicated that aluminum content in the middle of the primary α -Mg grains was close to $\sim 4\%$ wt.% compared to a value of over 11 wt.% Al in the Al-rich eutectic α -Mg regions surrounding the β -Mg₁₇Al₁₂ phases. Higher levels of aluminum around 30 - 40 wt.% were detected in the β -Mg₁₇Al₁₂ particles. Typical TEM/EDS spectra from the β -Mg₁₇Al₁₂ and the Al₈Mn₅ phases in the 2 mm DC AM50 alloy are shown in Fig. 4.5. The results of the analysis show that β -Mg₁₇Al₁₂ has an average composition (wt.%) of

58.4 ± 2.1 Mg, 41.6 ± 4.4 Al, and Al_8Mn_5 phase has a composition (wt.%) of 42.5 ± 4.7 Al and 55.3 ± 5.3 Mn and 2.2 ± 1.2 Mg. The Al_8Mn_5 phase should not contain Mg. It is therefore considered that the small amount of Mg detected in the spectrum could be from Mg in the matrix.



(a)



(b)

Fig. 4.5 Typical EDS spectra of: (a) $\beta\text{-Mg}_{17}\text{Al}_{12}$ and (b) Al_8Mn_5 phases in the 2mm DC AM50 alloy.

Fig. 4.6 shows TEM bright field (BF) micrograph and selected area diffraction pattern of β -Mg₁₇Al₁₂ phase in the 2 mm DC AM50 alloy. The β -Mg₁₇Al₁₂ precipitates, as shown in Fig. 4.6(a), are found to have a typical lamellar structure, and are distributed homogeneously in the matrix. The boundary between two layers of the β -phase can also be clearly observed. The selected area diffraction pattern shows that the lamellar structures have the same crystallographic orientation, which suggests that these lamellar β phase structures are either single crystals consisting of multiple lamellar structures or polycrystals which have the same crystallographic orientation. The length of the lamellar β -Mg₁₇Al₁₂ precipitate ranges from hundreds of nanometers to several microns. Indexing of the diffraction pattern for the β -Mg₁₇Al₁₂ confirmed that the β phase has a cubic crystal structure with $a = 1.056$ nm. Additionally, some rodlike Mg₁₇Al₁₂ precipitates were found in the matrix of the DC AM50 alloy, and it seems that these precipitates are parallel each other (Fig. 4.7(a)). The selected area electron diffraction pattern consists of the sum of the individual diffraction rings, as shown in Fig. 4.7(b), which means that the rodlike Mg₁₇Al₁₂ precipitates are polycrystals which contain crystals in several orientations. Meanwhile, it can be found that these crystals have the similar orientations because of the localized distribution of the diffraction spots along the diffraction rings.

Nano-scale particles of Mg₁₇Al₁₂ are also found in the grains of the 2 mm DC AM50 alloy, as shown in Fig. 4.8. These are mostly elongated platelets or needlelike precipitates. Frequently, such precipitates surround the rounded eutectic constituents. This may correspond to the SEM observations (Fig. 4.6(a)) and may serve as an alternative explanation to the lamellar eutectic described above. These particles may be formed by precipitation from the supersaturated solid solution during solidification.

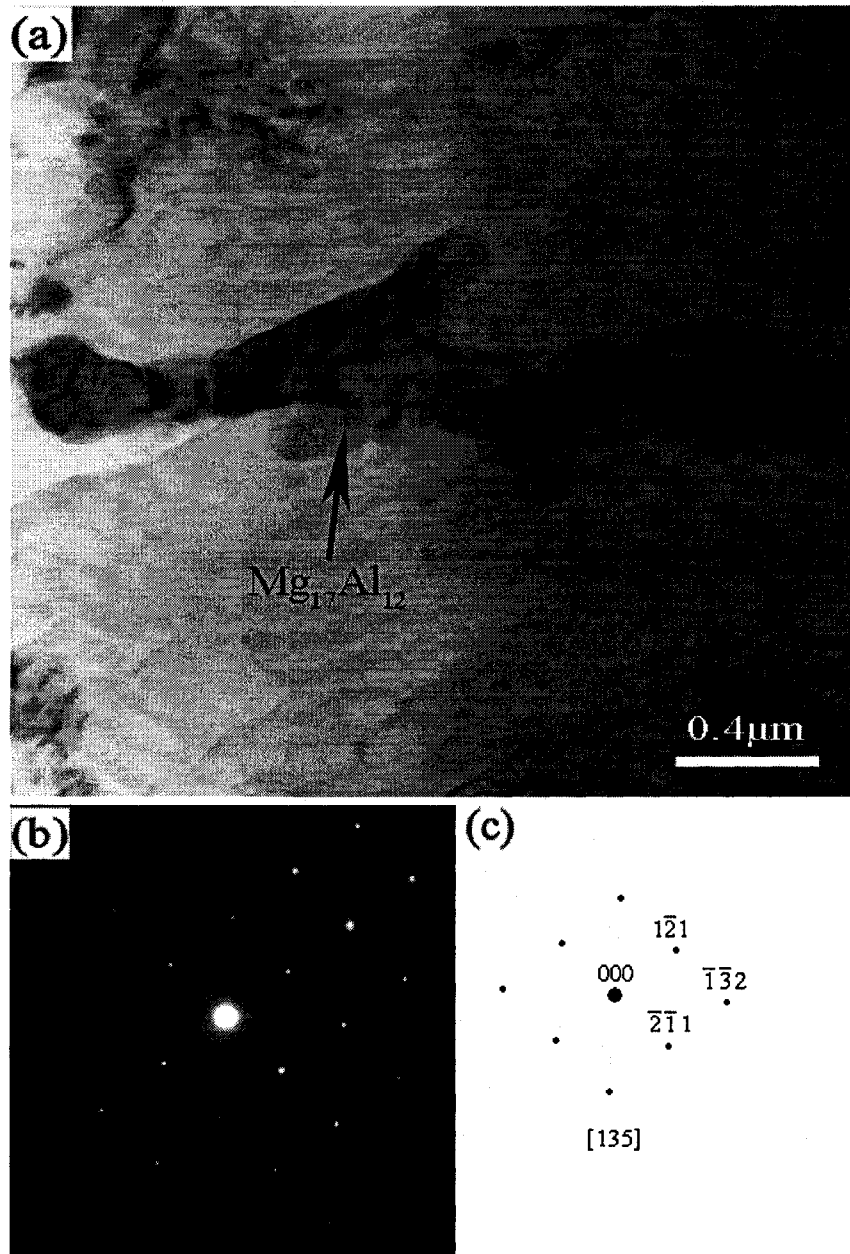


Fig. 4.6 Typical TEM image of (a) β - $Mg_{17}Al_{12}$ in the 2 mm DC AM50 alloy, (b) selected area diffraction pattern from β - $Mg_{17}Al_{12}$ phase with dark contrast, and (c) indexing of diffraction pattern in (b).

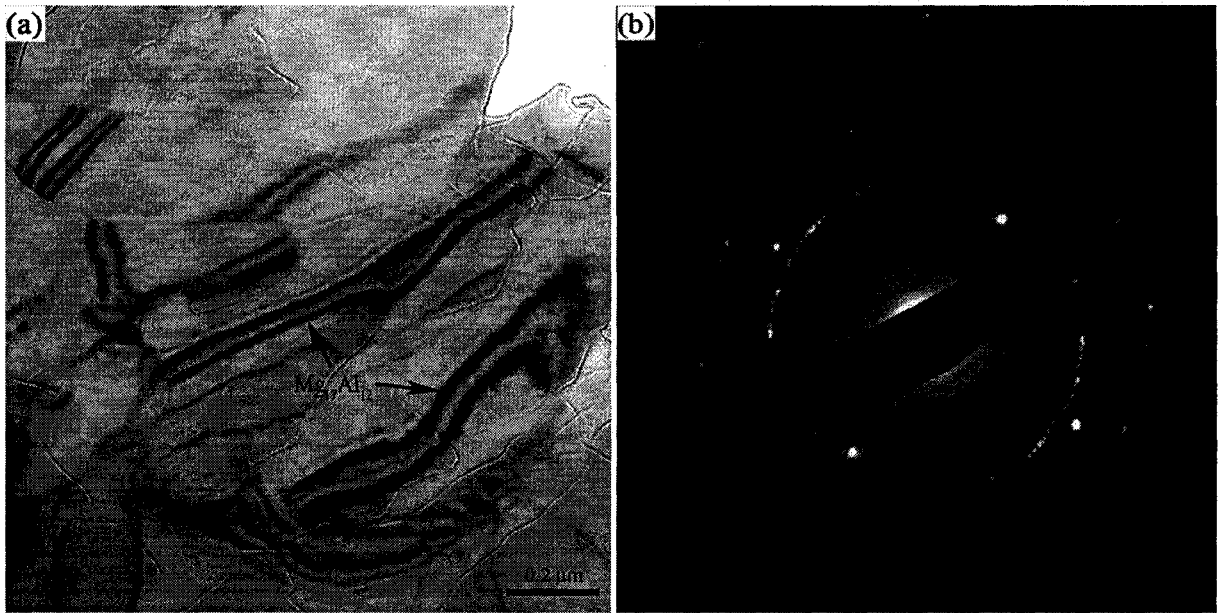


Fig. 4.7 Typical TEM image of (a) β -Mg₁₇Al₁₂ in the 2 mm DC AM50 alloy and (b) selected area diffraction pattern from β -Mg₁₇Al₁₂ phase with dark contrast.

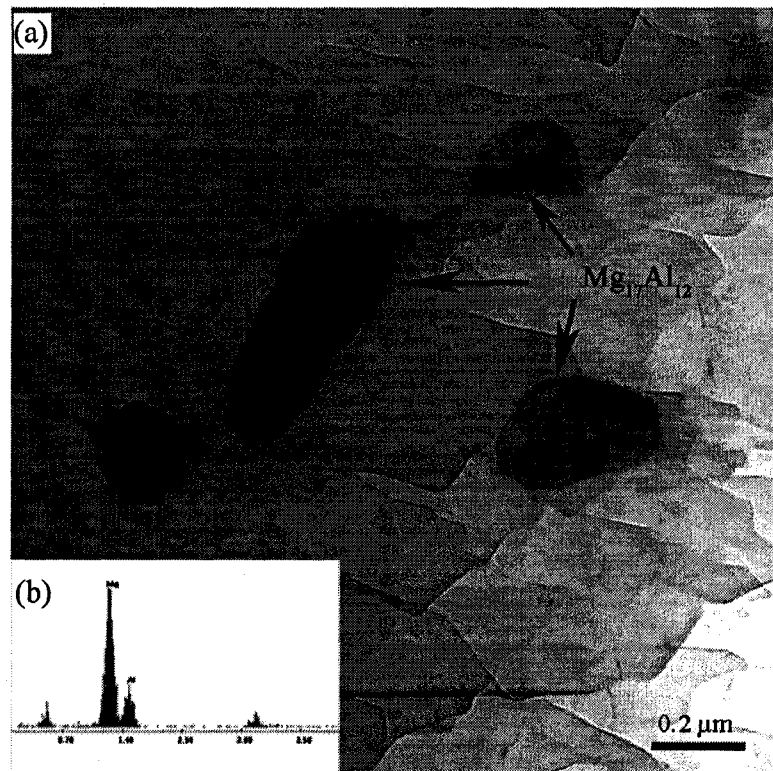


Fig. 4.8 (a) TEM image and (b) EDS result of nano Mg₁₇Al₁₂ particles in the 2 mm DC AM50 alloy.

With the addition of Mn(<1.0%), an additional phase containing mainly aluminum and manganese was also observed in the microstructure of the DC AM50 in the form of small particles on the microscale. These phases occupied less than 1% of the total volume fraction of eutectic phases in the alloy investigated. Although their compositions varied, they were present in similar amounts in all of the alloys examined in these experiments.

A TEM BF image, its selected area electron diffraction and an indexed diffraction pattern of the Al_8Mn_5 precipitate are shown in Fig. 4.9. The BF image shows that the Al_8Mn_5 precipitates have a polygonal morphology and are several microns in size. Selected area electron diffraction pattern confirmed that the dark particle visible in Fig. 4.9(a) is the Al_8Mn_5 phase. The Al_8Mn_5 particle is found to be a single crystal, since the diffraction pattern does not change as the diffraction beam moves back and forth along the dark phase. The Al_8Mn_5 phase has a hexagonal close-packed (HCP) crystal structure with $a = 1.273$ nm and $c = 1.588$ nm. The Al_8Mn_5 precipitates are found to have a polygonal morphology and are several microns in size. The Al_8Mn_5 precipitates are observed at grain boundaries or in the primary α grains, which is slightly different from the distribution of the $\beta\text{-Mg}_{17}\text{Al}_{12}$ that is mainly along the grain boundaries.

The polycrystalline Al_8Mn_5 particle was also present in the matrix of the 2 mm DC AM50 alloy. Fig. 4.10 shows a TEM BF image of the Al_8Mn_5 phase, combined diffraction patterns from the polycrystalline, and individual diffraction patterns from single crystal. The combined diffraction pattern consists of three individual single crystal diffraction patterns obtained at three different locations, which suggests that the polycrystalline particle includes three single crystals of different orientation. However, since the contrast of the particle is too dark, it is hard to distinguish any boundary from these individual crystals.

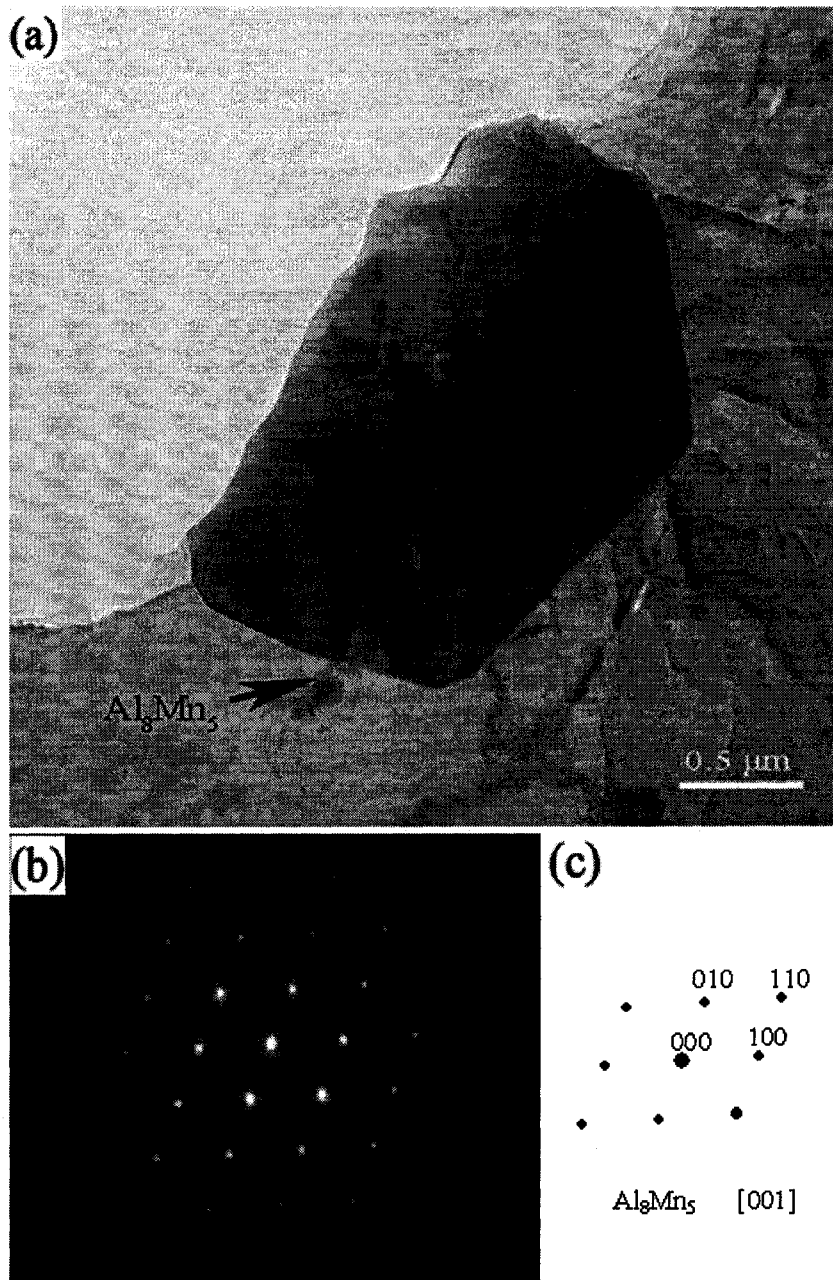


Fig. 4.9 (a) Typical TEM image of Al_8Mn_5 in die cast AM50 alloy with a 2 mm thickness, (b) selected area diffraction pattern from Al_8Mn_5 phase with dark contrast, and (c) indexing of diffraction pattern in (b).

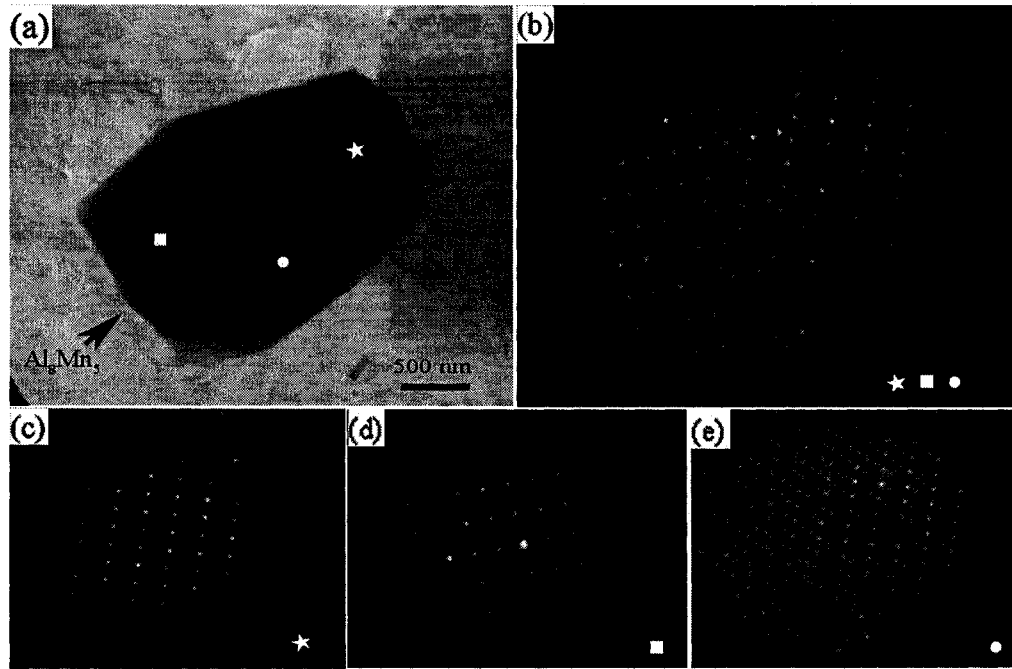


Fig. 4.10 (a) Typical TEM image of Al_8Mn_5 in the 2 mm DC AM50 alloy, and selected area diffraction patterns from (b) the whole Al_8Mn_5 phase with dark contrast, and (c) star location, (d) square location, and (e) circle location.

According to the data of TEM/EDS analysis, it seems that the Mn-containing particles had an average composition of 58.05 ± 20.78 at.%Mg - 26.12 ± 12.84 at.%Al - 15.83 ± 8.01 at.%Mn. This observation implies that the particles could involve the elements of Mg, Al and Mn with a very large scatter in data. However, there was a great possibility that the detected strong Mg EDS signal on the spectra resulted from the matrix surrounding the particles because of their relatively fine sizes. The uncertainty in the detected Mg content due to variation in EDS detection regions could be responsible for the large scatter in the data analysis which took Mg into consideration. Moreover, it has been pointed out in the previous studies [63, 157, 160] that magnesium is usually absent from manganese aluminides in magnesium alloys. Based on these considerations, Mg content was excluded during the calculation of the atomic ratio of Al to Mn in the particles. By taking into account only Al

and Mn EDS signals, the average compositions of three particles as indicated in Fig. 4.11 were calculated with a significant reduction in data scatter. They were 62.3 ± 2.93 at. % Al and 37.7 ± 2.93 at.% Mn. Hence, the average atomic ratio of Al to Mn in the particles becomes 1.65. The value of 1.65 identifies that the observed Al-Mn particles should be the Al_8Mn_5 phase of which atomic ratio is 1.6. This TEM/EDS observation is consistent with the experimental findings by Gertsman et al [160].

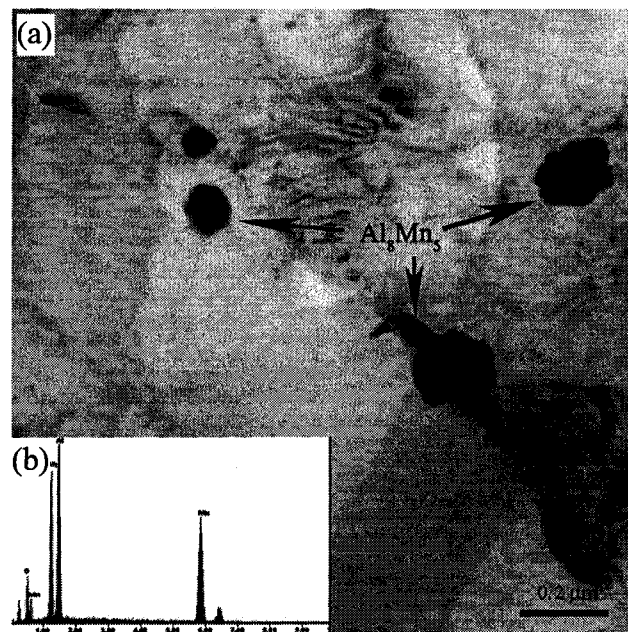


Fig. 4.11 (a) TEM image and (b) EDS result of finer Al_8Mn_5 particles in the 2 mm thick DC AM50 alloy.

Fig. 4.12 shows the morphology of twins in the 2 mm DC AM50 alloy. Fig. 4.12(a) is a SEM image of the twin structure. It can be seen that twin structures are distributed within the primary α -Mg grains. Some individual grains often include small twins, while large twins are observed to cross through several α -Mg grains. Also, it should be noted that these twins are parallel in the local area of the matrix, which suggests that they have an epitaxial relationship between twins and between the twins and the matrix. In the case of a

conventional grain boundary, the formation of a twin and orientation domain must be energetically favored, i.e., the change of the boundary free energy due to the formation of the twin boundary (domain boundary) must be a minimum. The free energy of a semi-coherent interface can be approximately considered as the sum of two terms: a chemical term resulting from the interaction energy of the interfacial atoms and a structural term brought about by structural misfit across the interface which is mostly associated with the crystallography of the interface. Although it is in general understood that the formation of a twin boundary is closely related with the low-stacking fault energy of the material investigated [161, 162], it is difficult to estimate the chemical term of the formation energy of the boundary without extensive computer simulations for the DC AM50 alloy. The TEM BF image in Fig. 4.12(b) also shows some fine precipitates appearing on the twin boundaries.

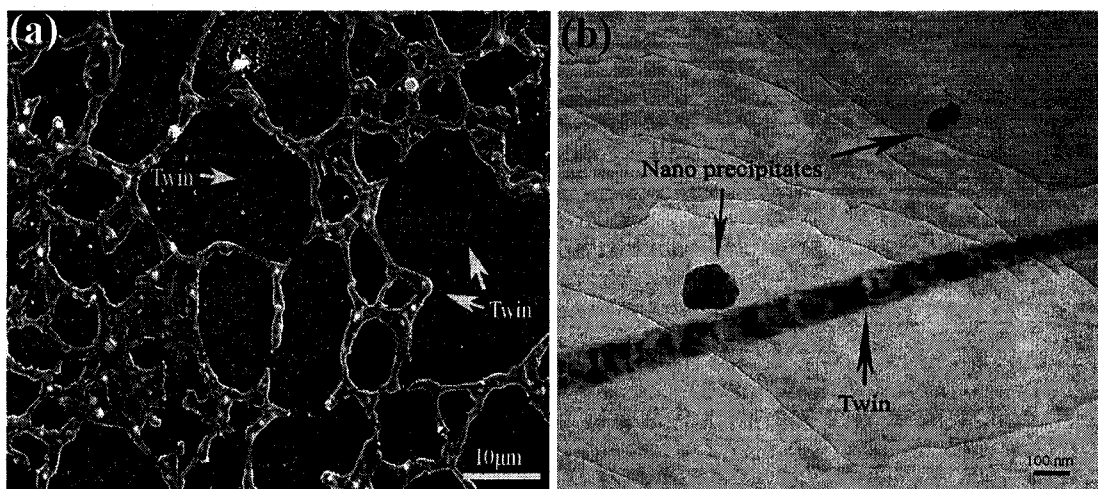


Fig. 4.12 Morphology of twin structure formed during solidification for the 2 mm DC AM50 alloy: (a) SEM and (b) TEM image.

The dislocation density in the primary α -Mg tended to be rather high, which is probably due to plastic deformation during fast cooling under geometric constraint experienced by the die cast specimens. As shown in Fig. 4.13, many of the dislocations were

arranged in networks indicating that considerable recovery had also occurred during cooling to room temperature. The dislocation appears as a dark line in the bright field image, because certain planes near dislocations are bent into a strongly diffracting orientation so that the intensity of the directly transmitted beam is reduced in columns near the dislocation. A row of parallel dislocations is observed in the TEM image (Fig. 4.13(b)). The dislocations extend from top to bottom of the grains. The deformation has resulted in the formation of dense tangles of dislocation within the grains, as shown in Figs. 4.13(a) and (c). Additionally, grain boundaries, precipitates, and stacking fault energy affect the distribution of the dislocations. The orientation difference between the α -Mg grains varies considerably for each set of grains. However, the interface between the α -Mg grains is often identified as a low angle grain boundary of less than 5° difference in orientation. A small amount of energy is stored when the dislocations are produced during solidification. However, a considerable amount of stored energy can be released if the dislocations locally rearrange themselves into configurations of lower energy, i.e. low-angle boundaries and can be represented by a uniform array of three or more sets of dislocations. Both these procedures involve climb of the dislocations. Solute atoms in high local concentrations may interact to form precipitates along the dislocations. As far as the mechanical properties are concerned, the importance of solute segregation and precipitates in or near the dislocations is that an extra stress is required to overcome the attractive dislocation-defect interactions and move the dislocations away from the concentrated solute or precipitate region. Some fine β -Mg₁₇Al₁₂ particles are also observed to precipitate along the grain boundaries (Fig.4.13(d)). Meanwhile, the dislocation tangles are observed around the grain boundaries and the precipitate. Some nanoscale precipitates are also present on the dislocation [63]. The structure of these nano precipitates

has not yet been determined. They appear to be a combination of $Mg_{17}Al_{12}$ and Al_8Mn_5 precipitates.

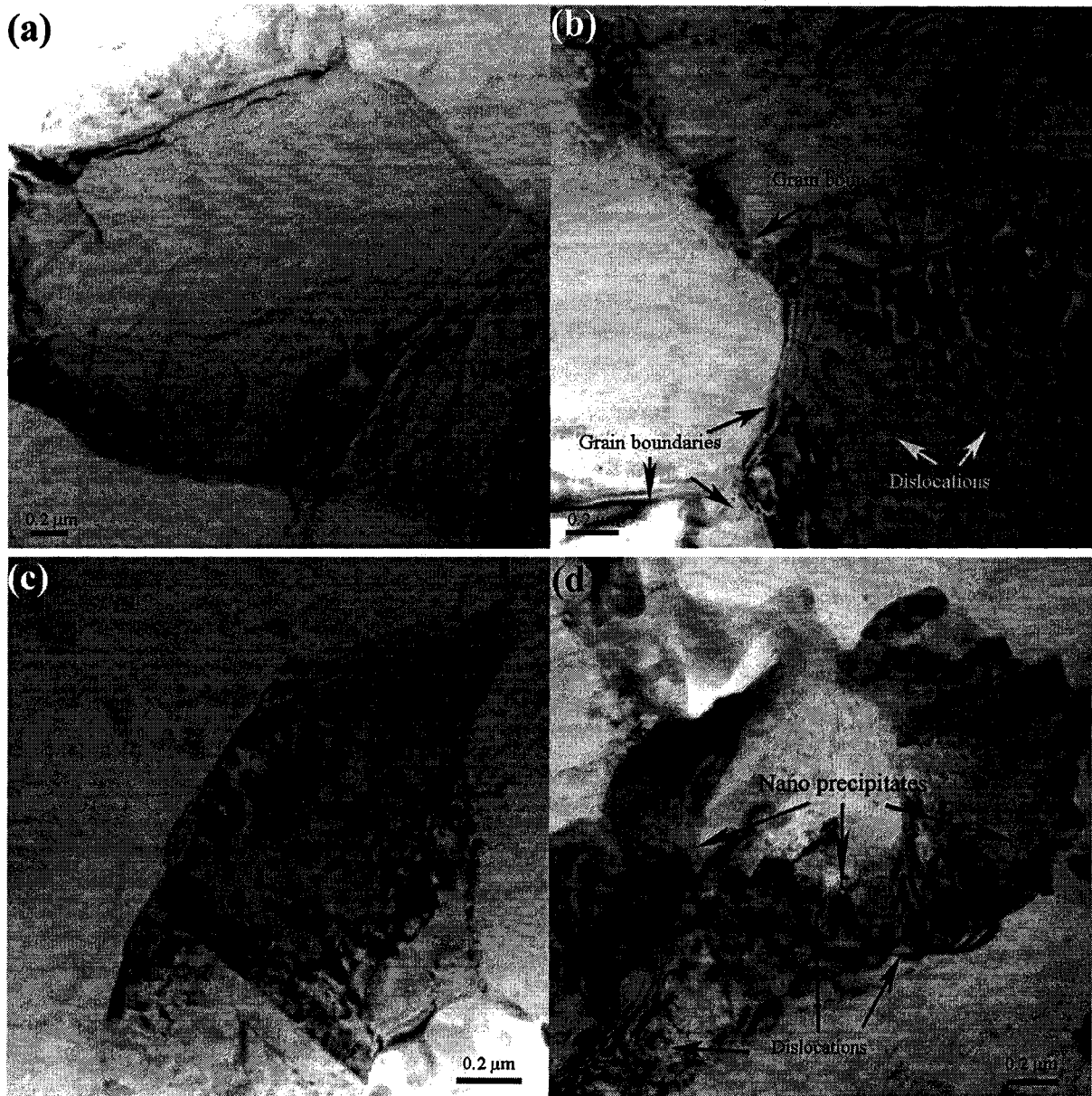


Fig. 4.13 TEM micrographs of grain and dislocation network in the 2 mm DC AM50 alloy.

(a) grain boundaries, (b) arranged dislocations, (c) stacking fault and (d) tangled dislocations and precipitates. Each dark line is produced by a dislocation.

4.2 Distribution of secondary dendrite arm spacing

There is non-uniform microstructure in the high pressure DC AM50 alloy with respect to the size and distribution of its main phases. A thin skin region close to the surface of the specimens has a finer microstructure than the central region. The microstructures in Fig. 4.1 illustrate the significant differences in the SDAS from the center to the edge of a DC specimen. Distributions of the SDAS across the DC AM50 castings with section thicknesses of 2, 6 and 10mm are shown in Fig. 4.14(a), (b) and (c), respectively.

The distribution of the SDAS in the skin of the castings is relatively uniform compared to that in the center. Typical sizes of the SDAS in the skin of the casting with a section thickness of 2 mm ranged from 1 to 7 μm , although a small number of larger values (8 to 10 μm) were also observed. The average SDAS in the skin of the casting with section thickness of 2 mm was around 3.98 μm . Similarly, the measured average SDASs are 5.12 and 8.6 μm in the skin regions of the castings with the section thicknesses of 6 and 10 mm, respectively. However, as section thickness increases, some larger dendrites were observed in the skin regions of the castings, which resulted in measured SDAS data with a relatively high scatter. Histograms showing the distribution of the SDAS in the skin regions of the castings with the section thicknesses of 2 and 10 mm are shown in Fig. 4.15. It can be noted that the average SDAS is around 8.6 μm , however, some large size SDASs ranging from 20 to 30 μm were measured in the skin of the casting with the section thickness of 10 mm. The measured average SDASs in the center regions of the castings with section thicknesses of 2, 6, and 10 mm are 10.5, 14.4 and 17.4 μm , respectively, with considerable scatter in the data.

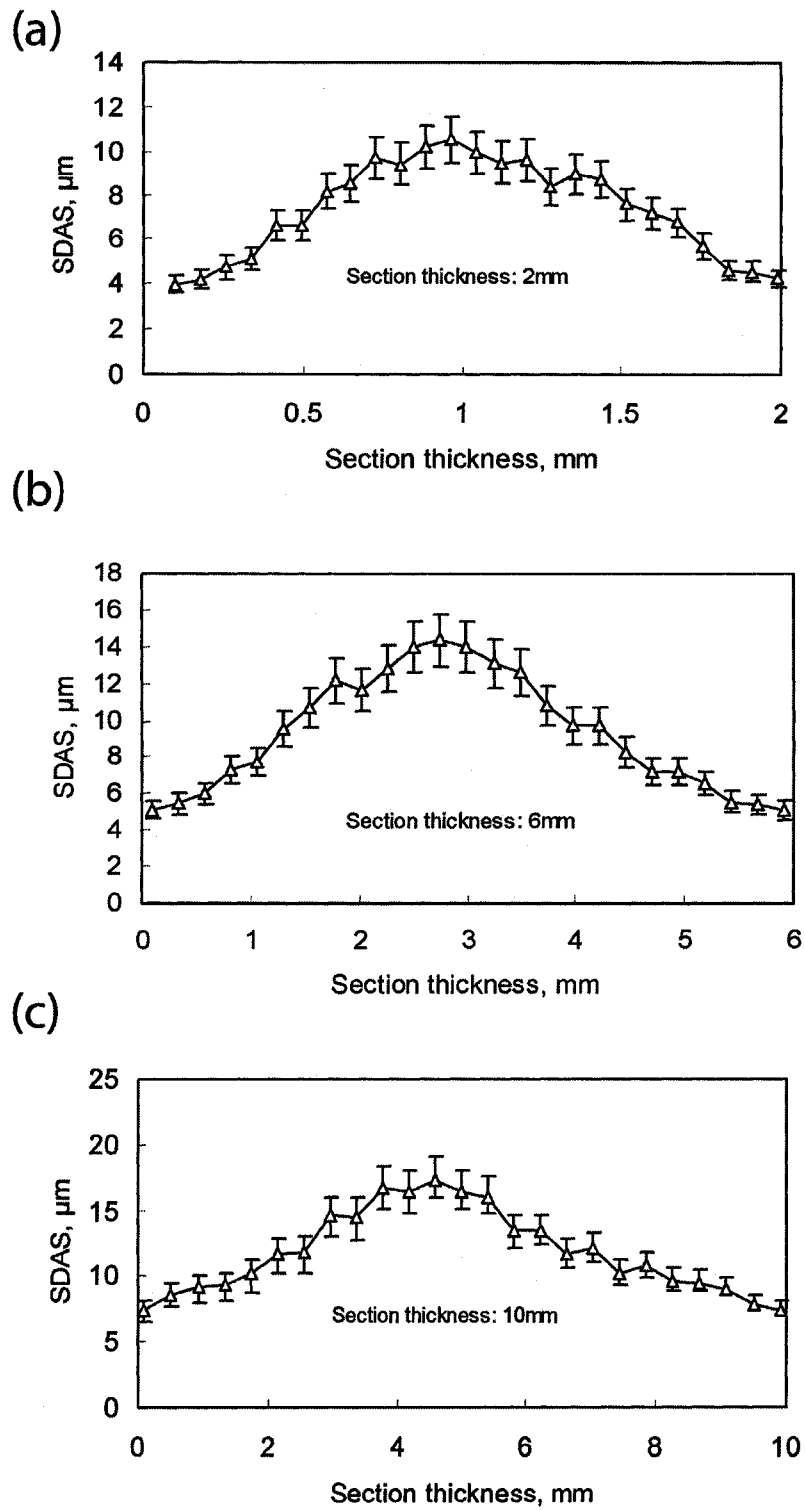


Fig. 4.14 Distribution of the SDAS across the DC AM50 castings with section thicknesses of (a) 2 mm, (b) 6 mm and (c) 10mm.

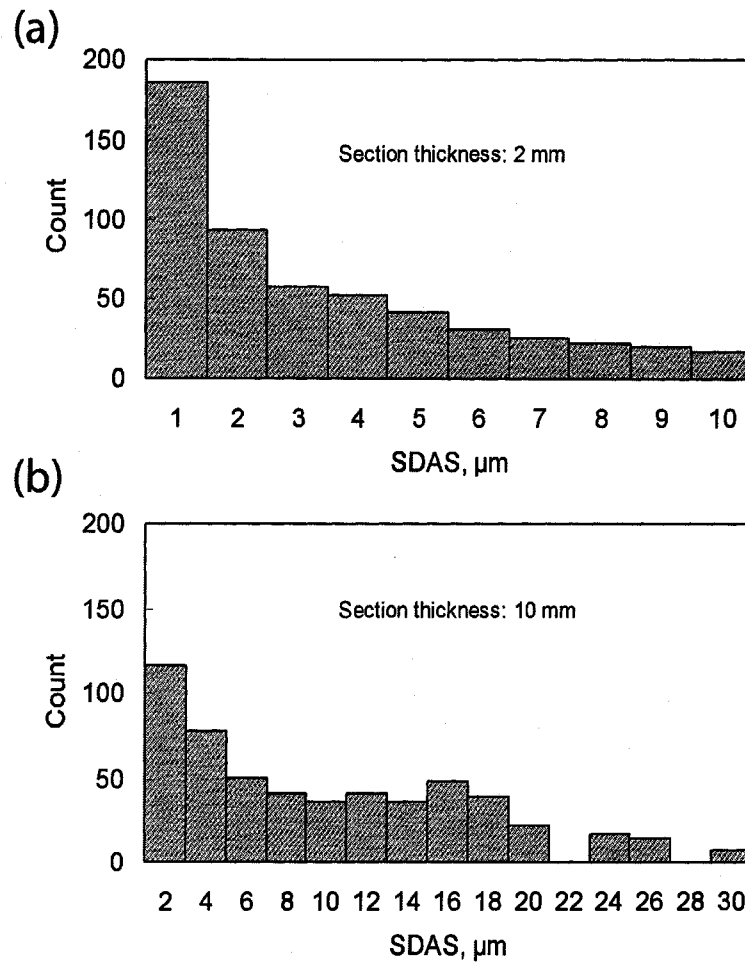


Fig. 4.15 Histograms showing the distribution of the SDAS in the skin regions of the castings with section thicknesses of: (a) 2 mm sample and (b) 10 mm.

The measured sizes of some of the large dendrites were close to 50 μm in the center of the casting with the section thickness of 10 mm. Additionally, it was found that some smaller dendrites ($<1\mu\text{m}$) were present in both the skin and the center regions for all the castings, which were not easily observed using the optical microscopy. However, as described in Section 4.1.1, the fine microstructures could be characterized with SEM. The SDAS (around 3.98 μm) measured in the skin region of the casting with the section thickness of 2 mm is in good agreement with the size of the primary $\alpha\text{-Mg}$ grains (around 4 μm) observed in the TEM BF image (Fig. 4.13).

The skin thickness of die cast coupons is dependent upon the casting parameters, the section thickness of the casting, the flow of the liquid and pre-solidified metal through the casting, and the shape of the surrounding mould. Liquid metal flowing through the die-casting is likely to solidify almost immediately upon contact with the mould walls. The extraction of heat through the walls forms a rigid skin, with a very fine microstructure and a high volume of eutectic when the section of the die cast coupons is somewhat thin. This cast surface layer is advantageous for the strength of the casting.

4.3 Distribution of eutectic phases

Optical micrographs of Figs. 4.2(a) and (b) show the higher volume fraction of eutectic $\beta\text{-Mg}_{17}\text{Al}_{12}$ with Al-rich eutectic $\alpha\text{-Mg}$ in the skin than in the central regions of a 2 mm thick die cast AM50 specimen.

The image analysis technique and optical micrographs are used to quantitatively determine the amount and distribution of eutectic phases in the matrix of the DC AM50 alloys. However, the similar contrast is present between the eutectic phase and the primary $\alpha\text{-Mg}$ phase in the polished and etched specimens with these two observation techniques. Hence, it is sometimes hard to distinguish the boundary between the primary and eutectic $\alpha\text{-Mg}$ phases. The obvious boundaries between the primary $\alpha\text{-Mg}$ and the eutectic $\alpha\text{-Mg}$ can be observed in the skin and the center areas of the 2 mm DC AM50, while the boundaries between the eutectic and the primary $\alpha\text{-Mg}$ solid solutions are not sharp, and are overlapped in some local areas for the 6 and 10 mm DC AM50 alloys. Nevertheless, approximate measurements of the amount of eutectic phases at various positions throughout the section thickness show a general increase in the amount of eutectic phases in the regions close to the skin of the castings as shown in the plot of Fig. 4.16.

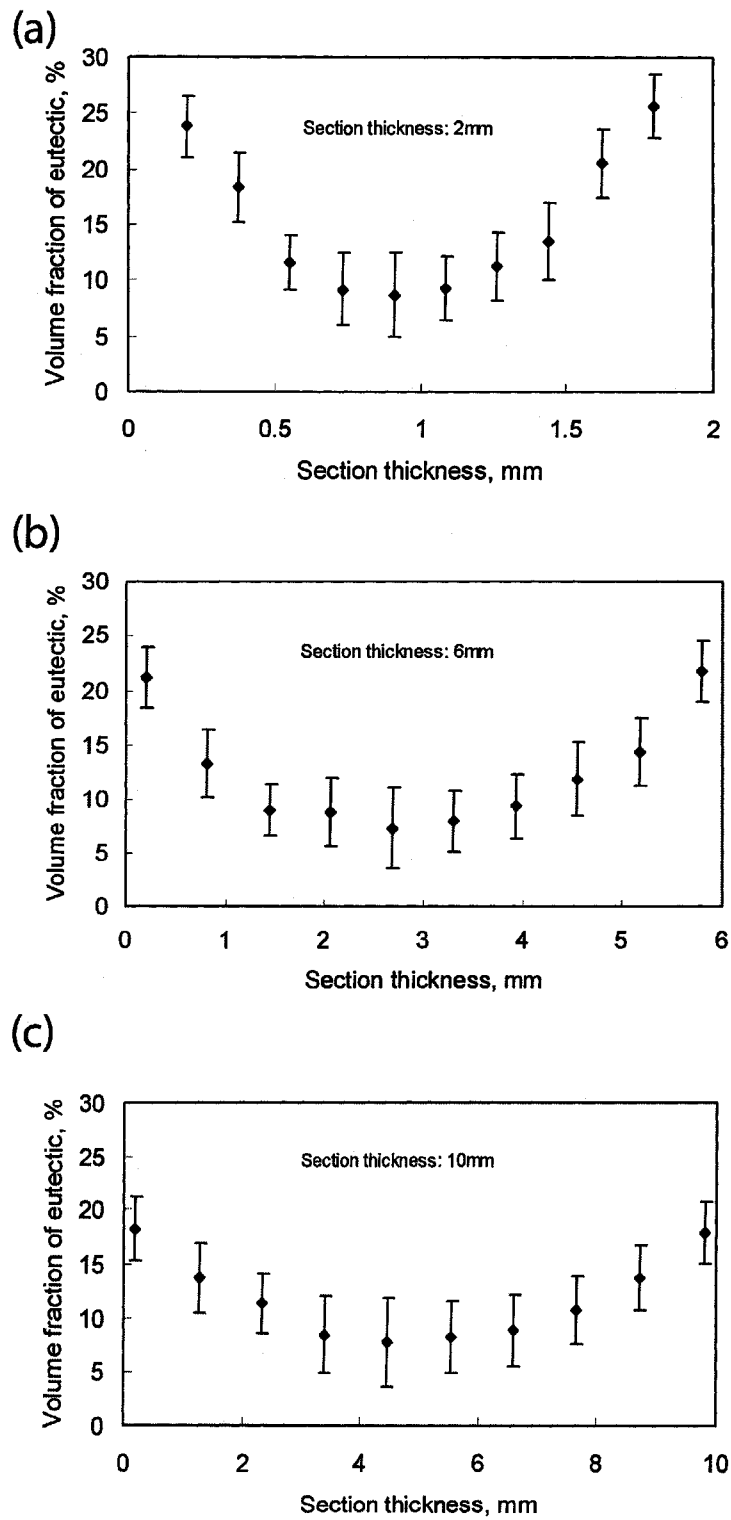


Fig. 4.16 Distribution of volume fraction of eutectic phase throughout the DC AM50 castings with section thicknesses of (a) 2 mm, (b) 6 mm and (c) 10 mm.

Also, the section thickness has an effect on the volume fraction of eutectic phases in the DC AM50 alloys. It can be noted that the volume fractions of the eutectic phases in the skin regions of the DC AM50 castings are obviously different, which are 24.7%, 21.5% and 18.1% for the DC AM50 alloys with section thicknesses of 2, 6 and 10 mm, respectively. However, there is no significant difference in the volume fractions of eutectic phase in the central regions between the 2, 6 and 10 mm thick DC AM50 coupons.

4.4 Summary

- (1). The microstructure of the die cast AM50 alloys consists of the primary α -Mg, together with the β -Mg₁₇Al₁₂, and Al₈Mn₅ phases. The intergranular β -Mg₁₇Al₁₂ phase is surrounded by a region of Al-rich eutectic α -Mg phase. The Al₈Mn₅ particles are often attached to the edge of the eutectic phases, or lie within the eutectic phases.
- (2). The dimensions and morphology of the phases in the DC AM50 alloys depend on solidification conditions. The Mg₁₇Al₁₂ phase is present in the forms of micro-scale eutectic phase along grain boundaries and nano precipitates in supersaturated solid solution. Also, micro and nano-scale Al₈Mn₅ particles are present in the DC AM50 castings.
- (3). Twin structures, small and large size, are present in the DC AM50 alloys. The small twins were distributed within the primary α -Mg grains while the observed large twins appear to cross through several primary α -Mg grains. Also, it should be noted that these twins are parallel in the local area of the matrix, which indicates

that the epitaxial relationships exist between twins, and between twin and the matrix.

- (4). A high dislocation density was revealed by TEM in the primary α -Mg due possibly to plastic deformation during fast cooling under a geometric constraint experienced in the die cast specimens. Parallel and tangled dislocations are present within the primary α -Mg. Some unidentified, very small precipitates were present at the dislocations.
- (5). A higher volume fraction of eutectic β -Mg₁₇Al₁₂ plus Al-rich eutectic α -Mg and a smaller SDAS were found in the skin than in the central regions of the die cast AM50 alloys. Examination of the corresponding regions in the 2, 6 and 10 mm thick coupons showed that the volume fraction of the eutectic phase decreased, while the SDAS increased, with increasing section thickness.

CHAPTER 5
RESULTS AND DISCUSSION OF MICROSTRUCTURES OF PM Mg-Al AND
Mg-Al-Ca ALLOYS

5.1 As-cast microstructures of Mg-Al alloy

Fig. 5.1 shows the typical microstructure in the permanent mold cast AM50 alloy. It can be seen that the microstructures consist of the primary α -Mg, β -Mg₁₇Al₁₂ and Al₈Mn₅ phases. The β -Mg₁₇Al₁₂, with a less bright contrast, is often surrounded by the eutectic α -Mg, while the bright white spots visible on the SEM image are Al₈Mn₅ precipitates. Some of these precipitates are in the middle of grains, while the majority of the Al-Mn particles are within the eutectic α -Mg phase.

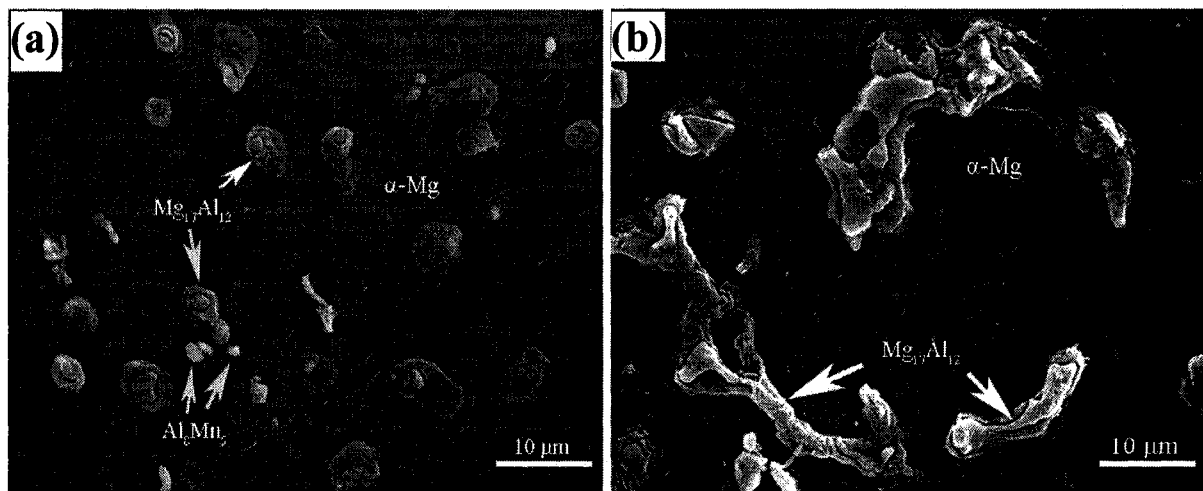


Fig. 5.1 SEM micrographs of the PM AM50 alloy in: (a) skin region and (b) central region.

The morphology of the eutectic phases, including β -Mg₁₇Al₁₂ and eutectic α -Mg in the skin and the central regions, was obviously different, as is shown in Figs. 5.1(a) and (b). A large amount of separate, round eutectic islands were observed in the skin of the PM casting. The β -Mg₁₇Al₁₂ particle is in the middle of the island, and was surrounded by the eutectic α -Mg. However, some long eutectic islands, as well as the round eutectic islands,

were found in the middle of the casting. The β -Mg₁₇Al₁₂ particles in these long islands are noticeably coarse compared to those in the skin region. Additionally, the β -Mg₁₇Al₁₂ phases were discontinuously distributed in both regions of the casting.

The microstructure of the 7 mm thick PM AM50 alloy was significantly coarser than that of the 2 mm thick DC AM50 alloy (Figs. 4.2(a) and (b)). This is because the different solidification rates are present in the two processes. Normally, Mg castings made by die casting experience higher cooling rates than those cast by permanent mold casting. In high pressure die casting, the steel dies used for casting magnesium alloys cool rapidly when the back of the dies are oil cooled and heat is transported rapidly from the casting through the metal-mold interface during rapid injection. The microstructure of the PM AM50 alloys with a moderate aluminum content shows the presence of low volume fractions of the divorced β -Mg₁₇Al₁₂ phase as intergranular particles along the grain boundaries, as shown in Fig. 5.1 (a) and (b) compared to that in the DC AM50 alloy (Figs. 4.2(b), (c) and (d)). The β -Mg₁₇Al₁₂ phase was not observed within the primary α -Mg grains for the PM AM50 alloys. The β -Mg₁₇Al₁₂ phase has a low melting temperature, which indicates that it is a relatively soft phase and is thermally unstable. Another significant difference in the microstructure of the as-cast AM50 alloys is that a continuous network of the Al-rich eutectic α -Mg was observed in DC AM50 while a discontinuous distribution of the Al-rich α -Mg was found in PM AM50 alloy.

Fig. 5.2 presents a SEM micrograph and the EDS line scan results, which show the compositional variation across a β -Mg₁₇Al₁₂ particle and the surrounding eutectic α -Mg phase on the grain boundaries. Concentrations of Mg and Al inside the primary α -Mg grains are constant, and a smooth increase in Al content was observed when the probe crossed the

eutectic α -Mg phase, indicating that the eutectic α -Mg phase would be Al-rich phase. Once the probe crosses the eutectic β -Mg₁₇Al₁₂ particle, there is a sharp increase in Al content. Local microsegregation was also found in the permanent casting due to the coring.

Fig. 5.3 shows a SEM micrograph and elemental maps for the PM AM50 alloy from the same region. Using the Mg, Al and Mn X-ray maps of the same field shown in Fig. 5.3(a), the β -Mg₁₇Al₁₂ phases and the Al₈Mn₅ phases (marked by arrows) can be identified. Also, Al-rich eutectic α -Mg phases surrounding the β -Mg₁₇Al₁₂ phases are distributed along the grain boundaries.

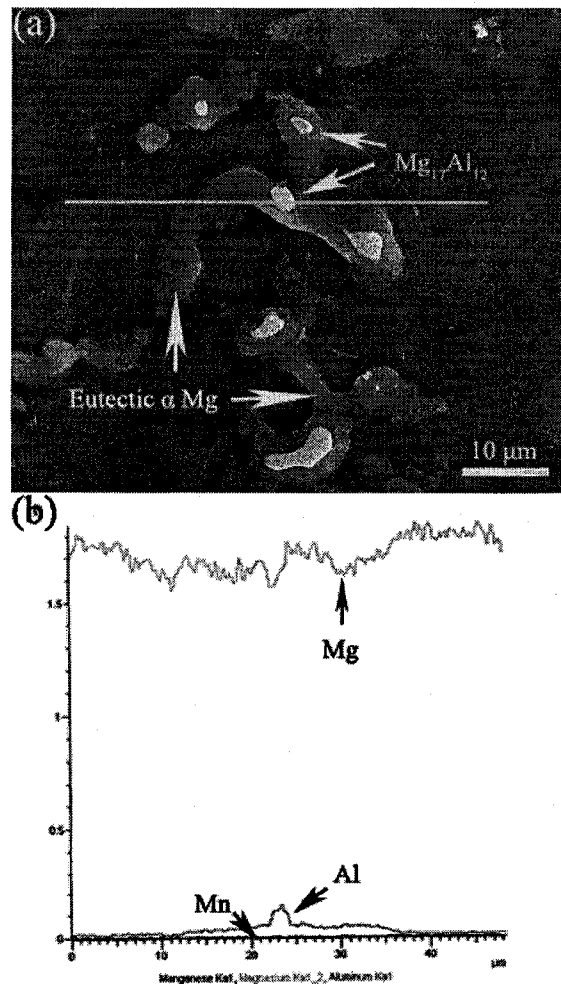


Fig. 5.2 (a) SEM micrograph and (b) EDS line scan in the PM AM50 alloy.

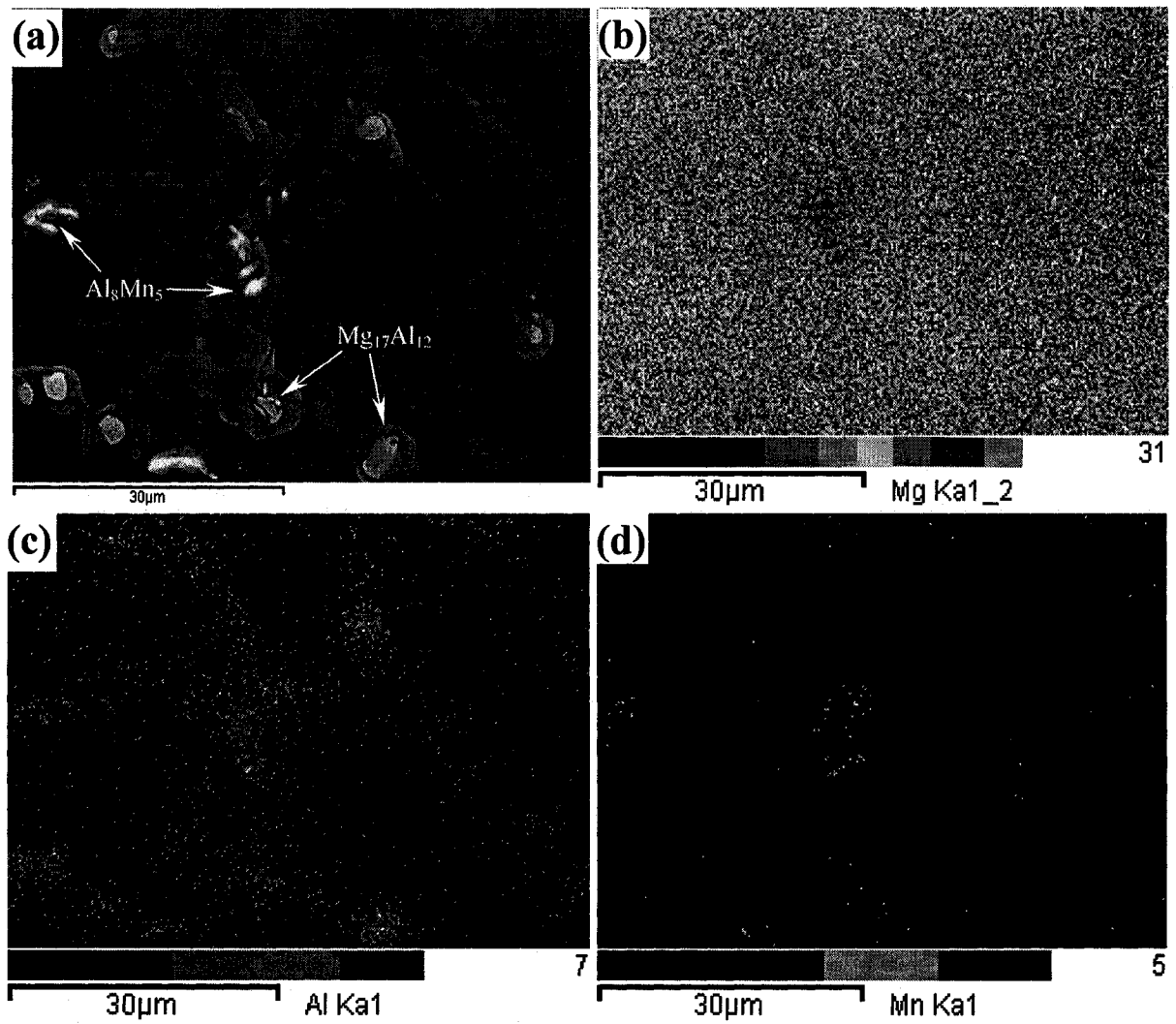


Fig. 5.3 EDS results for the PM AM50 alloy: (a) SEM micrograph, and elemental maps from the same region for (b) Mg, (c) Al and (d) Mn.

5.2 As-cast microstructures of Mg-Al-Ca alloys

To investigate the effect of Ca content on microstructure of the PM Mg-Al-Ca alloys, four different levels of Ca addition (0.5, 1.0, 1.5 and 2.0 wt.%) were introduced to the based alloy AM50 alloy.

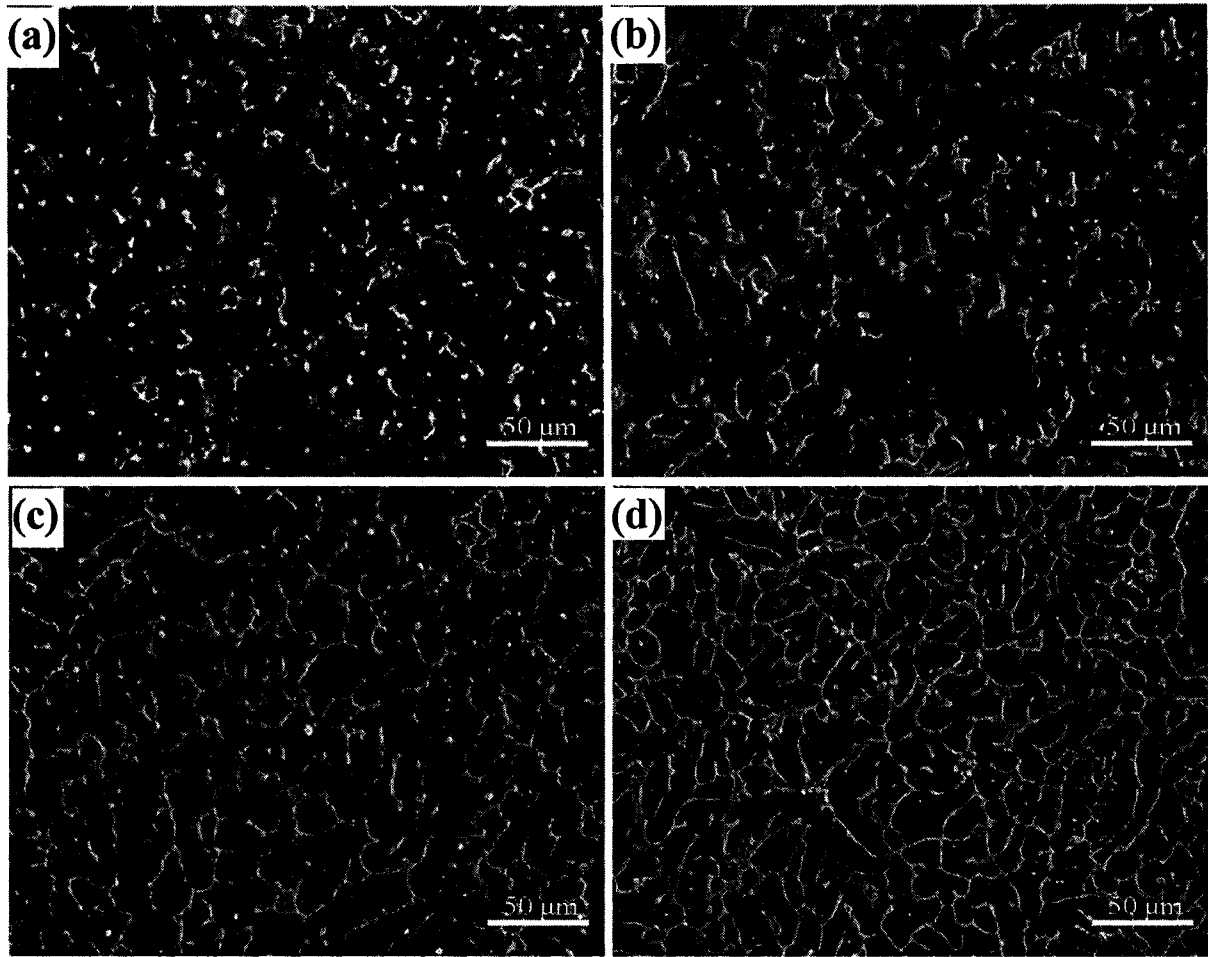


Fig. 5.4 SEM micrographs of the PM Mg-Al-Ca alloys with different Ca contents (wt.%):

(a) 0.5, (b) 1.0, (c) 1.5, and (d) 2.0.

SEM micrographs showing the development of the microstructure of the Mg-Al alloy with various Ca contents are presented in Fig. 5.4. The marked grain refining effect of a high Ca addition (Fig.5.4 (d)) is clearly evident compared to the specimen with low Ca addition (Fig.5.4 (a)) under the same casting conditions. The completely divorced, discontinuous eutectic phases have gradually been replaced by a continuous network of eutectic phases with increasing Ca content. Although a 2.0 wt.% Ca addition level exceeds the solid solubility limit of calcium in magnesium (0.82 wt.% at 516.5 °C), no excess insoluble Ca particles were

found in the microstructure of the PM AC52 alloy. The grain refining effect of Ca was further confirmed by quantitative image analysis to measure the secondary dendrite arm spacing (SDAS) and the volume fraction of the secondary eutectic phase. The results show that as the Ca content increases from 0.5 to 2.0 wt.%, the measured SDAS values decrease from $30.0 \pm 5.2 \mu\text{m}$ to $9.8 \pm 3.1 \mu\text{m}$, while the measured volume fractions of the eutectic phases increase from $7.4 \pm 2.2 \%$ to $21.4 \pm 4.2 \%$. The results on the effect of Ca content on the microstructure of the PM Mg-Al-Ca alloys are summarized in Table 5.1, and the relationships between Ca content and the SDAS and the volume fraction of eutectic are plotted in Figs.5.5 (a) and (b), respectively.

Table 5.1 SDAS and the volume fraction of eutectic phase measured
in the Mg-Al-Ca series alloys

Alloy	Ca content (wt.%)	SDAS (μm)	Volume fraction of eutectic (%)
PM AC505	0.5	29.96 ± 5.2	7.4 ± 2.2
PM AC51	1.0	22.87 ± 4.7	10.5 ± 2.6
PM AC515	1.5	17.27 ± 3.8	15.2 ± 3.4
PM AC52	2.0	9.76 ± 3.1	21.4 ± 4.2

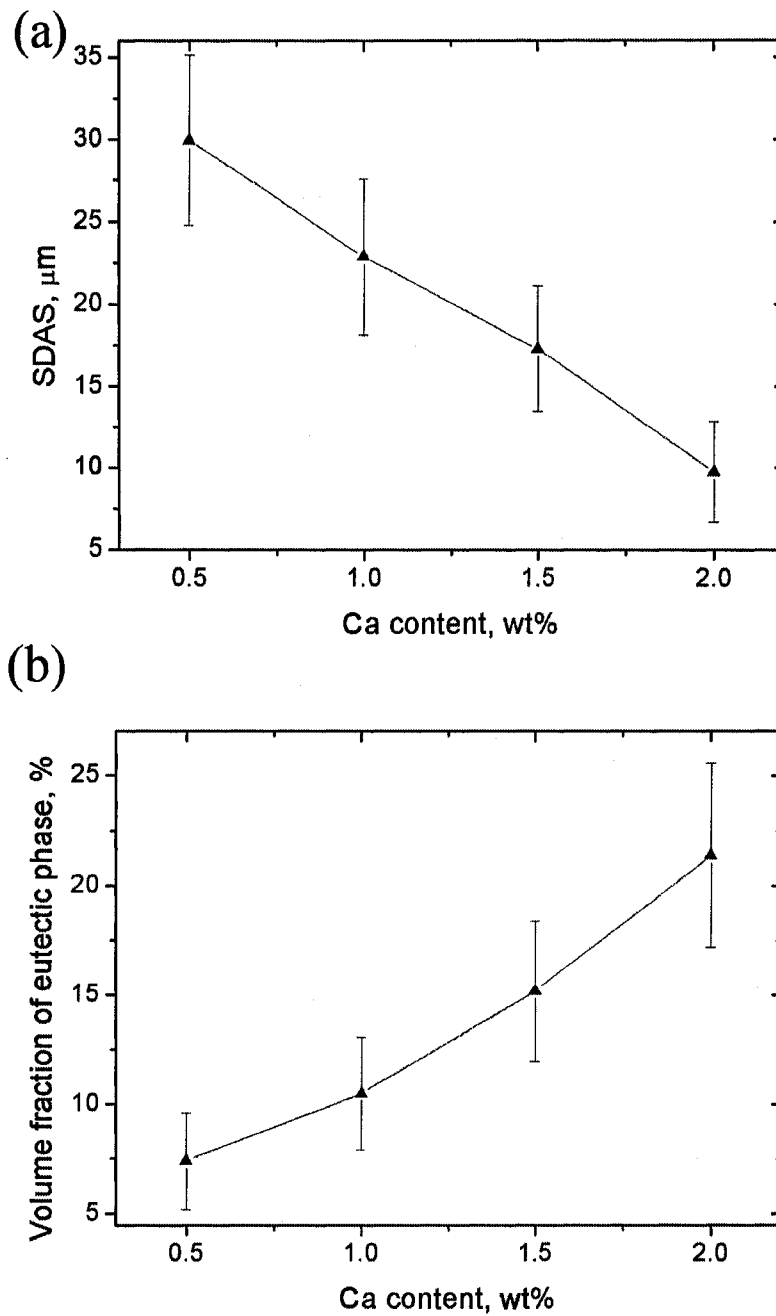


Fig. 5.5 Effect of Ca content on: (a) the SDAS and (b) the volume fraction of eutectic phase in the PM Mg-Al-Ca alloys.

Fig. 5.6 shows SEM images of the microstructure development in the center of the Mg-Al-Ca alloys with different Ca contents at high magnification for the purpose of phase identification. The volume fraction of the eutectic phase obviously increases in the PM

AC505 alloy (Fig. 5.6(a)) compared to the PM AM50 alloy without Ca addition under the same casting conditions (Fig. 5.1(b)). With the addition of Ca in the AM50 alloy, Ca-containing eutectic phases begin to appear in the microstructures of the castings. When the content of Ca is low, $Mg_{17}Al_{12}$ phases as well as the Ca-containing phases co-exist in the castings, as shown in Figs. 5.6 (a) and (b). The Ca-containing compound has better stability at higher temperatures, contributing to an increased creep resistance, while also suppressing the formation of the β - $Mg_{17}Al_{12}$ phase. Therefore, when the Ca content is 1.5 wt.% or higher in the casting, the β - $Mg_{17}Al_{12}$ phase was completely replaced by the Ca-containing phase as shown in Figs. 5.6 (c) and (d). Additionally, Al_8Mn_5 particles with bright contrast are also observed in all the Mg-Al-Ca alloys, and the volume fraction of the phase in all the castings is less than 1%. It seems that the addition of Ca has little effect on the precipitation of the Al_8Mn_5 phase. Since the β - $Mg_{17}Al_{12}$ and Ca-containing phases have the similar contrast in the microstructures of the castings with low Ca content (0.5 and 1.0 wt. %), it is hard to distinguish them in the optical and SEM images. Therefore, the volume fraction of eutectic phase measured in the alloy with low Ca contents was in fact the sum of volume fraction of two β - $Mg_{17}Al_{12}$ and Ca-containing eutectic phases. Although the β - $Mg_{17}Al_{12}$ and Ca-containing phases have similar contrast in the micrographs of castings with low Ca contents, they had very different morphologies. As described in Sections 4.1 and 5.1, the β - $Mg_{17}Al_{12}$ particles are often surrounded by the Al-rich eutectic α -Mg in the as-cast AM50 alloys (Fig. 5.1 and Fig. 4.2). However, there was no eutectic α -Mg surrounding the new Ca-containing phase in all the Mg-Al-Ca alloys. This observation suggests that the segregation of the solute (Al) in the primary α -Mg phases has been significantly reduced with the addition of Ca to the AM50 alloy.

Fig 5.7 shows a SEM image and EDS results for the PM AC51alloy. The probe crosses the primary α -Mg, $Mg_{17}Al_{12}$ and Ca-containing phases in turn along the gray line in Fig. 5.7(a). When the probe crossed the $Mg_{17}Al_{12}$ particle, a minor decrease in Mg and a small increase in Al were observed. However, a large sharp decrease in Mg, and a large and rapid increase in Ca were found when the probe touched the Ca-containing phase (Fig. 5.7 (b)). Additionally, the EDS mapping results showed that Ca and Al mostly precipitated along the grain boundaries (Fig. 5.7 (d) and (e)). Mn precipitation is observed in the matrix or at the grain boundaries (Fig. 5.7 (f)).

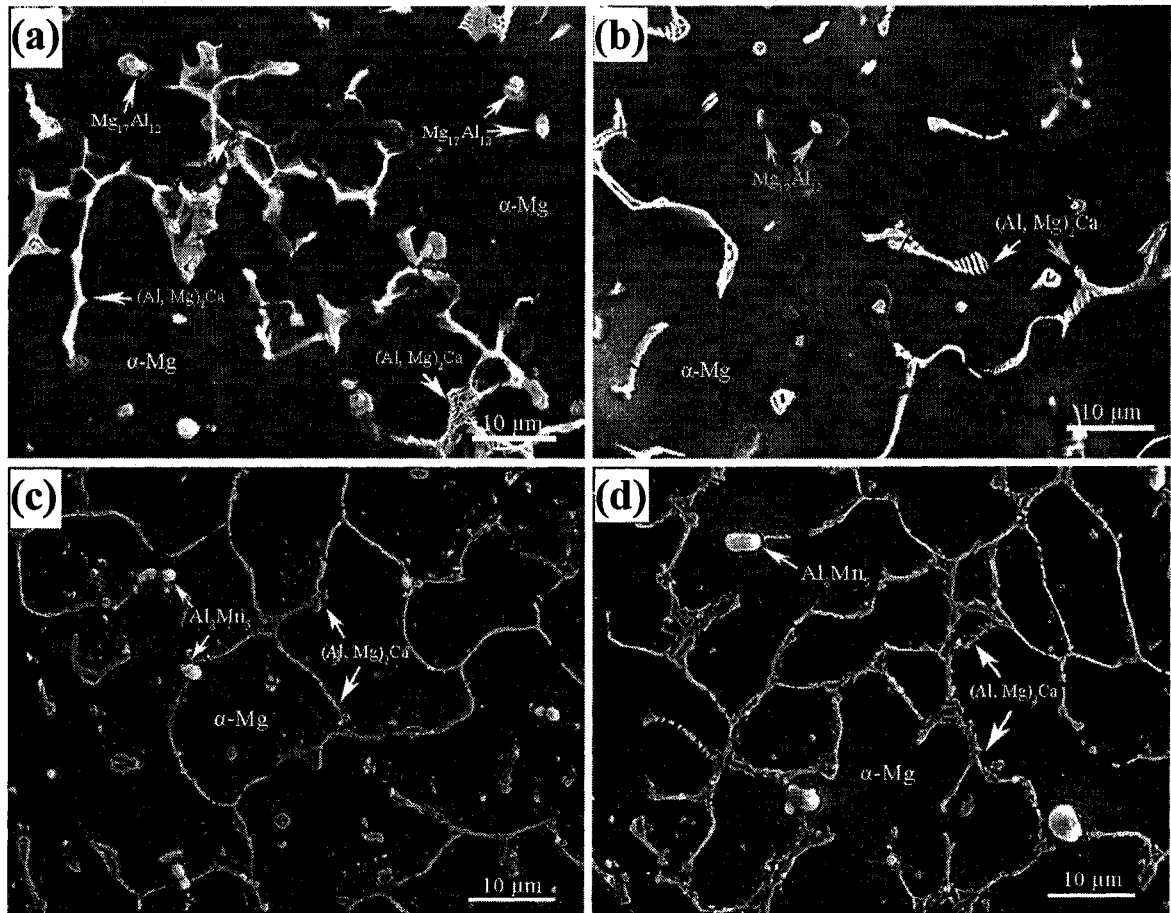


Fig. 5.6 Microstructure in the center of the Mg-Al-Ca alloys with the content of Ca (wt.%): (a) 0.5, (b) 1.0, (c) 1.5 and (d) 2.0.

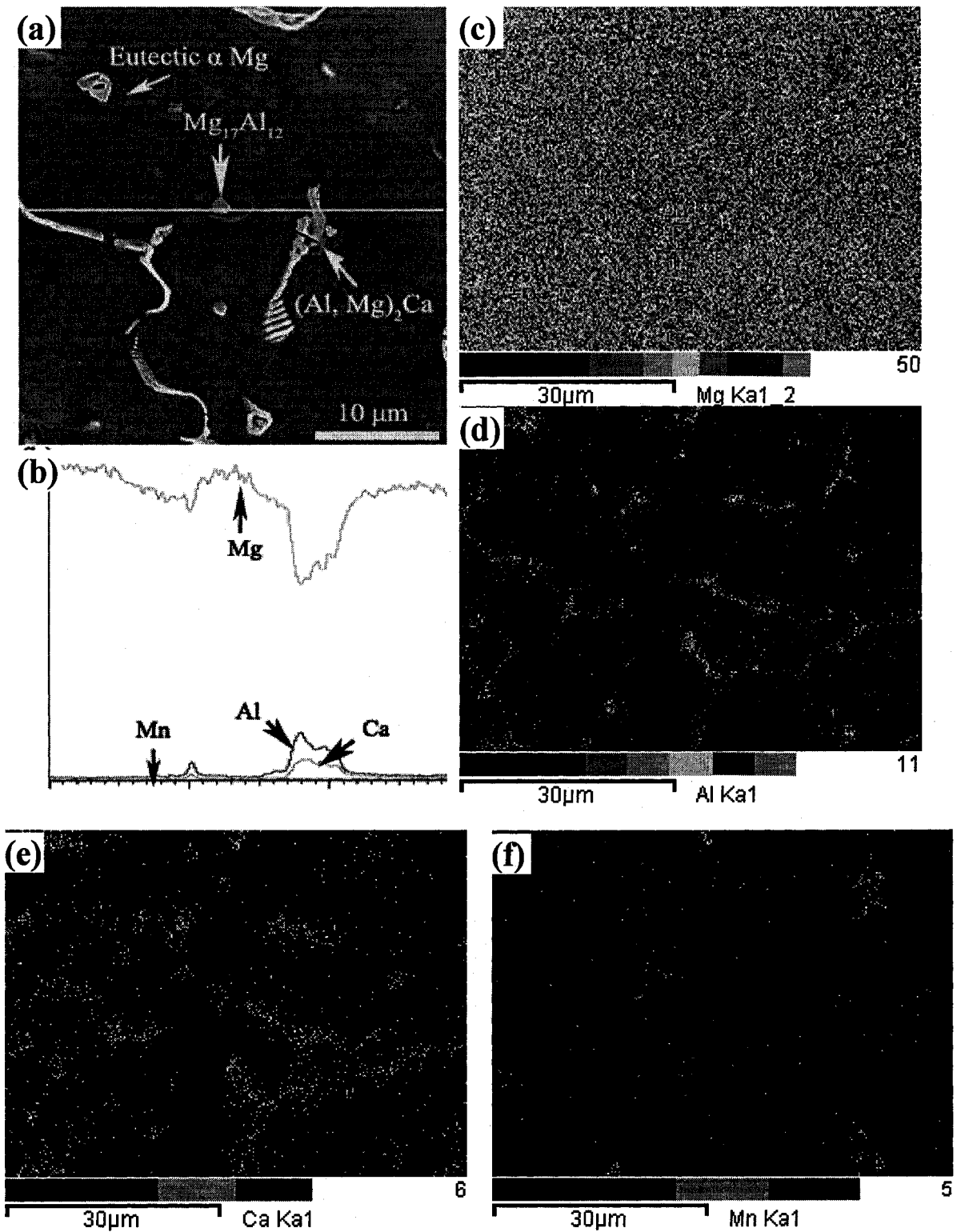


Fig. 5.7 EDS results for the PM AC51 alloy: (a) SEM micrograph, (b) EDS line scans, and elemental maps from the same region for (c) Mg, (d) Al, (e) Ca and (f) Mn.

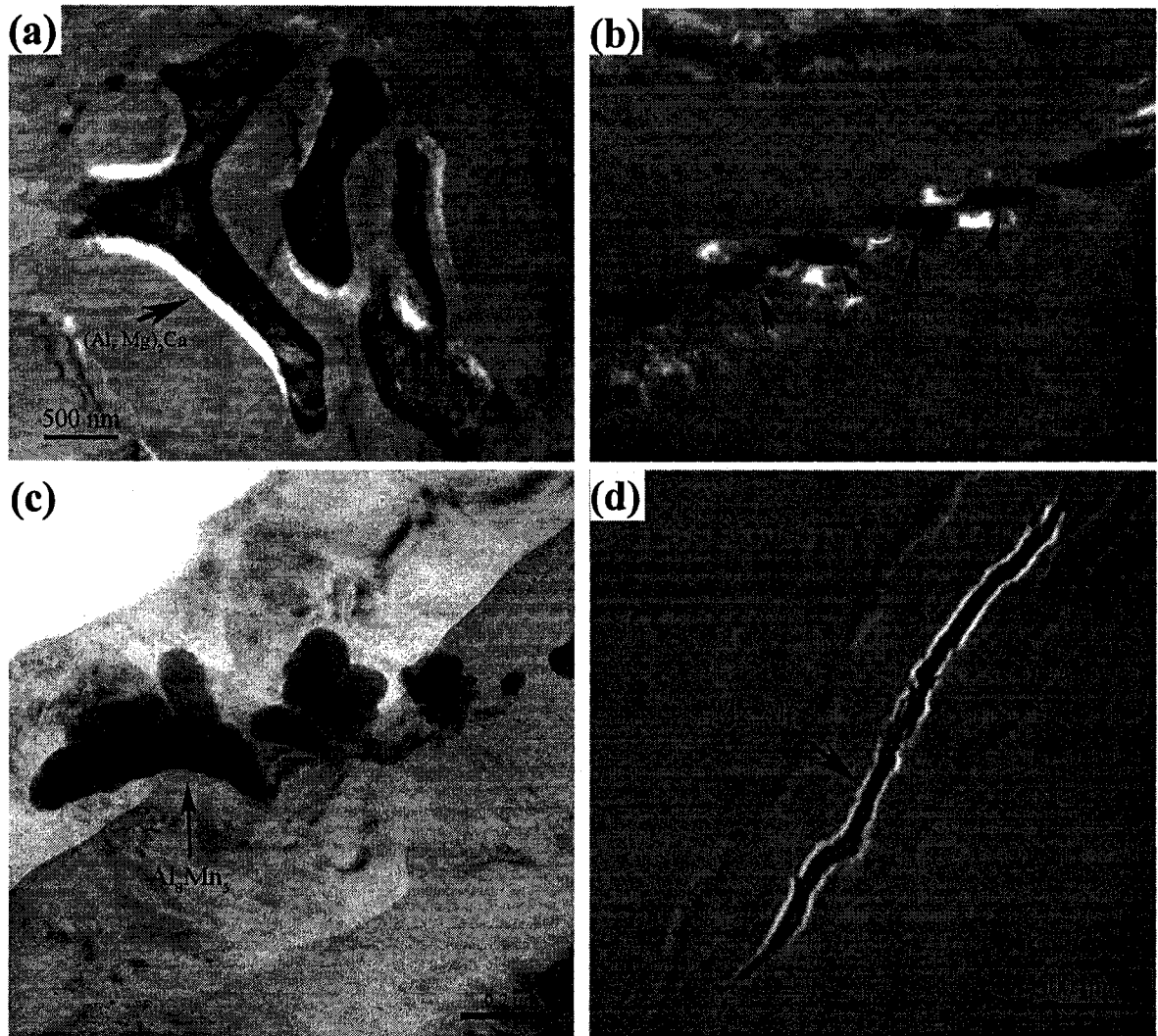


Fig. 5.8 TEM BF images of: (a) $(Al, Mg)_2Ca$ at triangular grain boundary, (b) $(Al, Mg)_2Ca$ at grain boundary, (c) Al_8Mn_5 and (d) $Mg_{17}Al_{12}$ in the PM AC51 alloy.

TEM BF images of the eutectic phases observed in the PM AC51 alloy are presented in Fig. 5.8. Three eutectic phases, $Mg_{17}Al_{12}$, Al_8Mn_5 and Ca-containing, were present in the matrix of the PM AC51 alloy. Their morphologies were significantly different. Coarse Ca-containing phases were often found at grain boundary triple-points while fine Ca-containing phases were present along grain boundaries. These Ca-containing phases were $(Al, Mg)_2Ca$ phase, as identified by the indexing of the selected area diffraction patterns. Details of the

selected area diffraction pattern and the indexing of the $(\text{Al}, \text{Mg})_2\text{Ca}$ phase are given in Fig. 5.10. Fine Al_8Mn_5 particles with lamellar structure were also present in Fig. 5.8 (c). However, coarse Al_8Mn_5 particles with polygonal shape were not found. This can be explained that, due to the low volume fraction of Al_8Mn_5 in the PM AC51 alloy, particles of this phase may simply not be encountered in arbitrary sections in the TEM foils. Also, polycrystalline eutectic phase, $\text{Mg}_{17}\text{Al}_{12}$, was found in the casting. One of the observed morphological forms of this phase was the narrow long eutectic constituent (Fig. 5.8 (d)).

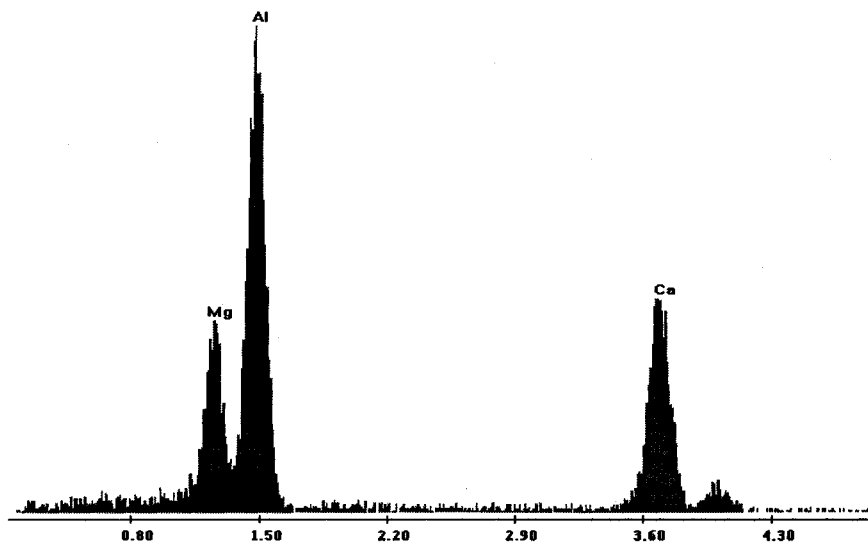


Fig. 5.9 Typical EDS spectra of $(\text{Al}, \text{Mg})_2\text{Ca}$ phase in the PM AC52 alloy.

Analysis of TEM/EDX (Fig. 5.9) gives an average composition for $(\text{Al}, \text{Mg})_2\text{Ca}$ phases (wt.%) of 19.2 ± 1.7 Al, 47.8 ± 3.2 Mg and 32.9 ± 2.1 Ca in the PM AC52 alloy. The TEM BF image of the $(\text{Al}, \text{Mg})_2\text{Ca}$ phase showed a ‘rib’ shape with lamellae structures that were arranged in alternating layers of Ca phase and eutectic Mg phase, as shown in Fig. 5.10 (a). The details of the diffraction pattern can be better understood by the indexed schematic solution in Fig. 5.10 (c). The selected area diffraction pattern confirms that $(\text{Al}, \text{Mg})_2\text{Ca}$

phase has a hexagonal close-packed (HCP) crystal structure with $a = 0.5764$ nm and $c = 0.9641$ nm, which is in agreement with the previous results [8, 55].

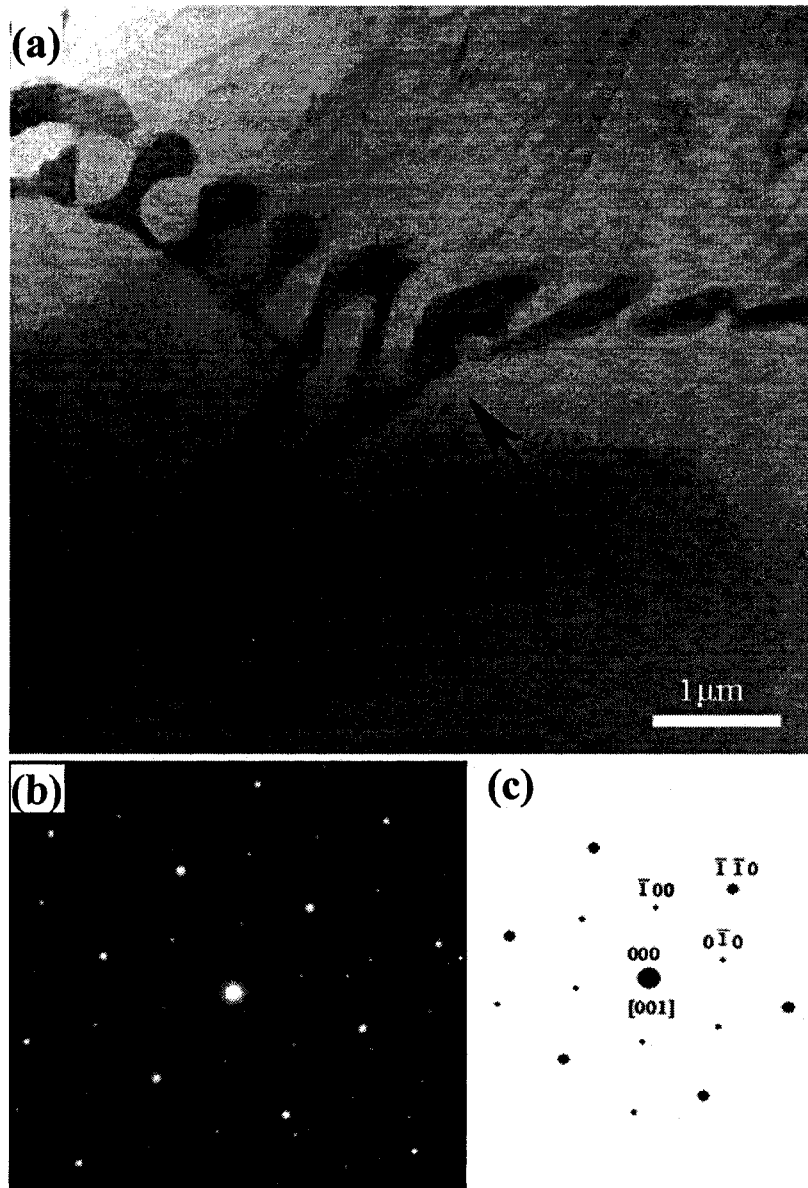


Fig. 5.10 (a) Typical TEM image of $(Al, Mg)_2Ca$ in PM AC52 alloy, (b) selected area diffraction pattern from $(Al, Mg)_2Ca$ phase with dark contrast, and (c) indexing of diffraction pattern in (b).

The following crystallographic orientation relationship between $(\text{Al}, \text{Mg})_2\text{Ca}$ precipitate and the matrix was determined from a series of selected area electron diffraction patterns such as that shown in Fig. 5.11.

$$(100)(\text{Al}, \text{Mg})_2\text{Ca} \parallel (1\bar{2}0)\text{Mg};$$

$$(02\bar{1})(\text{Al}, \text{Mg})_2\text{Ca} \parallel (\bar{3}02)\text{Mg}; \text{ and}$$

$$[012](\text{Al}, \text{Mg})_2\text{Ca} \parallel [213]\text{Mg}$$

Fig. 5.12 presents EDS compositional profiles obtained by scanning the beam from one primary α -Mg grain center across the $(\text{Al}, \text{Mg})_2\text{Ca}$ and Al_8Mn_5 phases on the grain boundary to the neighboring grains. When the probe crossed the $(\text{Al}, \text{Mg})_2\text{Ca}$ phase and Al_8Mn_5 phases in the PM AC52 alloy, distinct changes occurred in Mg, Al, Ca and Mn traces.

Fig. 5.13 presents a SEM micrograph and elemental maps from the same region of the PM AC52 alloy. The grain boundaries appear relatively thick due to the massive presence of Ca and Al enriched eutectic phase. The $(\text{Al}, \text{Mg})_2\text{Ca}$ phases, which are marked by arrows, can be seen along the grain boundaries. The bright particles, which are the Al_8Mn_5 phase, were distributed within the grains or at the grain boundaries throughout the matrix of the alloy. Also, the EDX results in Fig. 5.13 show that there was still some Al and Ca trapped within the grains due primarily to rapid solidification.

Fig. 5.14 shows HREM image of the $(\text{Al}, \text{Mg})_2\text{Ca}$ phase along the $[001]$ zone axis in the PM AC52 alloy. From the ordered structure characteristics, one can easily identify the crystal structural feature. The $(\text{Al}, \text{Mg})_2\text{Ca}$ phase can be identified by the relatively dark contrast. Obviously, there is a sharp interface between the $(\text{Al}, \text{Mg})_2\text{Ca}$ phase and the matrix.

A nanoscale Al_8Mn_5 particle was observed in the matrix of the PM AC52, as shown in Fig. 5.15.

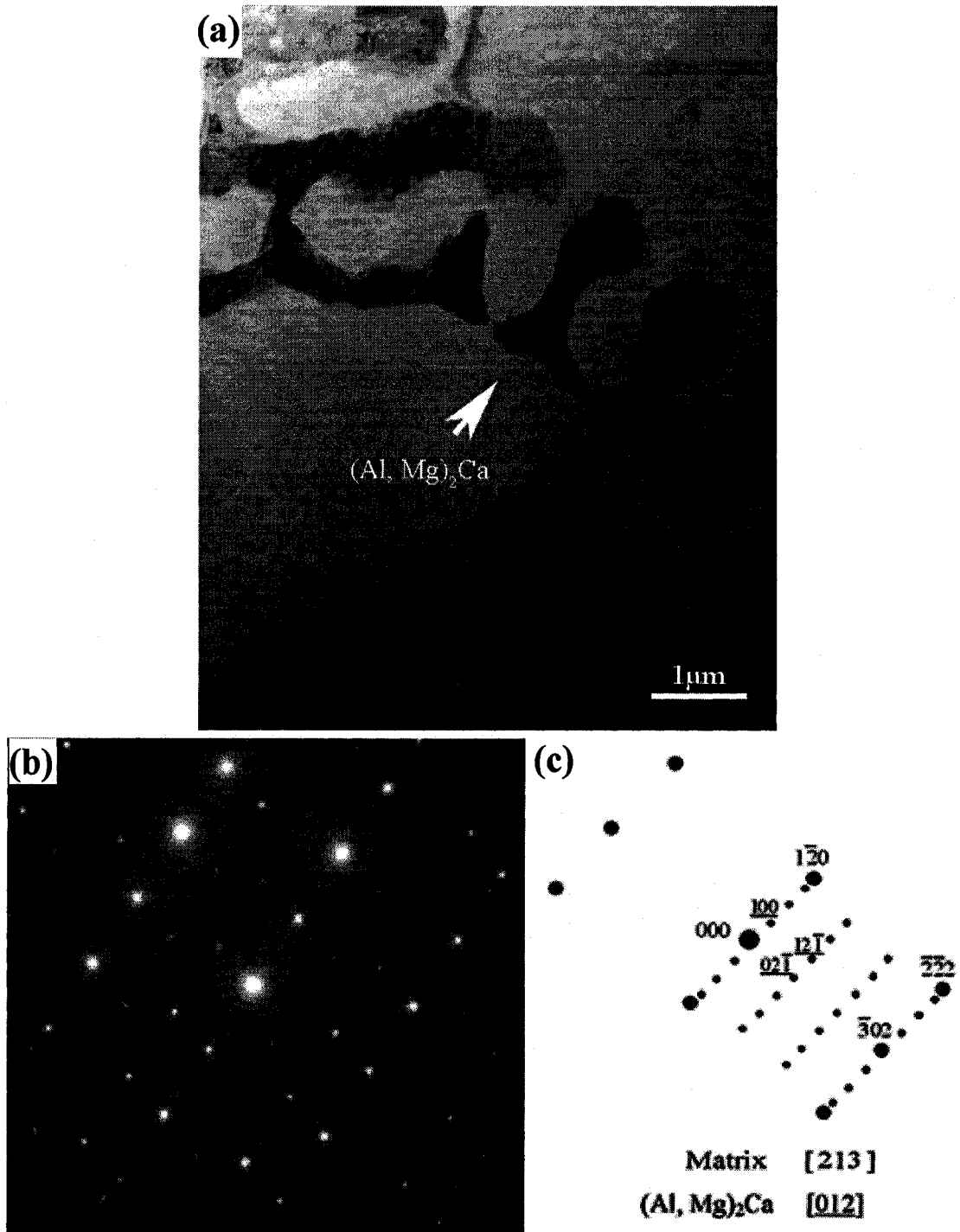


Fig. 5.11 (a) Typical TEM image of $(Al, Mg)_2Ca$ in PM AC52 alloy, (b) selected area diffraction pattern from $(Al, Mg)_2Ca$ phase with dark contrast, and (c) indexing of diffraction pattern in (b).

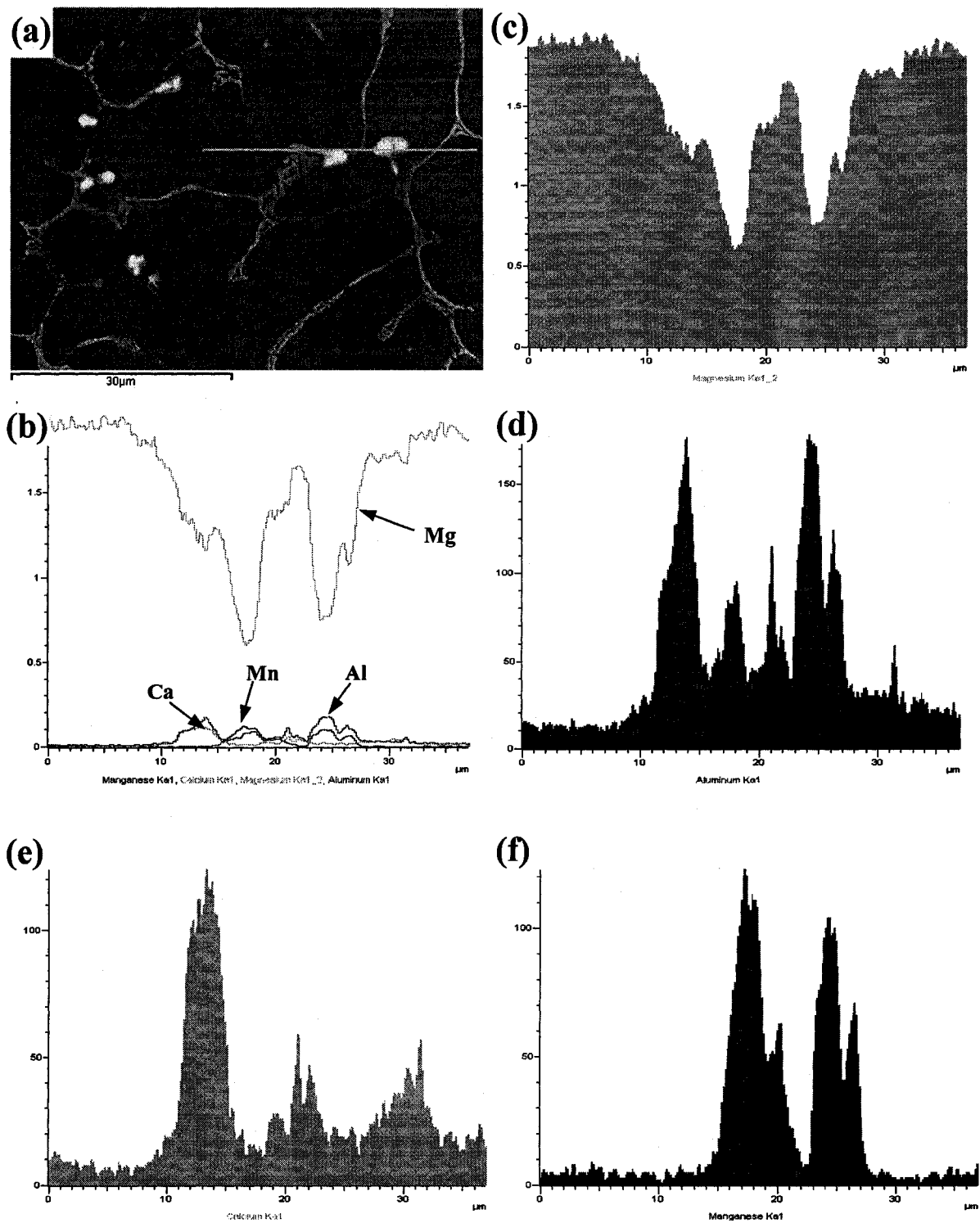


Fig. 5.12 (a) SEM micrograph, (b) total EDS line scans from the same region, and individual line scan: (c) Mg, (d) Al, (e) Ca and (f) Mn in the PM AC52 alloy.

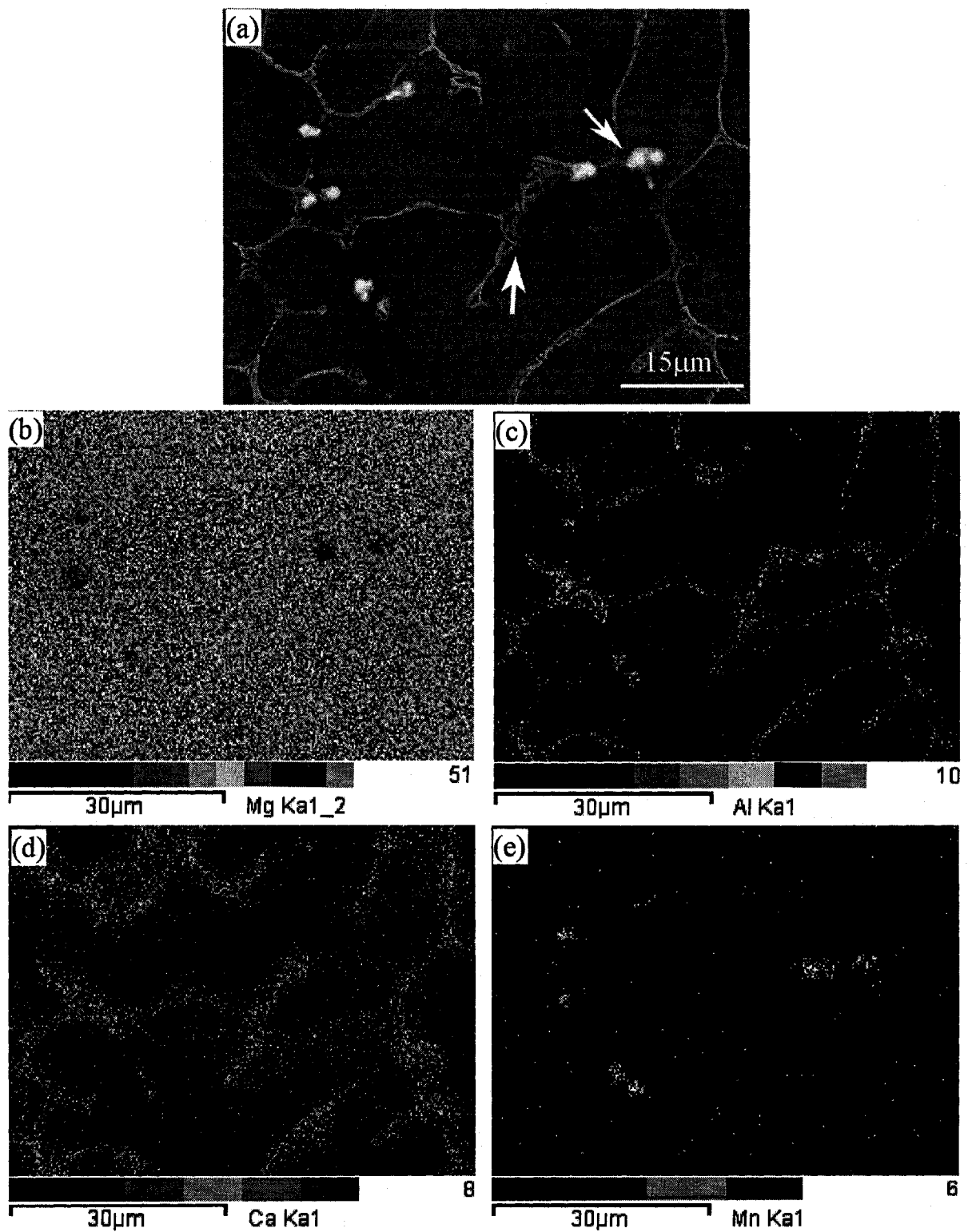


Fig. 5.13 EDS results for the PM AC52 alloy: (a) SEM micrograph, and elemental maps from the same region for (b) Mg, (c) Al, (d) Ca and (e) Mn.

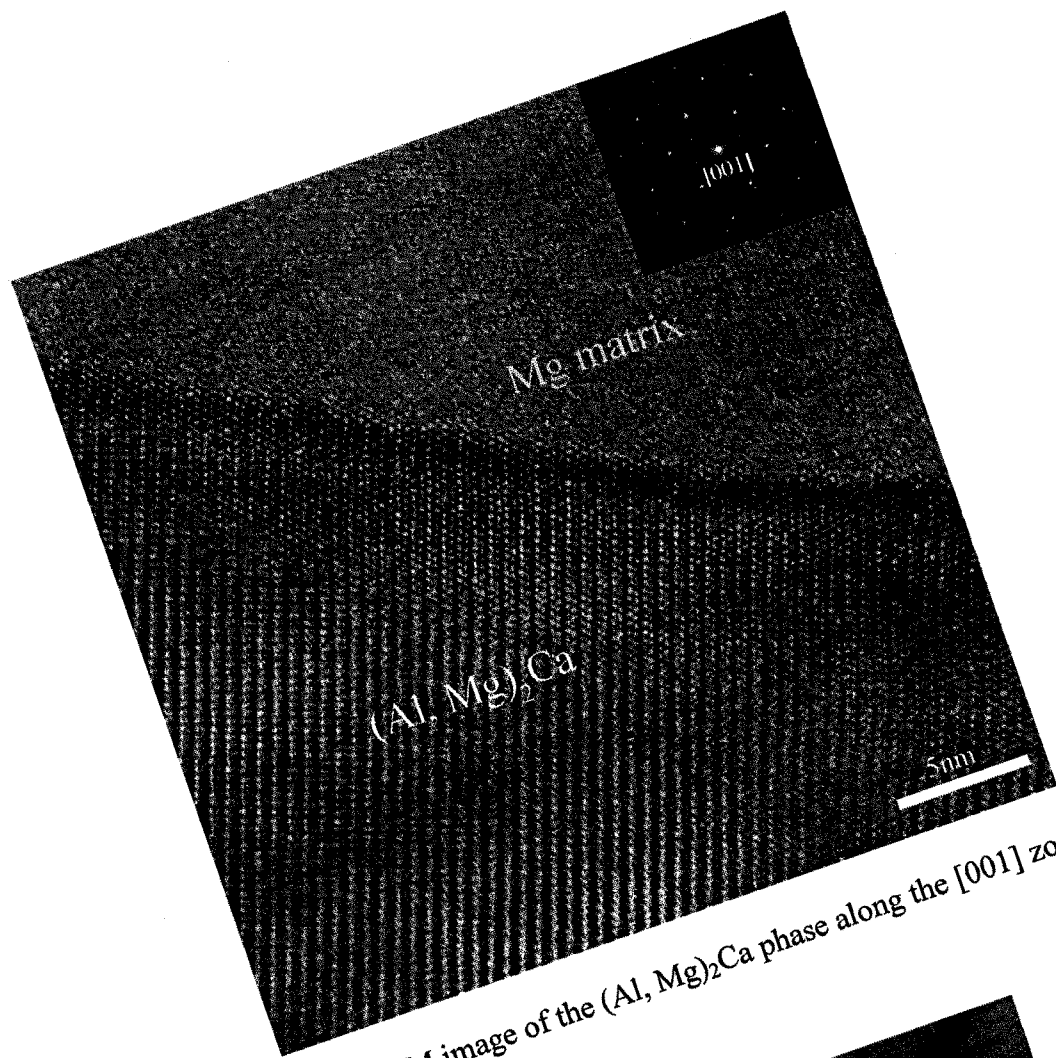


Fig. 5.14 HREM image of the $(Al, Mg)_2Ca$ phase along the $[001]$ zone axis in the PM AC52 alloy.

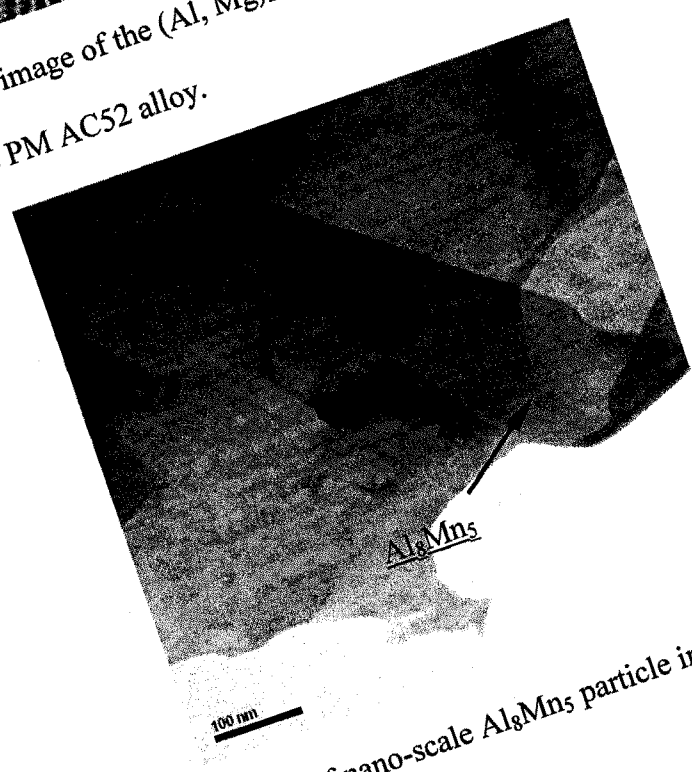


Fig. 5.15 TEM image of nano-scale Al_8Mn_5 particle in the PM AC52 alloy.

Fig. 5.16 showed SEM images at high magnification of the twin structures present in the Mg-Al-Ca alloys and their TEM BF images in the PM AC52 alloy. The twins are mostly distributed within the grains. The twin structures were parallel within an individual grain, while different orientations of the twin structures are present in neighboring grains. Additionally, some of the long twins that were observed crossed several grains in some regions.

Twinned microstructures have been observed in many materials [163-165]. In some cases [164], twins are related to phase transformations. In other cases [164, 165], twinning is an important mechanism for plastic deformation. In all cases, the knowledge of the atomic structure at the twin boundaries is of great interest.

Fig. 5.17 presents HREM images along the [011] zone axis showing the twin microstructure and a twin boundary in the PM AC52 alloy. Nanoscale strain fields give rise to image contrast effects at the structural modulations as shown in the rectangular boxes in Fig. 5.17 (a). The dashed line in Fig. 5.17 (b) indicates a twin boundary. A section of perfect twin boundary is highlighted by a small ellipse, and an imperfect dislocation boundary zone is outlined by a large ellipse along a twin boundary.

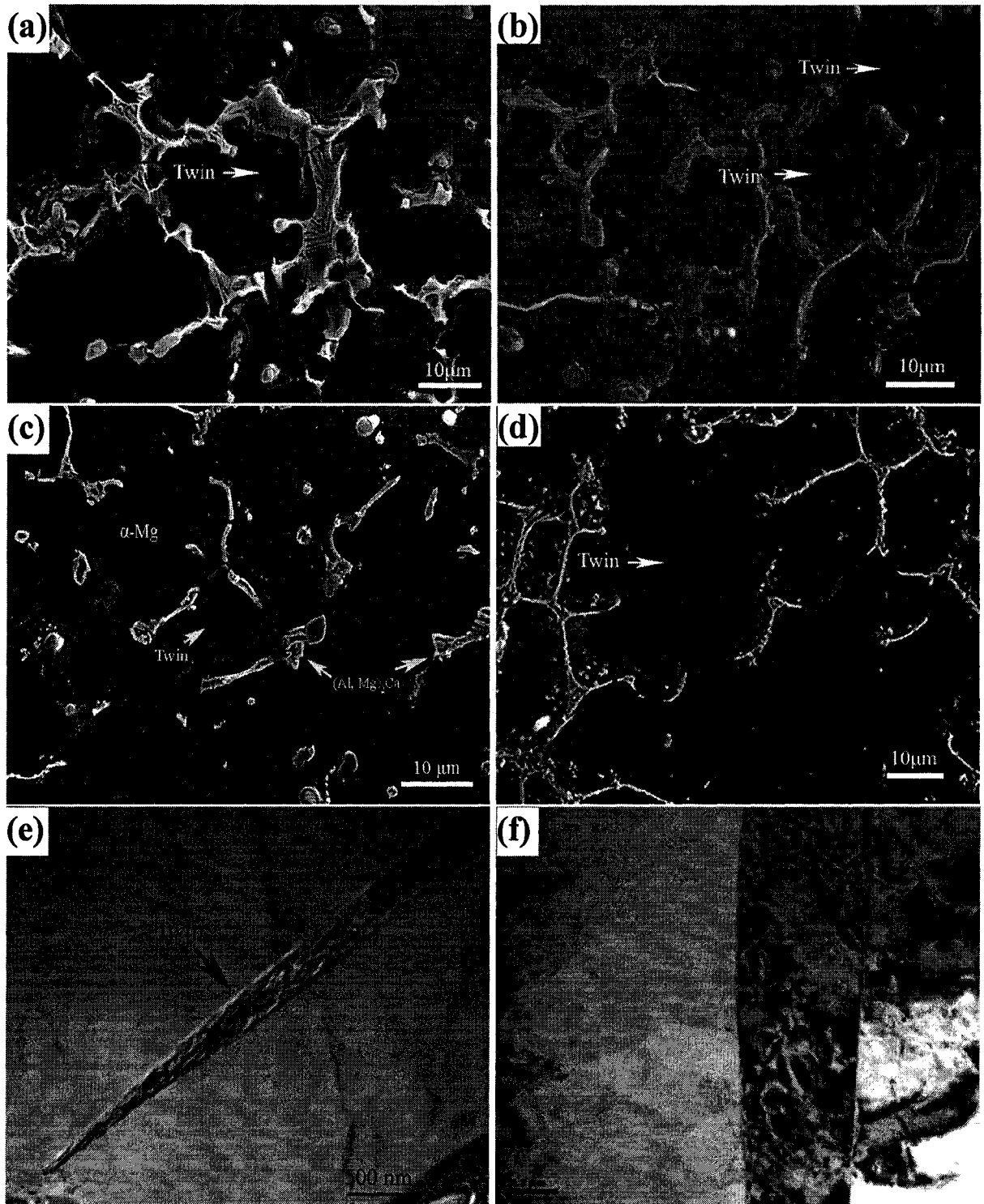


Fig. 5.16 Twin structures in SEM images of: (a) AC505, (b) AC51, (c) AC515, (d) AC52 alloys, and in (e) and (f) TEM images of AC52 alloy.

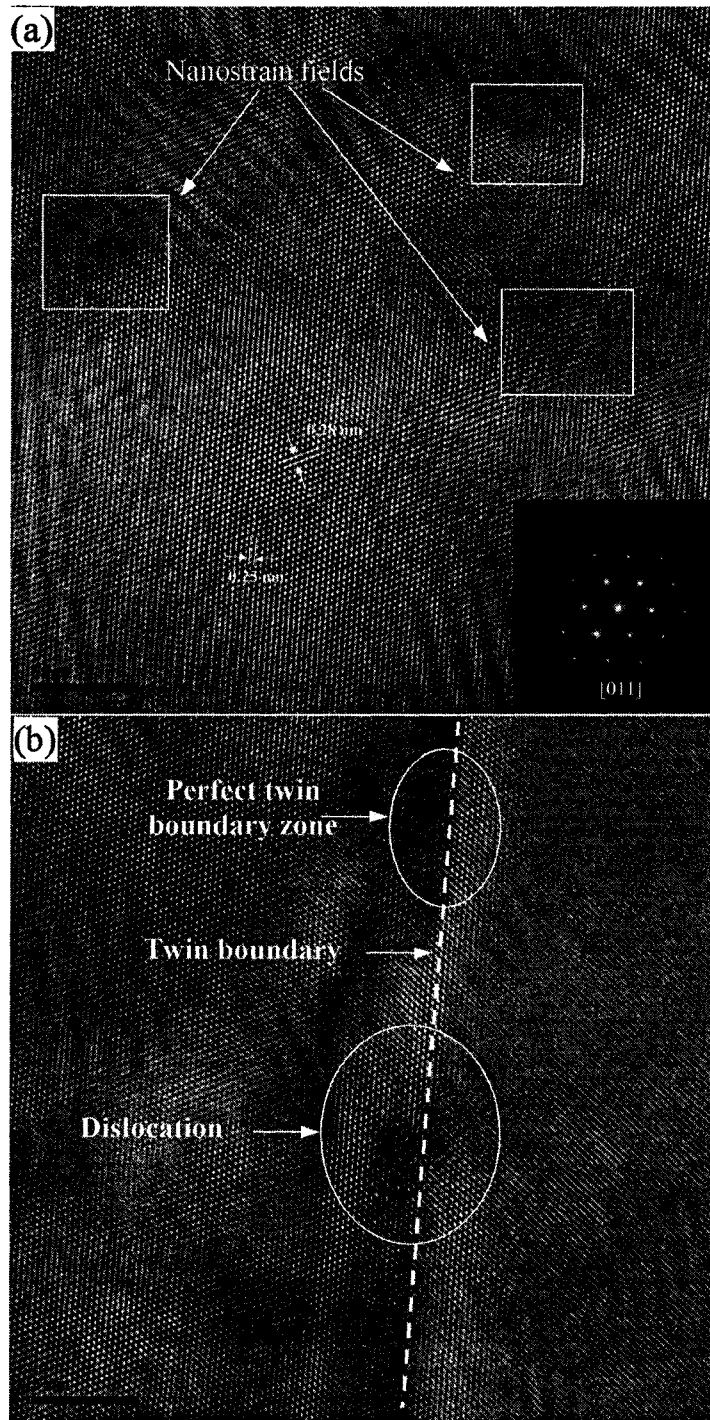


Fig.5.17 HREM images along the [011] zone axis in the PM AC52 alloy. Nanostrain fields are surrounded by squares in (a); Dash line denotes twin boundary in (b). The zone in small ellipse is a section of perfect twin boundary, while the zone in large ellipse is a dislocation boundary zone.

5.3 Effects of cooling rates on microstructure of PM AC52 alloy

5.3.1 Thermal analysis

The definition of cooling rate used in this study is related to the cooling speed of the AC52 alloy through its primary solidification range. This is reasonable since the measured cooling rates during this period are representative of the cooling rates that determine the actual as-cast microstructures. Using this definition of cooling rate, the thermal analysis was conducted at the following solidification conditions with a series of copper molds: (a) 0.5 °C/s (close to equilibrium freezing), (b) 0.75 ~ 1.2 °C/s (sandcasting range), (c) 3.0 ~ 9.2 (permanent mold casting range), and (d) 20 ~ 65 °C/s (die casting range). Typical cooling curves at rates of 0.5 to 65 °C/s are presented in Figs. 5.18 and 5.19 for calcium modified alloys (AC52 alloys) in the temperature-time and derivative formats, respectively. It can be seen from Fig. 5.18(a) that the temperatures of the eutectic reaction and the rates of the eutectic reactions during solidification are dependent on the cooling rate. A cooling curve at 0.5 °C/s and its first derivative are shown in Fig.5.18(b), in which inflections of the cooling curve appear as peaks on the dT/dt curve. The peak should correspond to the precipitation of the eutectic phase during solidification. A typical cooling curve (Fig. 5.18(b)) is characterized by the following reactions:

- (1) Formation of primary magnesium at about 615.9 °C.
- (2) The $(Al, Mg)_2Ca$ forming eutectic reaction at about 526.5 °C.

To determine a number of thermal parameters, the cooling curves obtained at 0.5 °C/s, 0.75 °C/s and 1.2 °C/s in the primary and eutectic regions are shown in Fig. 5.19. The results of the thermal parameters obtained at different cooling rates, such as primary nucleation temperature T_{Nuc}^p (Nucleation temperature is corresponding to the beginning of the peak on the derivative curve), the eutectic nucleation temperature T_{Nuc}^e , the temperature

at the minimum before the eutectic plateau T_{Min}^e , the primary growth temperature T_{Grow}^p , the eutectic growth temperature T_{Grow}^e , the end temperature of the eutectic reaction T_{Fin}^e for higher cooling rates, undercooling $\Delta\theta = T_{Grow}^e - T_{Min}^e$, and the eutectic reaction time $\Delta t = t_{Fin} - t_{Min}$ (t_{Min} is the time at the minimum on the curve and t_{Fin} the time corresponding to the end of the eutectic plateau), are summarized in Table 5.2.

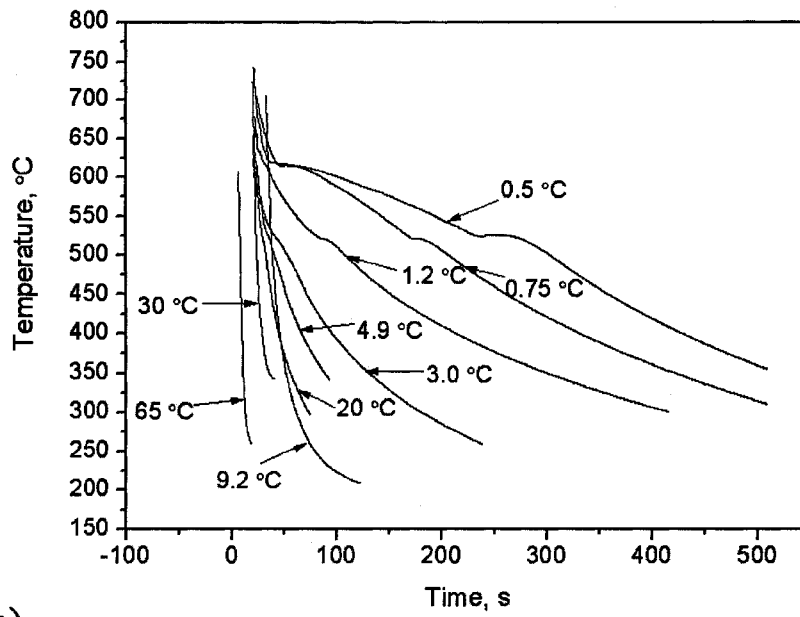
Table 5.2 Cooling curve parameters obtained at different cooling rates

Cooling rate (°C/s)	Reaction type	T_{Nucl} (°C)	T_{Grow} (°C)	T_{Fin}^e (°C)	Δt (s)	$\Delta\theta$ (°C)
0.5	Primary	619.3	615.9 (T_{Grow}^p)	-	69	0.5
	Eutectic	528.1	526.5 (T_{Grow}^e)	-	40	2.14
0.75	Primary	-	-	-	58	-
	Eutectic	524.3	521.68 (T_{Grow}^e)	-	10	0.14
1.2	Eutectic	-	~519.8 (T_{Grow}^e)	-	~5	-
3.0	Eutectic	-	-	510.6	<5	-
4.9	Eutectic	-	-	509.3	<5	-
9.2	Eutectic	-	-	507.9	<3	-
20.0	Eutectic	-	-	-	<1	-
30.0	Eutectic	-	-	-	<1	-
65.0	Eutectic	-	-	-	<1	-

- could not be determined.

The phenomena of undercooling and recalescence for the primary reaction during solidification were observed only on the cooling curve of 0.5 °C/s ($\Delta\theta = 0.5$ °C). As seen from Table 1, nucleation of primary α -Mg starts above the steady state growth temperature (T_{Grow}^p). This implies that nuclei can form, not only at the first contact of the melt with the cold walls of the mold, but also in the liquid ahead of the growing crystal front all the way from the walls to the center of the casting.

(a)



(b)

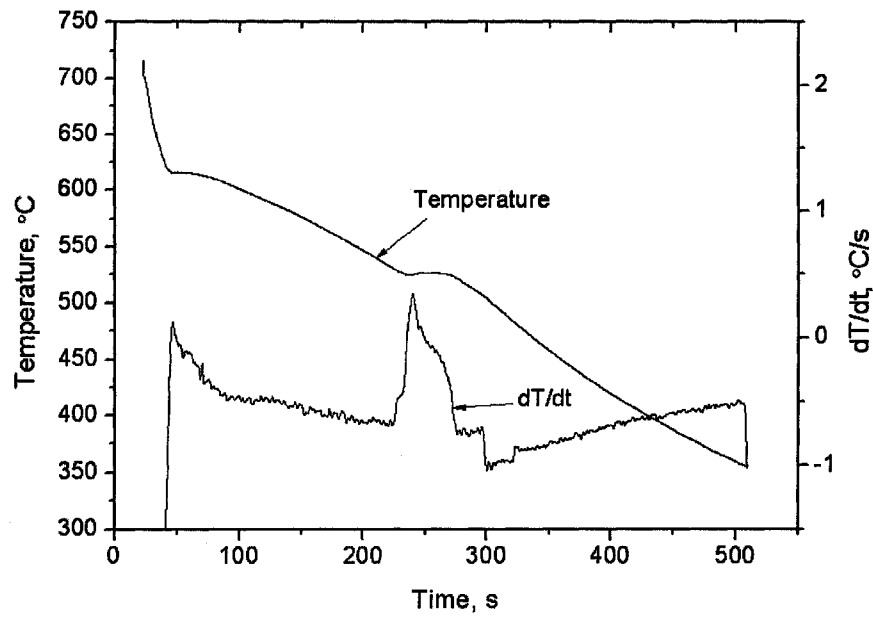


Fig.5.18 Cooling curves obtained during solidification of the AC52 alloy cast at (a) 0.5 ~ 65 °C/s and (b) $T-t$ and dT/dt curves at 0.5 °C/s (T : temperature, t : time)

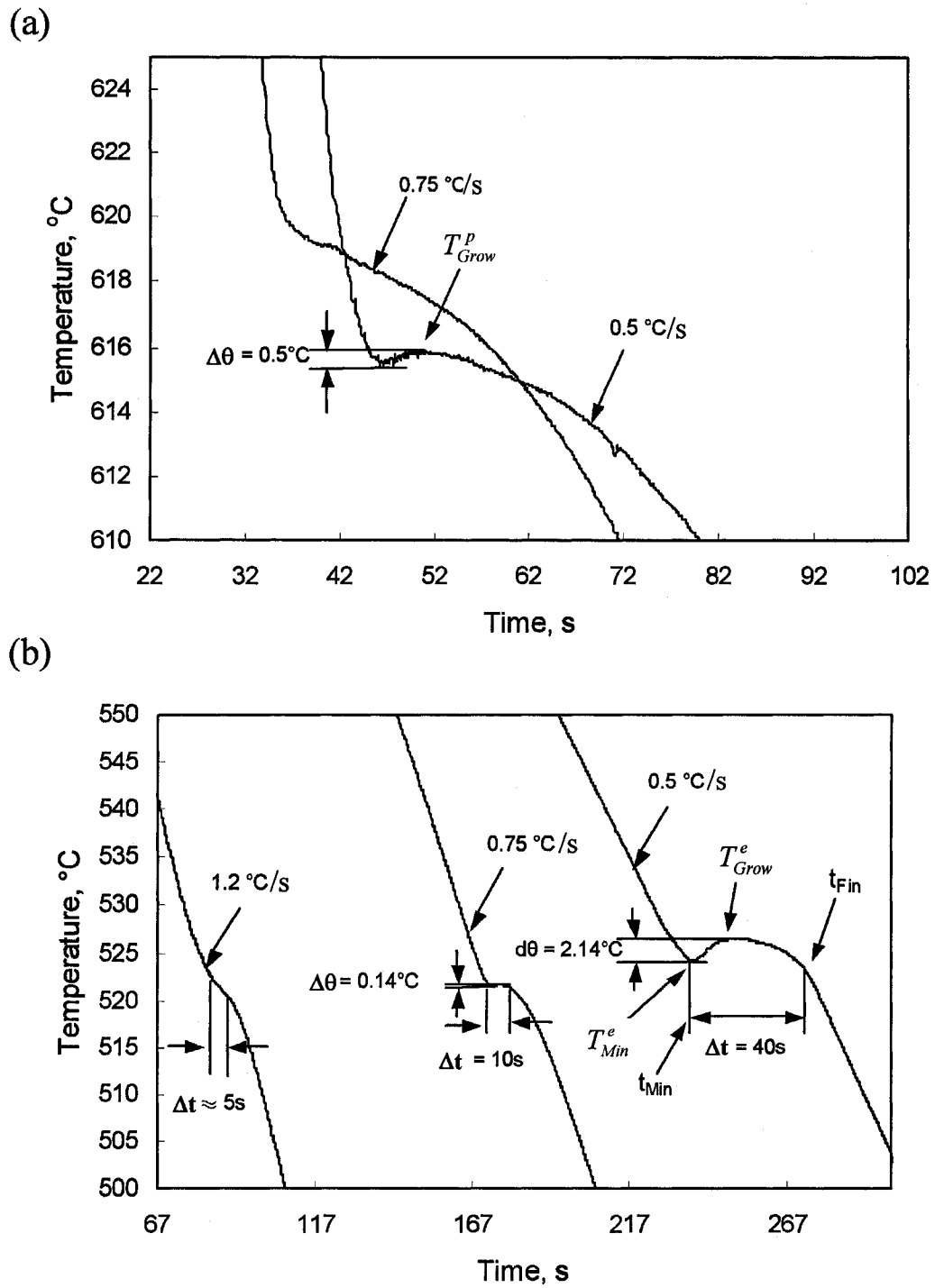


Fig. 5.19 Cooling curves in: (a) the primary and (b) the eutectic regions of the AC52 alloy cast at lower cooling rates from 0.5 to 1.2 °C/s (T : temperature, t : time).

Therefore, grain refinement is now possible, provided that the liquid is undercooled so that new fine crystals formed in the liquid at such a rate that they impinge upon each other and form a continuous dendritic network. It is worth noting that there is no undercooling before the actual growth temperature is reached and, hence, no recalescence effect for cooling rates higher than 0.5 °C/s (Fig. 5.19(a)). In this case, nucleation starts in areas highly enriched in calcium. Magnesium crystals develop already above the bulk equilibrium temperatures, and the constitutional undercooling created by calcium, and inclusions such as Al_3Mn_5 , possibly becomes enough for the magnesium crystals to form a continuous network of dendrites. For the eutectic reaction, undercooling and recalescence were observed only on the cooling curves of 0.5 °C/s ($\Delta\theta = 2.14$ °C) and 0.75 °C/s ($\Delta\theta = 0.14$ °C), and a eutectic reaction plateau (526.5 °C for 0.5 °C/s and 521.68 °C for 0.75 °C/s) can be observed in these cooling curves. However, at moderate cooling rates (1.2 to 9.2 °C/s) or higher, the eutectics no longer exhibit a plateau or a minimum, and the temperature dramatically decreases until the end of solidification. Thus, the cooling curve parameters associated with these cooling rates can not be determined.

The difficulty with thermal analysis at high cooling rates is that the entire sample is so far from equilibrium that very substantial thermal gradients develop within the sample. Thus, thermal analysis would appear to be of significantly less use at high cooling rates. Since no temperature plateau exists, the eutectic temperature is taken as the temperature corresponding to the end of the eutectic peak on the derivative curve. The only eutectic parameter that can be determined at moderate cooling rates is the end of the eutectic reaction. These values are also summarized in Table 5.2. The measured end temperatures of eutectic reactions are below the value of the eutectic temperature at 0.75 °C/s. This may be explained

by the different rates of heat transfer during permanent mold casting, in which the metal-mold interface is one of the barriers to heat flow from the interior of the casting. When the melt cools faster, heat can be quickly transported out of the casting through the metal-mold interface. Therefore, the melt would be directly undercooled below the eutectic temperature. In this case, the rate of evolution of latent heat is increased by the increased nucleation rate due to the high undercooling, while the growth of eutectic is suppressed considerably. The simultaneous effect of heat evolution and increased heat transfer rate, established a non equilibrium cooling condition at slightly low eutectic temperatures. For the alloys cast at much high cooling rates, such as 30 and 65 °C/s, the complete solidification process can be finished in a few seconds. Therefore, it is hard to find any inflection points on the derivative of the cooling curve, and thus no useful thermal parameters can be determined throughout the solidification process.

5.3.2 SDAS and volume fraction of eutectic

SEM examination reveals primary dendrites in all the PM AC52 alloys, with variations in size as a result of differences in cooling rates (Fig.5.20). All samples had a typical primary dendritic solidification microstructure with large amounts of the eutectic phases, which are formed along the grain boundaries by a divorced eutectic reaction. Fine, highly oriented dendrites are produced by fast cooling, while large, coarse dendrites are produced by slow cooling. Therefore, solidification occurs over a range of temperature during dendrite growth. Solidification of the AC52 alloys begins with the crystallization of the primary α -Mg, and then the composition of the remaining liquid shifts towards the eutectic composition where solidification proceeds by the eutectic reaction. The size and the distribution of the eutectic phases may be influenced by the interdendritic phase. Dendrites, exhibiting a bright contrast, can be observed in the SEM micrographs presented in Fig. 5.20.

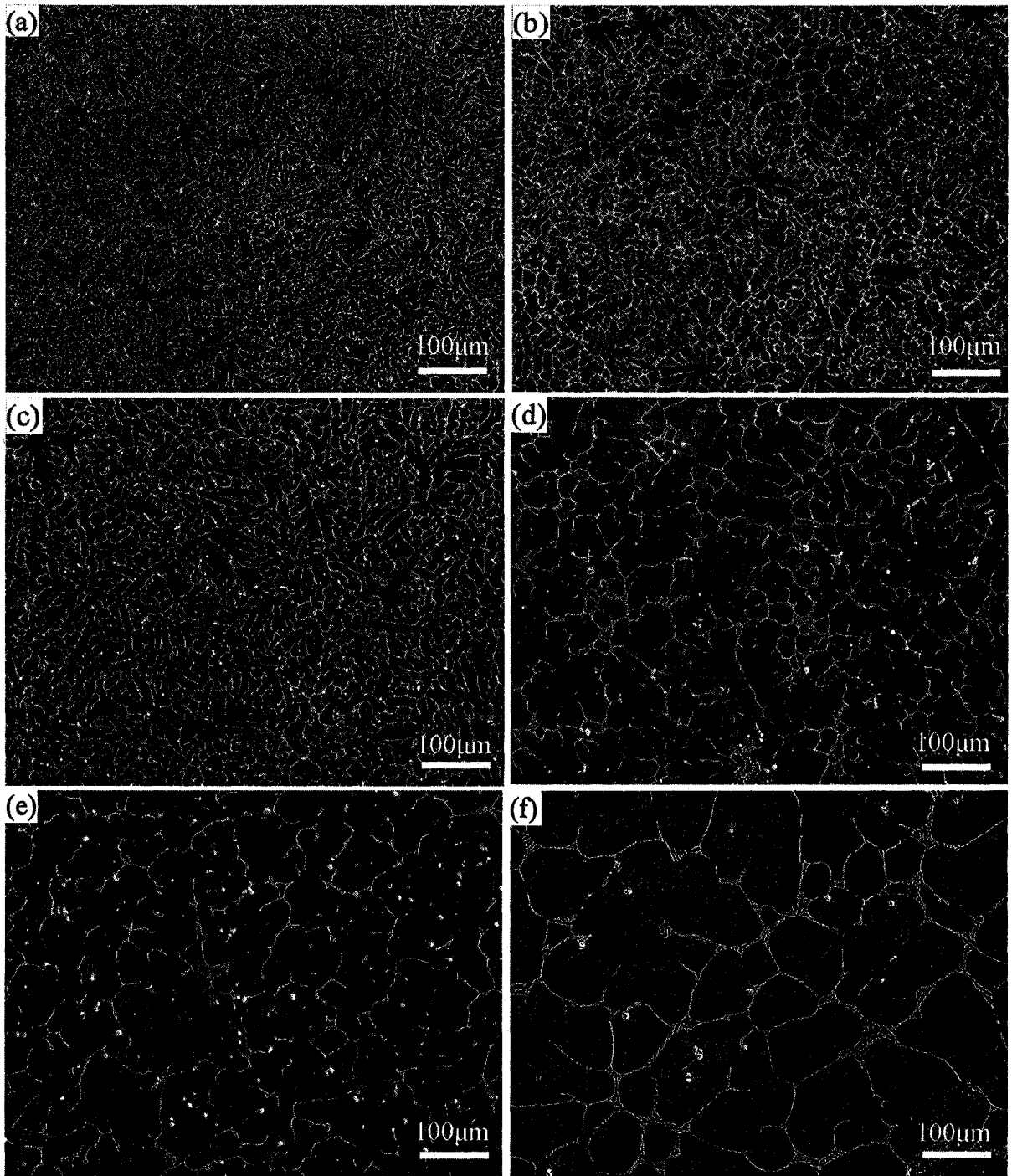


Fig.5.20 SEM micrographs of the microstructural evolution with cooling rates for:

(a) 65.0 °C/s, (b) 30.0 °C/s, (c) 20.0 °C/s, (d) 9.2 °C/s, (e) 3.0 °C/s and (f) 0.5 °C/s.

For each alloy, the structure of the dendrites was analyzed by determining the SDAS and the volume fraction of secondary eutectic phases. The effect of the cooling rate on the size of the dendritic structure was characterized by measuring the SDAS. The data for SDAS, λ , measured by the linear intercept method in the alloys cast at different cooling rates, are listed in Table 5.3.

Table 5.3 Average secondary dendrite arm spacing of the as-cast Mg-Al-Ca alloys

SDAS (μm)	Cooling rate ($^{\circ}\text{C/s}$)					
	0.5	3.0	9.2	20	30	65
Min	34.6	18.9	8.7	4.2	3.3	1.2
Max	143.3	54.6	38.5	23.5	20.5	12.5
Average	72.9	32.1	20.7	11.7	9.8	6.6
Std Dev.	5.33	3.41	3.04	1.23	3.12	1.04

The average SDAS, λ , for the alloys cast at different cooling rates are $6.6 \pm 1.0 \mu\text{m}$ for $65 \text{ }^{\circ}\text{C/s}$, $9.8 \pm 3.1 \mu\text{m}$ for $30 \text{ }^{\circ}\text{C/s}$, $11.7 \pm 1.2 \mu\text{m}$ for $20 \text{ }^{\circ}\text{C/s}$, $20.7 \pm 3.0 \mu\text{m}$ for $9.2 \text{ }^{\circ}\text{C/s}$, $32.1 \pm 3.4 \mu\text{m}$ for $3 \text{ }^{\circ}\text{C/s}$ and $72.9 \pm 5.3 \mu\text{m}$ for $0.5 \text{ }^{\circ}\text{C/s}$, respectively. Each SDAS average was calculated from 30 ~ 50 individual lines each of which included at least 5 secondary dendrite arms. Fig. 5.21 shows the relationships between the SDAS and cooling rates on logarithmic scale for all the as-cast AC52 alloys. It can be seen that there is an inverse linear relationship between the SDAS and the cooling rate on a logarithmic scale:

$$\text{Ln } \lambda = -0.4985 \text{ CR} + 3.9955 \quad (5-1)$$

where CR is the cooling rate.

A good correlation was found, as can be seen from the regression coefficient of $R^2 = 0.997$. This demonstrates that the cooling rate played a significant role in SDAS. It is evident

from Fig. 5.21 that coarser dendritic microstructures are produced at low cooling rates. As the cooling rate increased, the dendrites became finer. Quantitative analysis, i.e. measurement of the average SDAS, further confirmed the refinement of dendritic microstructure with increasing cooling rates.

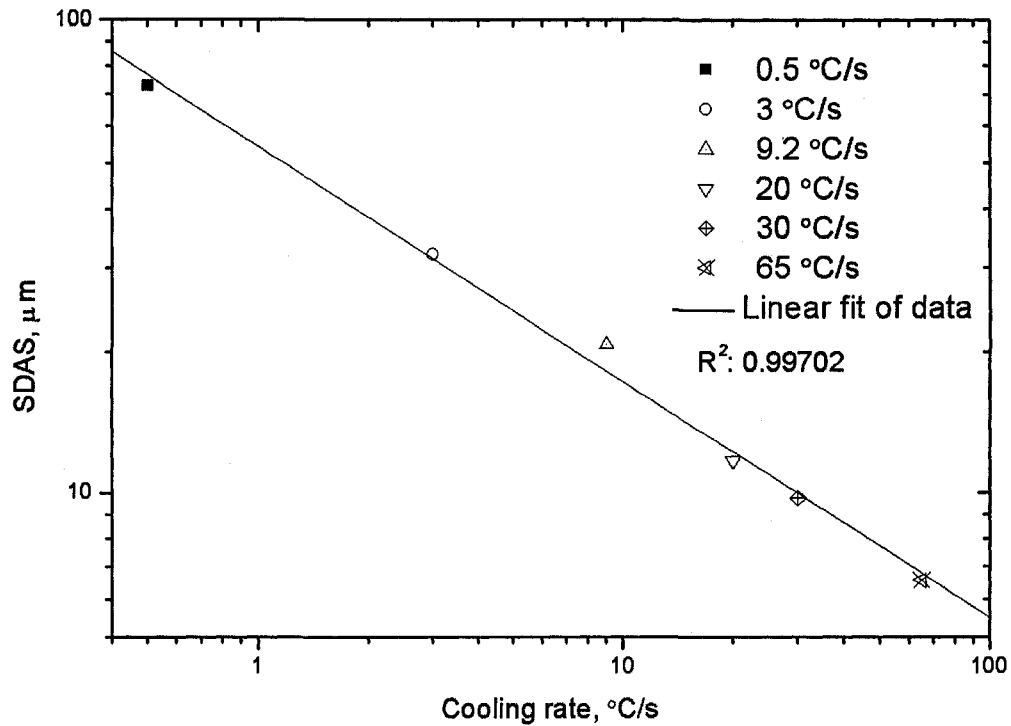


Fig. 5.21 Variation of the SDAS with cooling rate for all the tested AC52 alloys on logarithmic scale.

Chills are used for the production of quality castings in both permanent mold casting and die casting. Therefore, a chill zone (randomly oriented fine grains), a columnar zone (elongated grains having a preferred orientation) and an equiaxed zone (randomly oriented coarse grains) are typically found in the microstructure of the casting. Therefore, there are

significant differences in the microstructures from the edge to the center of the chill casting. AM50, AM60 and AZ91 magnesium alloys cast by die casting or permanent mold casting [160, 166-168] typically show these diverse microstructures, i.e. very fine grains in the skin region and coarse grains in the center region. However, with the addition of Ca to Mg-Al alloys, the significant grain refining effect of Ca is clearly evident compared to the non-Ca addition magnesium alloys (Fig. 5.1) under similar casting conditions. Also, the difference in the SDAS between the edge and the center of the castings is significantly reduced through the addition of Ca. For example, the average SDAS measured in the edge and the center of the alloy cast at 30 °C/s is $7.8 \pm 2.1 \mu\text{m}$ and $9.8 \pm 3.1 \mu\text{m}$, respectively (Fig. 5.22). Additionally, another important finding is that the Al-rich eutectic α -Mg phase disappear, which are usually present in die cast Mg-Al-Mn alloys [160, 166-168]. This demonstrates that the local segregation of the solutes has been greatly reduced, and that the Al-rich eutectic α -Mg and $\text{Mg}_{17}\text{Al}_{12}$ phases in the Mg-Al-Mn alloys are completely replaced by $(\text{Al, Mg})_2\text{Ca}$ phases in the AC52 alloys.

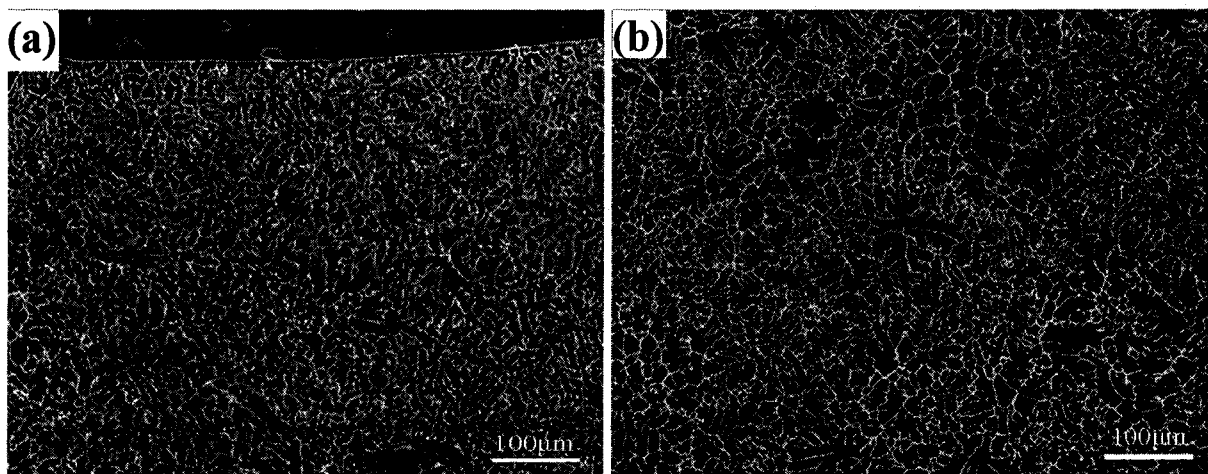


Fig.5.22 SEM micrographs of the microstructure in: (a) the skin and (b) the center of the AC52 alloy cast at 30 °C/s.

Fig.5.23 shows the relationship between the volume fraction of the secondary eutectic phase and the cooling rate for all the as-cast AC52 alloys. The average volume fractions of the secondary phases measured by point counting method in the alloys cast at different cooling rates are 10.8 ± 1.44 % for 0.5 °C/s, 12.2 ± 1.27 % for 3 °C/s, 15.5 ± 1.32 % for 9.2 °C/s, 20.4 ± 1.52 % for 20 °C/s, 21.4 ± 1.2 % for 30 °C/s and 21.8 ± 0.76 % for 65 °C/s, respectively. The detailed data are listed in Table 5.4.

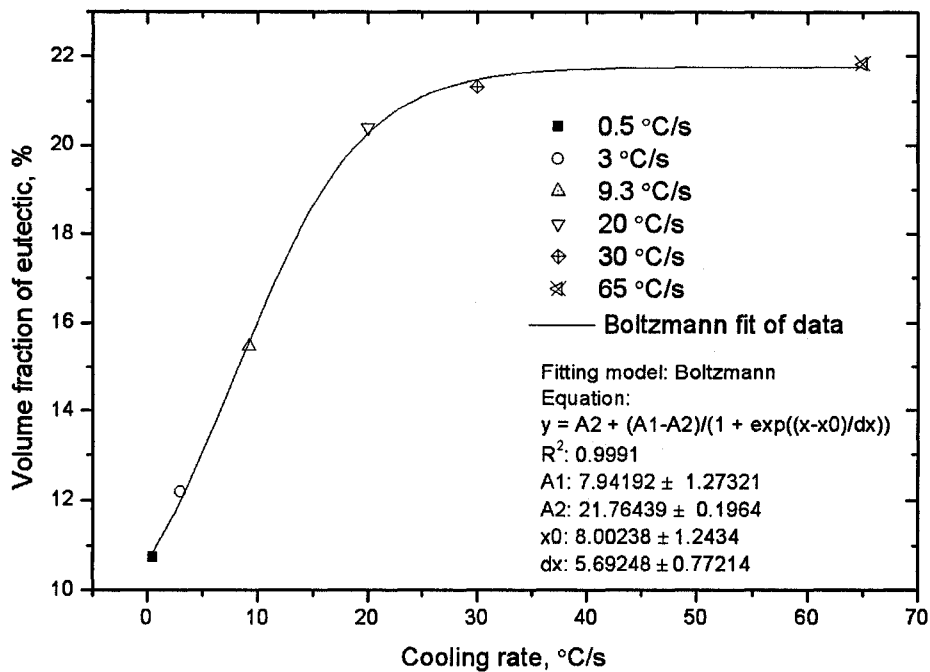


Fig. 5.23 Variation of the volume fraction of the secondary eutectic phase with cooling rates for all the tested AC52 alloys.

Table 5.4 Average volume fraction of $(Al, Mg)_2Ca$ phase in the PM AC52 alloy

Volume fraction of eutectic (%)	Cooling rate (°C/s)					
	0.5	3.0	9.2	20.0	30.0	65.0
Mean	10.8	12.2	15.5	20.4	21.4	21.8
Std Dev.	1.44	1.27	1.32	1.52	4.24	0.76

Using a Boltzmann model to fit the measured data, a good fit with a regression coefficient of R^2 (0.9991) was obtained. The relationship between the volume fraction of the eutectic and the cooling rate for the AC52 alloys can be expressed by:

$$VF(\%) = 21.76 - 13.82 / (1 + \exp((CR - 8.0) / 5.69)) \quad (5-2)$$

where VF is volume fraction of eutectic. The established model for the AC52 alloy shows that the volume fraction of the eutectic phases varies with cooling rates. When cooling rates are relatively low, i.e. below 30 °C/s, the volume fraction of the eutectic increases significantly with cooling rates. However, cooling rates have almost no influence on the volume fraction of the eutectic phase once reaching 30 °C/s and higher.

The distribution of the eutectic phases in the as-cast AC52 alloys tends to be dependent on the cooling rate. When the AC52 alloys were cast at a cooling rates of 30 °C/s or higher, a network of the $(Al, Mg)_2Ca$ eutectic phase was observed to be formed only along the grain boundaries. However, there were almost no fine dispersed eutectic phases within the primary α -Mg phases in the SEM micrographs (Fig. 5.20(a) and (b)). As the cooling rate decreased to 20 °C/s, a continuous eutectic phase network was observed at the grain boundaries, and also, microscale dispersed eutectic particles began to appear within the primary α -Mg grains. As cooling rate decreased further, the size of the dispersed eutectic particles within the primary α -Mg phases grew relatively larger. Finally, when the AC52 alloy solidifies at 0.5 °C/s, some needle-like eutectic phases appears inside the primary α -Mg phases. Since the size of the dispersed eutectic particles is very small, it is very hard to measure their volume fraction. The volume fractions of the eutectic phases given for all the tested AC52 alloys was calculated by measuring the eutectic phases appearing along the grain boundaries. Therefore, the measured volume fractions of the eutectic phases given for

the alloys cast at the lower cooling rates are likely underestimated. When the cooling of the alloys is slow, the dependence of the volume fraction of the eutectic phases on cooling rate becomes apparent for the alloys, which varies from $10.8 \pm 1.44\%$ at $0.5\text{ }^{\circ}\text{C/s}$ to $20.4 \pm 1.52\%$ for $20\text{ }^{\circ}\text{C/s}$. As cooling rate increased, however, there was almost no detectable change in the average volume fraction of the eutectic phases. The volume fraction of the eutectic phases in the alloy cast at $65\text{ }^{\circ}\text{C/s}$ increased by only 1.4% compared to that in the alloy cast at $20\text{ }^{\circ}\text{C/s}$. Thus, any further increase in the volume fraction of the eutectic phases is limited after the cooling rate of the AC52 alloy reaches a specific value for the same casting conditions (permanent mold casting). It was found that the volume fraction of the eutectic phases increased by about 20% for the AC52 alloy recast at $1\text{ }^{\circ}\text{C/s}$ in a High Temperature Observation Unit (HTOU). The difference in the casting conditions using the HTOU equipment is that the melt was held at $650\text{ }^{\circ}\text{C}$ for 5 min before the formation of the primary $\alpha\text{-Mg}$. Fig. 5.24 shows a SEM micrographs of the eutectic phases in the AC52 alloy recast in the HTOU at $1\text{ }^{\circ}\text{C/s}$ and $12.5\text{ }^{\circ}\text{C/s}$.

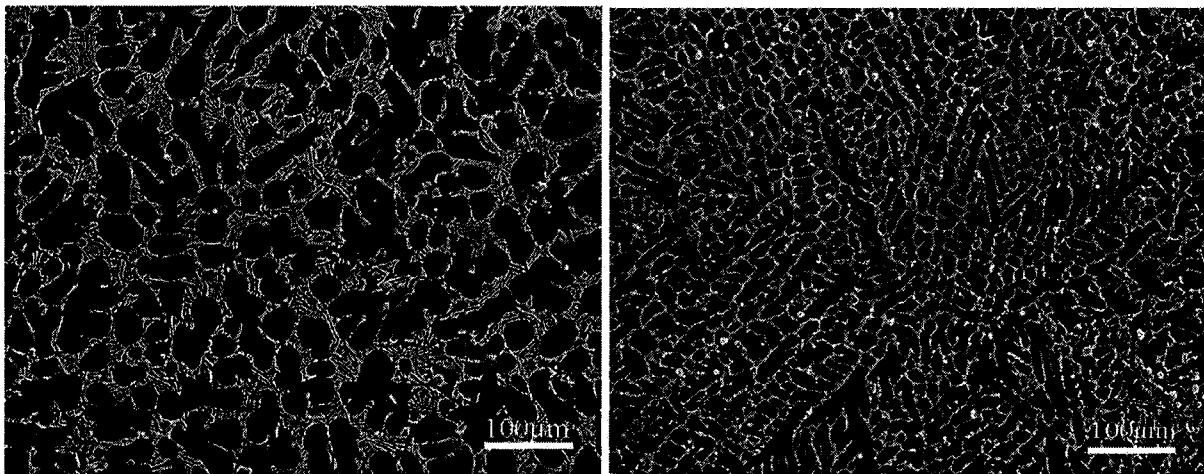


Fig.5.24 SEM micrograph of the microstructure in the AC52 alloy recast at $1\text{ }^{\circ}\text{C/s}$ and $12.5\text{ }^{\circ}\text{C/s}$ with HTOU.

The different precipitation mechanisms of the eutectic phases in the AC52 alloy deserve further study. Also, as can be seen in Fig. 5.20, the distribution of the dendrite structures appears to be uniform throughout all the as-cast AC52 alloys, except that the eutectic phases are somewhat depleted in certain local areas.

5.3.3 Phase transformations during permanent mold casting of the AC52 alloy

In this section, possible phase transformations are considered which could result in the precipitation of the secondary eutectic phases along the grain boundaries and the dispersed particles within the primary α -Mg that were observed in the present study and detailed in Section 5.3.2.

Although the solidification of an alloy during permanent mold casting is not an equilibrium solidification process, it is still instructive to analyze the potential phase transformations with either a binary or ternary equilibrium phase diagram. It has been established that the equilibrium phases at room temperature in Mg alloys with 2 to 9 at.% Al and less than 1 at.% Mn are primary α -Mg, β -Mg₁₇Al₁₂ and Al₈Mn₅ [169]. The presence of these phases in the castings has been confirmed by SEM or TEM analysis of the microstructure in die cast AM50, AM60 and AZ91 alloys [160, 166-168]. Also, the phase compositions at different casting temperatures can be deduced from the experimental results on rapidly quenched samples [170]. Maximum solubilities of ~0.3 wt.% Mn at 690 °C and ~0.7 wt.% Mn at 725 °C have been obtained by extrapolating the data on the solubility of Mn in melts of Mg-4wt.%Al-Mn. Therefore, this indicates that, for the given Mn concentration (~0.3wt.%), the Al₈Mn₅ phase should be present in the melt when the temperature of the liquid melt reaches 690 °C. When Ca is added to the Mg-Al-Mn alloy as a grain refiner, Mg₂Ca and/or Al₂Ca Laves phases are reported to precipitate during the final eutectic

reaction and the precipitation of β -Mg₁₇Al₁₂ phase is reportedly suppressed. It has been found in Section 5.2 that the presence of β -Mg₁₇Al₁₂ phase in the Mg-Al-Ca alloy depends on the Ca and Al contents of the Mg alloy. Some β -Mg₁₇Al₁₂ phases were still present in the matrix of our permanent mold cast Mg-5wt.%Al-1.0wt.%Ca alloy. However, when the Ca content was higher than 1.0 wt.%, the β -Mg₁₇Al₁₂ phase in the castings was completely replaced by (Al, Mg)₂Ca phase, e.g. in the Mg-5wt.%Al-1.5wt.%Ca alloy and the Mg-5wt.%Al-2.0wt.%Ca alloy. Therefore, no β -Mg₁₇Al₁₂ phases was found in all the alloys with 2.0 wt.%Ca addition in the present study and only (Al, Mg)₂Ca and Al₈Mn₅ phases were observed. It has been reported [171], however, that β -Mg₁₇Al₁₂ phase tends to reappear with a relatively low percentage in Mg-Al alloys containing high levels of Ca (23.4 wt.%) only when the Al content increases to 32.6 wt.%.

During solidification of Mg-Al-Ca, the primary α -Mg dendrites nucleated at the liquidus temperature, while Al₈Mn₅ particles had already nucleated in the solute field ahead of these growing dendrites at a temperature apparently above the liquidus and the eutectic temperatures of the alloy. As the primary α -Mg dendrites continued to grow, the liquid melt ahead of them became supersaturated with Al and Ca. When the composition of supersaturated liquid melt among primary dendrites reached the eutectic liquid composition, the eutectic reactions took place. As a result, the eutectic phases nucleated and precipitated. Since the primary α -Mg and the Al₈Mn₅ particles precipitated before the eutectic temperature, they may act as nucleation sites for the eutectic phases. As shown in Figs. 5.25 (a) and (c), a few eutectic phases in the microstructure have Al₈Mn₅ particles attached to their edge. This observation suggests that there are certain favored crystallographic orientations between the eutectic phase and Al₈Mn₅. Moreover, several Al₈Mn₅ particles are attached to more than one eutectic structure with different crystallographic orientations.

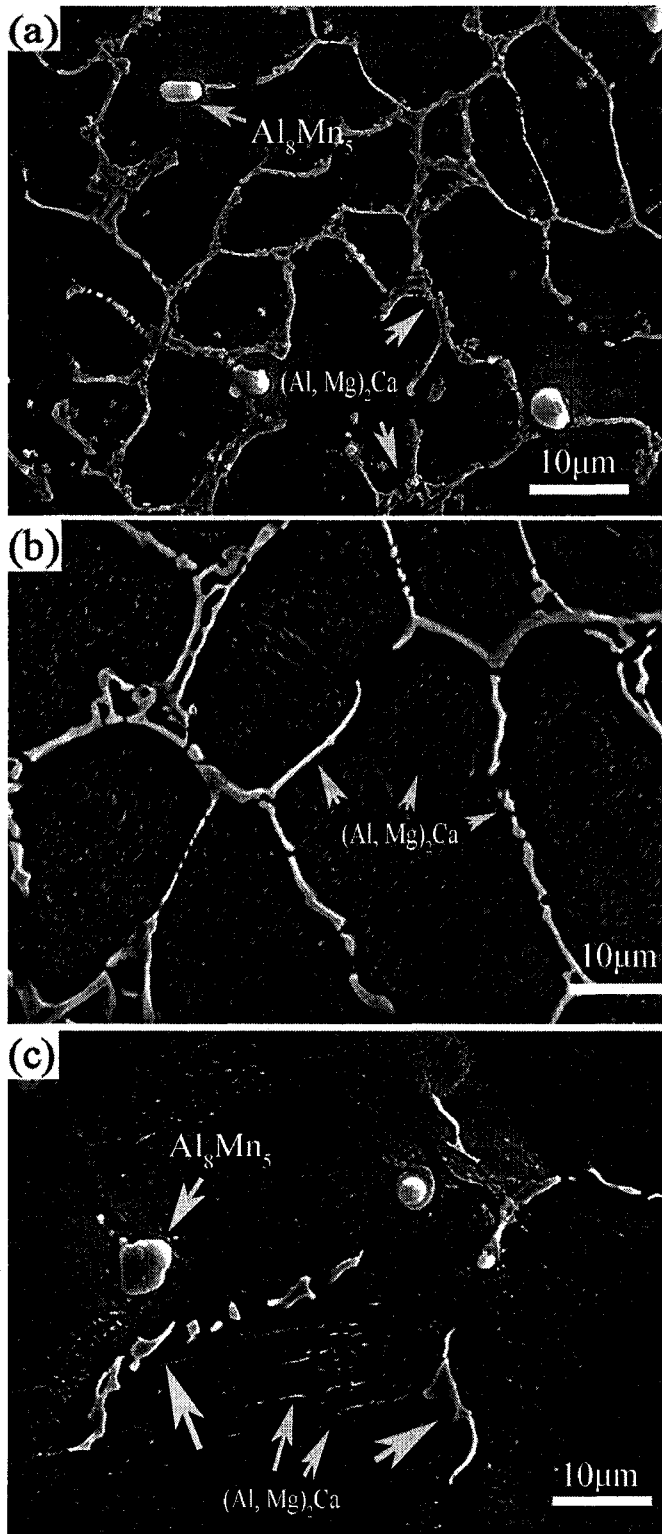


Fig. 5.25 SEM micrographs showing the microstructural evolution of the AC52 alloy with cooling rates of: (a) 30 °C/s, (b) 9.2 °C/s and (c) 0.5 °C/s.

It has been reported [172] that an increase in cooling rates refines the microstructural features of metal. At high cooling rates, a large thermodynamic driving force for the nucleation reaction generates heterogeneous nuclei. As a result, small or no supercooling (undercooling) appeared on the cooling curves, and the solidification and eutectic reactions tend to initiate at relatively low temperatures. When the AC52 alloys were cast with relatively high cooling rates, the undercooling was small as shown in Figs. 5.18 and 5.19, which resulted in the formation of fine Al_8Mn_5 particles (Fig. 5.25(a)). The fine Al_8Mn_5 phase, within the eutectic phases with regular polygonal shapes, could reduce the diffusivity of elements in the interdendritic region. Moreover, the presence of a large number of nuclei and high nucleation rate of primary α -Mg dendrites promoted by the small undercooling due to the rapid cooling may also increase the viscosity of the eutectic liquid ahead of the dendrites, which makes it difficult for the elements in the liquid to diffuse very fast. Therefore, Al and Ca supersaturation took place in the eutectic liquid which caused the precipitation of the eutectic phase, $(\text{Al}, \text{Mg})_2\text{Ca}$, with a very fine SDAS. As the cooling rate decreased, the solidification of primary α -Mg and eutectic $(\text{Al}, \text{Mg})_2\text{Ca}$ phase began at a high temperature. A coarse SDAS was observed in the microstructure of the castings. Also, Al_8Mn_5 particles not only coexisted with the eutectic $(\text{Al}, \text{Mg})_2\text{Ca}$ phase, but were also present in the primary α -Mg. These particles were relatively larger in size likely because of longer diffusion and growth times compared to those particles formed at high cooling rates. The observed inclusions, formed prior to the formation of primary α -Mg, had a regular polygonal shape, which is consistent with the microstructural observations of Simensen et al. [170].

It is worthwhile noting that, despite the fact that no dispersed precipitate were observed on the microscale in the primary α -Mg grains of the alloy cooled at a fast rate (Fig.5.25(a)), nanoscale Ca-containing precipitates in the primary phases were seen in the TEM bright field micrographs (Fig. 5.26).

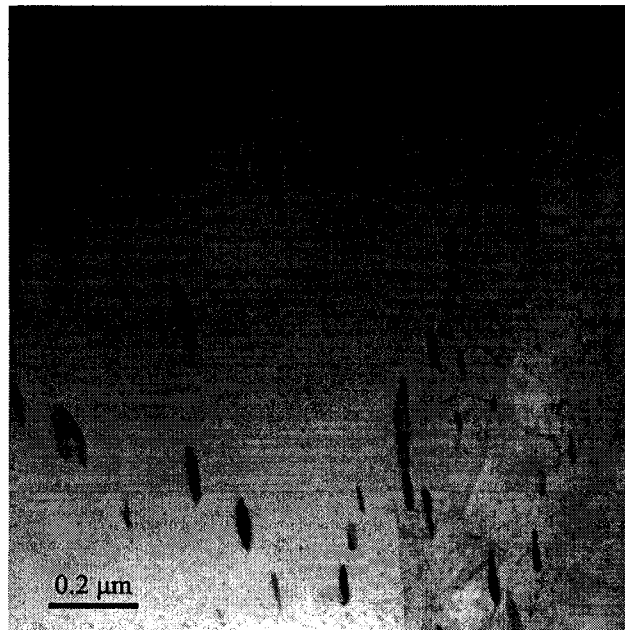


Fig.5.26 TEM bright field micrograph of dispersed eutectic phases in the AC52 alloy cast at 30 °C/s.

This observation suggests that the formation of the precipitates could be $(Al, Mg)_2Ca$ phase, resulting from a reaction taking place between Al in the AM50 alloy and the Mg_2Ca metallics present in the master alloy during the alloy preparation even above the liquidus temperature of the cast alloy. The rapid cooling had a quenching effect on these nanoscale particles during solidification. As the cooling rate decreased, the large undercooling and slow cooling enable the solutes of Al and Ca in the liquid to have sufficient time and energy to thermodynamically diffuse away from the tip of primary α -Mg dendrites towards the nano

(Al, Mg)₂Ca particles. As a result, small (Al, Mg)₂Ca particles precipitated inside the primary α -Mg grains after a certain growth period. A further reduction in cooling rates allowed (Al, Mg)₂Ca precipitates to grow into a larger size with a needle-like shape (Fig. 5.25(c)). Close examination of the needle-like (Al, Mg)₂Ca particles showed that, within one primary α -Mg grain, the particles tended to be grouped. The particles in each group appeared to be parallel to each other in a specific crystallographic orientation. The preferred crystallographic relationship is observed more clearly in the SEM micrographs of samples tested in a DSC run (Fig. 6.17). Fig. 5.25(b) shows that there were no Al₈Mn₅ particles formed with the eutectic phases, which confirms that the volume fraction of the Al₈Mn₅ phase is very low in the casting.

5.4 Heat treatment of PM Mg-Al and Mg-Al-Ca alloys

Conventionally, AM alloys processed by traditional gravity casting technique are subjected to a subsequent T6 heat treatment including solution treatment and aging. Solution treatment causes the β -Mg₁₇Al₁₂ phase to dissolve, and it might be expected that quenching and aging would induce significant precipitation hardening. During aging, the β -phase precipitates out from the supersaturated α -Mg solid solution in two forms, discontinuous precipitation and continuous precipitation with the two types of morphology competing with each other depending on Al content and aging temperature [173]. Discontinuous precipitation occurs preferentially along the grain boundaries at the early stage, and then continuous precipitation forms in the remaining regions of the α -Mg grains that have not been occupied by discontinuous precipitation [174].

5.4.1 Solution treatment

According to the Mg-Al equilibrium phase diagram (Fig. 2.1) and the DSC result (Fig. 6.1), solution treatment at 420 °C causes the β -Mg₁₇Al₁₂ to dissolve into the α -Mg solid for the PM AM50 alloy. Also, since it had been shown by DSC (Fig. 6.4) that solidification for the PM AC52 alloy was completed at a temperature of ~ 530 °C, the higher solution treatment temperature of 520 °C could be used for this alloy, thereby enabling more solution of the alloying elements. It was therefore decided to carry out the solution treatment for the PM AM50 alloy at 420 °C and for the PM AC52 at a higher temperature of 520 °C. Both of the PM AC505 and AC51 alloys consist of a certain amount of β -Mg₁₇Al₁₂ phase as well as (Al, Mg)₂Ca phase. If a higher temperature of 520 °C was selected, marked oxidation of the PM AC505 and AC51 alloys occurred due to liquid β -Mg₁₇Al₁₂ phase during the solution treatment. Therefore, the PM AC505 and AC51 are also solution treated at 420 °C.

Fig. 5.27 shows the variation of Vickers hardness of the AM50, AC51 and AC52 alloys against time at the solution temperature. The first point of the curves corresponds to the hardness in the as-cast state; it is always higher than that of the solution treated state. It is interesting to note that the hardness values decrease faster for the AM50 and AC51 alloys than the AC52 alloy, indicating an accelerated dissolution of the β -Mg₁₇Al₁₂ phase for the AM50 and AC51 alloys. In fact, the AM50 and AC51 alloys reached their minimum hardness values at 3 h, compared to 10 h for the AC52 alloy, as shown in Fig. 5.27. The hardness values reach a steady state with increasing solution time after 3 h exposure at temperature for the AM50 alloy and 10 h for the AC52 alloy, respectively, and the alloys solution treated at different temperatures exhibited essentially the similar hardness level after solution treatment for 15 h or longer. Additionally, it can also be seen that the AC51 alloy

exhibits a higher hardness than the AM50 and AC52 alloys after being solution treated for 5 h. This is because the solution treatment temperature for the AC51 is 420 °C, which is lower than the eutectic reaction temperature (about 530 °C) of the (Al, Mg)₂Ca phase. Although the β-Mg₁₇Al₁₂ phases dissolve into the matrix, a certain proportion of the (Al, Mg)₂Ca phases is still present and retains the as-cast morphology during the solution treatment of the AC51 alloy. Therefore, the AC51 alloy presents a higher hardness than the AM50 and AC52 alloys after solution treatment for 5 h.

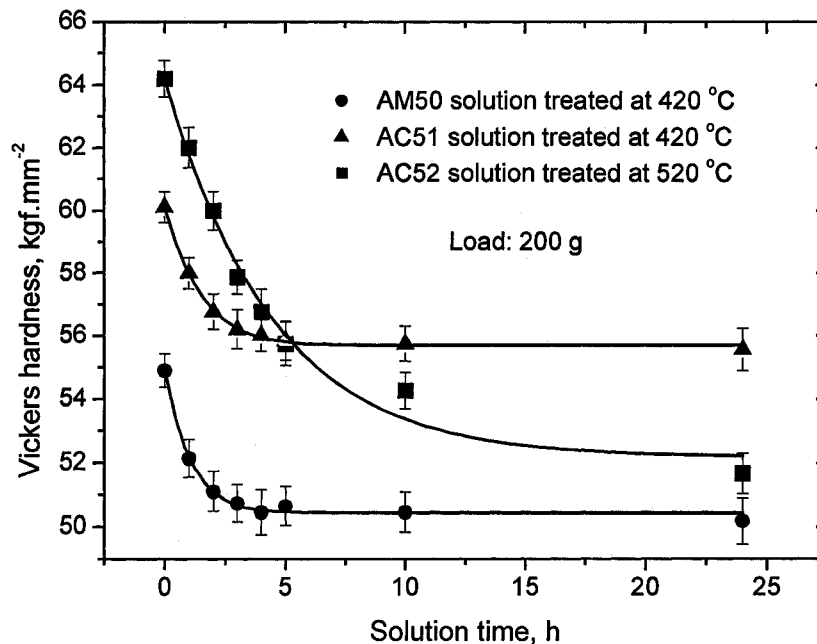


Fig. 5.27 Variation of the Vickers hardness of the solution treated (T4) AM50 and AC51 alloys at 420 °C, and AC52 alloy at 520 °C against solution time.

Detailed observations by OM and SEM revealed that the β-Mg₁₇Al₁₂ and (Al, Mg)₂Ca phases have been completely dissolved into the α-Mg solid solution after 24 h solution treatment at 420 °C and 520 °C, resulting in a single-phase material. Fig. 5.28 shows the

microstructures of the AM50 and AC51 alloys solution treated at 420 °C for 2 h and the AC52 alloy solution treated at 520 °C for 2 h and 24 h.

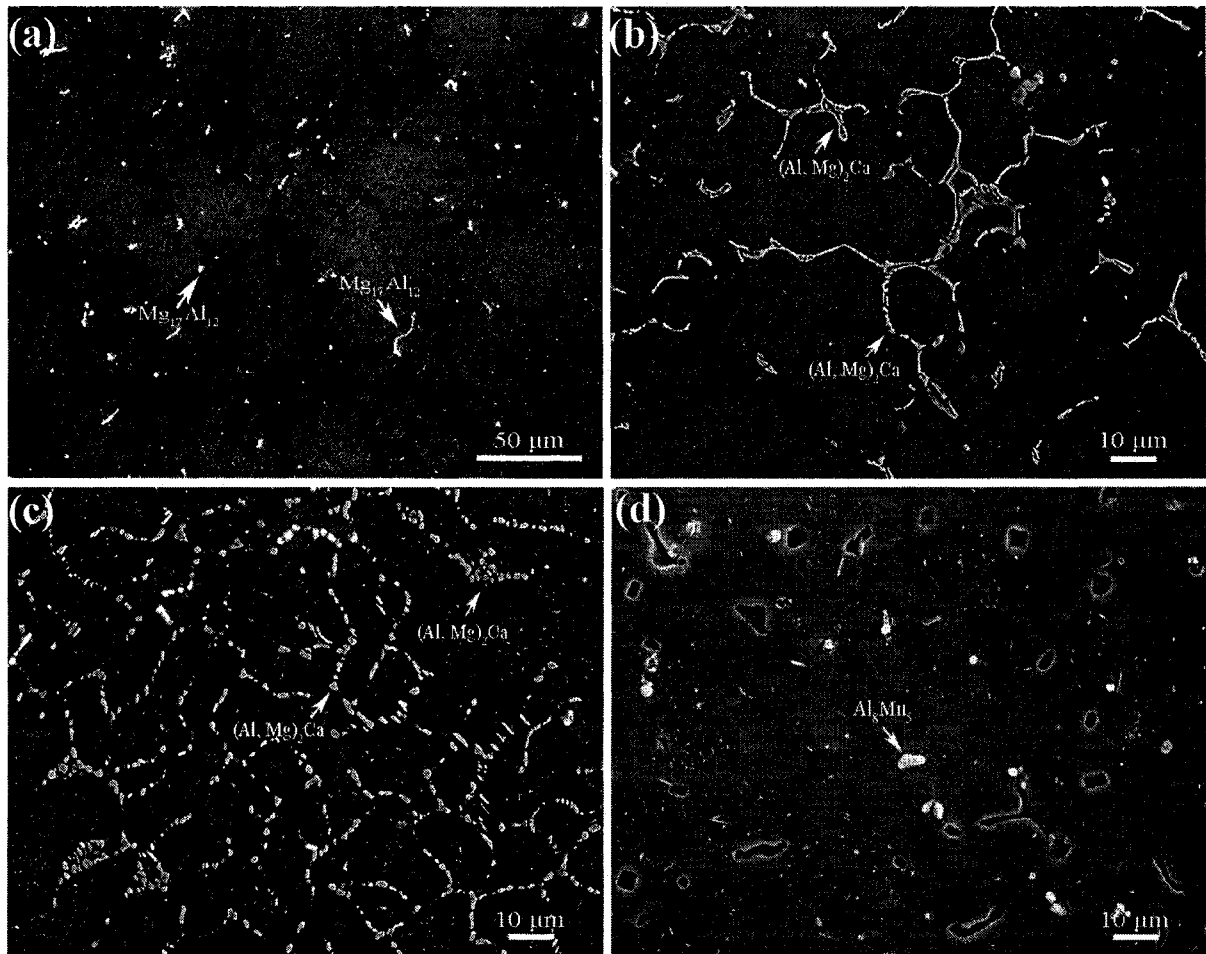


Fig. 5.28 Microstructures of: (a) AM50 and (b) AC51 alloys solution treated at 420 °C for 2 h, (c) and (d) AC52 alloy solution treated at 520 °C for 2 h and 24 h, respectively.

The dissolution of the β - $Mg_{17}Al_{12}$ phase in the AM50 alloy left grain boundaries with dark contrast behind and eventually evolved into the new α -Mg grains, which were well defined by the grain boundaries. The $(Al, Mg)_2Ca$ phase in the AC51 alloy still keeps the as-cast morphology after solution treatment (Fig. 5.28 (b)). In the as-cast AC52, the $(Al, Mg)_2Ca$ phase had a thin platelike shape. However, after solution treatment at 520 °C its

morphology became spherical with a smaller size (Fig. 5.28 (c)). With an increase in the time of solution treatment, the spheroidisation of the eutectic phase developed further, and finally completely dissolved into the matrix of the AC52 alloy (Fig. 5.28 (d)). Additionally, it can be noted in Fig. 5.58(d) that a large amount of pores are present due to the significant oxidation or overburning of the matrix of the AC52 alloy during the solution treatment at the longer time (24 h).

Therefore, four processes are involved in the microstructural evolution of the Mg-Al and the Mg-Al-Ca alloys during solution treatment: (a) dissolution of eutectic phase into the α -Mg phase, (b) formation of new primary α -grain, (c) morphological change of primary α -Mg grain into regular grain, and (d) grain growth. The first three processes occur simultaneously at the early stage of solution. Indeed, quantitative metallography reveals that the eutectic phase dissolves quite quickly at the early stage of solution, as shown in Fig. 5.29. It can be seen that it took ~ 2 h for the β -Mg₁₇Al₁₂ phase to completely dissolve in the AM50 alloy, compared to more than 10 h in the AC52 alloy. The maximum difference in the dissolution kinetics of the β -phase between the AM50 and AC52 alloys was found during the early stage of the solution treatment. For instance, in the first 0.5 h, the volume fraction of the β -Mg₁₇Al₁₂ phase was reduced from 6.2 to 2.6 vol.% at a dissolution rate of 7.2 vol.%/h for the AM50 alloy, compared to a rate of 5.2 vol.%/h from 21.4 to 18.8 vol.% for the AC52 alloy. The difference in the dissolution rate of the eutectic phase decreased with increasing solution time. This accelerated dissolution kinetics of the eutectic phase verifies the faster hardness reduction shown in Fig. 5.27 for the tested AM50, AC51 and AC52 alloys.

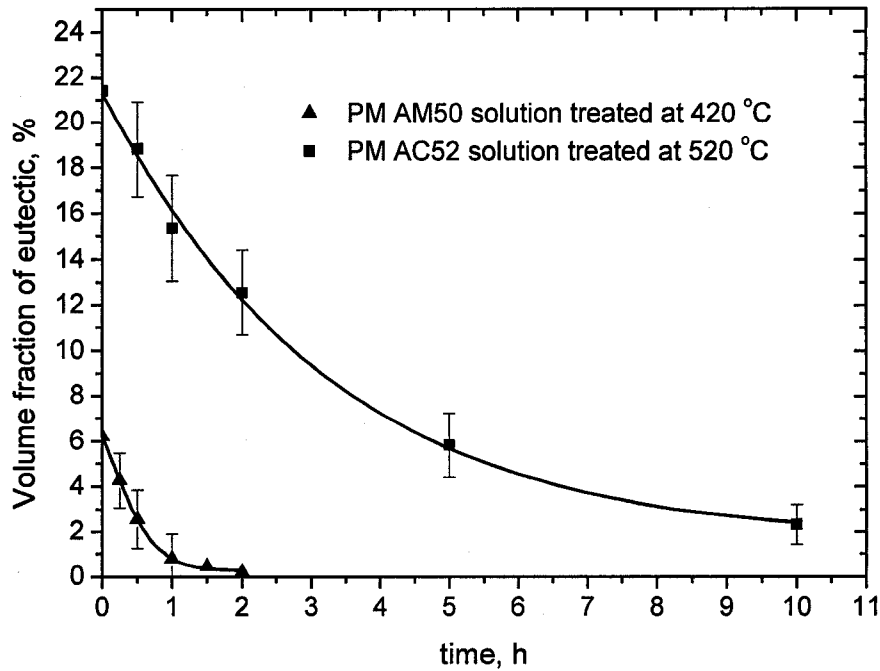


Fig. 5.29 Relationship between solution time (*h*) and the volume fraction (%) of the eutectic phase during the early stage of the solution treatment (T4) at 420 °C for the AM50 alloy and 520 °C for the AC52 alloy.

5.4.2 Aging without solution treatment

To study the age hardening mechanisms, the PM Mg-Al and Mg-Al-Ca alloys solidified at cooling rate of 30 °C/s were selected since their primary α -Mg phase is supersaturated. It is expected that the precipitation can occur when the alloys are aged. Fig. 5.30 shows the age-hardening curve of the PM Mg-Al and Mg-Al-Ca alloys aged at 200 °C without solution treatment for various times. In order to clearly observe the early stage of precipitation, a logarithmic time scale has been used for the curves. Before reaching the peak hardness, the hardness increases steadily as a function of the aging time. It can be seen from Fig. 5.30 that there is an obvious increase in hardness of the AM50 after being aged for 2 h,

while the aged AC52 alloy shows an increase in hardness after 10 h. This indicates that there is an accelerated age-hardening response at this aging temperature for the AM50 alloy, which corresponds to the accelerated solution treatment response (Fig. 5.27). The aged AC505 alloy has a similar trend of hardness variation to the AM50 alloy. However, for the AC51 and AC515 alloys, there were very weak hardening effects with increasing aging time to 100 h.

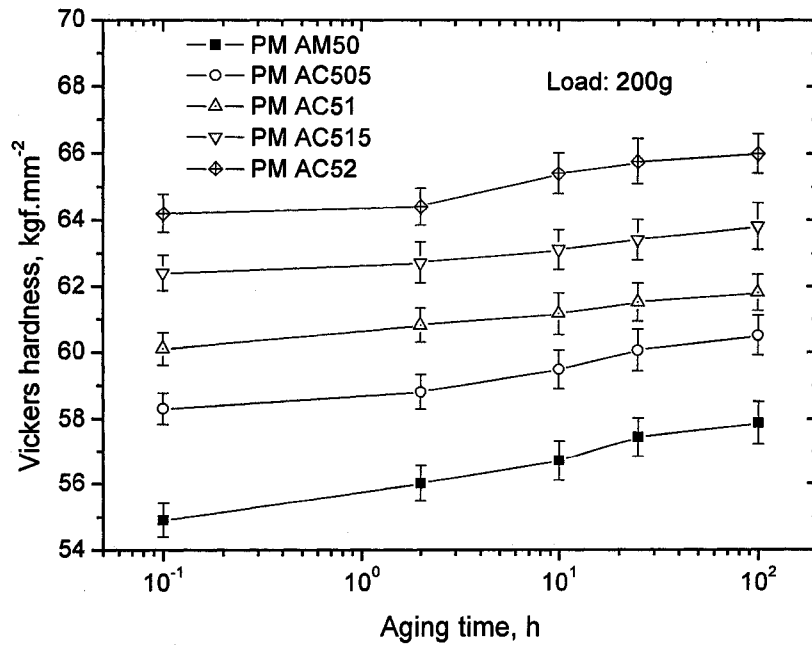


Fig. 5.30 Age-hardening curves for the Mg-Al and Mg-Al-Ca alloys aged at 200 °C without solution treatment.

Figs. 5.31 and 5.32 are SEM micrographs showing the microstructure of the Mg-Al-Ca alloys for different aging times: (a) 2 h and (b) 10 h. The precipitation of the β -Mg₁₇Al₁₂ phase occurs from the supersaturated α -Mg solid solution, during aging at 200 °C for different lengths of time, as shown in Fig. 5.31. In the alloys with a lower Ca content, colonies of discontinuous Mg₁₇Al₁₂ precipitates formed around the intergranular Mg₁₇Al₁₂ particles. Also, some fine discontinuous Mg₁₇Al₁₂ particles were observed having been

precipitated along the grain boundaries (Fig. 5.31 (a) and (b)). However, as the Ca content increased up to 1 wt.% in the Mg-Al alloy, the amount of the discontinuous $Mg_{17}Al_{12}$ particles precipitated along the grain boundaries significantly decreased (Fig. 5.31 (c) and (d)). The distribution of the $Mg_{17}Al_{12}$ precipitates did not develop further when the aging time increased from 10 to 100 h. No continuous precipitation of $Mg_{17}Al_{12}$ occurred in the matrix of these alloys that had not been solution treated.

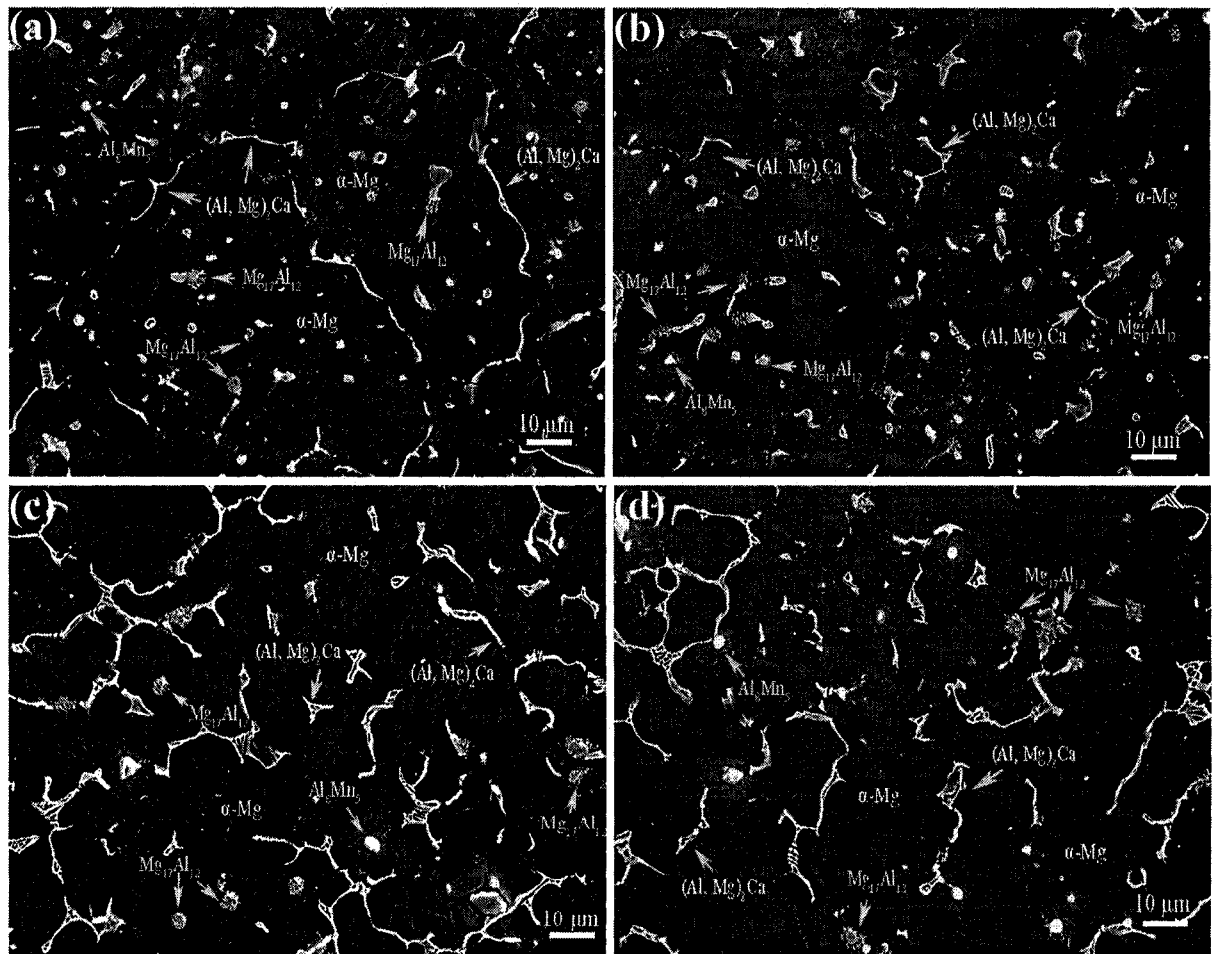


Fig. 5.31 Effect of aging at 200 °C for 2 and 10 h on microstructures of the AC505 and AC51 alloys without solution treatment: (a) 2 h (AC505), (b) 10 h (AC505), (c) 2 h (AC51) and (d) 10 h (AC51).

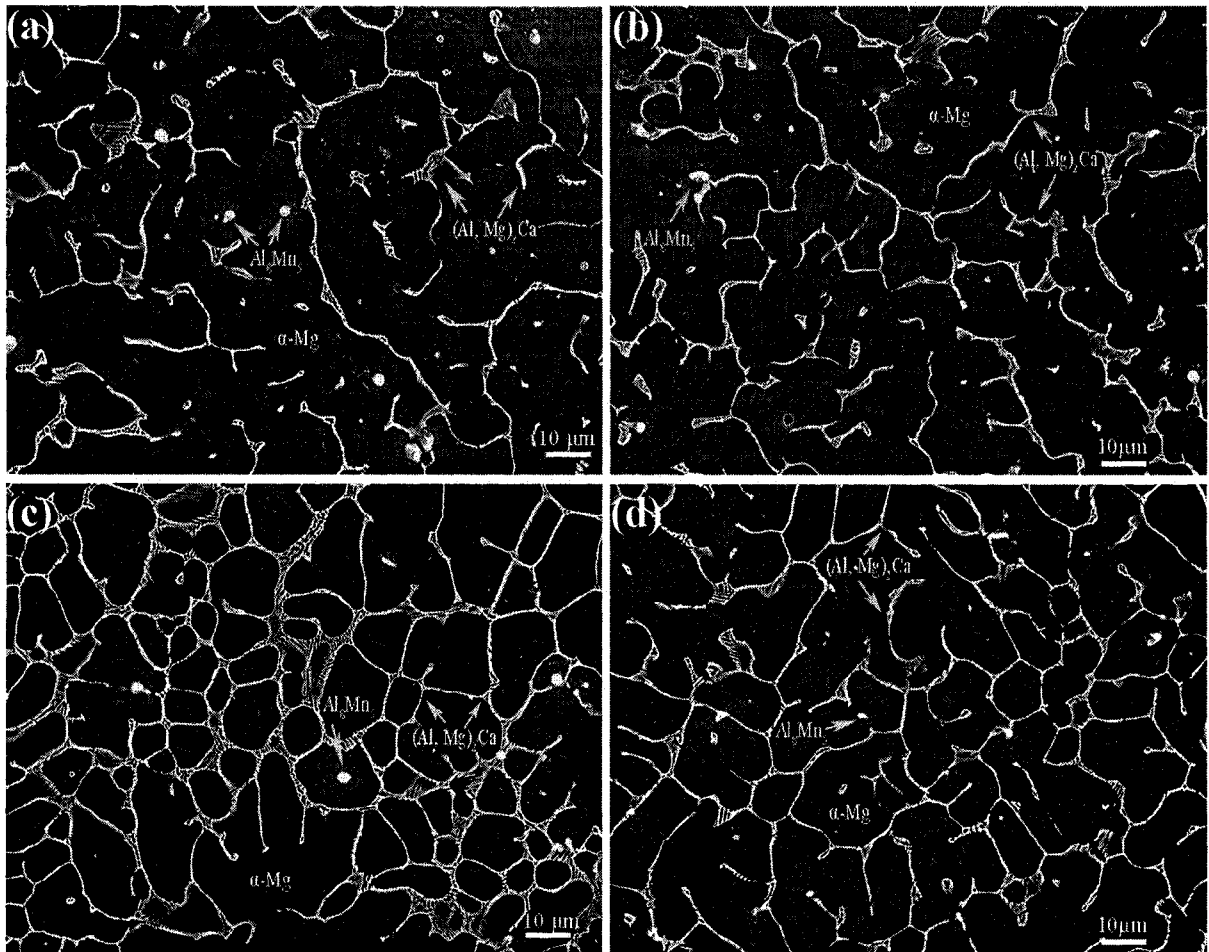


Fig. 5.32 Effect of aging at 200 °C for 2 and 10 h on microstructure of the AC515 and AC52 alloys without solution treatment: (a) 2 h (AC515), (b) 10 h (AC515), (c) 2 h (AC52) and (d) 10 h (AC52).

Although the AC52 alloy was found to increase in hardness after being aged for 10 h, there is almost no microstructural change in the alloy, i.e. no obvious continuous or discontinuous precipitates containing Ca were observed under SEM (Fig. 5.32 (c) and (d)). Since it is difficult using SEM to observe nanoscale precipitates which form during aging, TEM should be used to characterize the aged microstructure. Compared to the AC52 alloy with a higher Ca content of 2 wt.%, there should be few Ca-containing precipitates in the

aged AC515 alloy, based on the fact that the hardness of the AC515 alloy varied very little with increasing aging time up to 100 h.

5.4.3 Aging after solution treatment

The characteristics of the distributions of the $Mg_{17}Al_{12}$ precipitate in the Mg-Al alloy, and $(Al, Mg)_2Ca$ precipitate in the Mg-Al-Ca alloys were studied extensively, after both isochronal and isothermal aging. Fig. 5.33 shows the age-hardening curves for the Mg-Al and Mg-Al-Ca alloys aged at different temperatures after solution treatment for 2 h at 420 °C and 520 °C, respectively. The measurements of the microhardness of the specimens indicated that softening occurred in the AM50, AC505 and AC51 alloys at aging temperatures higher than 200 °C, and occurred in the AC515 and AC52 alloys at aging temperatures above 250 °C.

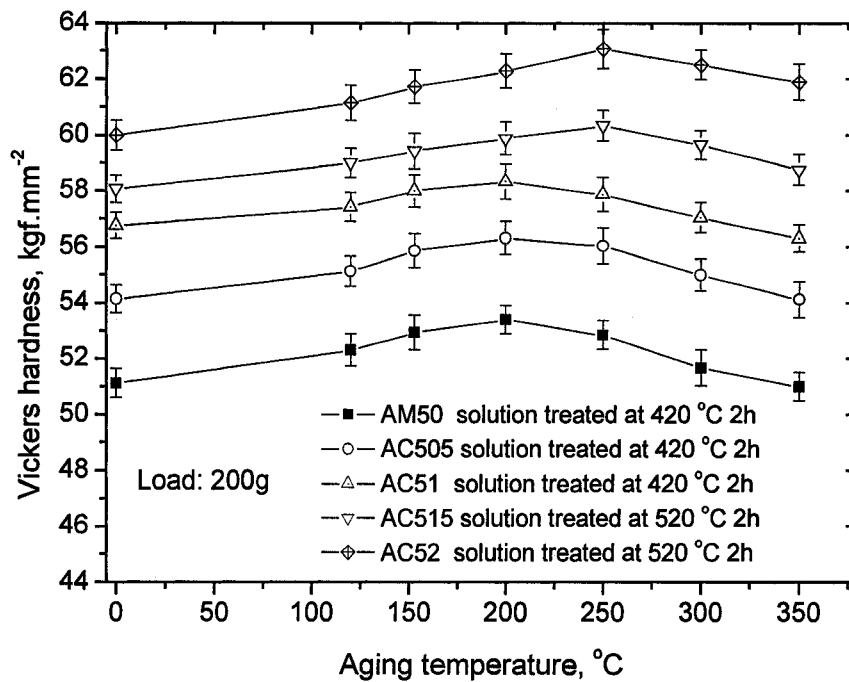


Fig. 5.33 Age-hardening curves for the Mg-Al and Mg-Al-Ca alloys aged at different temperatures for 100 h after solution treatment for 2 h at 420 °C and 520 °C, respectively.

Fig. 5.34 shows SEM micrographs of the microstructures of the AC52 alloy after aging for 100 h at temperatures between 120 and 350 °C. The early stages of discontinuous precipitation are obvious at the grain boundaries of the specimen aged at 120 °C. Also, a small amount of continuous precipitates were also observed in the primary α -Mg grains. At higher aging temperatures, continuous precipitates dominated the primary α -Mg grains. The size of $(\text{Al, Mg})_2\text{Ca}$ precipitates increased with increasing aging temperature. Spheroidisation and coarsening occurred during aging at temperatures higher than 250 °C.

Fig. 5.35 depicts the evolution of microhardness with aging times for the AM50, AC505 and AC51 alloys aged at 200 °C after solution treatment at 420 °C for 2 h, and for the AC515 and AC52 alloys aged at 250 °C after solution treatment at 520 °C for 2 h. Despite that age hardening peaks occurring in the as-cast specimens with aging time are not as visible as those with aging temperature, the four expected regimes for precipitation strengthening, due to formation of $\text{Mg}_{17}\text{Al}_{12}$ or $(\text{Al, Mg})_2\text{Ca}$ precipitates, can be observed sequentially: (i) a short region where hardness remains equal to the as-cast value (incubation); (ii) a rapid increase in hardness (under-aging); (iii) a plateau in hardness values (peak-aging); and (iv) a slow decrease in hardness (over-aging). Peak-aging occurs around 100 h for the all tested alloys. However, the incubation period of the $(\text{Al, Mg})_2\text{Ca}$ precipitates in the AC515 and AC52 alloys aged at 250 °C was much longer than that of the $\text{Mg}_{17}\text{Al}_{12}$ precipitates in the AM50, AC505 and AC51 alloys aged at 200 °C. Additionally, the peak hardness for the AC52 alloy aged at 250 °C is higher than that of other alloys, while the hardness of the cast, solution treated and aged AC52 is lower than that of the cast and aged AC52 alloy.

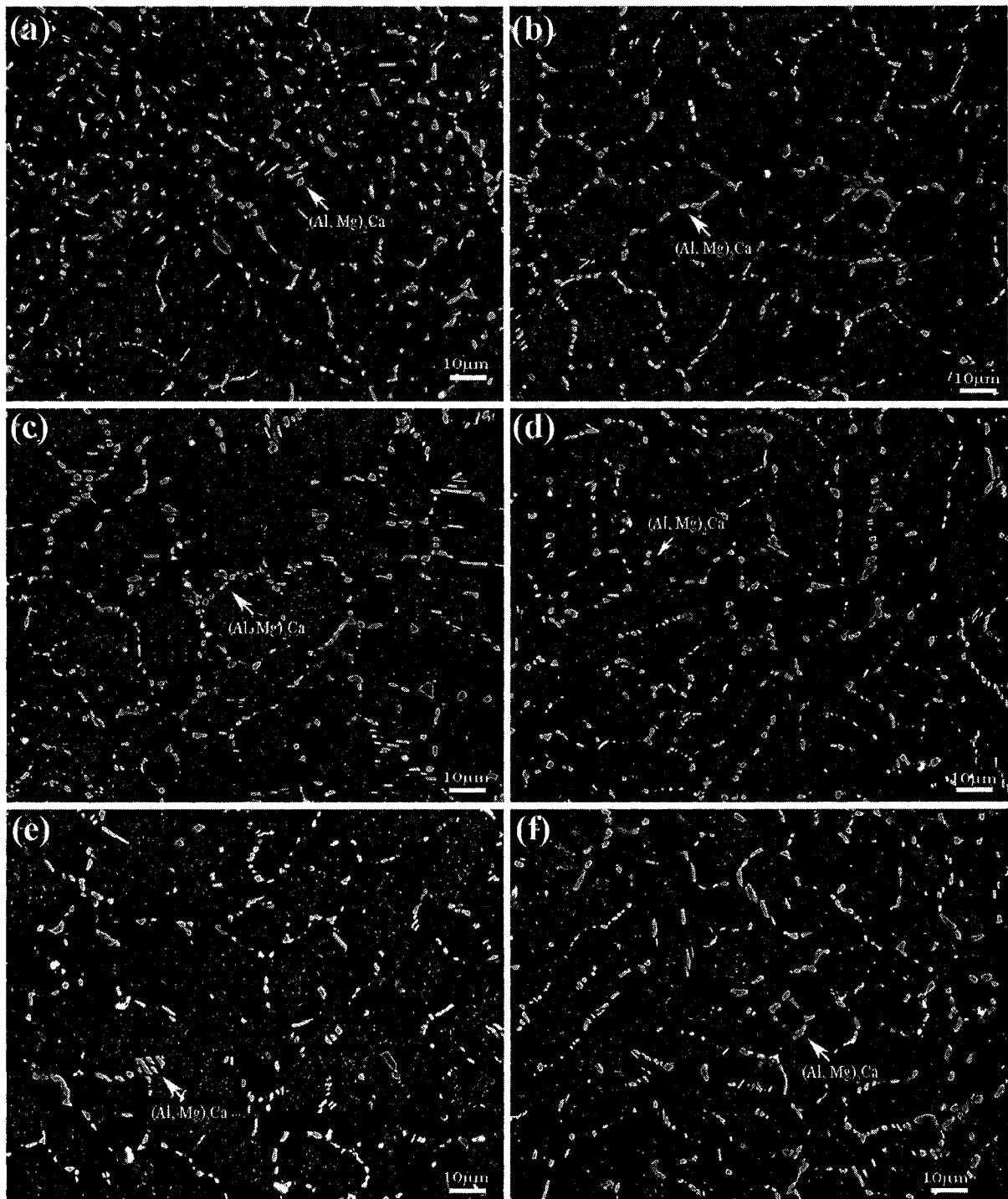


Fig. 5.34 Effect of aging at different temperatures: (a) 120 °C, (b) 150 °C, (c) 200 °C, (d) 250 °C, (e) 300 °C and (f) 350 °C for 100 h on microstructures of the AC52 alloy solution treated at 520 °C for 2 h.

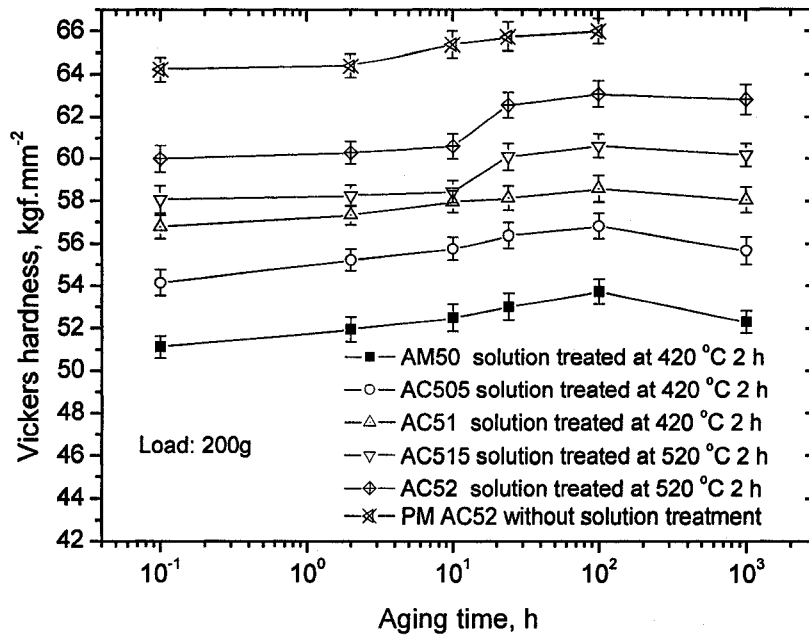


Fig. 5.35 Age-hardening curves for the Mg-Al and Mg-Al-Ca alloys aged at 200 °C and 250 °C for different times after solution treatment for 2 h at 420 °C and 520 °C, respectively.

Figs. 5.36 to 5.38 present SEM micrographs illustrating the microstructures of the PM AM50 and AC51 alloys solution treated at 420 °C for 2 h and aged for 2 to 1000 h, and the AC52 alloy solution treated at 520 °C for 2 h and aged for 2 to 100 h, respectively. Discontinuous $Mg_{17}Al_{12}$ particles began to precipitate at the grain boundaries at the early stage of aging (Fig. 5.36(a)). Then, the amount and size of the $Mg_{17}Al_{12}$ phase increased with increasing aging time. Spheroidisation and coarsening of the precipitate at grain boundaries were observed after aging for 1000 h (Fig. 5.36(d)). It is worth noting that a large number of continuous $Mg_{17}Al_{12}$ particles appeared even within some of the primary α -Mg grains when the aging time reached 1000 h, and some of the $Mg_{17}Al_{12}$ particles grew into needle-like shapes. However, no colonies of $Mg_{17}Al_{12}$ phases were found around the undissolved $Mg_{17}Al_{12}$ particles. Similar to the aging of the AM50 alloy, discontinuous $Mg_{17}Al_{12}$ particles appeared at the grain boundaries in the AC51 alloy as the aging time increased (Fig. 5.37(a)).

The $(Al, Mg)_2Ca$ phases retained their original as-cast morphology during aging, and no observed discontinuous or continuous Ca-containing phases were observed within the primary α -Mg grains (Fig. 5.37) probably due to the low aging temperature. However, Ca-containing phases at grain boundaries tended to coarsen as the aging time increased. It should be noted that the sizes of the primary α -Mg grains varied little during aging possibly because of the pinning effect of the undissolved $(Al, Mg)_2Ca$ phase at the α -Mg grain boundaries. However, the average size of the primary α -Mg grains after aging became larger than $50\ \mu m$ for the AM50 alloy (Fig. 5.36).

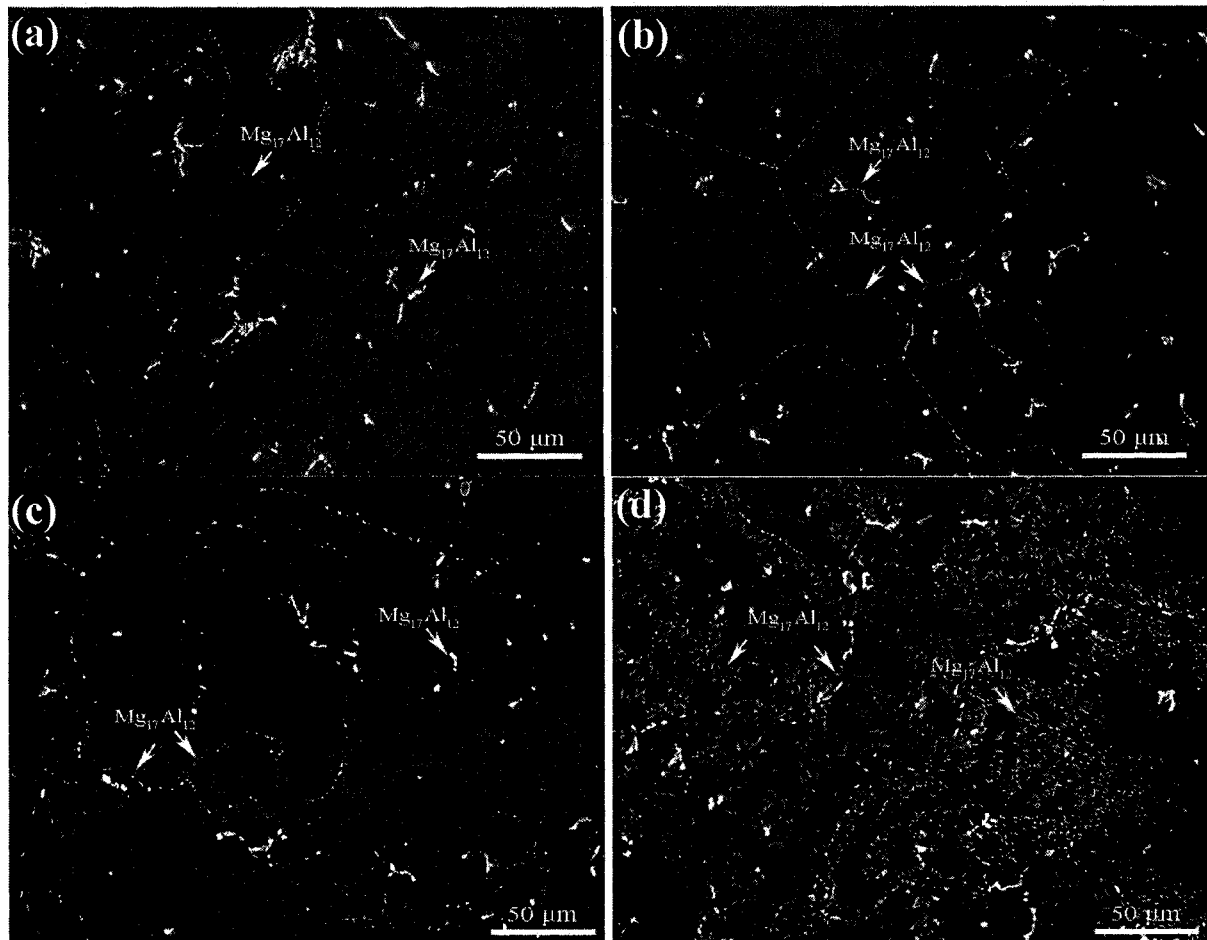


Fig. 5.36 Effect of aging at $200\ ^\circ C$ for given times: (a) 2 h, (b) 24 h, (c) 100 h, and (d) 1000 h on microstructure of the AM50 alloy solution treated at $420\ ^\circ C$.

For the AC52 alloy, a small amount of typical discontinuous and continuous particles of the $(Al, Mg)_2Ca$ were seen to initiate preferentially at some of the grain boundaries and within the primary α -Mg grains, respectively. After aging for 10 h, a large number of the continuous $(Al, Mg)_2Ca$ particles appeared within the α -Mg grains. Significant spheroidisation occurred after aging for 24 h or longer, while coarsening of the precipitates was not distinct. Additionally, no obvious growth of the primary α -Mg grains was observed during aging due to the existing $(Al, Mg)_2Ca$ particles at the grain boundaries.

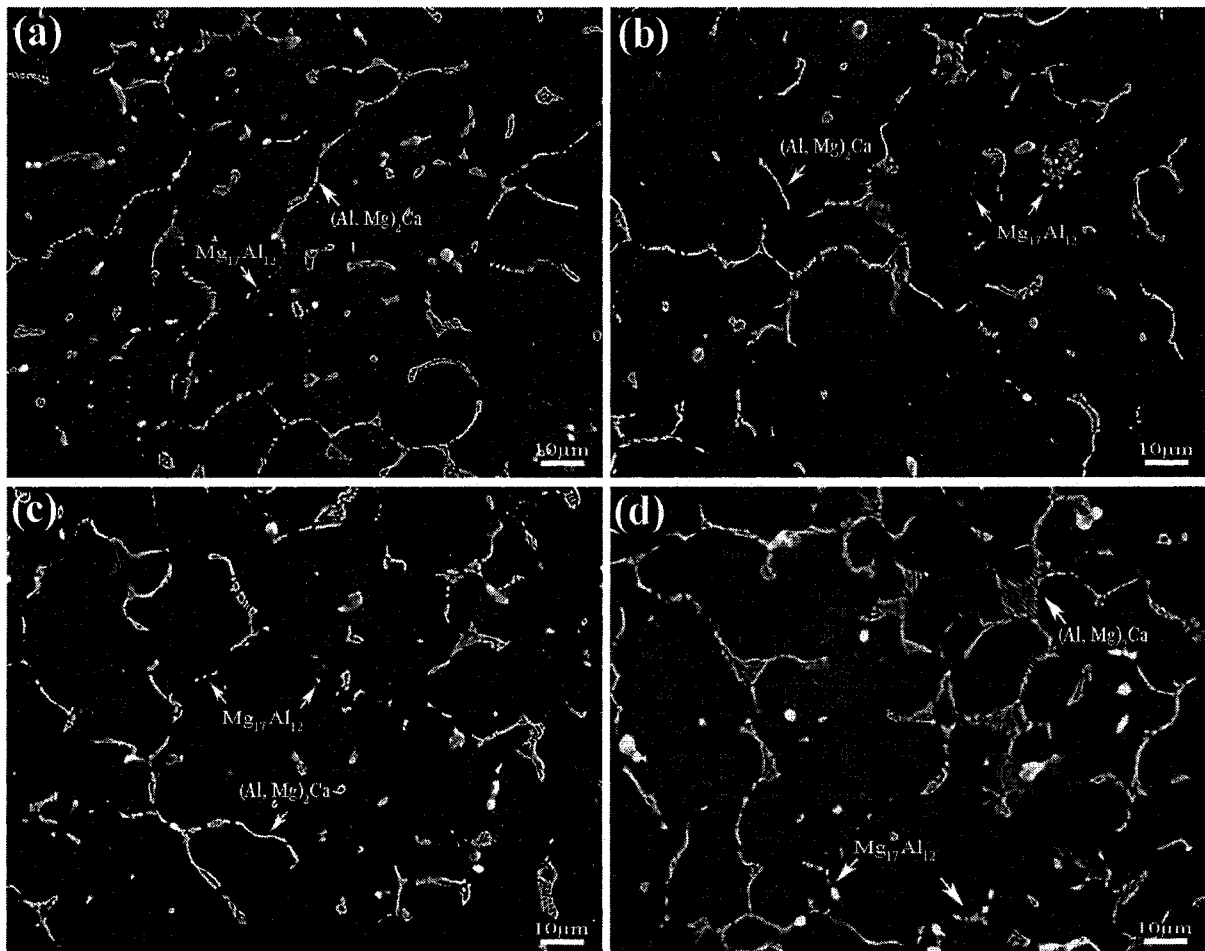


Fig. 5.37 Effect of aging at 200 °C for given times: (a) 2 h, (b) 24 h, (c) 100 h, and (d) 1000 h on microstructure of the AC51 alloy solution treated at 420 °C.

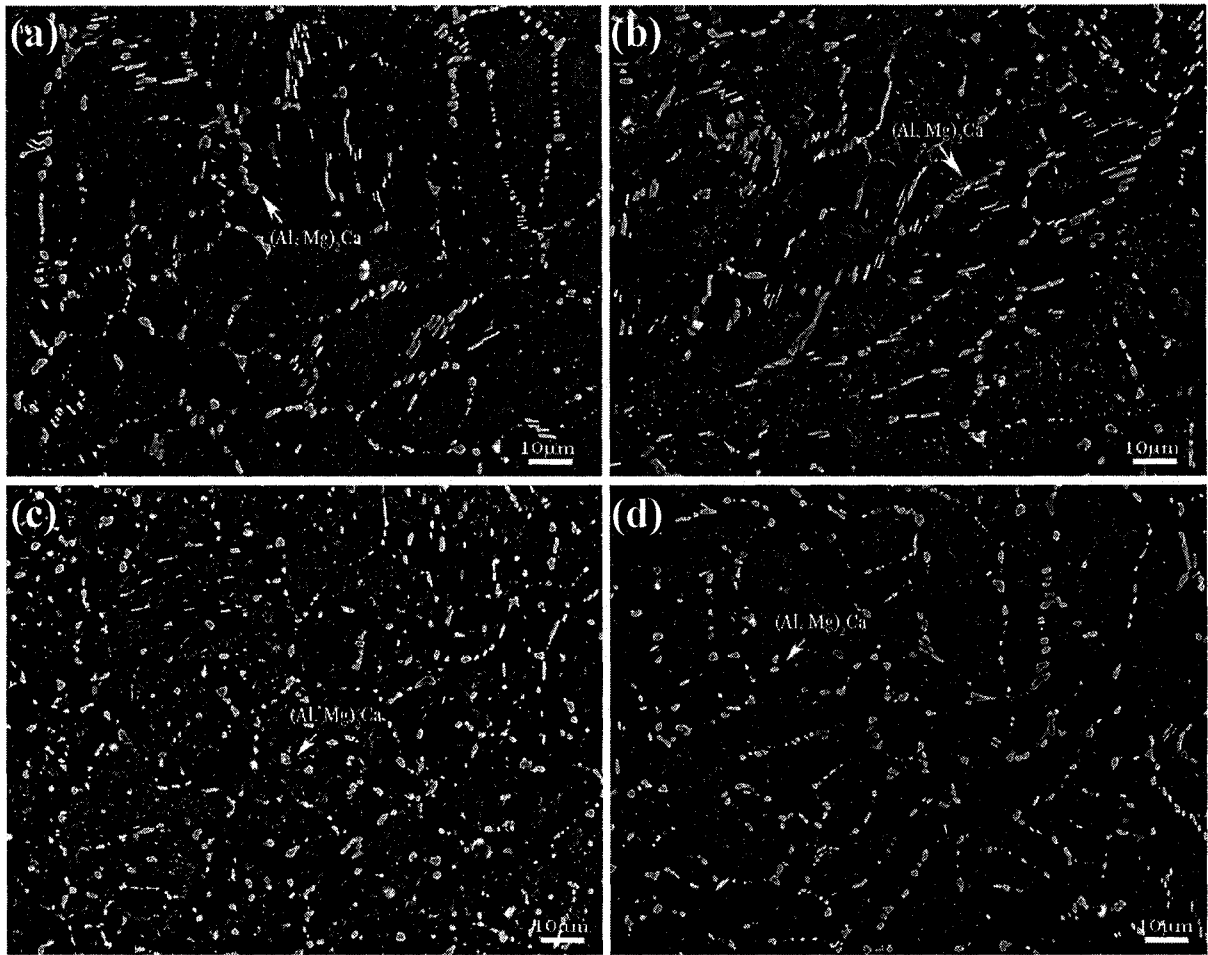


Fig. 5.38 Effect of aging at 250 °C for given times: (a) 2 h, (b) 10 h, (c) 24 h, and (d) 100 h on microstructure of the AC52 alloy solution treated at 520 °C.

5.5 Summary

- (1). The microstructures of the PM AM50 alloy consisted of the primary α -Mg, β -Mg₁₇Al₁₂ and Al₈Mn₅ phases. The β -Mg₁₇Al₁₂ was often surrounded by the eutectic α -Mg. The microstructure of the PM AM50 alloy was significantly coarser than that of the 2 mm DC AM50 alloy, because of different solidification rates.
- (2). The microstructures of the PM Mg-Al-Ca alloys were highly dependent on the Ca content. Quantitative analysis showed that, with increasing Ca content, the average

size of SDAS decreased, while the volume fraction of the eutectic phases increased. The eutectic phases tended to form a continuous network with increasing Ca content instead of being distributed in the form of completely divorced phases at low Ca contents.

- (3). When the Ca content was 1.5 wt.% or higher, the β -Mg₁₇Al₁₂ phase was completely replaced by the (Al, Mg)₂Ca phase. Also, the Ca-containing eutectic phases in all the PM Al-Mg-Ca alloys were the (Al, Mg)₂Ca phase, as confirmed by TEM examination.
- (4). The measurement of the average SDAS in the as-cast AC52 alloy showed a refinement of the dendritic microstructure with increasing cooling rates.
- (5). The experimentally determined volume fraction of non-equilibrium eutectic phases in the as-cast AC52 alloy increased significantly from 10.8 ± 1.44 % at the lower cooling rate of 0.5 °C/s to 20.4 ± 1.52 % for the moderate cooling rate of 20 °C/s. As the cooling rate increased further, the increase in the volume fraction of the eutectic phase became very small. The volume fraction of the eutectic phase in the alloy cast at 65 °C/s increased by only 1.4% compared to that in the alloy cast at 20 °C/s.
- (6). A large amount of dispersed eutectic phases were observed in the primary α -Mg of the AC52 alloy cast at lower cooling rates. Although there were no dispersed eutectic phases observed by SEM in the AC52 alloys cast at a cooling rate of 30 °C/s, some nanoscale eutectic phases were seen by TEM observation at high magnifications.
- (7). The dimensions and morphology of the Al₈Mn₅ phase in the as-cast AC52 alloy were dependent on the cooling rate. The Al₈Mn₅ particles were smaller at higher cooling rates than at lower cooling rates, and the majority of Al₈Mn₅ particles were found to

be attached to the eutectic phases. This was due probably to nucleation of the eutectic phase on the Al_8Mn_5 particles present in the melt.

- (8). Twin structures were formed within the primary α -Mg grains of the as-cast Mg-Al and Mg-Al-Ca alloys during solidification. These twins were often parallel within an individual grain, while different orientations of the twin structure were often observed in neighboring grains. However, some long twins were found to cross several grains in certain regions. Additionally, the high-resolution TEM images showed that there were some nanostrain fields within the twin structures, and a dislocation region was present along the twin boundaries.
- (9). A fast decrease in hardness for the AM50 and AC51 alloys than the AC52 alloy during solution treatment (420 °C for the AM50 and AC51 alloys, and 520 °C for the AC52 alloy) indicated that the dissolution rates of the β - $\text{Mg}_{17}\text{Al}_{12}$ phase in the AM50 and AC51 alloys was higher than that of the $(\text{Al}, \text{Mg})_2\text{Ca}$ in the AC52 alloy.
- (10). Two types of $\text{Mg}_{17}\text{Al}_{12}$ precipitates (discontinuous $\text{Mg}_{17}\text{Al}_{12}$ particles at grain boundaries and continuous $\text{Mg}_{17}\text{Al}_{12}$ particles within the primary α -Mg grains) occurred in the matrix of the PM AM50 alloy after solution treatment plus aging.
- (11). Spheroidisation and coarsening of the discontinuous $\text{Mg}_{17}\text{Al}_{12}$ phase in the PM AM50, AC505 and AC51 alloys took place with extended aging time. However the discontinuous $(\text{Al}, \text{Mg})_2\text{Ca}$ phase in the PM AC515 coarsened. Spheroidisation of the Ca-containing phase in the AC52 alloys occurred after aging temperatures and times increased.

CHAPTER 6

RESULTS AND DISCUSSION OF DSC ANALYSIS

6.1 DSC analysis

6.1.1 DSC runs of the DC AM50 alloy

Typical DSC curves of the DC AM50 alloy at heating rates from 10 to 50 °C/min are shown in Fig. 6.1. In the DSC curves the reaction peaks reflect the specific phase changes and the peak area is proportional to the heat of reaction (ΔQ) associated with the phase transformation. Positive values of ΔQ are due to the endothermic reactions of liquid formation during heating, while negative values result from the latent heat released during solidification. As can be clearly seen all of the heating curves show a wide peak ranging from about 330 to 450 °C as clearly shown in Fig. 6.1 with label B. Another two peaks can also be observed: a large and smooth peak at about 150 °C (labelled as A), and a significant exothermic deviation of the heat flow curves can be detected just before the maximum temperature (labelled C). Each peak was characterized by initial (T_i), peak (T_p) and end (T_e) temperatures and heat content (ΔQ), although it was not possible to determine all these parameters with the same accuracy. As an endothermic peak, peak A has a wide range of temperature from 100 to 240 °C. The peak temperatures at different heating rates are around 420 °C for endothermic peak B. However, peak C is an exothermic peak with the peak temperatures that are around 523 °C. After peak C, the DSC traces sharply go downward, which characterized the onset of the melting peak of the DC AM50 alloy. Since the area under the peaks needs to be normalized and integrated for calculating the heat content of the solid-state phase transformation, it is essential to properly determine initial and end temperatures for each peak. Obviously, the initial and end temperatures for peaks A and B

can be assessed easily. But for peak C it was impossible to estimate the initial and end temperatures. Only peak temperatures can be determined correctly for peak C. DSC results of peak temperatures and heat content obtained at different heating rates are summarized in Table 6.1.

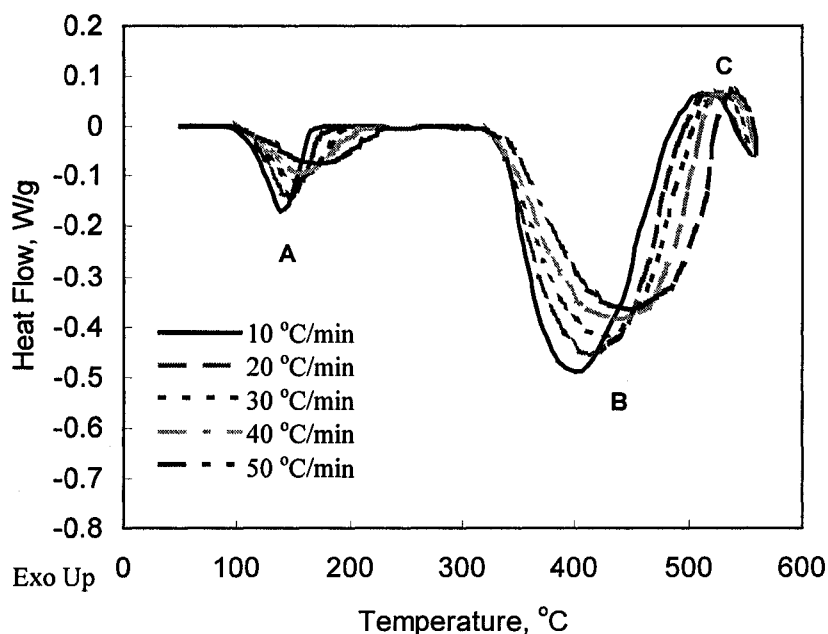


Fig.6.1 DSC traces of the DC AM50 alloy obtained at different heating rates ($^{\circ}\text{C}/\text{min}$).

Table 6.1 DSC results measured at different heating rates for the DC AM50 alloy

Heating rate ($^{\circ}\text{C}/\text{min}$)	Peak A			Peak B			Peak C
	T_i ($^{\circ}\text{C}$)	T_p ($^{\circ}\text{C}$)	ΔQ (J/g)	T_i ($^{\circ}\text{C}$)	T_p ($^{\circ}\text{C}$)	ΔQ (J/g)	T_p ($^{\circ}\text{C}$)
10	109.68	137.20	6.2	332.52	400.03	12.5	524.0
20	110.64	146.18	4.8	333.67	413.20	12.0	523.3
30	112.26	153.00	3.5	335.77	424.87	11.6	524.0
40	114.48	158.06	2.6	336.44	435.32	10.8	525.2
50	115.29	163.80	2.0	338.18	440.59	10.2	523.6

Based on the peak temperatures of the DSC traces of the DC AM50 at different heating rates, the activation energies for the dissolution reactions can be calculated using Eq. (2-38) in Section 2.3.3.2, which is deduced with a Kissinger-type isoconversion method [175, 176]. E_A was calculated as 83.8 kJ mol^{-1} , and E_B as $141.4 \text{ kJ mol}^{-1}$, as shown in Fig. 6.2. Both correlation coefficients of the plots were higher than 0.985.

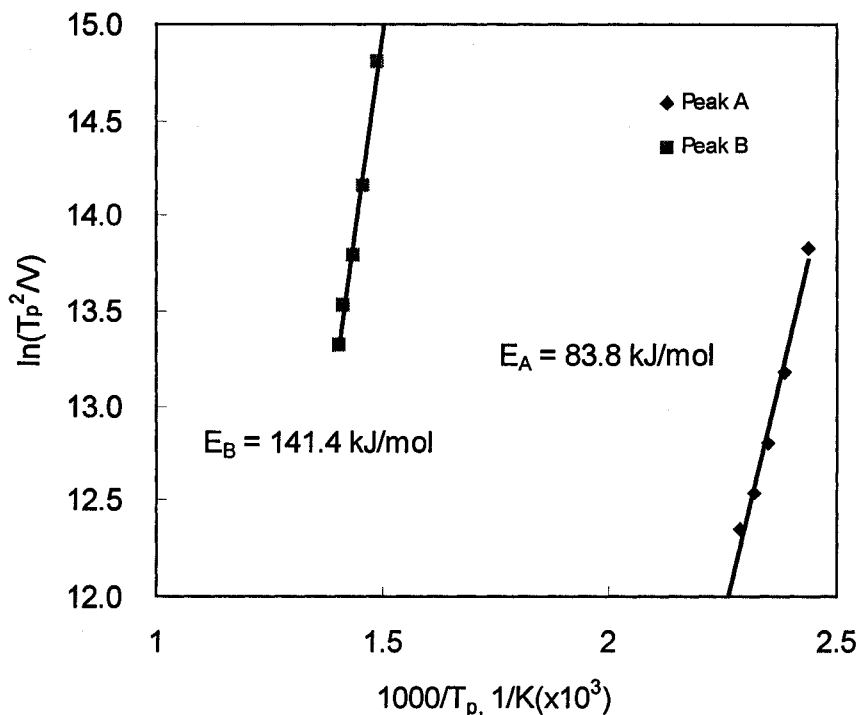


Fig. 6.2 A plot of $\ln T_p^2/V$ vs. $1/T_p$ for determining activation energies of the dissolution of the secondary phases.

6.1.2 DSC runs of the PM AC series alloys

DSC curves of the PM AC series alloys obtained at a heating rate of $30 \text{ }^\circ\text{C}/\text{min}$ are shown in Fig. 6.3. A large and sharp peak with a T_p temperature around $535 \text{ }^\circ\text{C}$ was observed in all of the DSC curves (labelled P2 in Fig. 6.3). However, another small peak with a T_p

temperature around 443 °C (labelled P1 in Fig. 6.3) was only present in the DSC curves of the AC505 and AC51 alloys, not in the DSC curves of the AC515 and AC52 alloys. Both of the two peaks are endothermic peaks, and the temperatures (T_i , T_p and T_e) of the two peaks can be accurately determined. A summary of the DSC results including the initial and peak temperatures and the heat contents of P1 and P2 for the PM AC series alloys obtained at a heating rate of 30 °C/min is given in Table 6.2.

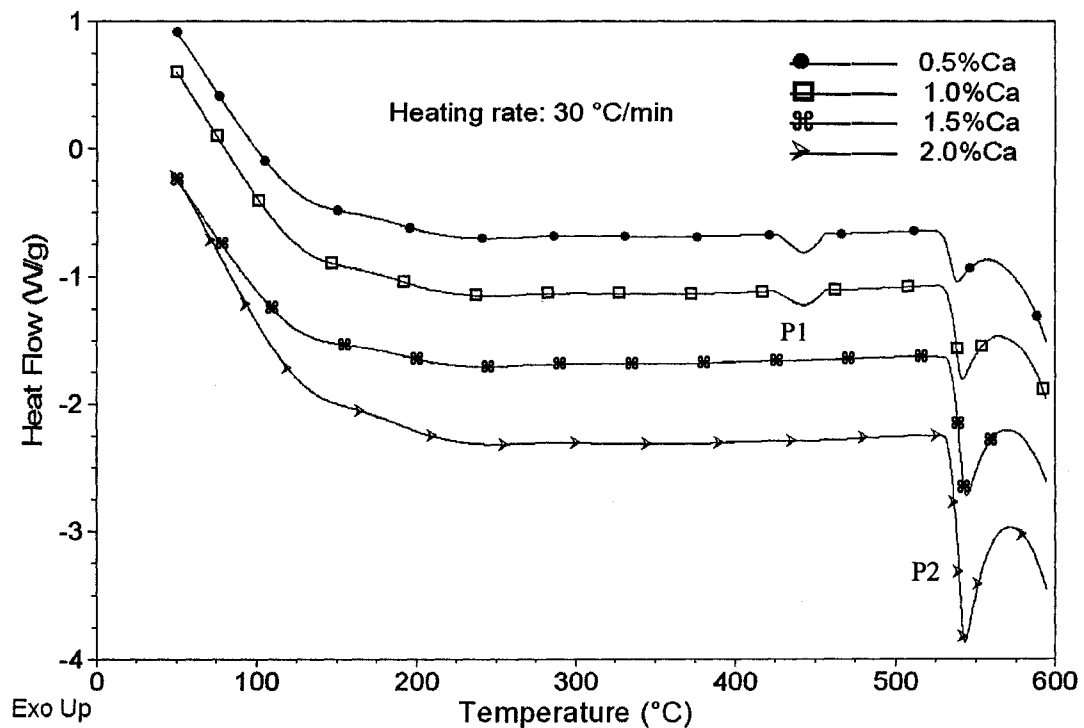


Fig.6.3 DSC traces of the PM AC series alloys: (a) AC505, (b) AC51, (c) AC515 and (d) AC52 obtained at a heating rate of 30 °C/min.

Table 6.2 DSC results of the PM AC series alloys obtained at a heating rate of 30 °C/min

Alloy	P1			P2		
	T _i (°C)	T _p (°C)	Q (J/g)	T _i (°C)	T _p (°C)	Q (J/g)
PM AC505	427.73	443.13	4.880	529.29	538.20	8.132
PM AC51	428.82	443.35	3.477	531.53	541.52	17.75
PM AC515	-	-	-	532.40	543.65	27.62
PM AC52	-	-	-	532.74	542.96	43.79

- could not be determined.

6.1.3 DSC runs of the PM AC52 alloy

6.1.3.1 DSC runs with heating

DSC curves of the PM AC52 alloy obtained at different heating rates are shown in Fig. 6.4. Only a large and sharp endothermic peak with a T_p temperature ranging from 534.65 to 565.27 °C (P2) was observed in all of the DSC curves. A summary of the DSC results for the PM AC52 alloy obtained at different heating rates from 10 to 50 °C/min is given in Table 6.3.

Figs. 6.5 and 6.6 show the effect of heating rates on the dissolution of the secondary phase in the PM AC52 alloy during the DSC runs. It can be clearly seen that higher heating rates result in an increase in the temperature of the dissolution of the eutectic phase, i.e. a shift of the transformation range to higher temperatures. Moreover, they are associated with wider transformation intervals (Fig. 6.6). The differences between the temperatures where the eutectic transformations start and end increase with increasing cooling rate, while the dissolution time of the eutectic phase decrease with increasing heating rate. A closer look at the data shown in Figs. 6.5 and 6.6 reveals that the widths of the phase transformation

intervals increase from 21.11 to 44.27 °C, and that the time intervals of the dissolution of the eutectic phase decrease from 2.29 to 0.93 min when the cooling rate increases from 10 to 50 °C/min.

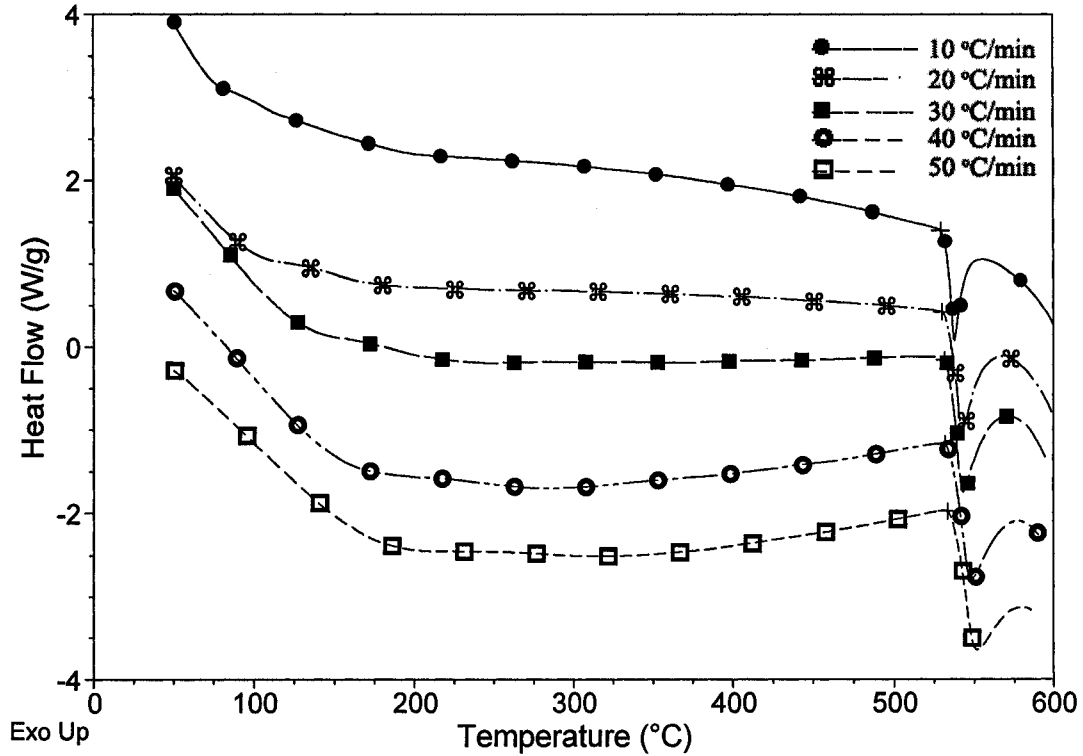


Fig. 6.4 DSC traces of the PM AC 52 alloy obtained at different heating rates.

Table 6.3 DSC results of the PM AC52 alloy obtained at different heating rates

Heating rate (°C/min)	P2		
	T _i (°C)	T _p (°C)	ΔQ (J/g)
10	530.83	534.65	63.18
20	531.76	538.18	54.74
30	532.74	546.96	43.79
40	533.21	554.40	36.22
50	535.22	565.27	28.15

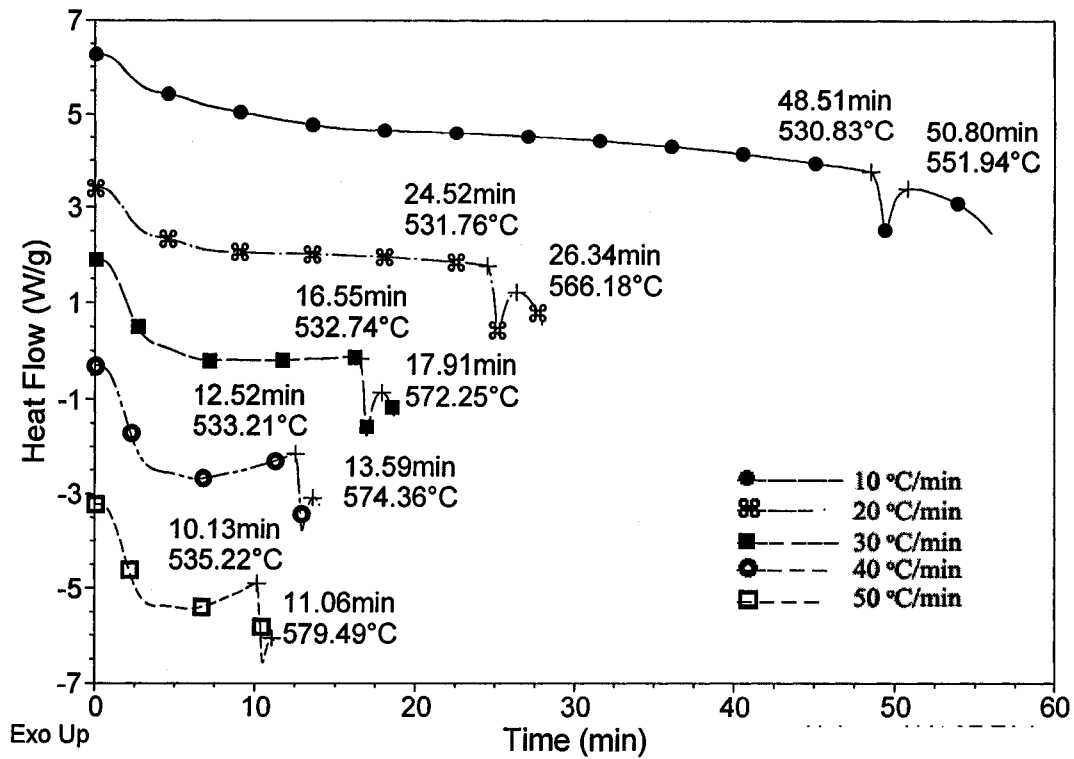


Fig. 6.5 Effect of heating rates on the dissolution time of the secondary phase in the PM AC52 alloy during the DSC runs.

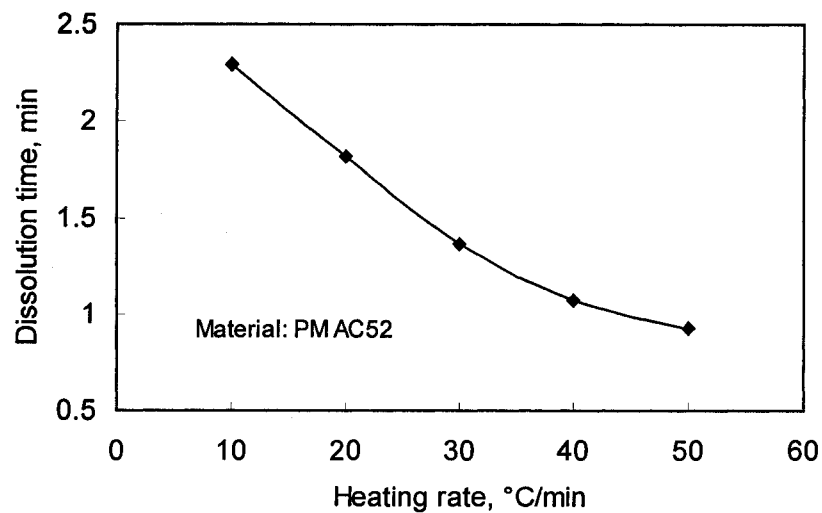


Fig. 6.6 Variation of dissolution time with heating rates for the PM AC52 alloy.

Activation energies for the precipitation reactions were obtained using a Kissinger-type isoconversion method [175, 176] with the peak temperatures of DSC traces of the PM AC52 alloy at different heating rates. The calculated activation energy E_{P2} is $224.5 \text{ kJ mol}^{-1}$, as shown in Fig. 6.7, and the correlation coefficient of the plot is 0.93.

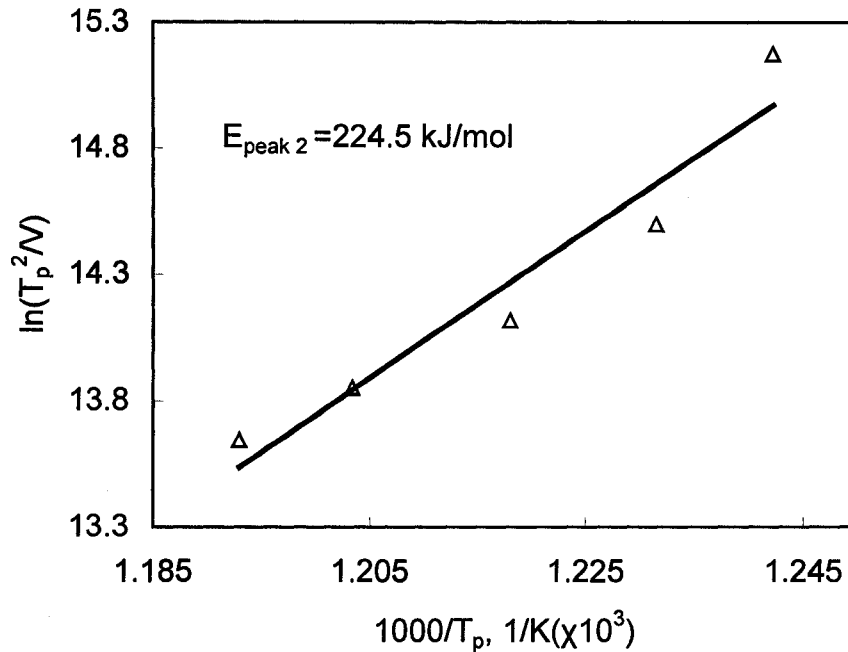
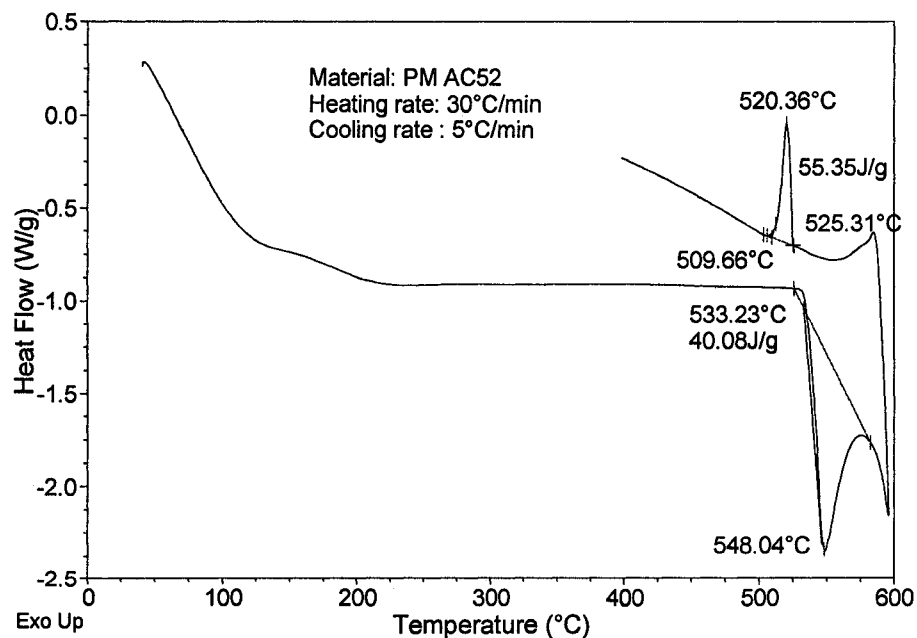


Fig. 6.7 A plot of $\ln T_p^2/V$ vs. $1/T_p$ for determining activation energies of the dissolution of the secondary phases in the PM AC52 alloy.

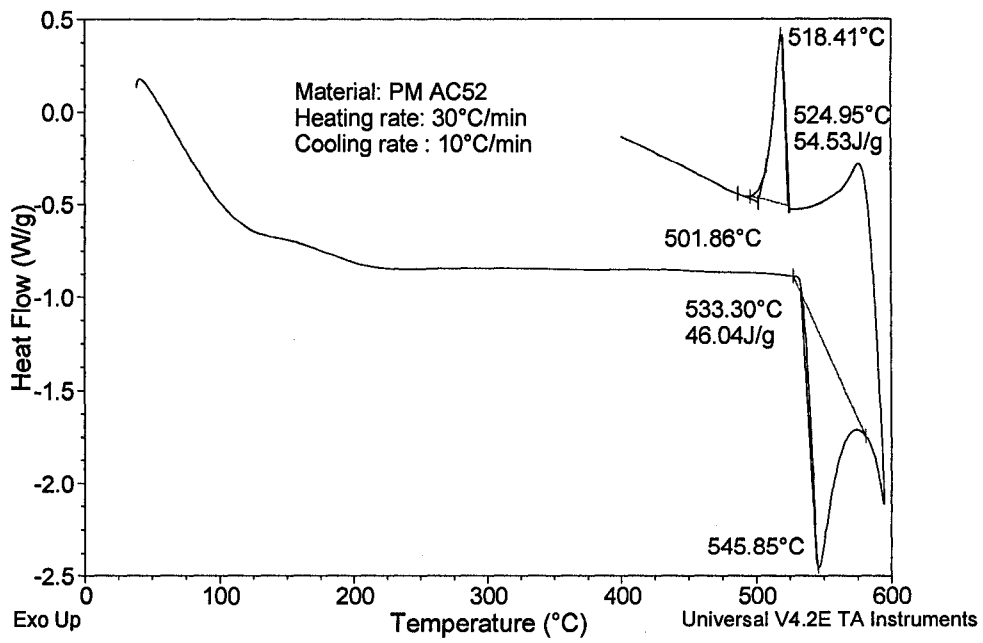
6.1.3.2 DSC runs with cooling after heating

The DSC heating and cooling results for the AC52 are shown in Fig. 6.8. Each sample for DSC measurement was first heated at $30 \text{ }^\circ\text{C/min}$ from room temperature to the temperature indicated in the Fig. 6.8, and then subsequently cooled at different cooling rates. One sharp endothermic peak was observed on the heating curve while a sharp exothermic peak subsequently appeared on the cooling curve. The identified phase transformation with average peak temperatures of 547°C (heating) and 517°C (cooling) corresponds to the

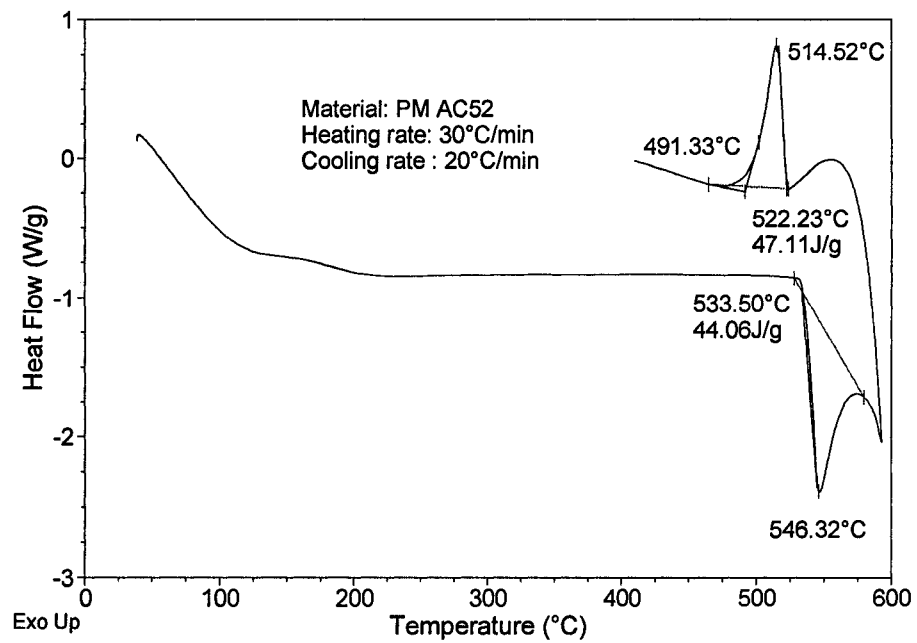
dissolution and precipitation of the $(Al, Mg)_2Ca$ phase, respectively. The transformation temperatures measured during heating are more representative of the true values than those measured on cooling due to undercooling effects. The curve in the Fig. 6.8(a) was obtained for the sample cooled at 5 °C/min. A sharp exothermal peak appeared with a large enthalpy (55.35 J/g) due to precipitation. For the sample cooled at 10 °C/min (Fig. 6.8(b)), the melting peak area becomes slightly smaller (54.53 J/g). In the cases of cooling at 20 and 30 °C/min, Figs. 6.8(c) and (d), the enthalpy continues to decrease, reaching values of 47.11 and 45.89 J/g, respectively. Since the precipitation peak presupposes the presence of secondary phase nuclei, the high enthalpy value suggests that there were relatively fewer nuclei of the precipitation phase at 5 °C/min. However, the number of nuclei dramatically increases with increase in cooling rate. A summary of the DSC results of the PM AC52 alloy obtained at different cooling rates after heating is given in Table 6.4.



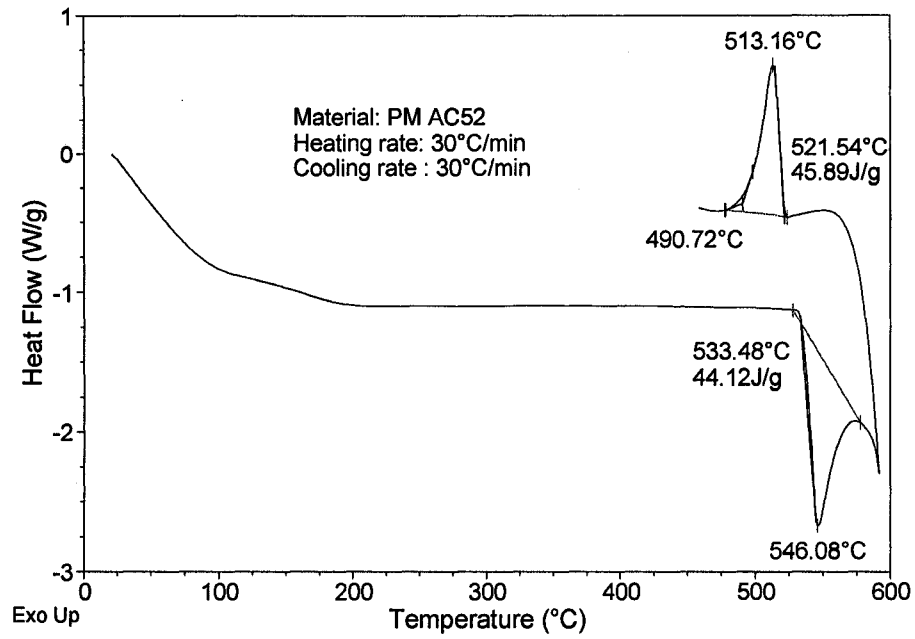
(a)



(b)



(c)



(d)

Fig. 6.8 DSC traces for the PM AC 52 alloy run at a heating rate (30 °C/min) /different cooling rates (°C/min): (a) 5, (b) 10, (c) 20 and (d) 30.

Table 6.4 DSC results of the PM AC52 alloy obtained at different cooling rates after heating

Cooling rate (°C/min)	P2			
	T _i (°C)	T _p (°C)	T _e (°C)	ΔQ (J/g)
5	525.31	520.36	509.66	-55.35
10	524.95	518.41	501.86	-54.53
20	522.23	514.52	491.33	-47.11
30	521.54	513.16	490.72	-45.89

6.2 Microstructural development during DSC runs

6.2.1 Effect of heating rate on the microstructure in the PM AM50 alloy

SEM observation coupled with EDS analysis was performed on the tested specimens after the DSC runs. Fig. 6.9(a) shows the microstructure of the DC AM50 alloy after DSC run at a heating rate of 10 °C/min followed by air quenching. It can be seen that some relatively coarse round particles and fine needle-like plates are present in the matrix of the alloy. Specimens after DSC runs at other heating rates (20 ~ 50 °C/min) showed a similar microstructure. EDS results showed that the round particles were the Al_8Mn_5 phase (marked by open circles in Fig. 6.9 (a)) while fine needle-like plates were the $\beta\text{-Mg}_{17}\text{Al}_{12}$ phase (marked by a cross in Fig. 6.9 (a)). EDS spectra from the matrix, Al_8Mn_5 particle and $\beta\text{-Mg}_{17}\text{Al}_{12}$ plates are shown in Figs. 6.9 (b), (c) and (d). Oxygen was also detected in the specimens after a DSC run: this arises from oxidation of the alloy after the heating temperature exceeds the eutectic temperature (app. 437 °C) during the DSC run, even if a protective argon gas was used (6.9 (c)). Specimens heated up to 550 °C at different heating rates and cooled at the same rate (air quenched) showed significant homogenization. No appreciable differences in the microstructure were detected apart from occasional, slightly coarsened grains. The average Al content in the matrix of the alloy after a DSC run at different heating rates is given in Table 6.5.

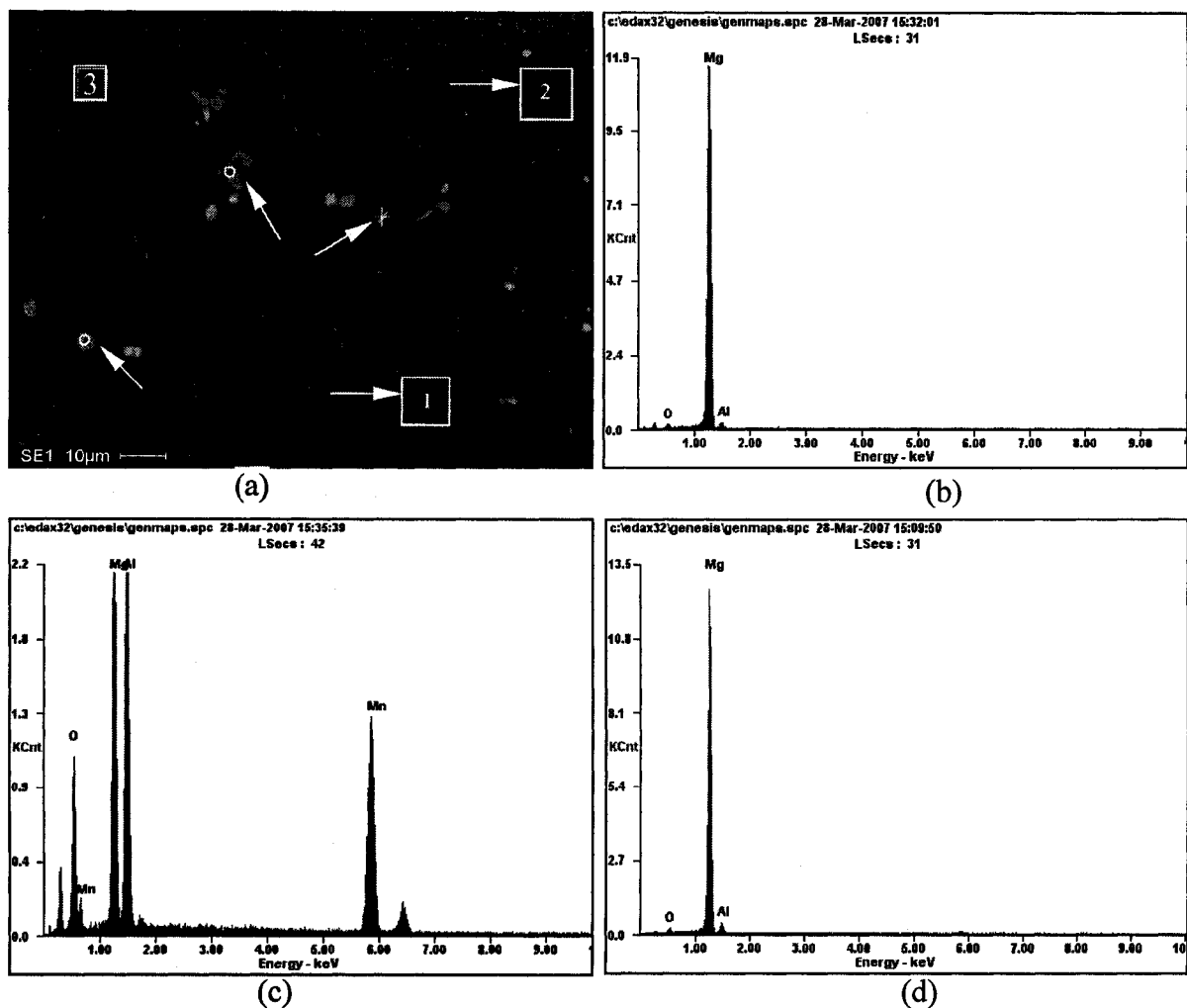


Fig. 6.9 (a) SEM image and typical EDS spectra from the main constituents of: (b) primary α -Mg solid solution, (c) Al_8Mn_5 and (d) β - $\text{Mg}_{17}\text{Al}_{12}$ in the AM50 after DSC runs.

Table 6.5 Averaged Al content (wt.%) in the matrix of the AM50 alloy after DSC runs

Al content (wt.%)	Heating rate ($^{\circ}\text{C}/\text{min}$)				
	10	20	30	40	50
Location 1	4.30	4.35	5.12	5.48	5.58
Location 2	4.12	4.56	4.67	3.78	5.15
Location 3	4.57	4.36	4.45	5.15	4.90
Average	4.33	4.42	4.73	4.80	5.21

It can be seen that the average Al content increased with increasing heating rating, which indicates that heating up to 550 °C at the various heating rates results in a progressive elimination of the coring that characterized the die-cast microstructure. In the die-cast condition, the Al content was lower in the larger grains that were probably the first solidified regions. As the temperatures increased during a DSC run, the Al content tended to increase in the grains, as a consequence of diffusion of Al from the Al-rich eutectic α -Mg phases at the grain boundaries. Thus, the Al content at the center of the grains tended to converge to an 'average' value. When the heating rates increased, the diffusion path of the solute became short. Thus, the measured Al content (around 5.21 wt.%) in the specimen after DSC run at a heating rate of 50 °C/min was slightly higher than that measured at 10 °C/min (around 4.33 wt.%). The distribution of the fine β -Mg₁₇Al₁₂ plates (formed during DSC) confirmed the modification of the distribution of Al content in the matrix of the alloy.

6.2.2 Variation of the microstructure in the AC series alloys after a DSC run

Fig. 6.10 compares the microstructures of the AC series alloys after DSC run at a heating rate of 30 °C/min and followed by air quenching. For the alloys with lower Ca concentrations, the discontinuous characteristics of the microstructure are more pronounced. The discontinuous needle-like particles in the low Ca AC505 alloy were mainly β -Mg₁₇Al₁₂ and (Al, Mg)₂Ca phases, which were distributed along the grain boundaries (Fig. 6.10(a)). These two phases have a similar contrast and morphology so that it is hard to distinguish them in the SEM images. As the Ca content increases, more discontinuous eutectic particles appear at the grain boundaries (Fig. 6.10(b)). When then Ca content is higher than 1.5 wt.%, the eutectic phases gradually form an eutectic network in the microstructure of the AC515 alloy, and at the same time, clusters of very fine plates appear within the primary α -Mg

grains (Fig. 6.10(c)). The two morphologies of the microstructures shown in Fig. 6.10(c) suggest that an increase in Ca content resulted in an increase of the volume fraction of eutectic microstructure. In the case of the low Ca alloys of Fig. 6.10 (a) and (b), the volume fraction associated with the eutectic microstructure was significantly lower than that in the AC515 alloy (Fig. 6.10(c)). These eutectic phases, which were present at the grain boundaries and within the primary α -Mg grains of the AC515 alloy, were the $(Al, Mg)_2Ca$ phases. The β - $Mg_{17}Al_{12}$ phase was completely replaced by the $(Al, Mg)_2Ca$ phase. Finally, more fine eutectic plates precipitated within the primary α -Mg grains of the AC52 alloy. Additionally, it should be noted that numerous fine eutectic plates formed at the grain boundary triple-points (Fig. 6.10(d)). Higher magnification SEM images of the microstructures in the AC505 and AC52 alloys after DSC run are shown in Fig. 6. 11. The discontinuous eutectic particles were mainly distributed along the grain boundaries in the AC505 alloy. Both eutectic phases in the AC505 alloy had needle-like shapes while their sizes were different. EDS results showed that these fine needle-like plates were mainly the β - $Mg_{17}Al_{12}$ phase while the coarse plates were $(Al, Mg)_2Ca$ phase. In the AC52 alloy, a large amount of fine $(Al, Mg)_2Ca$ plates were present within the primary α -Mg grains while coarse $(Al, Mg)_2Ca$ plates were mainly distributed along the grain boundaries. Additionally, it was observed that these fine $(Al, Mg)_2Ca$ plates were parallel within an individual α -Mg grain, which suggested that there was a preferred crystallographic relationship between the fine $(Al, Mg)_2Ca$ plates and the matrix of the alloy.

The quantitative details of grain sizes of the AC series alloys after the DSC run are reported in Fig. 6.12. It can be seen that the grain size gradually decreased with increasing Ca content in the AC series alloy after DSC runs at a heating rate of 30 °C/min followed by air quenching.

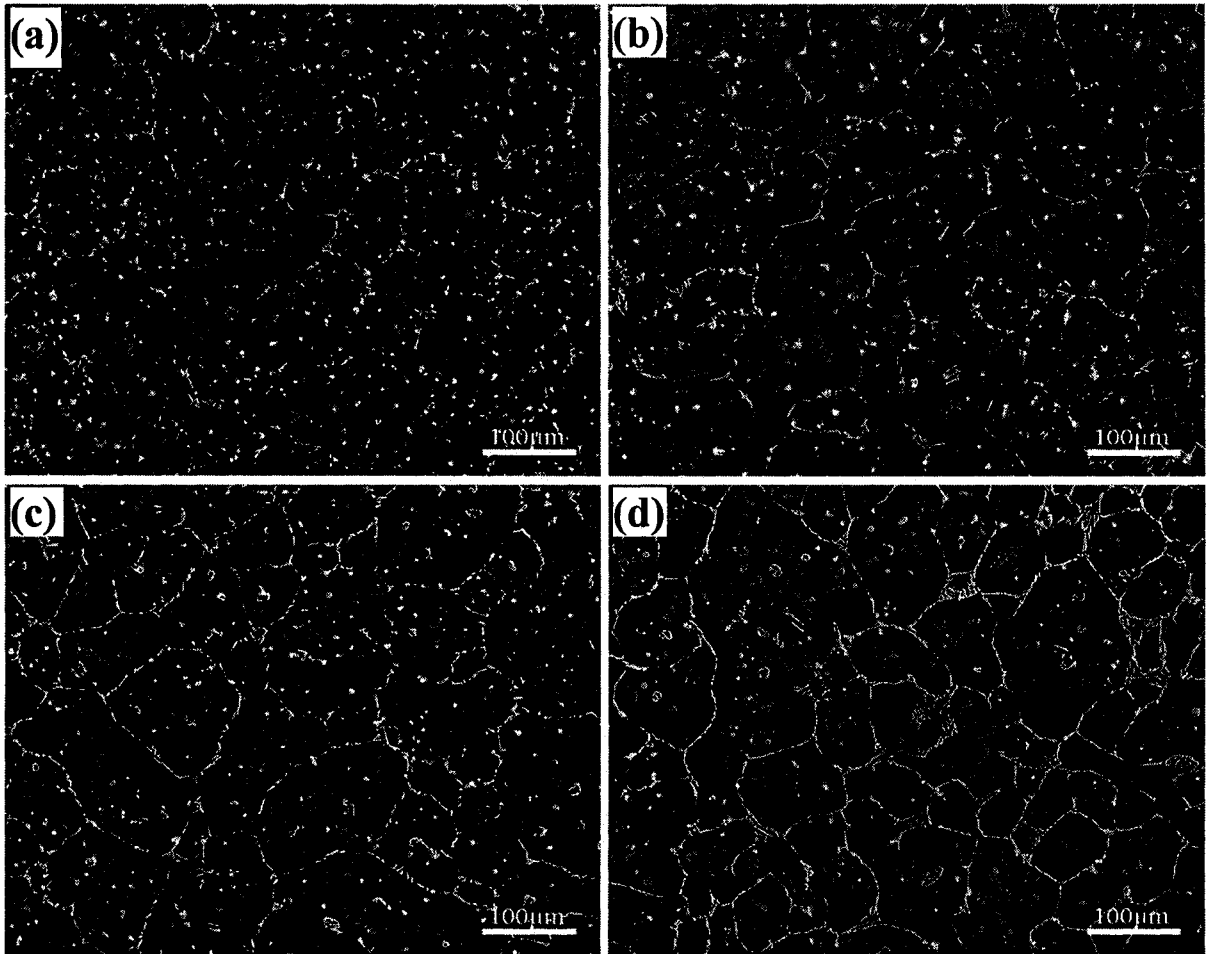


Fig. 6.10 Microstructural evolution in the AC series alloys: (a) AC505, (b) AC51, (c) AC515 and (d) AC52 after DSC run at a heating rate of 30 °C/min followed by air quenching.

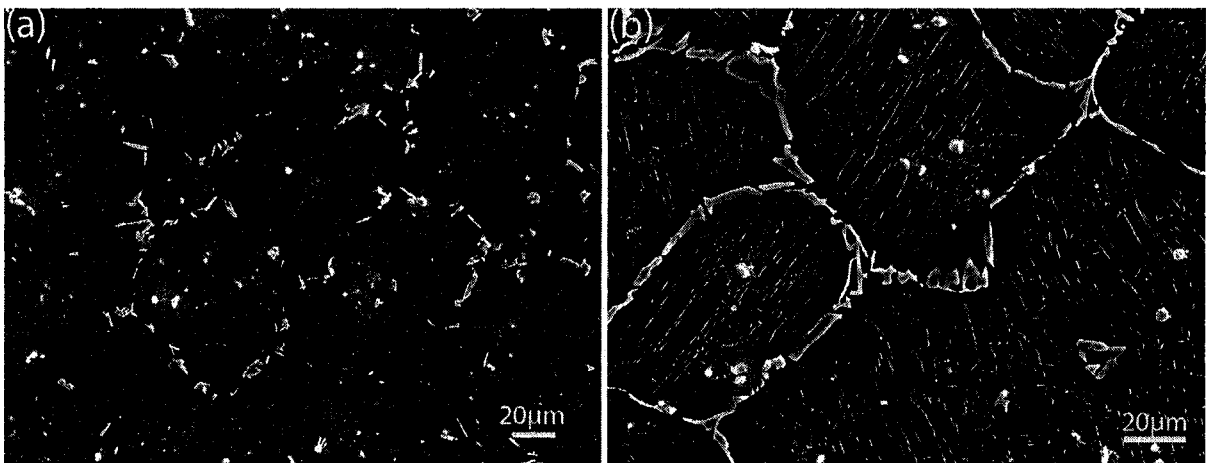


Fig. 6.11 Higher magnification of the microstructures in: (a) the AC505 and (b) AC52 alloys after DSC run at a heating rate of 30 °C/min followed by air quenching.

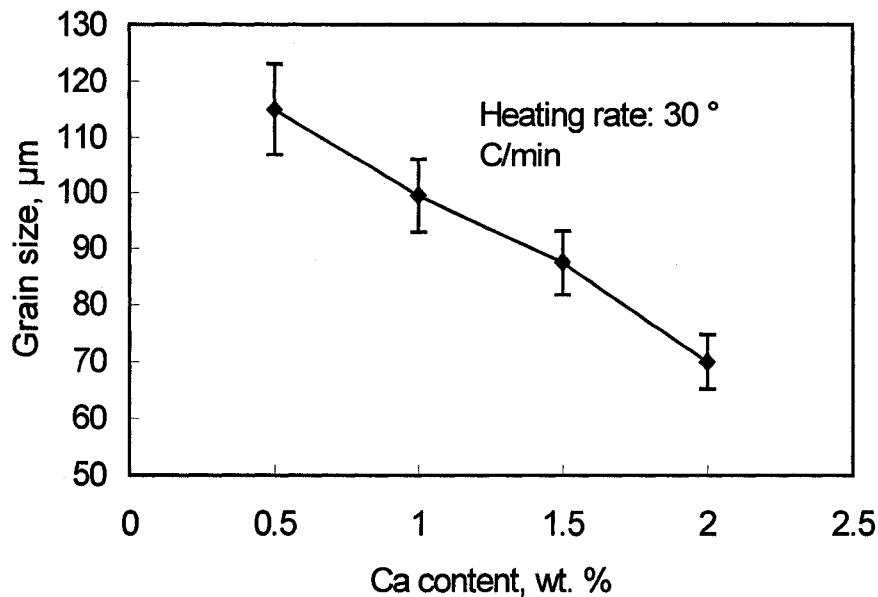


Fig. 6.12 Effect of Ca contents on grain size in the AC series alloys after DSC run at a heating rate of 30 °C/min followed by air quenching.

6.2.3 Effect of heating rate on the microstructure of the PM AC52 alloy

OM and SEM were performed to investigate the microstructural evolution of the AC52 alloy after DSC runs at different heating rates ranging from 10 to 50 °C/min followed by air quenching. Fig. 6.13 shows representative OM images of the specimens heated at heating rates of 10, 30 and 50 °C/min. It can be clearly seen in Fig. 6.13(a) that the grain size was very large in the specimen after a DSC run at a heating rate of 10 °C/min. The majority of grains were between 50 and 100 μm in size. Several large grains with sizes over 200 μm are also present in the alloy. As the heating rates increased, however, smaller grains in great numbers, of which size is less than 50 μm , emerged in the specimen (Fig. 6.13(b)). Also, a few large grains around 200 μm could still be observed. When the heating rate reached 50 °C/min, all grains were smaller than 200 μm . At the same time, some small grains less than 30 μm formed in the specimen after the DSC run. Also, a small number of grains larger than

100 μm were still present. Although the grain size was relatively large, the distribution of grain sizes was relatively uniform in the specimen after a DSC run at a heating rate of 10 $^{\circ}\text{C}/\text{min}$, compared to that in the specimen after a DSC run at a heating rate of 50 $^{\circ}\text{C}/\text{min}$. The measured grain size of the AC52 alloy after DSC runs at the different heating rates is plotted in Fig. 6.14. It can be seen that grain size changed from 83.1 to 80.6 μm , i.e. decreased by 2.5 μm in average, when the heating rate increased from 10 to 20 $^{\circ}\text{C}/\text{min}$. A significant decrease in grain size, 10.7 μm , was observed as heating rates increased from 20 to 30 $^{\circ}\text{C}/\text{min}$. However, the change in the grain size is minor (by only 3.2 μm) while increasing heating rates from 30 to 50 $^{\circ}\text{C}/\text{min}$.

The results in Fig. 6.14 demonstrate that heating rates play an important role in determining the grain size of the AC alloy, which is controlled by the redistribution of Ca through diffusion during the DSC runs. The higher magnification SEM images of the microstructures of the specimens after DSC runs at heating rates of 10 and 40 $^{\circ}\text{C}/\text{min}$ are shown in Fig. 6.15. Three morphologies of the $(\text{Al}, \text{Mg})_2\text{Ca}$ phase were observed in the specimens after the DSC runs. Coarse $(\text{Al}, \text{Mg})_2\text{Ca}$ plates were present at the grain boundaries while a large number of fine needle-like $(\text{Al}, \text{Mg})_2\text{Ca}$ plates precipitated within the primary α -Mg grains. It should be noted that some round $(\text{Al}, \text{Mg})_2\text{Ca}$ islands with the shape of Chinese Script also formed within the primary α -Mg grains. Very few $(\text{Al}, \text{Mg})_2\text{Ca}$ islands were present when the heating rate was low (Fig. 6.15 (a)). However, as the heating rate increased up to 40 $^{\circ}\text{C}/\text{min}$, more $(\text{Al}, \text{Mg})_2\text{Ca}$ islands with fine structure appeared within the primary α -Mg grains. The presence of the $(\text{Al}, \text{Mg})_2\text{Ca}$ islands in the specimens after the DSC runs can be attributed to the precipitation kinetics, i.e. shorter diffusion process at higher heating rate.

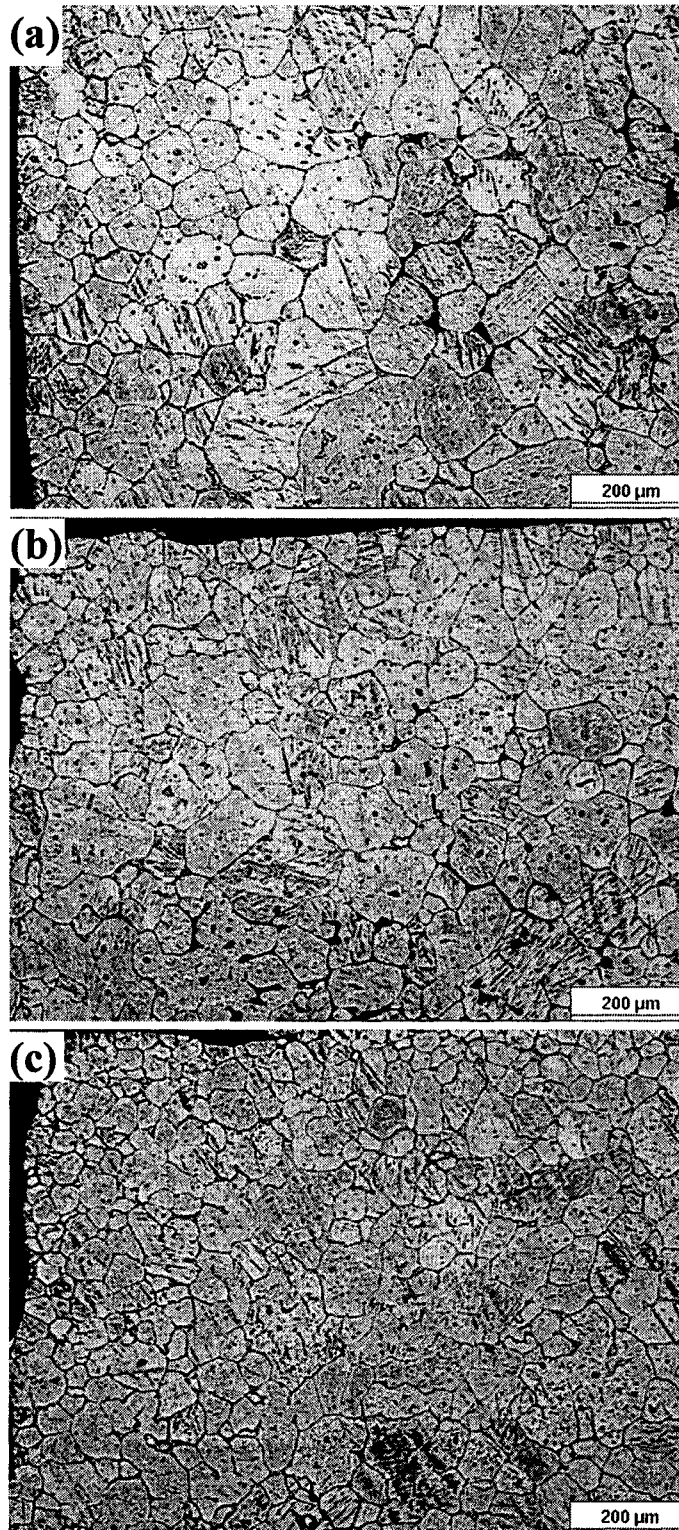


Fig. 6.13 Optical micrographs of the microstructures in the AC52 alloy after DSC run at heating rates ($^{\circ}\text{C}/\text{min}$) of: (a) 10, (b) 30 and (c) 50.

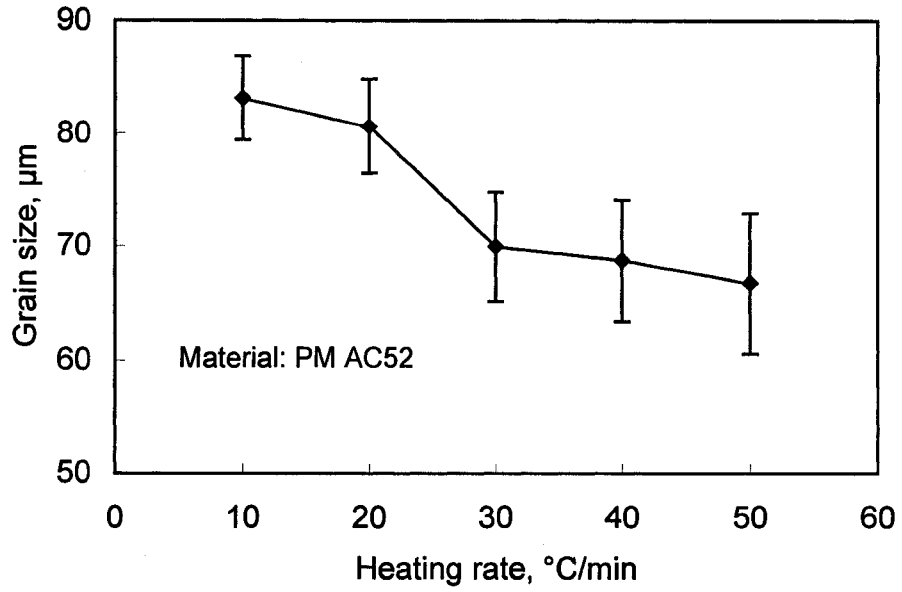


Fig. 6.14 Variation of grain size with heating rate for the AC52 alloy after DSC run.

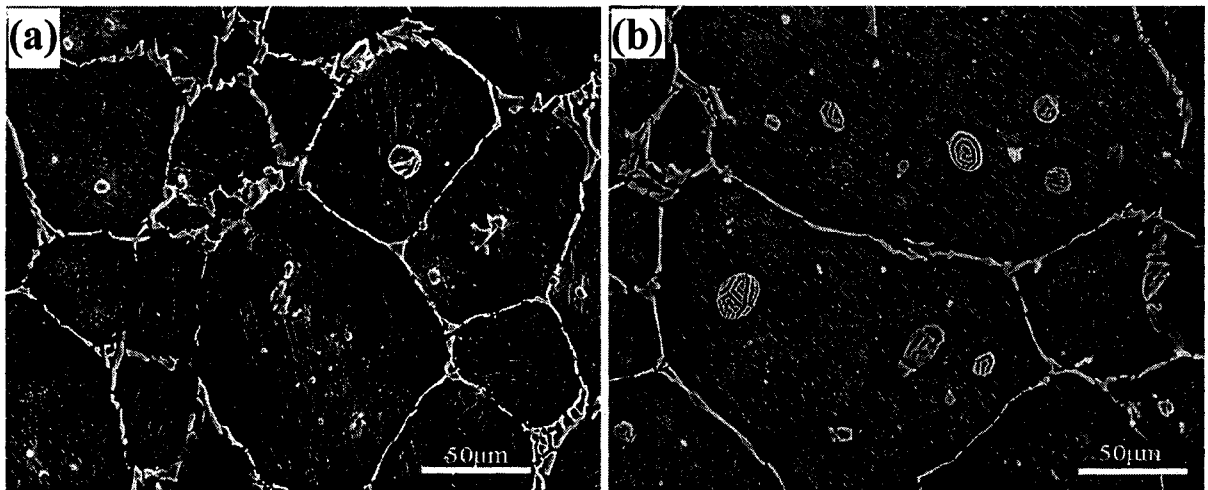


Fig. 6.15 SEM micrographs of the microstructures in the AC52 alloy after DSC run at heating rates ($^{\circ}\text{C}/\text{min}$) of: (a) 10 and (b) 40.

6.2.4 Effect of cooling rate after heating on microstructure of the PM AC52 alloy

The dependence of the microstructure of the AC52 alloy on the cooling rate after heating was also examined. The DSC tests were conducted at a heating rate of 30 °C/min to 580 °C, and were followed by the cooling rates varying from 5 to 30 °C/min. The measured cooling rate was around 50 °C/min for the specimen air quenched after heating. Representative low and high magnification SEM micrographs of the AC52 alloy processed at the different cooling rates are presented in Figs. 6.16 and 6.17.

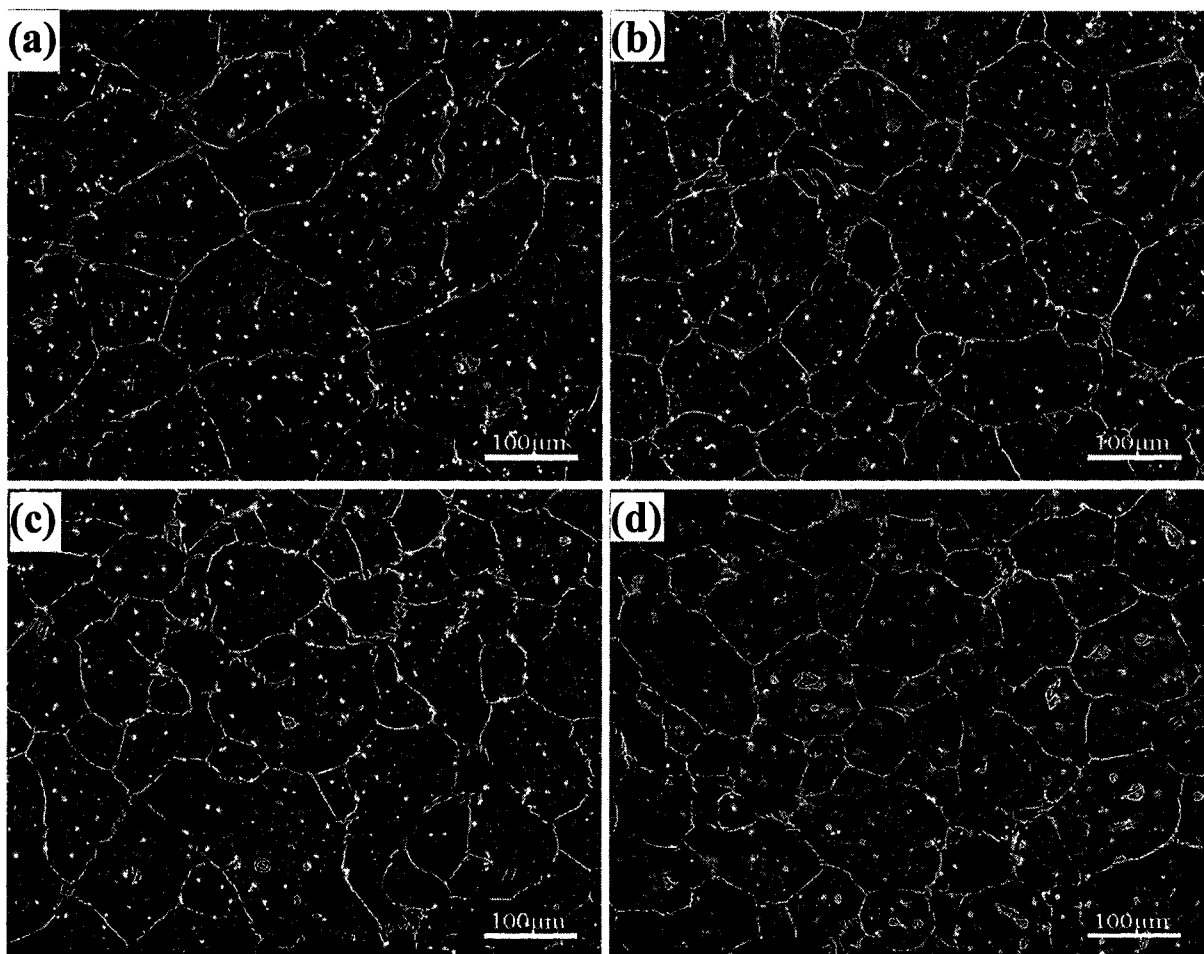


Fig. 6.16 Variation of the microstructure of the AC52 alloy with cooling rates (°C/min) of:

(a) 5, (b) 10, (c) 20 and (d) 30 after heating at 30 °C/min to 580 °C.

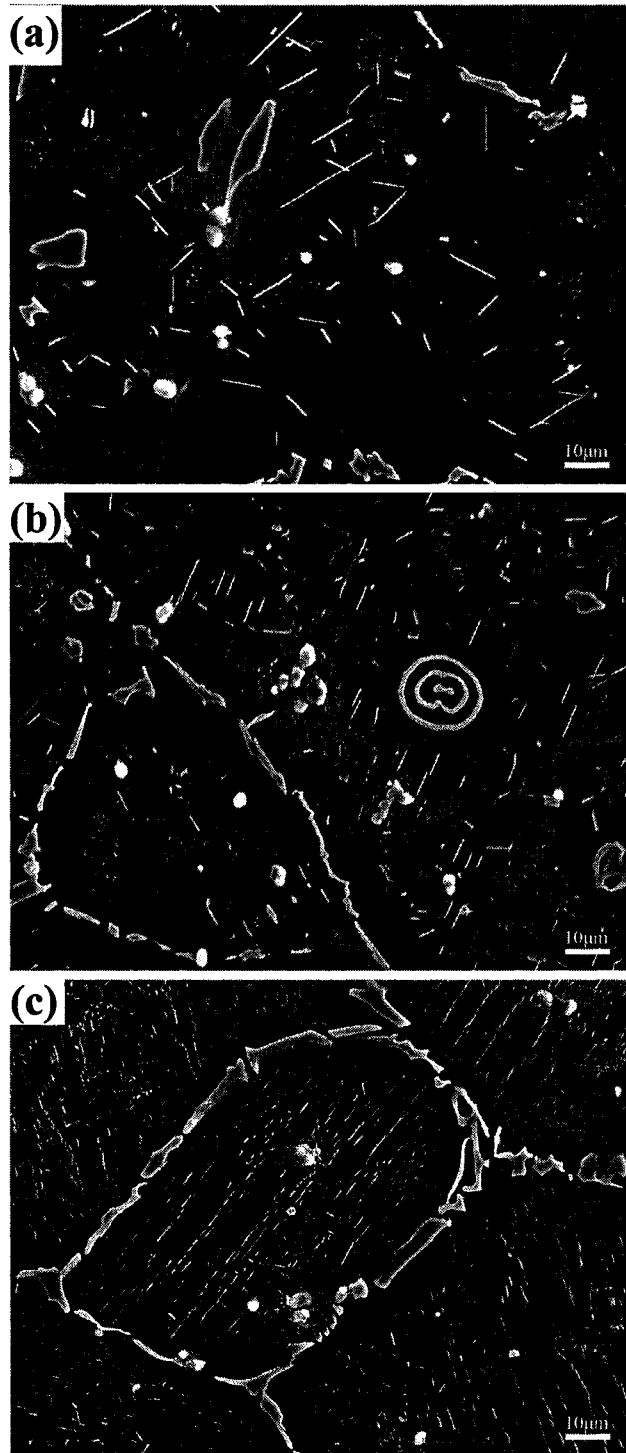


Fig. 6.17 High magnification micrographs of the AC52 alloy obtained at cooling rates of ($^{\circ}\text{C}/\text{min}$): (a) 5, (b) 20 and (c) 50 (air quenched) after heating at $30\text{ }^{\circ}\text{C}/\text{min}$ to $580\text{ }^{\circ}\text{C}$.

The primary microstructural constituents at both low and high cooling rates were coarse polygonal $(Al, Mg)_2Ca$ particles or plates at the grain boundaries and fine, needle-like $(Al, Mg)_2Ca$ rods within the primary α -Mg grains. The average grain size of the AC52 alloy processed at the different cooling rates after heating was significantly different. The effect of cooling rate after heating on the measured average grain size is shown in Fig. 6.18.

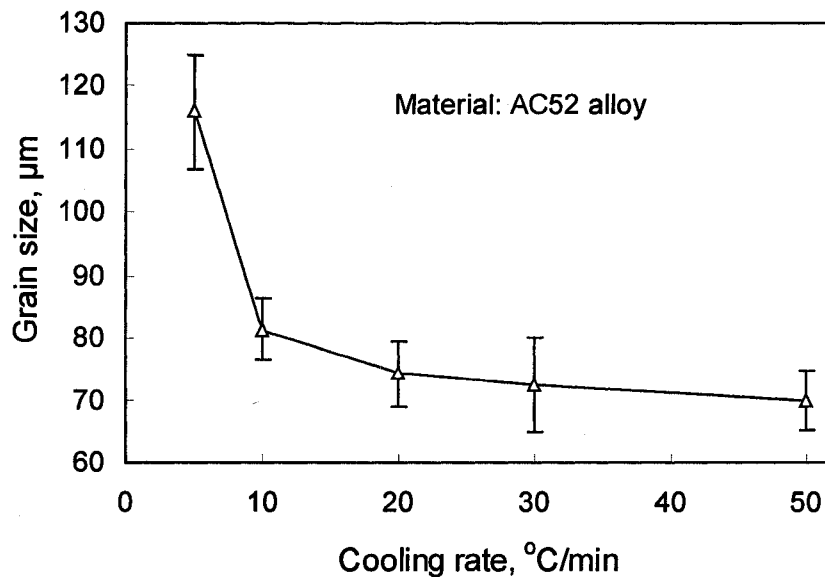


Fig. 6.18 Effect of cooling rate after heating on the grain size of the AC52 alloy.

It can be seen that the average grain size of the specimen after a DSC run at a cooling rate of 5 °C/min increased by about 45 μm compared to that of the specimen processed at a cooling rate of 30 °C/min. The coarse $(Al, Mg)_2Ca$ particles at the grain boundaries at a low cooling rate (5 °C/min) were mainly single, plate-like phases. As the cooling rate increased to 10 °C/min or higher, more coarse $(Al, Mg)_2Ca$ particles with a lamellar structure were present at the grain boundary triple-junctions so that the volume fraction of the eutectic phase at the grain boundaries significantly increases with increasing cooling rate. In addition, the

size of the fine needle-like $(\text{Al}, \text{Mg})_2\text{Ca}$ rods produced at low cooling rates was somewhat large. Some needle-like rods were larger than $10\ \mu\text{m}$. The longest was around $30\ \mu\text{m}$ (Fig. 6.17 (a)). At intermediate cooling rates, the size of the needle-like rods became less than $10\ \mu\text{m}$. With a further increase in cooling rate, there was an increased tendency towards formation of round $(\text{Al}, \text{Mg})_2\text{Ca}$ particles in the microstructure.

6.3 Calorimetric kinetics of as-cast Mg-Al and Mg-Al-Ca alloys

6.3.1 Peaks on DSC traces of as-cast Mg-Al alloy

At lower temperatures, peak A is the first peak developed on the DSC traces of the Mg-Al alloy (AM50), and covers a range of temperatures from 100 to $240\ ^\circ\text{C}$ with peak temperatures around $150\ ^\circ\text{C}$. The activation energy of peak A, calculated using a Kissinger-type isoconversion method, was about $83.8\ \text{kJ mol}^{-1}$, which is similar to the activation energy of grain boundary self-diffusion (about $90\ \text{kJ mol}^{-1}$) for Mg alloys [177]. Other authors [9,148] have obtained similar results for the activation energy of peak A in Mg alloys. Because peak A is an endothermic peak, it should be related to the dissolution of specific phases in the as-cast AM50. Thus, when the heating temperature was below 150°C , there must be a range of temperatures within which the specific phase precipitated in the matrix of as-cast AM50 as the heating temperature was increasing. Lower heating rates, such as 0.5 and $2\ \text{K/min}$ were used to find the exothermic peak that corresponds to the precipitation of the phase formed before 150°C . However, no exothermic signals were found at temperatures lower than 150°C . At the same time, heat flows measured within the initial stage of DSC run were not suitable for analysis and are generally discarded [178]. This is because although modern DSC instruments are reliable, and can achieve remarkably high accuracies in measurement of kinetic transformations, no instruments are perfect. When calorimetric tests

were carried out, especially at lower temperatures, some negative effects are often induced by the disturbances from outside of the measuring cell causing transients in heat flows within the zones where heat evolution from the sample and the reference are measured. The measurements for kinetic data became unstable, because an initial transient period appeared in the very first stage of DSC runs, during which the heating rate increases quickly from zero to the desired heating rate within a very short time. The variation of heat flow data depended on the mass of sample, the type of pan and initial equipment temperature. Although no exothermic signals were detected at lower temperatures, based on the phase diagrams for the Al-Mn system calculated by Liu et al [179], it can be seen that a precipitate, maybe a B2 ordered phase, is formed by a peritectoid reaction at 152 °C after the $Al_{11}Mn_4$ phase decomposes into the Al_8Mn_5 and Al_4Mn phases by a eutectoid reaction at 340 °C. However, both reactions have not been experimentally observed and were not reported by Liu et al. [179]. Also, the B2 ordered phase was not observed by SEM analysis in this study.

Peak B is the second endothermic peak, which is related to the dissolution of the $Mg_{17}Al_{12}$ phase. The amount of precipitated $Mg_{17}Al_{12}$ in the as-cast AM50 was relatively high compared with the other phases. The DSC signal of peak B is wide and smooth. Moreover, according to Bassani [148], the redistribution of Al in the matrix of Mg alloys during heating also contributes to the development of the DSC thermal signal for peak B. The activation energy calculated for peak B is $141.4 \text{ kJ mol}^{-1}$, which is slightly higher than self-diffusion activation energy, 136 kJ mol^{-1} , in Mg alloys [177]. This indicates that the dissolution process corresponding to peak B was not only a self-diffusion process. The sample used for DSC analysis was an AM50 alloy cast by the die casting process with 2 mm thickness. It is well known that one of the features of high-pressure die-casting is the so-

called skin effect. The use of metallic dies results in rapid cooling, producing a surface layer characterized by an extremely fine grain size, and the larger grains subsequently formed in the center of the as-cast AM50, as shown clearly in Fig. 4.1. EDS results before the DSC runs showed that the content of the main alloy elements, such as Al and Mn, in the skin zone are higher than those in the center zone. Also, the Al content in the eutectic Al-rich α -Mg phase is much higher than in primary α -Mg phase. Any local segregation and coring of the main alloying elements could be eliminated during heating, which gives rise to the higher activation energy for peak B.

Peak C is the third thermal signal detected at higher temperatures, and is an exothermic peak. Peak C is an abnormal thermal signal. No new phase or reactions were detected corresponding to peak C. It was thought in this study that peak C was related to the high temperature oxidation or burning. Typically, the eutectic phases near the surface of as-cast AM50 were attacked dramatically if there was no protective atmosphere during the solution heat treatment or the DSC run. The high-temperature oxidation is particularly rapid when eutectic melting occurs. The oxidation phenomenon was verified by observing the surface of as-cast AM50 samples after the DSC runs. Although grade 5 argon gas was selected as the protective atmosphere, the presence of significant oxidization residues in the form of black powder was observed on the surface of the samples after heating. A flow rate of 100 mL/min was used for the DSC tests. Obviously, a flow rate of 100 mL/min was not sufficient to avoid oxidization of the AM50 alloy at temperatures higher than the eutectic temperatures. To minimize oxidization, it should be considered in future experiments to use a higher grade argon gas as the protective gas, and/or employ intelligent control to automatically increase flow rates when heating temperatures go beyond the eutectic

temperature of Al-Mg phases during the DSC heating runs. Because of its association with the oxidization of the AM50 alloy, no calculations were made for the activation energy of this peak.

Al_8Mn_5 is another phase precipitated in the DC AM50 alloy. However, no thermal signal, which corresponded to its dissolution, was found on the DSC traces upon heating. This is because Al_8Mn_5 is a stable phase below 637 °C [180], and the range of heating temperatures was from 50 to 550 °C for all the DSC runs in this study. Theoretically, the thermal signal for the dissolution of Al_8Mn_5 phase appear if the final heating temperature was set to 620 °C. However, it is apparent that some overlap occurs between the thermal endothermic peak for Al_8Mn_5 phase and the thermal peak for the melting of the matrix of the as-cast AM50. Additionally, the amount of Al_8Mn_5 phase is low in the DC AM50 alloy, and it is difficult to extract a DSC signal for Al_8Mn_5 phase from the overlapped DSC signals.

6.3.2 Peaks on DSC traces of as-cast Mg-Al-Ca alloys

The DSC traces in Fig.6.3 show that two sharp endothermic peaks (P1 and P2) are present in the low Ca-containing alloys (AC505 and AC51), while only one endothermic peak (P2) is present in the high Ca-containing alloys (AC515 and AC52). Peak P1 (425 to 457 °C) corresponds to the peak B on the DSC trace of AM50 alloy, which is due to the dissolution of the eutectic $\beta\text{-Mg}_{17}\text{Al}_{12}$ phase. All the alloys showed an endothermic peak P2 (530 to 565 °C), which corresponds to the dissolution of the $(\text{Al}, \text{Mg})_2\text{Ca}$ eutectic phase. The Ca-containing phase has enhanced stability at higher temperatures, contributing to an increased creep resistance, while also suppressing the formation of the $\beta\text{-Mg}_{17}\text{Al}_{12}$ phase. Therefore, for Ca contents of 1.5 wt.% or higher, the $\beta\text{-Mg}_{17}\text{Al}_{12}$ phase was completely replaced by the Ca-containing phase, which results in the disappearance of the endothermic

peak for the dissolution of the β -Mg₁₇Al₁₂ phase. The marked difference between peak P1 and peak B is that peak P1 is sharp and narrow while peak B is smooth and wide. This may be related to the amount of eutectic phases including eutectic β -Mg₁₇Al₁₂ and Al-rich eutectic α -Mg phases present in the as-cast Mg alloys. The addition of Ca into the Mg-Al alloy results in a reduced volume fraction of the eutectic β -Mg₁₇Al₁₂ and Al-rich eutectic α -Mg phases in the microstructures of the Mg-Al-Ca alloys, so that segregation is significantly reduced. The redistribution of Al in the matrix of Mg alloys during heating plays a less important role in the development of the DSC thermal signal for peak P1. Thus, peak P1 becomes sharp and narrow.

The activation energy for peak P2 was calculated to be about 220.0 kJ mol⁻¹ for the AC52 alloy, which is significantly higher than self-diffusion activation energy 136 kJ mol⁻¹ in Mg alloys. It is postulated that the higher activation energy for peak P2 is related to two main reasons. On the one hand, it has been observed that the diffusion of elements, such as calcium in magnesium single crystals, depends strongly on their atomic diameters. Thus, the slow diffusion of precipitates into the matrix would occur as a result of the larger atomic size of calcium than that of magnesium. On the other hand, the higher value of activity energy for peak P2 may be associated with the existence of a certain amount of liquid β -Mg₁₇Al₁₂ phase present in the matrix of the AC52 alloy when the DSC tests were run at temperatures higher than peak temperature of peak P2. Although SEM and TEM results did not show any β -Mg₁₇Al₁₂ phase in the matrix of the AC52 alloy, some dispersed, nanoscale size β -Mg₁₇Al₁₂ phase with may be present in the AC52 alloy. Therefore, the liquid phase, which is caused by the melting of β -Mg₁₇Al₁₂ phase when heating temperature is above 437 °C, appears in the matrix of the AC52 alloy.

6.3.3 Microstructural evolution during homogenization

The microstructure of the AC52 alloy is modified by the preheat treatment used to bring the as-cast samples to the required homogenization temperature (580 °C). The DSC results (Fig.6.3) suggest that this temperature lies above the Ca-phase solvus. Therefore, in order to obtain complete dissolution of the precipitates formed during casting, a higher homogenization temperature is required when samples are heated (without holding at homogenization temperature) during homogenization.

Low heating rate results in the sufficient diffusion of Ca-containing precipitates into the matrix of the AC52 alloy during preheat treatment. The time to reach the solvus temperature of the Ca-containing phase at a heating rate of 10 °C/min is around 49 min, which is much higher than the 10 min measured at a heating rate of 50 °C/min. The scatter in data for grain size is large when the sample is heated at a higher heating rate of 50 °C/min, as a result of the highly inhomogeneous distributions of the alloying elements. However, as expected, low heating rates followed by air quenching do lead to a greater grain size (Fig.6.13). Also, as another result of the highly inhomogeneous distribution of alloying elements after preheat treatment, some globular (Al, Mg)₂Ca islands, with the shape of a Chinese Script or multiple rings, appear within the primary α -Mg grains during cooling.

6.3.4 Microstructural evolution on cooling

Non-isothermal precipitation can likely occur when the sample is cooled after homogenization. In this case, the slow cooling rates allow a long time for precipitation and coarsening, resulting in the formation of new particles with large size. The large particles may influence the evolution of microstructure in the intervening processing steps and degrade the mechanical properties.

The peaks observed on the DSC heat flow curves (Fig. 6.8) during cooling are strong exothermal reactions. These peaks have been associated with a precipitation reaction of the Ca-containing phase. The temperatures of these transformations decrease with increasing cooling rate as is common in thermally activated transformations. The microstructural results also confirm that the $(Al, Mg)_2Ca$ phase, which forms during cooling of the AC52 alloy after heating, invariably takes the form of either coarse lath-like precipitates along grain boundaries or fine needle-like rods of large aspect ratio (length:section diameter) extended uniaxially parallel to specific directions within the grains, i.e. $(Al, Mg)_2Ca$ precipitates in Mg alloys have facets and preferential orientations relative to matrix's crystallographic axes. Also, such particles may form preferentially in association with pre-existing dislocations or vacancy condensation loops, but it is common to observe particles that are not obviously associated with pre-existing defects. Thus, the epitaxial relationship between precipitates and matrix may be deduced from examination of SADPs. Additionally, as cooling rate decreases, the volume fraction of the precipitate at the grain boundaries decreases while the grain size increases. Also, the size of the needle-like precipitate significantly increases with decreasing cooling rates.

The morphology of the precipitates in Mg alloys may be related to some kinetic aspects: (i) bulk energetics of the Mg solid solution and precipitates, (ii) precipitate/matrix interfacial energies, and (iii) stress-free misfit and coherency strains energies of the precipitate/matrix system. The aspect ratio of precipitate is determined by the sum of elastic energy and interfacial energy anisotropy caused by a volume misfit. Also, anisotropic interface diffusion will control the precipitate shape. The plate-like precipitates and the faces of polyhedral particles could be formed by planes with isotropic interface diffusion.

However, interface diffusion anisotropy results in formation of rod-like precipitate. Its longest dimension is corresponding to the fastest diffusion direction. The various forms including needle-like and spherical shapes suggest that interface diffusion plays an important role in the morphology of the precipitates.

6.4 Summary

- (1). DSC curves for the DC AM50 show two endothermic peak A & B and one exothermic peak C at various heating rates from 10 to 50 °C/min. Peak A is possibly related to the dissolution of the B2 ordered phase, and peak B corresponds to the dissolution of the eutectic $Mg_{17}Al_{12}$ phase alloy during heating. Peak C is related to the rapid oxidation of the molten eutectic phases at higher temperatures.
- (2). The activation energy for peak A, calculated using a Kissinger-type isoconversion method, was 83.8 kJ mol^{-1} , which is similar to the grain boundary self-diffusion activity energy 90 kJ mol^{-1} . The activation energy for peak B is $141.4 \text{ kJ mol}^{-1}$, which is slightly higher than the self-diffusion activation energy 136 kJ mol^{-1} . The redistribution of the main alloying elements, such as Al and Mn, in the matrix of the DC AM50 during the DSC runs, may also contribute to higher activation energy for peak B.
- (3). A low amount of the Al_8Mn_5 phase, and overlap of the DSC signals upon the melting of AM50, are considered to be the reason for the difficulty in measuring the DSC signal from the Al_8Mn_5 phase.
- (4). DSC curves of the PM AC series alloys at a heating rate of 30 °C/min show that two endothermic peaks P1 (the dissolution of β - $Mg_{17}Al_{12}$) and P2 (the dissolution of (Al,

$(\text{Mg})_2\text{Ca}$) are present in the DSC curves of the AC505 and AC51 alloys while only one large and sharp peak P2 are observed in the DSC curves of the AC515 and AC52 alloys. This observation suggests that when the Ca content reaches 1.5 wt.% or higher, the $\beta\text{-Mg}_{17}\text{Al}_{12}$ phase was completely replaced by the $(\text{Al}, \text{Mg})_2\text{Ca}$ phase.

- (5). The activation energy calculated for peak P2 is $224.5 \text{ kJ mol}^{-1}$, which is significantly higher than self-diffusion activation energy of Mg alloys. The larger atomic size of calcium, and the dispersed, ultrafine $\beta\text{-Mg}_{17}\text{Al}_{12}$ phase may result in the higher activation energy for peak P2.
- (6). The heating/cooling rates during a DSC run play an important role in the redistribution of alloying elements and the dissolution or precipitation of the eutectic phases in the as-cast Mg alloys. The average Al content in the DC AM50 alloy increases with increasing heating rates, indicating that a low heating rates result in the progressive removal of coring effects that characterize the primary $\alpha\text{-Mg}$ in the die-cast microstructure. The peak temperature of these eutectic transformations decreases with increasing cooling rates and increases with increasing heating rate for both the DC AM50 and the PM AC52 alloy.
- (7). For the AC alloys with low Ca concentrations after heating and air quenching, discontinuous needle-like $\beta\text{-Mg}_{17}\text{Al}_{12}$ and $(\text{Al}, \text{Mg})_2\text{Ca}$ particles were distributed along the grain boundaries. As the Ca content is increased to 1.5 wt.% or higher, the eutectic phases gradually form a eutectic network in the microstructure of the alloys. In the case of the AC52 alloy, a large amount of fine $(\text{Al}, \text{Mg})_2\text{Ca}$ plates are present within the primary $\alpha\text{-Mg}$ grains, while coarse $(\text{Al}, \text{Mg})_2\text{Ca}$ plates are mainly distributed along the grain boundaries. Additionally, it is observed that these fine $(\text{Al},$

Mg_2Ca plates are parallel within individual $\alpha\text{-Mg}$ grains, which suggests that there are preferred crystallographic relationships between the fine $(\text{Al}, \text{Mg})_2\text{Ca}$ plates and the matrix of the alloy.

- (8). The grain size decreases with increasing heating rates for the AC52 alloys after DSC runs at various heating rates and air quenching. Three morphologies of the $(\text{Al}, \text{Mg})_2\text{Ca}$ phase were observed in the alloy, and these are controlled by redistribution of Ca through diffusion. Coarse $(\text{Al}, \text{Mg})_2\text{Ca}$ plates are often present at the grain boundaries while a large amount of fine needle-like $(\text{Al}, \text{Mg})_2\text{Ca}$ plates precipitate within the primary $\alpha\text{-Mg}$ grains. Additionally, more round $(\text{Al}, \text{Mg})_2\text{Ca}$ islands with the shape of Chinese Script also form within the primary $\alpha\text{-Mg}$ grains when the heating rate is higher.
- (9). The average grain size of the AC52 alloy at first significantly decreases, and then slowly decreases to a constant value as cooling rate increases, and more coarse $(\text{Al}, \text{Mg})_2\text{Ca}$ precipitates with a lamellar structure are present at grain boundaries so that the volume fraction of the eutectic phase significantly increases. In addition, the size of the fine needle-like $(\text{Al}, \text{Mg})_2\text{Ca}$ rods at low cooling rates is relatively large while there is an increased tendency towards formation of round $(\text{Al}, \text{Mg})_2\text{Ca}$ particles at higher cooling rates.

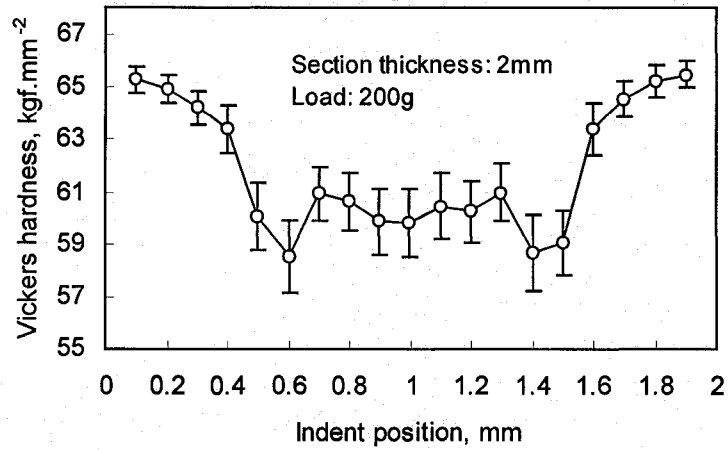
CHAPTER 7

RESULTS AND DISCUSSION OF MICRO-AND NANO-INDENTATION STUDIES

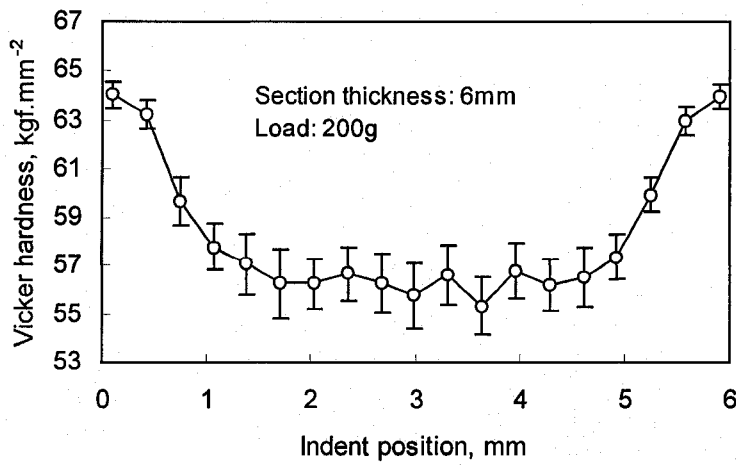
7.1 Measurement of hardness and modulus

7.1.1 Vickers microhardness of DC AM50 alloy

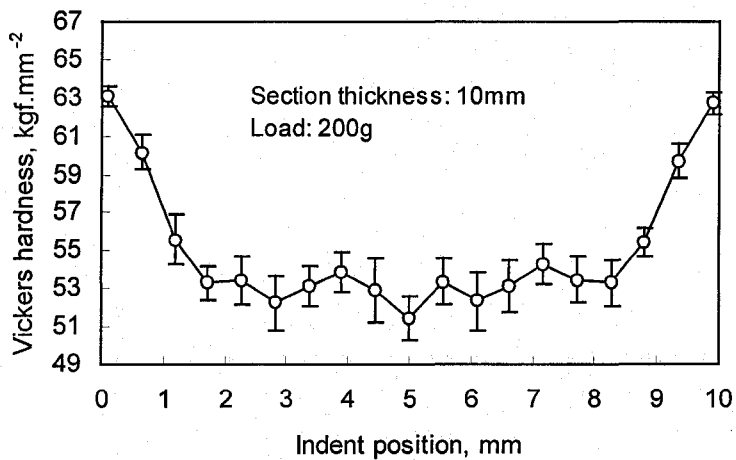
The microhardness measurements were made using a Vickers indenter with a 200g load to perform approximately 19 indents across the casting thickness of the polished DC AM50 alloy surfaces. Fig. 7.1 shows the hardness profile across the thickness of the three DC AM50 alloys tested in this study. It can be seen that the total hardness profiles of the three specimens consist of two distinct regions, i.e. the skin and central regions. A significant increase in the measured hardness near the casting edges of the three specimens in relation to neighbouring hardness results was observed, supporting the idea of a harder layer near the outer surface in high pressure die casting [76]. The hardness results (Fig. 7.1) indicate that the three specimens show a decrease in hardness of 8-16 % from the skin to the central region. However, some indentations, which result in relatively large hardness, are also present in the central area of the samples. There were a number of hardness values, either unusually low or high, in each hardness profile. For example, at approximately 0.6 mm in the specimen with section thickness 2 mm, an average Vickers hardness of 58.6 kgf.mm^{-2} was observed, which is a 10 % decrease from the highest recorded value (around 65 kgf.mm^{-2}). The microstructures around these indentations were examined using both optical microscopy and scanning electron microscope analysis [157]. The averaged Vickers hardness across the casting thickness was approximately 62 kgf.mm^{-2} for 2 mm specimen, 58 kgf.mm^{-2} for 6 mm specimen, and 55 kgf.mm^{-2} for 10 mm specimen, respectively. The relationship between hardness and section thickness is plotted in Fig. 7.2. These results, which are related to the microstructures of the specimens, are further discussed in Section 7.1.5.



(a)



(b)



(c)

Fig. 7.1 Hardness profiles across casting thickness for the DC AM50 alloy with the thicknesses of: (a) 2mm, (b) 6 mm, and (c) 10 mm.

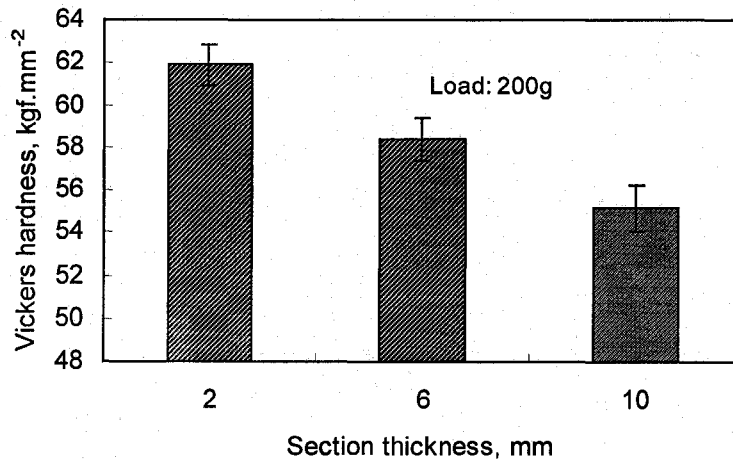
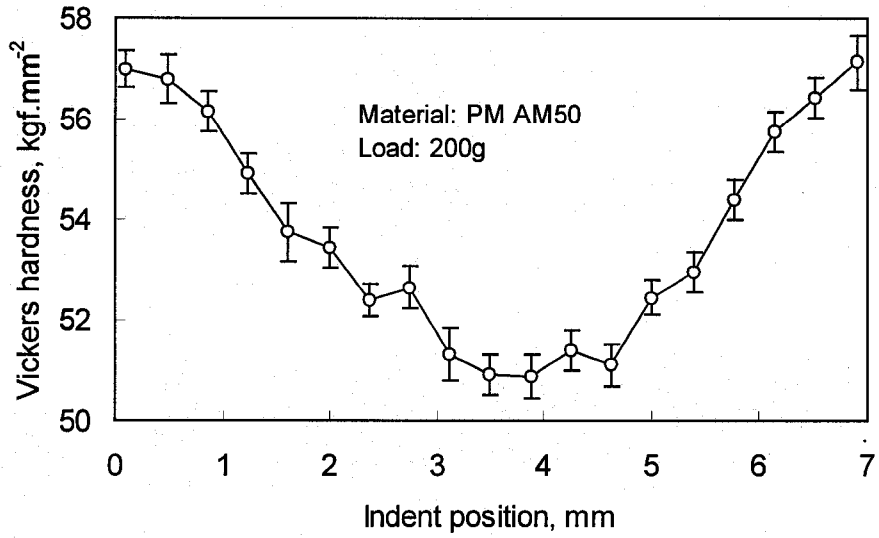


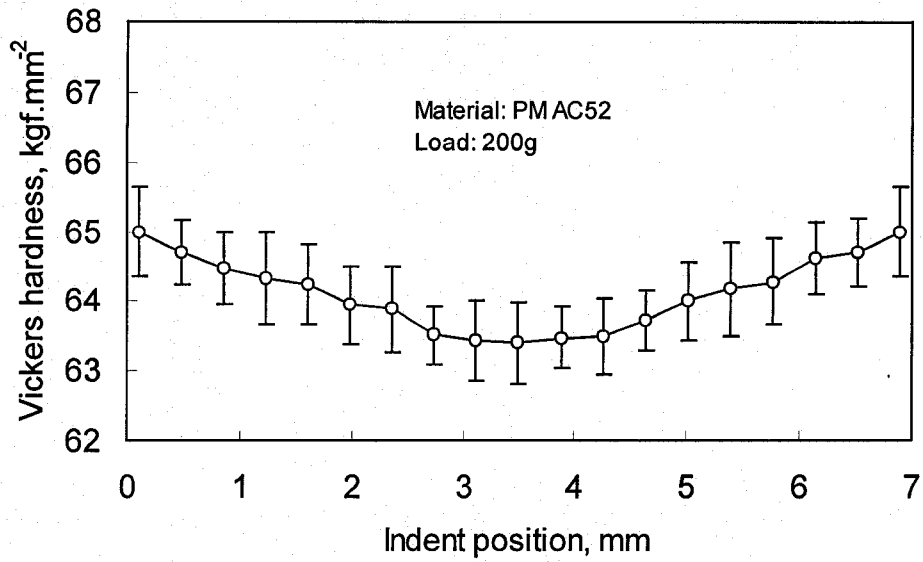
Fig. 7.2 Average measured hardness across the casting thickness for the three tested DC AM50 alloys with different section thicknesses.

7.1.2 Vickers microhardness of the PM Mg-Al and Mg-Al-Ca alloys

The hardness profile across the thickness of the casting for the PM AM50 and AC52 alloys is shown in Fig. 7.3. Similar to the hardness profiles for the DC AM50 alloys, the hardness profile of the PM AM50 alloy also exhibits the skin and central regions, and the narrow skin region is consistently harder than the central region, and the lines of best fit are curved upwards, i.e., the hardness values are higher close to the surface, as observed for the Mg-Al specimen in Fig. 7.3(a). An average Vickers hardness of 50.6 kgf.mm⁻² for the PM AM50 alloy was measured in the central region, which is 6.6 kgf.mm⁻² less than the hardness in the skin region. However, the difference in hardness between the skin and central regions was insignificant in the PM AC52 alloy in comparison to that in the PM AM50 alloy. The hardness in the skin region is only slightly higher than that in the central region, as shown in Fig. 7.3(b).



(a)



(b)

Fig. 7.3 Hardness profiles across the casting thickness of 7 mm for: (a) PM AM50 alloy and (b) PM AC52 alloy.

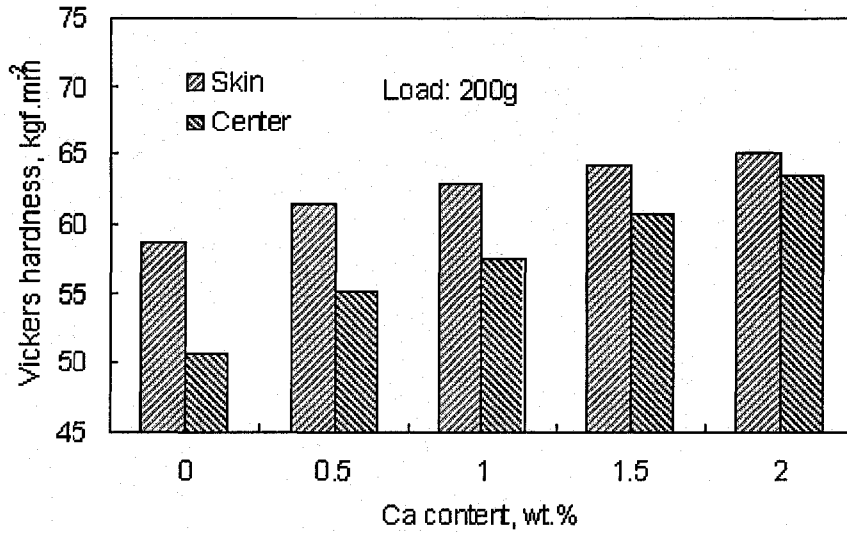


Fig. 7.4 Average measured hardness values in the skin and central regions for the five PM Mg-Al and Mg-Al-Ca alloys.

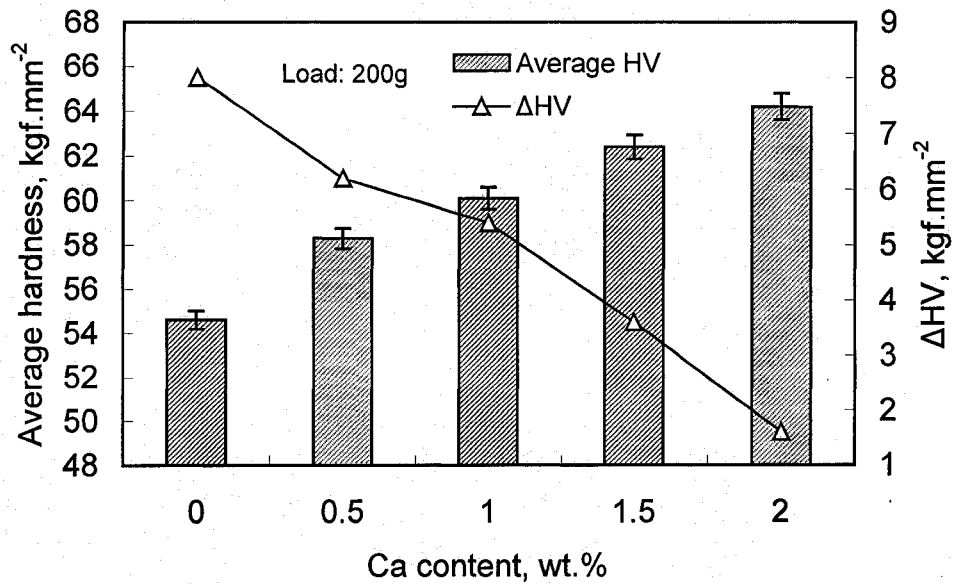


Fig. 7.5 Average hardness values across the casting thickness and the hardness difference between the skin and central regions for the five PM Mg-Al and Mg-Al-Ca alloys.

The average measured hardness values in the skin and central regions for the five PM Mg-Al and Mg-Al-Ca alloys are shown in Fig. 7.4, and the average hardness values across the casting thickness and the difference in hardness between the skin and central regions for the five PM Mg-Al and Mg-Al-Ca alloys are shown in Fig. 7.5, respectively. In all five alloys, the skin region is consistently harder than the central region. It is also found that the difference in hardness between the skin and central regions decreases with increasing Ca content in Mg-Al alloy. Additionally, the average hardness across the casting thickness increases with increase in Ca content, indicating the hardening effect of the Ca addition. Compared to the average hardness of the PM AM50 (54.6 kgf.mm^{-2}), the average hardness of the PM AC52 alloy increased by 9.6 kgf.mm^{-2} .

7.1.3 Nanohardness and composite modulus

The Ubi[®]1 Nanomechanical Test Instrument employed in this study is equipped with a Scanning Probe Microscope (SPM), in which a sharp probe tip is moved in a raster scan pattern across a sample surface using a three-axis piezo positioner. The Berkovich indenter tip was calibrated with fused silica using the approach outlined by Oliver and Pharr [75]. Tip-shape calibration is based on determining the area function of the indenter tip, which is based on the assumption that Young's modulus of elasticity is constant and is independent of indentation depth. Fused quartz with Young's modulus of 72 GPa is used as a standard sample for calibration purpose, and an area function relating the projected contact area, A , to the penetration depth, h_p , is obtained. The projected contact area functions, A , with and without tip shape corrections are shown in Fig. 7.6.

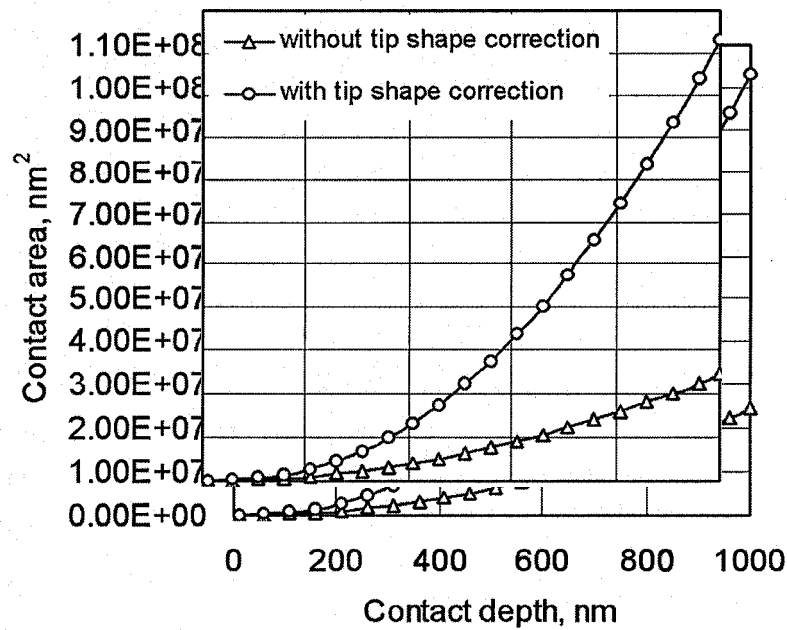
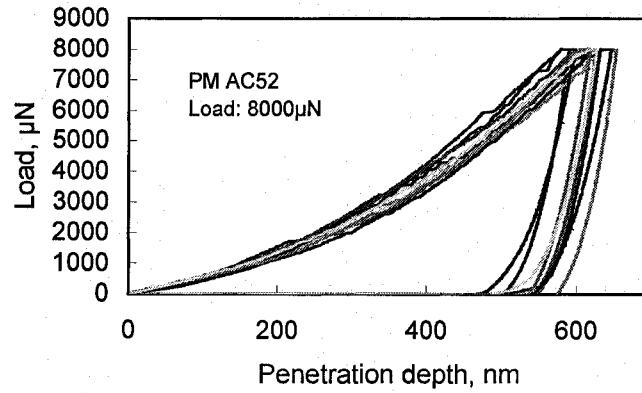
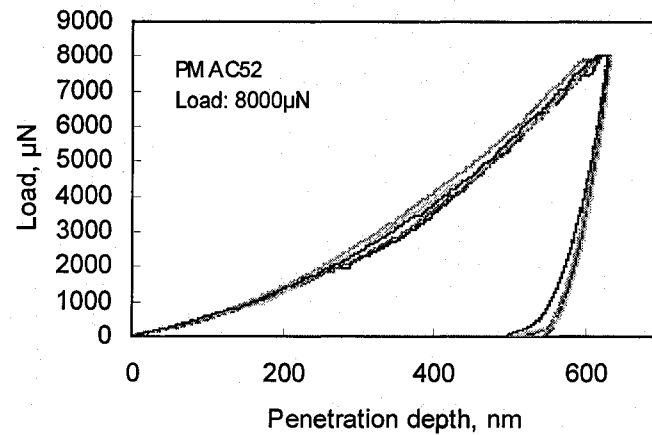


Fig. 7.6 Projected contact area functions, A , with and without tip shape corrections.

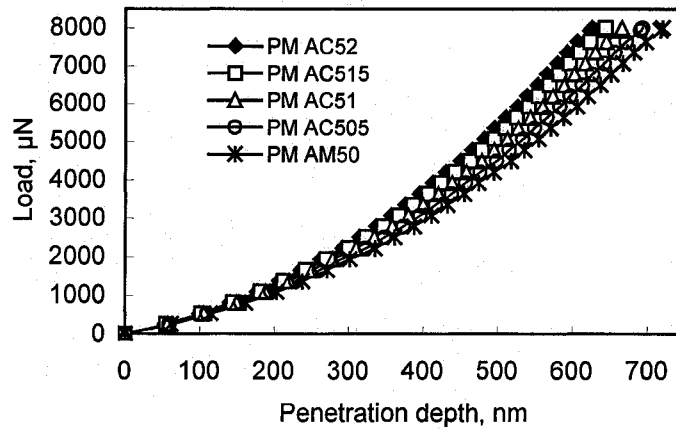
Fig. 7.7(a) shows typical load-unload curves obtained at ten random individual locations within the primary α -Mg grains of the PM AC52 alloys using a Berkovich indenter with a maximum load of 8 mN. These curves present the variation of the local mechanical properties with individual indent locations within the α -Mg grains, which is related to solid solution strengthening or/and precipitation strengthening occurring during solidification. Fig. 7.7(b) shows five homologous load-unload curves of the as-cast AC52 alloy. To truly represent the local mechanical deformation behavior (hardness behaviour) within the α -Mg grains of the alloys, it was necessary to choose only those curves that have homologous characteristics so that microdefects, such as porosity and microcracks, and/ or the segregation have the smallest effect on the deformation behaviour. The variations of the average measured nanohardness and composite modulus with Ca content in Mg-Al base alloys are plotted in Fig. 7.8.



(a)

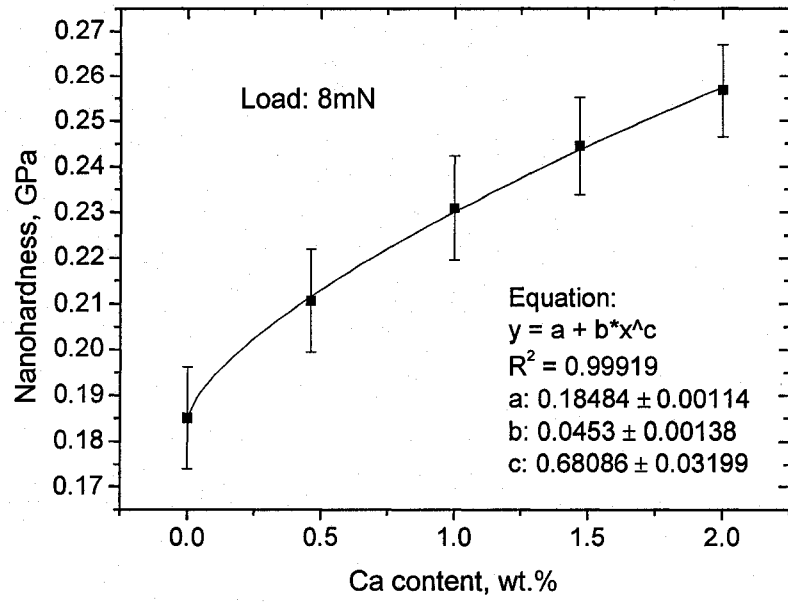


(b)

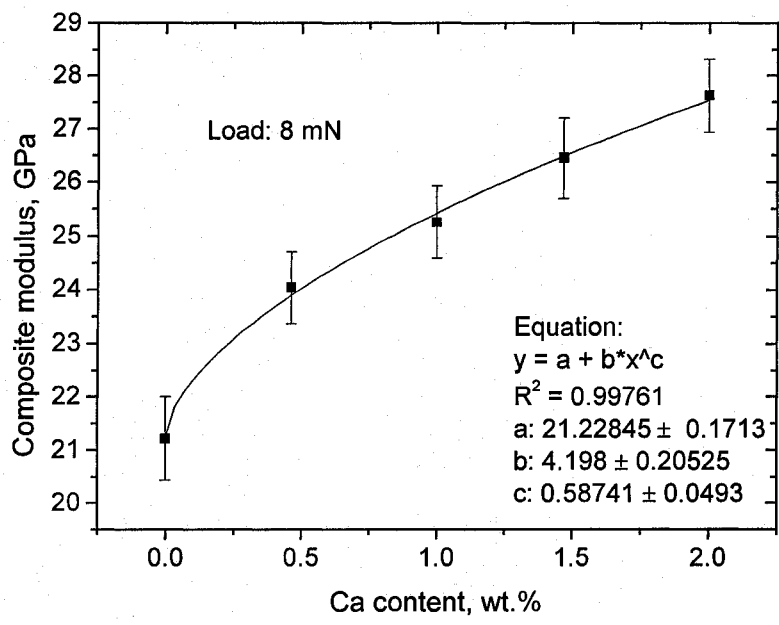


(c)

Fig. 7.7 Typical load-unload curves for the indentation within the primary α -Mg grains for the as-cast Mg alloys using a Berkovich indenter with a maximum load of 8 mN: (a) ten individual locations on AC52 alloy, (b) five homologous load-unload curves, and (c) averaged load curves for these five Mg alloys.



(a)



(b)

Fig. 7.8 Variations of: (a) nanohardness and (b) composite modulus with Ca content in Mg-Al base alloy.

The results for hardness in Fig. 7.8(a) are for the primary α -Mg. Also, the elastic modulus was extracted from the unloading segment of the same set of load-displacement curves as the hardness (see Fig. 7.7). The results are given in terms of the so-called 'composite' modulus, which is a direct result of the Oliver-Pharr method [75]. The composite modulus is slightly lower than the true modulus of the specimen under consideration, since the low compliance (high stiffness) of the diamond tip adds, to a moderate extent, to the total compliance of the whole mechanical contact. It can be seen in Fig. 7.8 that both hardness and composite modulus significantly increase with increasing Ca content in the Mg-Al base alloys. The curves of best fit in Fig. 7.8 can be described by Eq. $y = a + b \cdot x^c$ (where y is composite modulus, x is Ca content, and a , b and c are constants.), and good correlation coefficients of 0.999 and 0.998 are obtained for hardness data and composite modulus data, respectively.

7.1.4 Continuous hardness and composite modulus

7.1.4.1 Experimental and calculated results

Each curve in Fig. 7.9 gives an averaged value of a number of homologous load-unload curves chosen from the ten individual curves for each alloy. Fig. 7.10 presents contact stiffness vs. penetration depth curves for all four alloys at room temperature. All plots exhibit a linear relationship between contact stiffness and penetration depth.

Fig. 7.11 shows experimental and calculated hardness values versus penetration depth curves for the as-cast Mg alloys at room temperature. The details to calculate hardness value are discussed in Section 7.1.4.2. Both of the experimental and calculated hardness vs. penetration depth curves consist of two segments. The initial segment, for which the penetration depth is very small, mainly involves elastic deformation. During this initial segment, the hardness increases rapidly and reaches a peak value of around 1.2 GPa. As the

indenter further penetrates into the α -grains, the contact area between the indenter and the as-cast Mg alloys increases. Since the hardness is inversely proportional to the contact area, the hardness values drop rapidly from the peak value to about 0.3 GPa as the penetration depth increases from 50 to 300 nm. As the penetration depth further increases to 400 nm and beyond, the hardness gradually decreases, and tends to reach a steady value of around 0.2 GPa. This observation can, in part, be attributed to the fact that, once the penetration reaches a certain depth, any further increase in penetration depth has a limited influence on the contact area.

Fig.7.12 shows the relationship between the experimental and calculated composite modulus values and the penetration depth for all four alloys at room temperature. The composite modulus values were calculated based on Eq. (2-2). After the indenter contacts the surface of the as-cast Mg samples, the composite modulus quickly reaches a peak value of around 40 GPa. As the indenter further penetrates the samples, the composite modulus values slightly decrease, and finally tend to be a constant value of around 25 GPa.

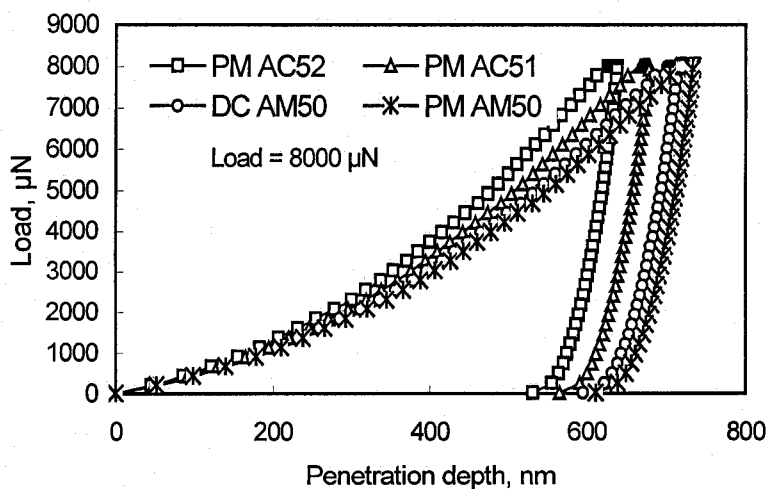


Fig. 7.9 Typical averaged load-unload curves for the indentation within the primary α -Mg grains for the as-cast Mg alloys using a Berkovich indenter with a maximum load of 8 mN.

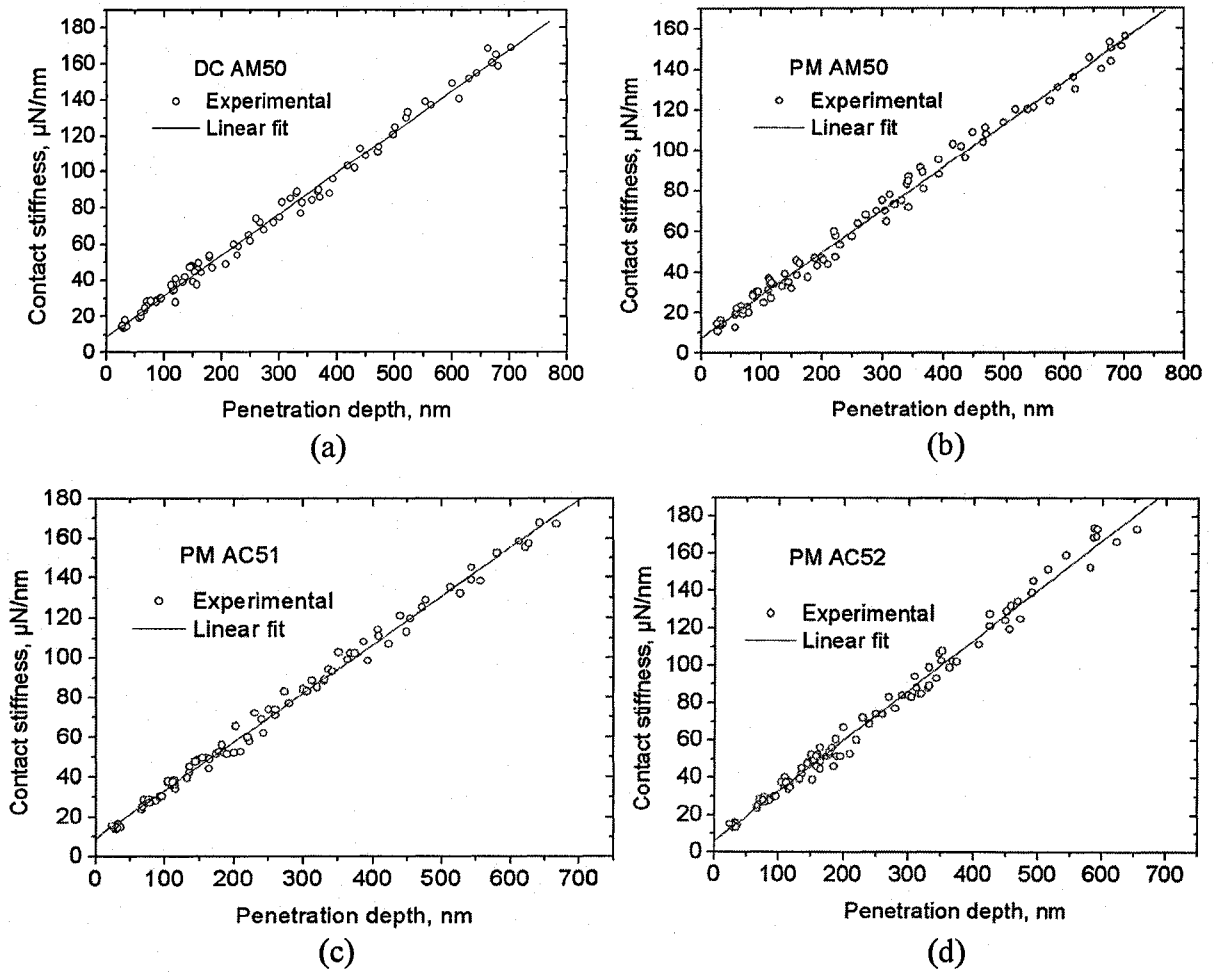


Fig. 7.10 Contact stiffness vs. penetration depth curves for the as-cast Mg alloys at room temperature. The open circles represent the experimental contact stiffness. The straight line is a linear fit to the experimental data.

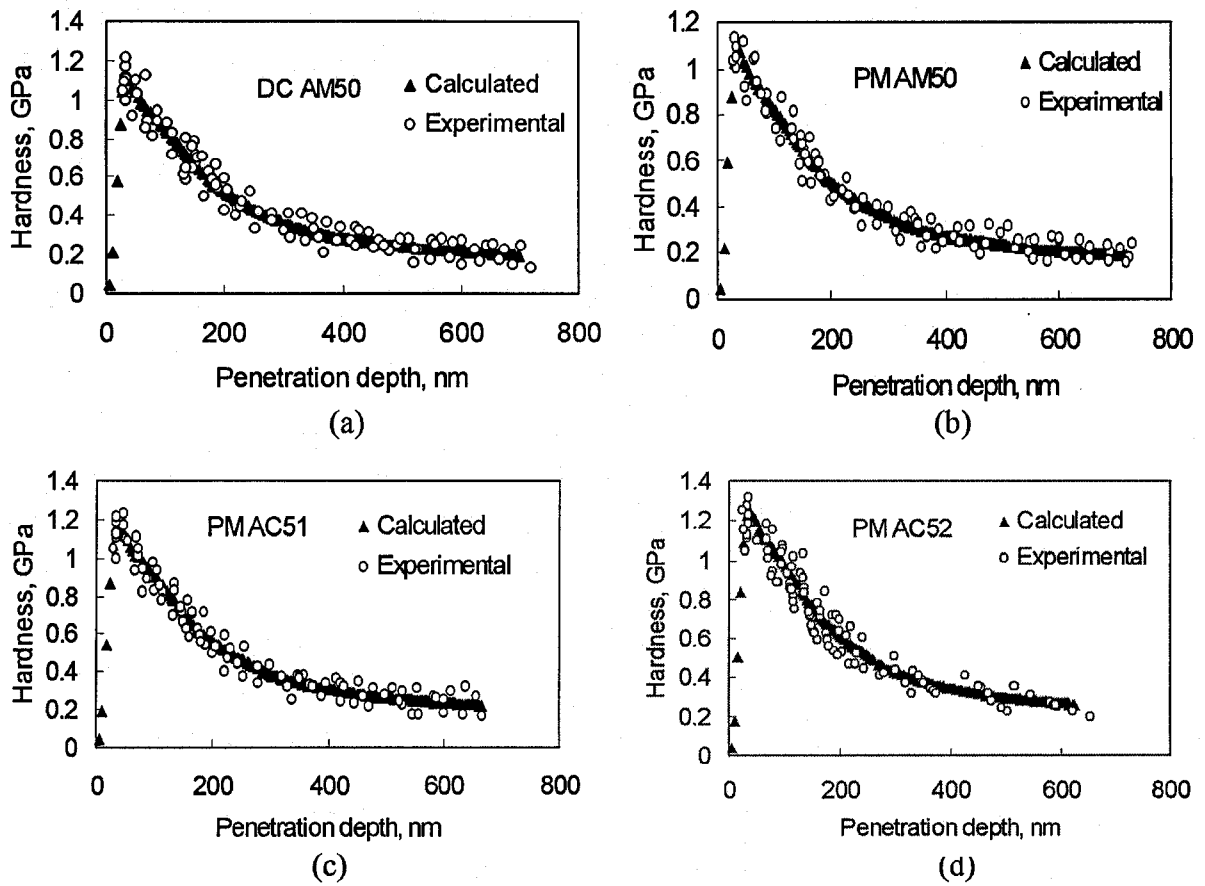


Fig. 7.11 Experimental and calculated hardness values vs. penetration depth curves for as-cast Mg alloys at room temperature. The open circles represent the experimental hardness values measured at the different loads. The solid triangles represent the calculated hardness values.

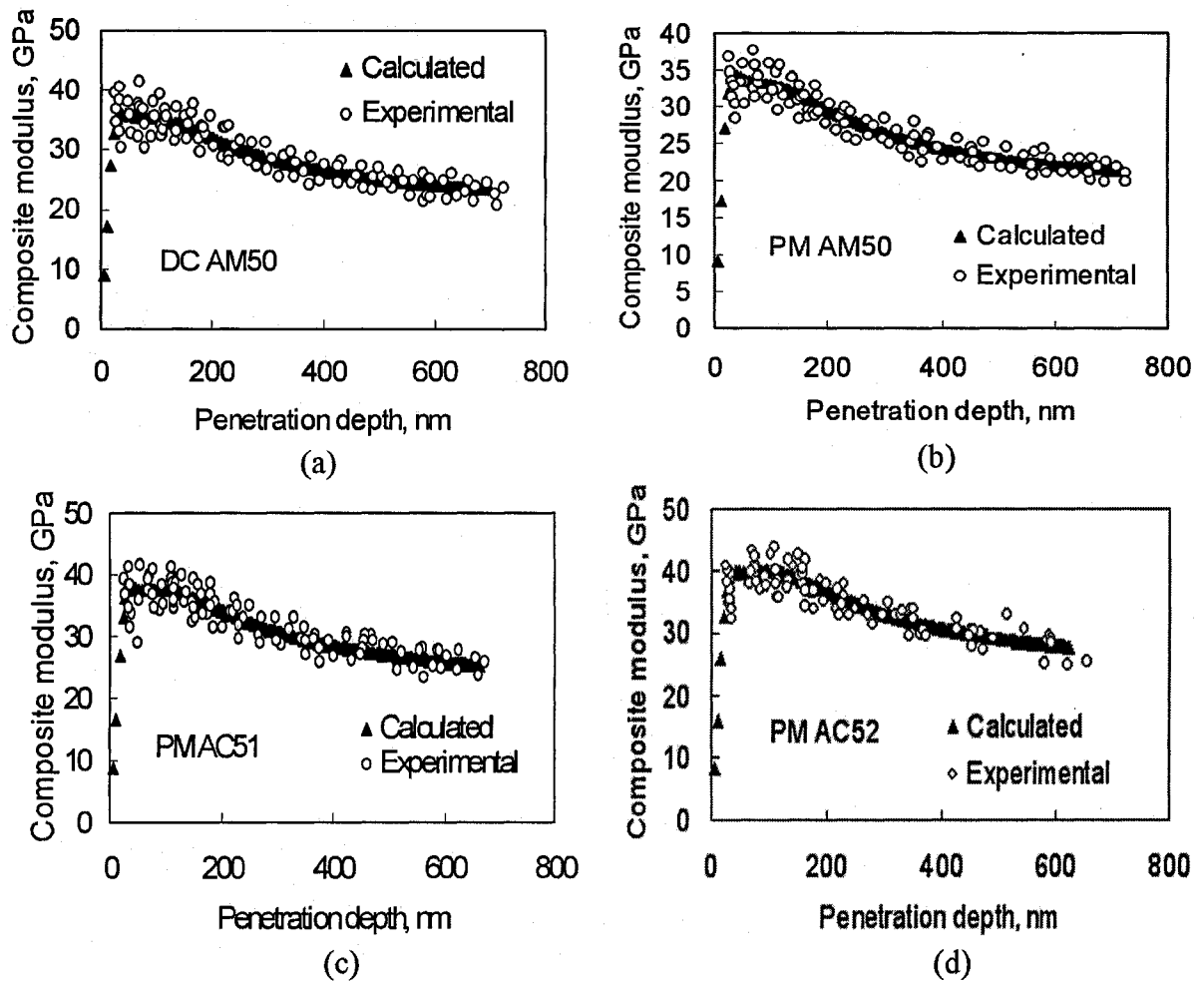


Fig.7.12 Experimental and calculated composite modulus values vs. penetration depth for as-cast Mg alloys at room temperature. The open circles represent the experimental composite modulus values measured at the different loads. The solid triangles represent the calculated composite modulus values.

7.1.4.2 Correlation analysis

A regression analysis of the experimental indentation data shows that the stiffness of the as-cast Mg alloys has a linear relationship with penetration depth as exhibited by the good linear fit to the $S-h$ data, as shown in Fig. 7.10.

$$S = ah_t + b \quad (7-1)$$

where S is the contact stiffness, a and b are the constants, and h_t is the maximum penetration depth. The regression coefficients (R^2) and the constants (a and b) of the $S-h$ lines for the as-cast Mg alloys are listed in Table 7.1. Malzbender et al [181] have derived a similar analytical expression for the indentation load-depth relationship during loading in an indentation test, in which there is a linear relationship between the contact stiffness and penetration depth. It is demonstrated that the derived expression was in excellent agreement with the results from finite element simulation.

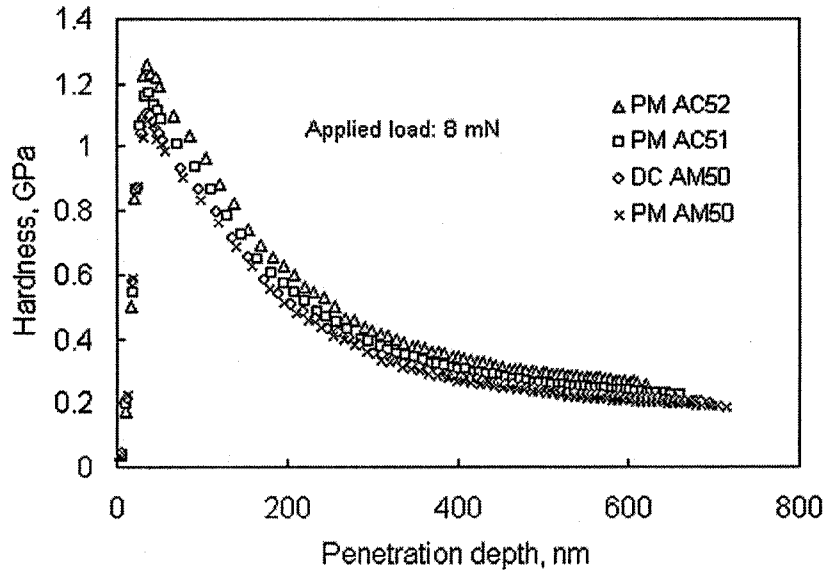
Table 7.1 Regression coefficient (R^2) and the constants (a and b) of the $S-h$ lines for the as-cast Mg alloys.

Alloy	a	b	R^2
DC AM50	0.227	8.7296	0.9929
PM AM50	0.2096	7.5881	0.9908
PM AC51	0.2433	8.9517	0.9938
PM AC52	0.2679	6.1334	0.9905

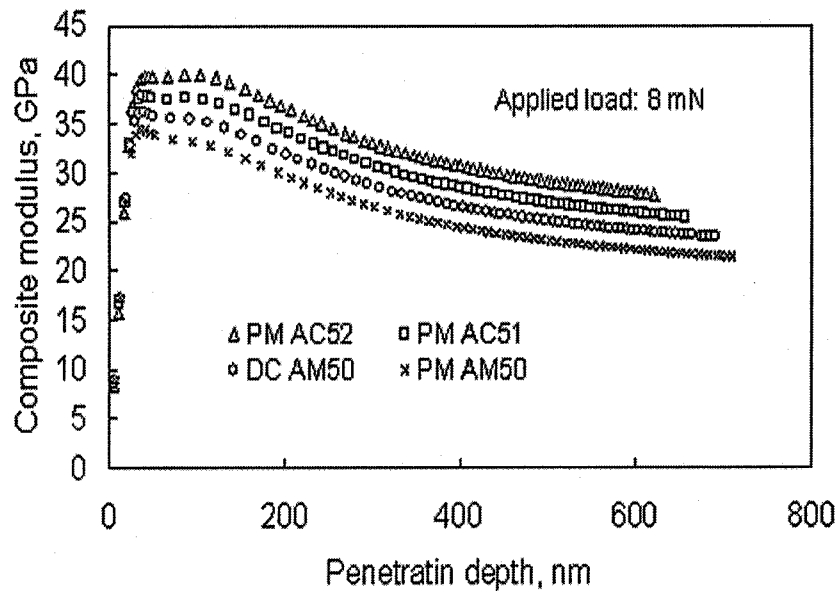
To accurately calculate the contact stiffness, hardness and composite modulus, the effects of the material parameters (microstructure, microdefects, segregation of elements) and the nanoindentation system parameters (thermal drift, initial penetration depth, instrument compliance and indenter geometry) on the nanoindentation test data should be considered. Therefore, representative load curves that exhibit homologous load-unload behavior should

be selected from the indentation data to determine the real local deformation behavior of the four alloys (Fig. 7.7). At a certain time step (i) during the indentation test, the contact stiffness value of $(S)_i$ can be obtained using Eq. (7-1), and the value of $(h_t)_i$ can be obtained from the averaged load curve (Fig. 7.7). Then, the $(h_p)_i$ values can be calculated from Eq.(2-16) using known $(h_t)_i$ and $(P)_i$ values. Finally, the hardness $(H)_i$ and composite modulus $(E^*)_i$ can be calculated using Eqs. (2-1) and (2-2). The calculated and experimental values of hardness or composite modulus have been plotted against the penetration depth in Fig 7.13. It can be seen from Fig.7.13 that the hardness is very sensitive to the penetration depth in the initial segment, since hardness values exhibit peak load dependence, i.e. an indentation size effect (ISE), for all the tested alloys.

Therefore, the hardness value is strongly dependent on the penetration depth of the indentation at the nanoscale level. The mechanisms of ISE are very complex. It may be caused not only by an oxide film of substantially different mechanical properties than the bulk material [182], but also by the presence of residual stresses and the strain-hardening arising from the specimen preparation and polishing procedure [183]. The presence of friction between the indenter and specimen could also lead to an indentation size effect [184]. Also, it can be seen that there is very good agreement between the experimentally measured hardness and the calculated hardness. However, the composite modulus values are not significantly affected by the penetration depth as long as the shape of the indenter is well characterized by the area function. The values of composite modulus at the maximum load showed a lower inelastic response with the penetration depth, being only about 25% lower than the highest value. Also, the agreement between the experimental composite modulus and the calculated composite modulus is good.



(a)



(b)

Fig. 7.13 Calculated indentation hardness and composite modulus for the as-cast Mg alloys with a load of 8 mN: (a) hardness vs. penetration depth, and (b) composite modulus vs. penetration depth.

Thus, in order to determine the continuous hardness and composite modulus values using an indentation system without a CSM capability, it is essential to develop the relationship between the contact stiffness and penetration depth during the indentation testing. Once the relationship between the contact stiffness and penetration depth is linear, the linear equation can be conveniently determined by two stiffness values experimentally obtained at a low load and at a high load. Dynamic hardness and composite modulus values can then be determined by the regression analysis procedure as described in this Section.

7.1.5 Hardness behavior of as-cast Mg-Al and Mg-Al-Ca alloys

Optical and SPM images of the residual indent impression left by a typical Berkovich indenter and a Vickers indenter are shown in Fig. 7.14.

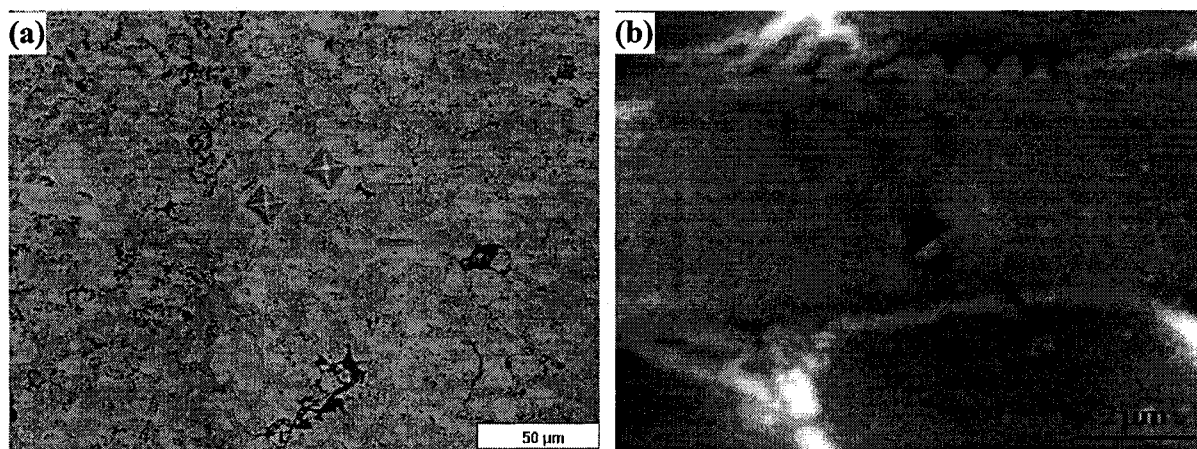


Fig. 7.14 (a) Optical image of residual indent left by micro Vickers indenter and (b) SPM image of residual indent left by nano Berkovich indenter on the polished surface of the as-cast Mg-Al and Mg-Al-Ca alloys.

The indentation results showed that hardness values vary with testing locations (Fig. 7.1). The regions surrounding these indentations were carefully analyzed by Zhou using both optical and scanning electron microscopy [157]. Three sources, which affect the scatter of the hardness data, could be easily identified: microporosity, the primary α -Mg and eutectic phases including the Al-rich eutectic α -Mg and $Mg_{17}Al_{12}$. Optical microscopy revealed that the locus of the lower Vickers hardness values correlates with contact primarily with distinctive pore bands or larger primary α -Mg grains, while the higher Vickers hardness values are related to the contact primarily with the eutectic grain boundary region. The β -phase intermetallic is reported to be approximately 1.33 times harder than the α -Mg grains [185].

Clusters of small or large pores with different porosity patterns were observed towards the center of the DC AM50 alloys, although the porosity was not distributed symmetrically [157]. It was found that distinctive bands of concentrated porosity were present beneath the surface of the 2mm thick specimen. A similar pattern was observed in the 6 and 10 mm specimens, but the concentrated bands were somewhat more diffuse and had no clearly delineated boundaries. This explained the reason for a 10 % decrease in hardness from the highest recorded value (around 65 kgf.mm^{-2}) at approximately 0.6 mm beneath the surface of the 2 mm thick specimen happens. Although 2, 6 and 10 mm specimens were produced in the same batch with the same die-casting machine, the porosity patterns are slightly different. On the other hand, isolated pores throughout the rest of the specimens could not be pinpointed. Hence, some intrinsic uncertainty is present in the hardness profiles due to microporosity.

A more detailed view of the microstructures present in the DC AM50 alloys has been presented in Fig. 4.2. The intermetallic network is very fine close to the outer surface (skin region), and large primary α -grains appear within the central region. In the thinner castings, the finer intermetallic structure covered a relatively larger proportion of the cross-section, particularly near the narrow skin regions. In some regions of the castings, localized segregation of the $Mg_{17}Al_{12}$ intermetallic phase was observed. Indentations on these segregated regions are responsible for the occasional high hardness values. Additionally, the aluminum content was found to be higher in the skin of the casting in all the tested DC AM50 specimens. The increased presence of eutectics around small grains indicated a high aluminum content. The increase in measured hardness in the skin region of the casting can, in part, be attributed to the increased aluminum content in those regions.

Figs. 4.2 and 5.1 are the typical SEM micrographs of the AM50 alloy cast by die casting and permanent mold casting, respectively. The microstructure of the PM AM50 alloy was significantly coarser than that of the DC AM50 alloy, likely because of the different solidification rates present in the two processes. The very fine α -Mg grains were surrounded by eutectic phases precipitated along the grain boundaries in the DC AM50 alloys, which results in a higher hardness. With the addition of Ca to the Mg-Al alloy, a typical dendritic microstructure was observed in the PM AC51 and AC52 alloys, as shown in Figs. 5.6(b) and (d), respectively. Also, compared to the two as-cast AM50 alloys, there were larger amounts of the $(Al, Mg)_2Ca$ interdendritic phase formed along the grain boundaries by the eutectic reaction in the PM AC51 and AC52 alloys. It has also been shown in Section 6.1.2 that the $(Al, Mg)_2Ca$ phases are precipitated at temperatures over 100 K higher than for the β - $Mg_{17}Al_{12}$ phase, thus contributing to improved creep properties. The $(Al, Mg)_2Ca$ phases also

suppress the formation of the β - $Mg_{17}Al_{12}$ phase. Continuous network eutectic phases were formed along the grain boundaries, together with some Al_8Mn_5 particles (bright contrast), in the PM AC52 alloy. However, due to the relatively lower amount of Ca (1%), discontinuous divorced eutectic phases were formed in the matrix of the PM AC51 alloy. Also, some β - $Mg_{17}Al_{12}$ phase was observed. Moreover, it was difficult to distinguish the $(Al, Mg)_2Ca$ phase from the β - $Mg_{17}Al_{12}$ phase in SEM micrographs due to their similar contrast. The volume fraction of the secondary phases in the PM AC52 alloy was significantly higher than in the PM AC51 alloy.

In metallic microstructures, the size and shape of the grains can be important in determining structural performance and functional applications. With their excellent castability, the common magnesium-aluminum alloys can be cast by a wide variety of methods, such as die casting and permanent mold casting. These casting methods involve a wide range of cooling rates, especially die casting. Normally, Mg castings cast by die casting experience higher cooling rates than those cast by permanent mold casting. In high pressure die casting, the steel dies used for casting magnesium alloys cool rapidly when the back of the dies are water cooled and heat is transported rapidly from the casting through the metal-mold interface during rapid injection. Thus, a fine grain structure is formed in the skin region of the Mg casting and coarse grains are formed in the central region [186]. The microstructure of as-cast AM50 alloys with a moderate aluminum content shows the presence of large volume fractions of the β - $Mg_{17}Al_{12}$ phase as intergranular particles along the grain boundaries, as shown in Figs. 4.2 and 5.1. The β - $Mg_{17}Al_{12}$ phase was not observed within the α -Mg grains for the as-cast AM50 alloys. The β - $Mg_{17}Al_{12}$ phase has a low melting temperature, which means that it is a relatively soft phase and is thermally unstable. Due to

the difference in cooling rates, the β -Mg₁₇Al₁₂ phase observed in the PM AM50 alloy is significantly coarser than that in the DC AM50. Another significant difference in the microstructure of the as-cast AM50 alloys is that a continuous network of the Al-rich regions was observed in DC AM50, while a discontinuous distribution of Al-rich regions was found in PM AM50 alloy. With the addition of Ca to the Mg-Al alloys, the (Al, Mg)₂Ca interdendritic phases then form along the grain boundaries by a eutectic reaction in the AC51 and AC52 alloys, as shown in Figs. 5.6(b) and (d). The (Al, Mg)₂Ca phase suppressed the formation of the β -Mg₁₇Al₁₂ phase. Therefore, the β -Mg₁₇Al₁₂ phase was not observed in PM AC52 alloy. However, a small amount of the β -Mg₁₇Al₁₂ phase was still observed in the PM AC51 alloy. Compared with the β -Mg₁₇Al₁₂ phase, the (Al, Mg)₂Ca phase is very stable at high temperature, thus contributing to better mechanical properties at elevated temperatures. A key microstructural characteristic is that (Al, Mg)₂Ca phase has a step-like shape, which is capable of effectively blocking the sliding of grain boundaries.

To illustrate the effects of solidification conditions and Ca content on the hardness and composite modulus of the four alloys, the calculated dynamic hardness values from Fig. 7.11 and the composite modulus values from Fig. 7.12 are compared directly in Figs. 7.13(a) and (b), respectively. The DC AM50 alloy has higher hardness and composite modulus values than the PM AM50 alloy. This reflects the fact that the solidification rate of the DC AM50 alloy is higher than that of the PM AM50 alloy. This is further confirmed by the EDS results, which show a relatively high aluminum content within the primary α -Mg grains of the DC AM50 alloy compared to the PM AM50 alloy. Therefore, the DC AM50 alloy exhibits an improved solution strengthening and enhanced mechanical properties, as compared to the PM AM50 alloy. The PM AC52 alloy with the higher Ca content has a

higher hardness and composite modulus than the PM AC51 alloy, which suggests the fact that the PM AC52 alloy has higher solution strengthening.

In this study, the indentation tests were carried out within the α -Mg grains of the four alloys. Therefore, the measured nano-scale micromechanical properties should be influenced by solid strengthening directly and by precipitation strengthening indirectly. The higher the level of intermetallic phase formation along the grain boundaries, the smaller the amount of alloying elements retained in solution. To obtain good nano-scale micromechanical properties for as-cast Mg alloys, the amount of the intermetallic phases that are precipitated must be controlled within a defined range so that any solid solution strengthening has a optimum effect. A large increase in nano-scale mechanical properties by solid solution strengthening requires a high solubility of an element with an appreciable size difference from the base metal. Unfortunately, this leads to an increase in the heat of solution and a decrease in the solubility. Kelly and Nicholson [187] suggested that a possible solution lay in the use of two solutes, which interacted strongly with each other but not with the solvent element. An interesting parallel with this suggestion in solid solution strengthening can be found in the work of Baird and Jamieson [188] on Fe-Mn-N alloys where the strength of the ternary alloy is superior to either binary due to the strong Mn-N interaction. Although Al can interact with Mn to form the stable Al_8Mn_5 phase with a high melting temperature, the as-cast AM50 alloys have a poor solid solution strengthening response. This is because Al in the as-cast AM50 alloys also interacts with the base element Mg to form the β - $Mg_{17}Al_{12}$ phase. In addition, the Al_8Mn_5 phase has a very regular polygonal morphology so that grain boundary sliding readily occurs at the interface between the Al_8Mn_5 phase and the matrix of the as-cast Mg alloys. With the addition of Ca to Mg-Al alloys, the $(Al, Mg)_2Ca$ intermetallic

phase precipitates along the grain boundaries by an eutectic reaction. Although the intermetallic phases include the base element Mg, the PM AC51 and AC52 alloys still exhibit improved solid solution strengthening than the as-cast AM50 alloys. As a result, the solid solution strengthening mechanism of Ca-containing magnesium alloys should be further investigated.

7.1.6 Correlation of hardness and yield strength

According to Eq. (2-19), the hardness was theoretically related to yield strength [72]:

$$H = cY \quad (7-2)$$

where Y is the (initial) uniaxial yield strength and c is the elastic constraint factor. For blunt Vickers hardness, $c = 0.3$ when the yield strength is measured in MPa and the hardness is measured in kgf.mm^{-2} . To determine whether there is a correlation between the overall microhardness of the cross-sections and the tensile yield strength, an average hardness value was calculated for each thickness, and the final hardness values are the mean of the measurements from the five specimens used for the study at each thickness. The average hardness values are plotted in Fig. 7.15 as a function of the mean yield strength determined from the tensile tests [157]. Linear regression analysis gives the solid line of best fit between hardness and yield strength for the DC AM50 alloys. The macro-hardness values measured at the surface of the tensile bars are also included in Fig. 7.15 Unlike the surface hardness (squares), the microhardness data in Fig. 7.15 (triangles) closely follow a linear relationship with the yield strength. The lines of best fit in Fig. 7.15 are:

$$H_v = 0.1284Y_S + 44.372 \quad (7-3)$$

where Y_S is the 0.2% proof stress.

The linear relationship between the micro-hardness and yield strength was present in Fig. 7.15, while straight line could not be determined through regression analysis with the macrohardness data measured on the surface of the specimen. A decrease in the value for c in Eq. (7-2) would occur because of the low strain-hardening rate for high pressure die casting alloys. The good correlation based on the microhardness data shows that the yield strength of the DC AM50 alloy is the combined strengthening of the bulk and narrow skins of the test bars. Hence, the DC AM50 casting looks like a sandwich structure, i.e. two skin regions with fine microstructure plus middle region with relatively coarse microstructure. The measured yield strength mainly exhibits the effect of the bar geometry on the solidification, which is dependent on the total cross-section.

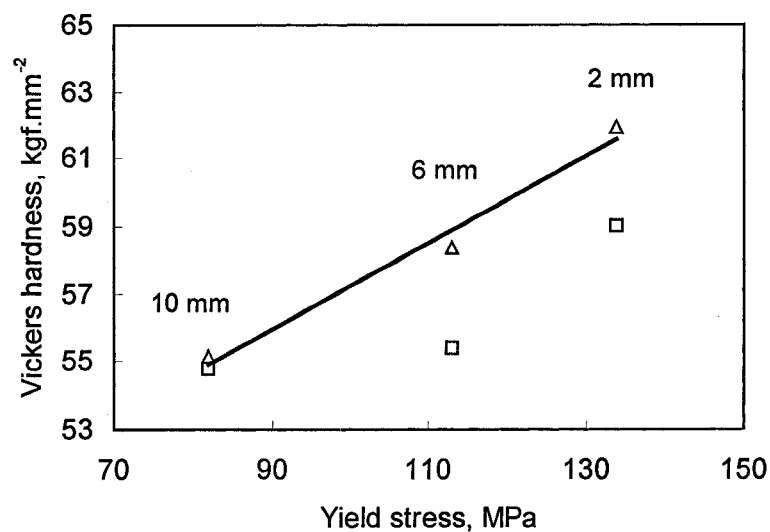


Fig. 7.15 Vickers hardness values as a function of the yield strength of DC AM50 alloy. The squares are macrohardness measured on the casting surface (1 kg). The triangles represent the average Vickers micro-hardness (200 g). The solid line indicates the observed linear relationship between the hardness and yield strength in the DC AM50 alloy.

7.2 Indentation size effect

An ISE was always observed for all the investigated as-cast Mg alloys on the nanoscale as has been reported in Section 7.1.4. The indentation displacement dependence of hardness for the DC and PM AM50 alloys, PM AC51 and AC52 alloys is presented in Fig. 7.16. Clear ISEs were observed in all of the as-cast Mg alloys that were tested. The hardness increases with decreasing the displacement at both the micro- and nano-scales. However, the extent of the increase is much more dramatic in the nano-scale region than in the micro-scale region. Hence, as the displacement decreases from about 700 to 50 nm, the nano-hardness increases by a factor of about 10.

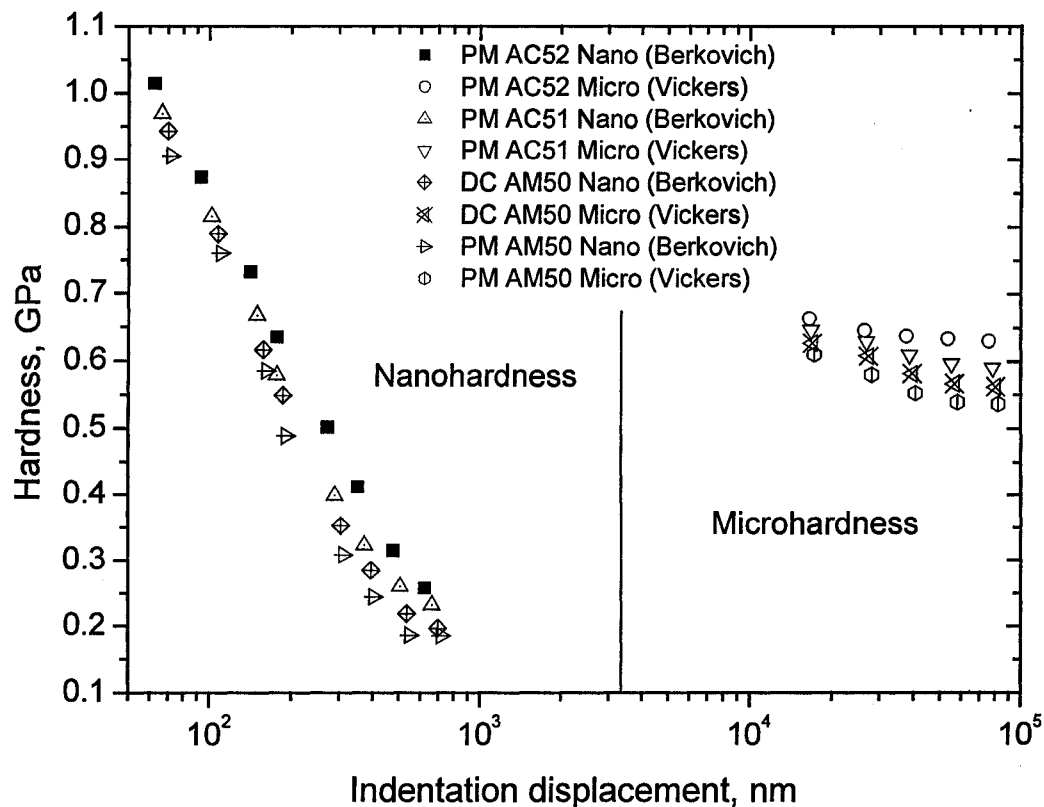


Fig. 7.16 Hardness size effect in the as-cast DC AM50, PM AM50, PM AC51 and PM AC52 alloys on the micro- and nano-scales.

The most widely used empirical expression, Meyer's Law [189], can be used to describe the ISE behavior by fitting a linear $\log P$ - $\log h$ or $\log H$ - $\log h$ relationship confirming the power law relation:

$$P = kh^n \text{ or } H = ch^{-m} \quad (7-4)$$

where P is load, h is penetration depth, H is hardness, n and m are the Meyer exponents, and k and c are the Meyer prefactors. The value of Meyer exponent n or m is used as a measure of ISE. When $n < 2$, the microhardness has a load dependent behavior, i.e. ISE behavior. However, when $n = 2$, the hardness is independent of applied load P .

Dependence of the hardness on the indentation displacement for the as-cast Mg alloys on the logarithmic scale is shown in Fig. 7.17.

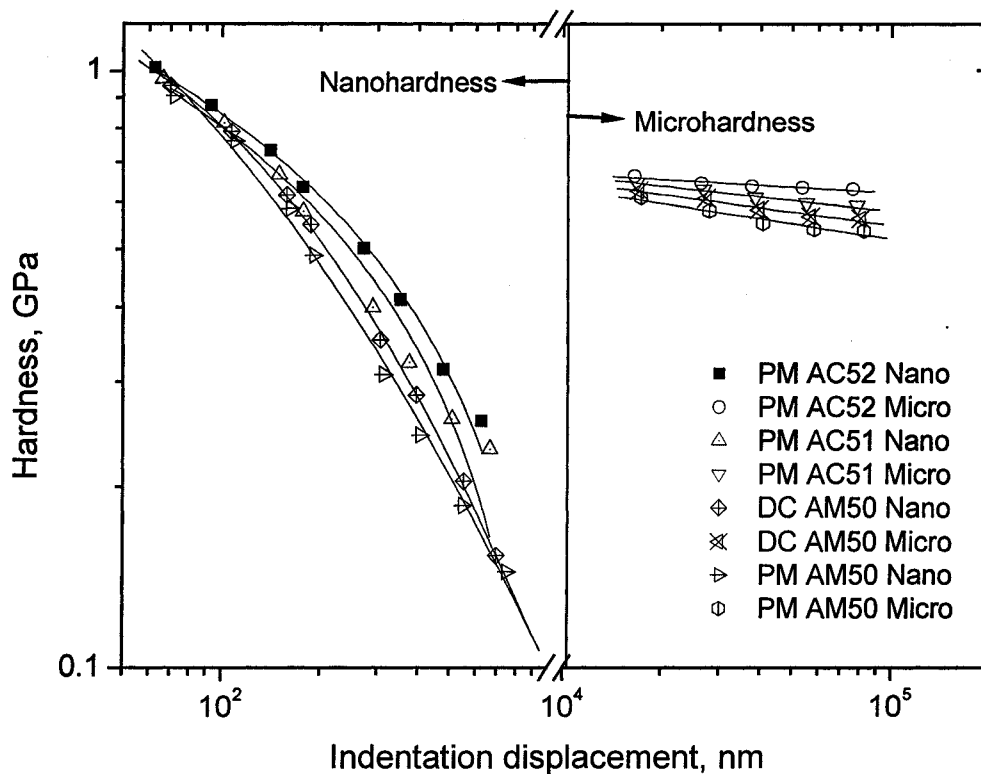


Fig. 7.17 Dependence of the hardness on the indentation displacement for the as-cast Mg alloys on the logarithmic scale.

It can be seen in Fig. 7.17 that the nanoindentation hardness data points obtained at ultra-low loads from the load-displacement diagrams are markedly above the extrapolated $\log H$ - $\log h$ line for the microindentation of the as-cast Mg alloys. However, for comparatively high loads, the nanoindentation data points are below the extrapolated $\log H$ - $\log h$ lines.

It is worth noting that the regression analysis shows linear relationships between $\ln H$ and $\ln d$ (the indentation displacement) in the region of the microhardness data. However, the nanohardness data obtained in the present study do not obey the linear $\ln H$ and $\ln d$ relationship as shown in Fig. 7.17. Thus, the linearity is observed only in limited intervals of the indentation displacement. This indicates that the traditional Meyer's Law is only suitable for describing the ISE behavior of the as-cast Mg alloys on the microscale. The calculated n values and correlation coefficients from the linear relationships in the microscale region of Fig. 7.17 for the as-cast Mg alloys are listed in Table 7.2.

Table 7.2 Calculated n values and correlation coefficients for the as-cast Mg alloys

Material	PM AC52	PM AC51	DC AM50	PM AM50
Meyer exponent: n	1.96	1.94	1.92	1.89
Correlation coefficient: R^2	0.998	0.995	0.997	0.998

The calculated n values from 1.89 to 1.96 suggest the presence of ISE; in other words, higher microhardness values would be measured at lower loads. However, ISE is relatively weak for all the tested Mg alloys.

Meyer's law can explain the ISE behavior of the microscale region of the as-cast Mg alloys qualitatively, but the nanohardness behavior is still not well understand.

Mechanisms of ISE based on the theory of strain gradient plasticity (SGP) have been developed [93]. It has been suggested that the statistically stored dislocations (SSD), which are created by a homogenous strain, and geometrically necessary dislocations (GND), which are related to the strain gradients, both contribute to the hardness. The ISE is related to the increased contribution of geometrically necessary dislocations at small indentation depths. Nix and Gao [117] have developed a mechanism-based strain gradient (MSG) model to rationalize the indentation size effects:

$$\frac{H}{H_0} = \sqrt{1 + \frac{h^*}{h}} \quad (7-5)$$

where H is the hardness for a given indent depth h , H_0 the size independent hardness, and h^* is a length parameter that characterizes the depth dependence of the hardness. This model predicts that the square of the hardness should be linearly related to the reciprocal of the indentation depth. The linear relationship is in agreement with the plots of both nano- and micro-indentation data obtained from the as-cast Mg alloys examined in this study. For example, Fig. 7.18 shows that linear relationships are obtained between H^2 and $1/h$. However, the slopes of the lines are different in the nano- and micro-scale regions. Furthermore, by fitting the data to Eq. (7-5), values of H_0 and h^* were obtained for the nano- and micro-scale indentation regimes, which are presented in Table 7.3.

Table 7.3 Summary of fitting parameters for the micro- and nano-scale regimes

Material		PM AC52	PM AC51	DC AM50	PM AM50
H_0 (GPa)	Nano	0.245	0.229	0.184	0.173
	Micro	0.619	0.575	0.542	0.510
h^* (nm)	Nano	845.61	945.27	1035.84	1116.0
	Micro	2357.96	4600.98	5981.67	7465.97

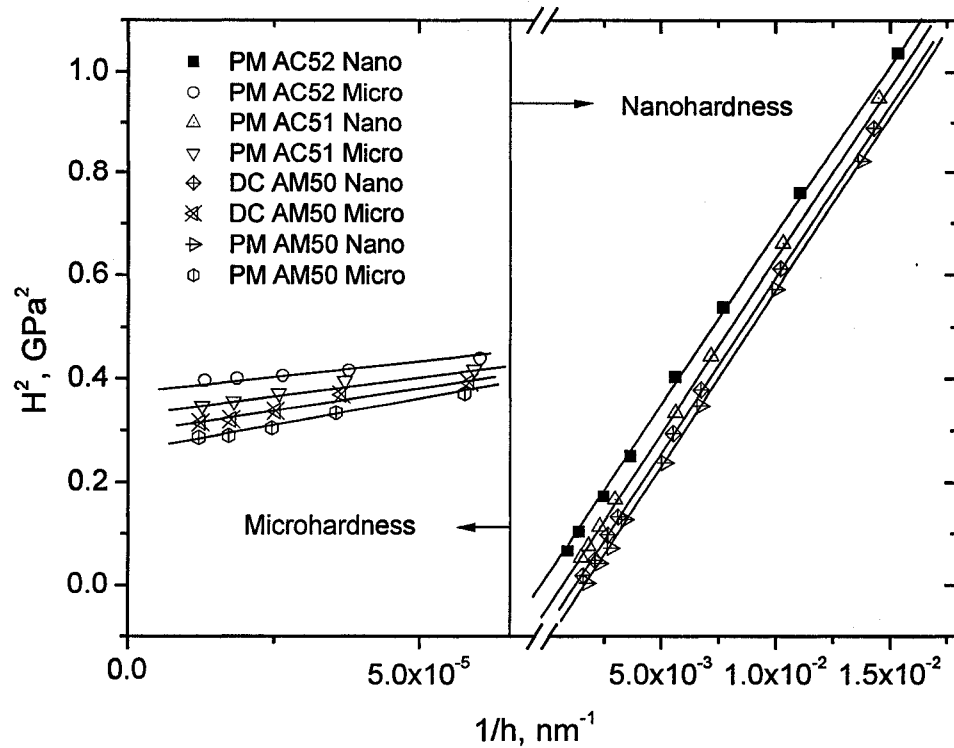


Fig. 7.18 H^2 vs. $1/h$ for the as-cast Mg alloys.

It was reported [190] that the density for GNDs in the single fcc crystal metals is calculated to be $\sim 10^{16} \text{ m}^{-2}$ for an average indent size of around 100 nm, and $\sim 10^{15} \text{ m}^{-2}$ for an indentation size of 100 μm . Hence, the average dislocation spacing, L , of the GNDs is calculated to be $\sim 7 \text{ nm}$ for 100 nm nano-indentation size and $\sim 45 \text{ nm}$ for 50 μm microindentation size according to the equation $L = 1/\sqrt{\rho_{GND}}$. When the indentation size reaches around 100 nm, only a few rows of GNDs are introduced into the deformed region underneath the indenter. Thus, the dislocation source is in the limited condition, and a large number of dislocations are required to be nucleated and propagated to develop the indentation deformation further. Greer and Nix [191] have also reported that very high stresses were required to nucleate more new dislocations under the dislocation-starved conditions, which results in the observed high strength (or hardness). In addition, discrete

displacement bursts observed in single crystal metals during the initial stages of nanoindentation could possibly confirm the evidence of the nucleation of dislocations [192, 193]. However, an established dislocation substructure is present beneath the indenter for microscale indentation, which is associated with deformation at sub-micro and microscales.

The ISE is considered as an intrinsic property of the surface. Therefore, for nanoscale indentation size, the discrete dislocations concept may be used to explain the nature of the interactions between individual dislocations, while, for indents in the microscale region, SGP theory can be used to account for size effects. However, other factors, such as oxide and contaminant films, photomechanical and electromechanical effects, work-hardening effects during the preparation of the samples and so on, can result in ISE behavior of materials at low loads.

7.3 Nanoindentation creep

7.3.1 Constitutive equation of indentation creep

The indentation creep technique is essentially a hardness test in which the time-dependent penetration rates of an indenter are measured under a constant applied load. With a sharp Berkovich indenter, the stress distribution in an indented material is similar for any depth of indenter penetration, i.e. the deformed zone maintains its geometrical self-similarity. Fujiwara and Otsuka [194] suggested a constitutive equation for self-similar indentation creep:

$$\dot{h} = A_1 h \left(\frac{P}{E_s h^2} \right)^n \left(\frac{b}{d} \right)^q \exp\left(-\frac{Q}{RT} \right) \quad (7-6)$$

where \dot{h} is the indenter velocity, A_1 is constant, b is the magnitude of the Burgers vector, d is the grain size, q is the grain size exponent, R is the gas constant, T is the experimental

temperature and Q is the activation energy. Stresses and dislocation density are very high in the elastic-plastic zone beneath a sharp indenter. For indentation creep performed at room temperature, dislocation glide is considered to be the main mechanism of indentation creep. Moreover, grain size has little influence on the creep rate, which is controlled by dislocation glide. Therefore q is usually set at zero in Eq.(7-6). When T and d are constant during indentation creep under a constant load F , the stress exponent n in Eq.(7-6) is obtained from:

$$n = \frac{1}{2} \left(1 - \frac{\partial(\ln \dot{h})}{\partial(\ln h)} \right)_{T,d} \quad (7-7)$$

The flow stress in the plastic region beneath an indenter can be approximated [195] as:

$$\bar{\sigma} \approx H/3 \propto F/h^2 \quad (7-8)$$

The indentation strain rate is defined as [196]:

$$\dot{\epsilon}_i = \dot{h}/h = d(\ln h)/dt \quad (7-9)$$

Substituting the flows stress and the indentation strain rate into Eq. (7-6), the expression for strain rate is given as:

$$\dot{\epsilon}_i = A_2 \left(\frac{\bar{\sigma}}{E_s} \right)^n \left(\frac{b}{d} \right)^q \exp\left(-\frac{Q}{RT} \right) \quad (7-10)$$

The stress exponent for creep, n , is given by:

$$n = \left(\frac{\partial(\ln \dot{\epsilon}_i)}{\partial(\ln(\bar{\sigma}/E_s))} \right)_{T,d} \quad (7-11)$$

7.3.2 Nanoindentation creep results

The changes of the experimentally measured penetration depth h , the indenter velocity \dot{h} , and average equivalent stress $\bar{\sigma}$ of the PM AC52 alloy (cast at 30 °C/s) with time at a load of 5 mN at room temperature are shown in Fig. 7.19. As the penetration depth

increases, the projected area beneath the indenter increases so that the average equivalent stress gradually decreases with time based on Eq. (7-8). Therefore, the indenter velocity also decreases as a function of indentation creep time.

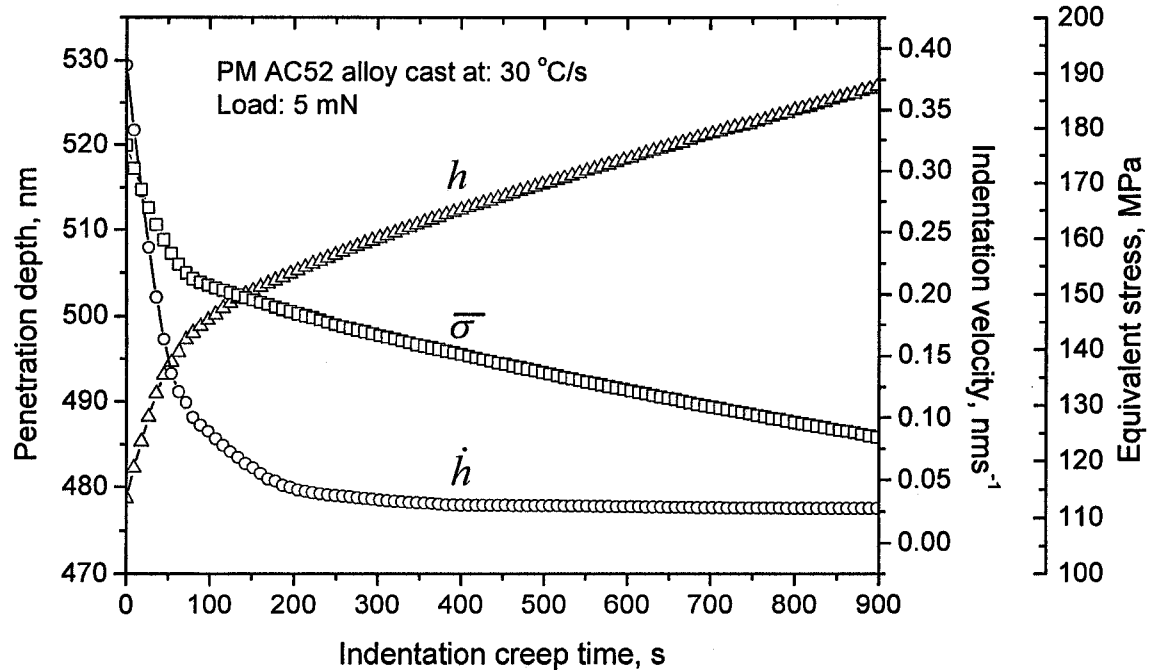
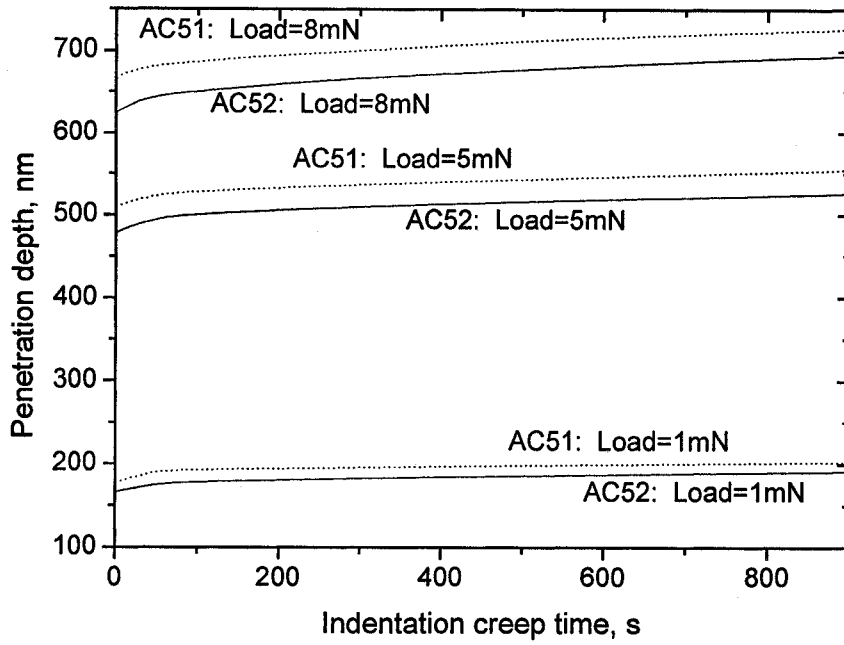


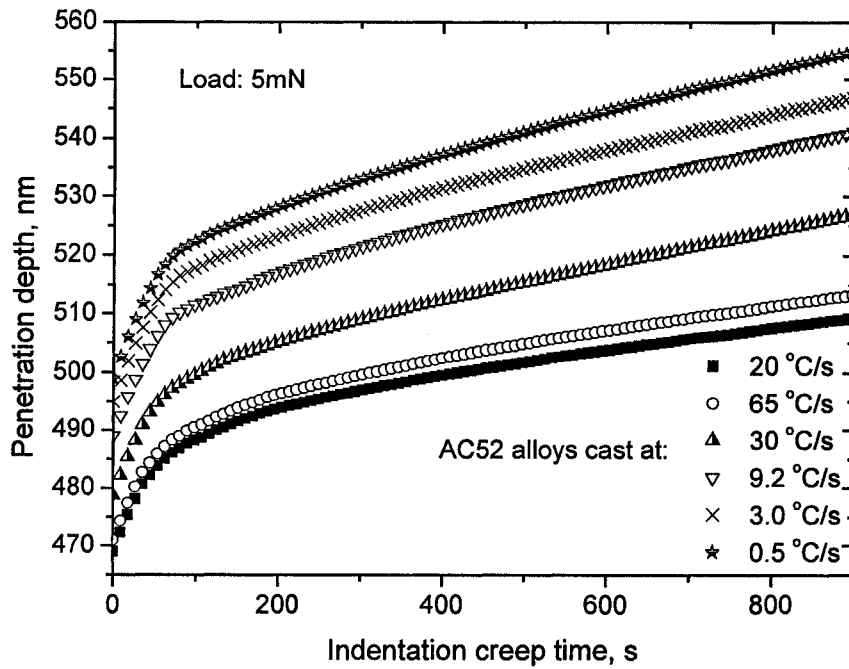
Fig. 7.19 Changes of the experimentally measured penetration depth h , the indenter

velocity \dot{h} , and average equivalent stress $\bar{\sigma}$ of the PM AC52 alloy with time at a load of 5 mN and at room temperature.

Fig. 7.20 shows the nanoindentation creep curves for the PM AC51 and AC52 alloys cast at the same solidification condition (30 °C/s) at applied loads of 1, 5, 8 mN and for the AC52 alloys cast at different cooling rates (0.5 ~ 65 °C/s) at a applied load of 5 mN at room temperature. The indentation penetration depth rapidly increases in a short time at the beginning of the indentation testing (primary stage) when a Berkovich indenter is pressed into the surface of the samples, and then the indenter slowly penetrates the samples by creeping until an apparent steady-state rate is finally reached (the secondary stage).

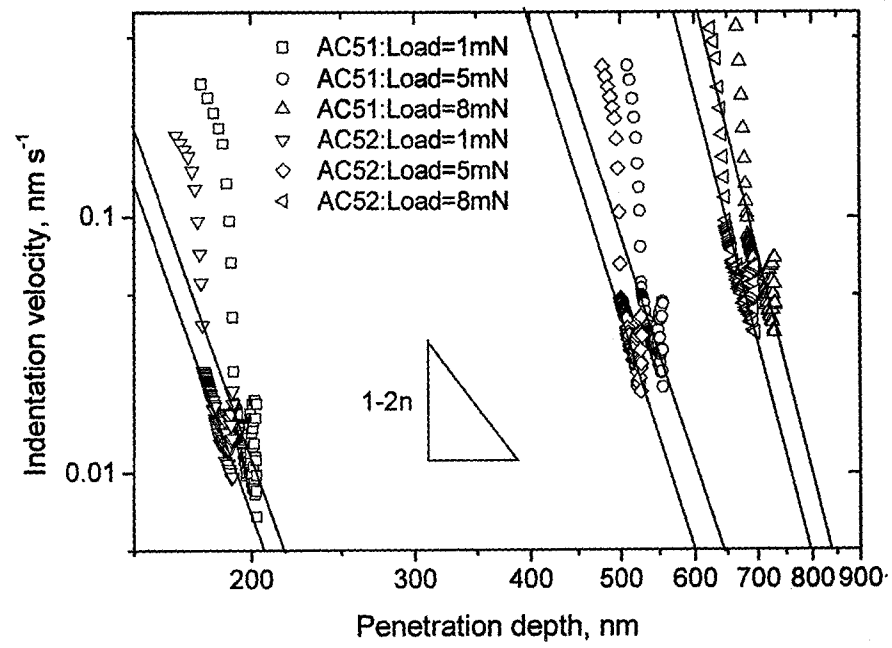


(a)

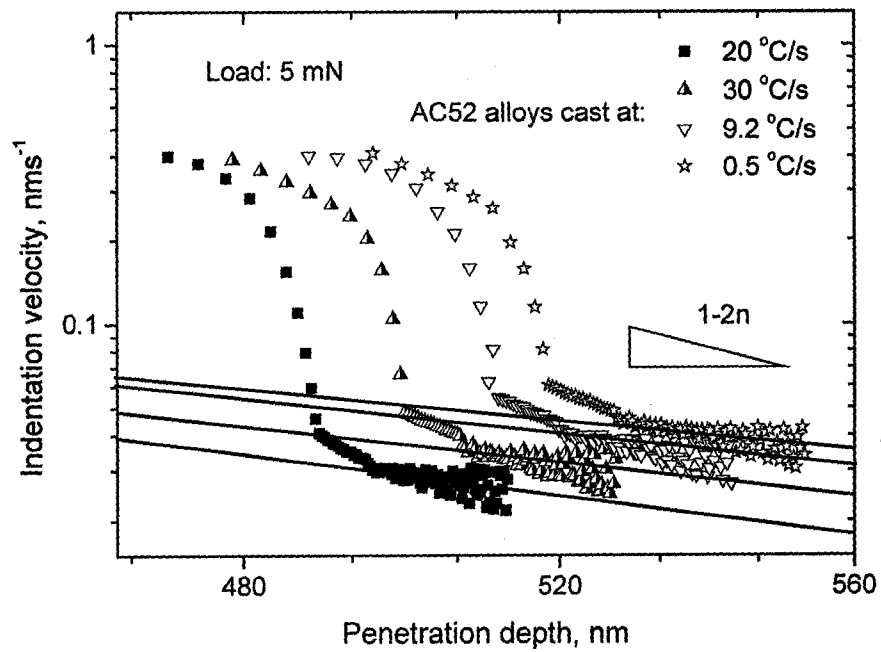


(b)

Fig. 7.20 Indentation creep curves for: (a) the AC51 and AC52 alloys (cast at 30 °C/s) at applied loads of 1, 5, 8 mN, and (b) the as-cast AC52 series alloys (cast at different cooling rates) at an applied load of 5 mN at room temperature.

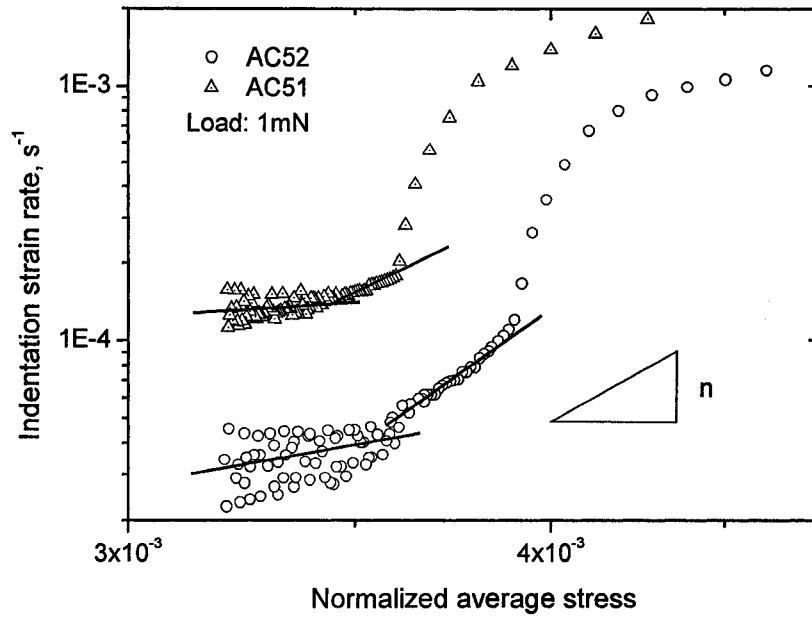


(a)

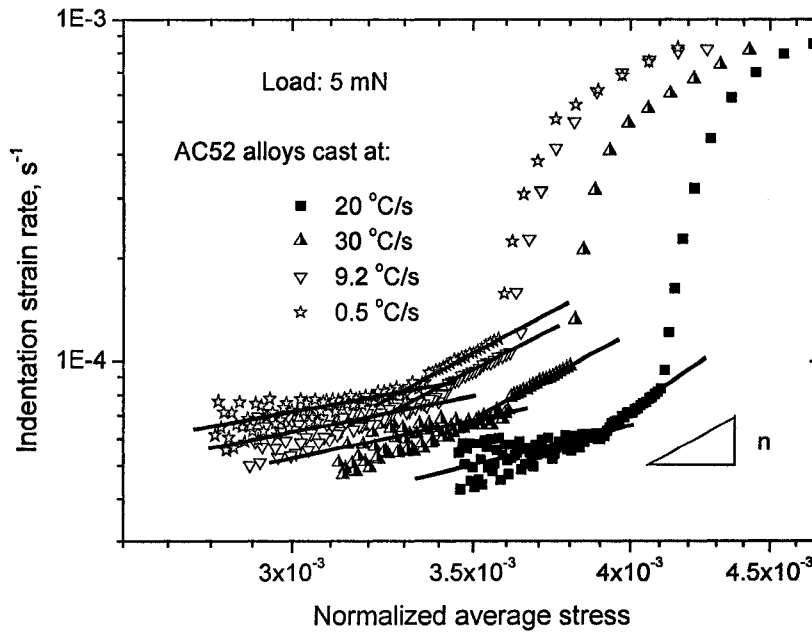


(b)

Fig. 7.21 Relationship between the indentation velocity and penetration depth on logarithmic scales for: (a) the as-cast AC51 and AC52 alloys at loads of 1, 5 and 8 mN, and (b) the as-cast AC52 series alloys at a load of 5 mN at room temperature.



(a)



(b)

Fig. 7.22 Indentation strain rate vs. normalized average equivalent stress ($\bar{\sigma}/E$) curves on a logarithmic scale for: (a) the as-cast AC51 and AC52 alloys at a load of 1 mN, and (b) the as-cast AC52 series alloys at a load of 5 mN at room temperature.

It can be seen in Fig. 7.20(a) that the penetration depth h for the AC51 and AC52 alloys significantly increases with increasing applied load at the same indentation creep time, and the AC51 alloy shows higher penetration depth than the AC52 alloy at the same indentation time. It is worth noting in Fig. 7.20(b) that the penetration depth for the AC52 alloy cast at 20 °C/s is very close to that at 65 °C/s although a cooling rate of 20 °C/s is obviously lower than 65 °C/s. For all the cooling rates except for 20 °C/s, the final stationary penetration depth clearly increases with decreasing cooling rate.

Indentation creep constitutive parameters can be extracted from the above curves. Fig. 7.21 shows the relationship between the indentation velocity and penetration depth on logarithmic scales for the PM AC51 and PM AC52 alloys (cooling rate: 30 °C/s), and the as-cast AC52 series alloys (cooling rate: 0.5 ~ 30 °C/s). Note that the logarithmic scale means that the indentation velocity can only be estimated to an order of magnitude. It can be seen from Fig. 7.21 that the indentation creep data exhibit a good linear relationship in the secondary stage. The slope of the straight lines is equal to $1-2n$. The stress exponent, n , values calculated using Eq. (7-7) for the AC51 alloy at the different loads are 3.0~3.6, and 3.2~3.9 for AC52 (Fig. 7.21(a)), and 3.3~3.7 for the as-cast AC52 series alloys at a load of 5 mN, respectively.

Fig. 7.22 shows the indentation strain rate vs. normalized average equivalent stress curves on a logarithmic scale for the as-cast AC51 and AC52 alloys. The creep behavior can be described by a power law (Eq.(7-10)), where two stress exponent regimes can be distinguished, in addition to the primary stage at the beginning of the indentation testing. Using Eq.(7-11), the stress exponents, n , can be determined by the slopes of the straight lines. In the low stress exponent regime at low strain rates, n is around 3.0, while in the high stress

exponent regime, the stress exponents are around 7.0. It can be seen from Fig. 7.22(a) that, as indentation creep progresses, the stress exponent n abruptly changes from 6.3 to 3.0 for the AC51 alloy and from 6.6 to 3.2 for the AC52 alloy at a critical stress value, i.e. when the applied load is larger than the critical stress, the stress exponent, n , is close to 6.3 for the AC51 alloy and 6.6 for the AC52; when the applied load is less than the critical stress, the stress exponent, n , is close to 3.0 for the AC51 alloy and 3.2 for the AC52. The critical stresses were calculated to be 132 MPa and 145 MPa, respectively for the AC51 and the AC52 alloys. Similarly, the sudden changes of the stress exponent n (Fig. 7.22(b)) were also observed at critical stresses for the as-cast AC52 series alloys. The creep parameters obtained from creep data of the as-cast AC51 and AC52 alloys are summarized in Tables 7.4 and 7.5. The transition in the creep behavior could be associated with a distinct change in the deformation mechanisms that should be mainly related to the movement of the dislocations during the indentation tests.

Table 7.4 Creep parameters obtained for the as-cast AC51 and AC52 alloys (cast at 30 °C/s) at applied loads of 1, 5 and 8 mN

Alloy (Cooling rate: 30 °C/s)	Creep parameters		Applied load (mN)		
			1	5	8
AC51	Stress exponent n	Low	3.0	3.4	3.6
		High	6.3	-	-
	Critical stress (MPa)		132	-	-
AC52	Stress exponent n	Low	3.2	3.5	3.9
		High	6.6	6.9	-
	Critical stress (MPa)		145	147	-

Table 7.5 Creep parameters obtained for the as-cast AC52 alloys (cooling rate: 0.5 ~ 30 °C/s) at an applied load of 5 mN

AC52 alloys (Applied load: 5mN)		Cooling rate (°C/s)			
		0.5	9.2	20	30
Stress exponent n	Low	3.3	3.4	3.7	3.5
	High	6.4	6.6	7.2	6.9
Critical stress (MPa)		140	142	152	147

7.3.3 Nanoindentation creep behavior and mechanisms

It has been theoretically and experimentally realized that plastic deformation cannot take place without the nucleation and movement of the dislocations [197, 198]. The method to strengthen a metal is to introduce a structure in which dislocations cannot move or can move only with difficulty. The motion of a dislocation will be hindered by other dislocations (strain or work hardening), by the introduction of foreign atoms of different sizes into the lattice (solid solution strengthening), by a grain boundary (grain boundary strengthening) and by a phase boundary at which the crystal structure changes (precipitation hardening, dispersed-phase hardening, or phase-transformation hardening). In this study, the nanoindentation tests were performed within the primary α -Mg grains of the as-cast Mg alloys on the nanoscale. The height and width of the imprint left by the Berkovich indenter is around 500 nm at an applied load of 5 mN, which is much smaller than the size of primary α -Mg grains. Therefore, creep deformation mechanisms that are related to solid solution strengthening and dispersed-phase hardening should be the predominant deformation mechanisms. In addition, as discussed in Section 5.3, changes in cooling rates alter the volume fraction of the precipitates and SDAS, while variations in the volume fraction of the

precipitates and SDAS allow alloying elements with the different contents to be left within the interdendritic regions, as shown in Fig. 7.23. Therefore, precipitation hardening could also indirectly influence the nanoscale creep properties.

It was observed in Section 5.3 that, although the total volume fraction of the fine precipitates in PM AC52 alloy is very low and the distribution of the fine precipitates is not uniform, some nano precipitates still can be observed in some local areas in the matrix. These nano precipitates also act as obstacles to dislocation movement on the glide plane. The fine precipitates and higher content of alloying elements within the primary α -Mg grains of the AC52 alloy result in the better creep resistance compared to the AC51 alloy (Fig. 5.26).

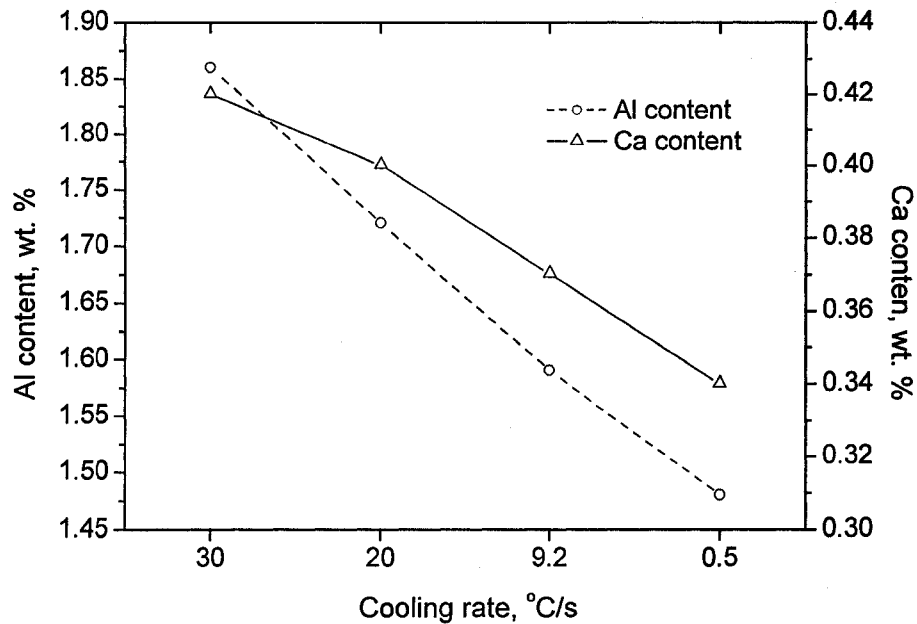


Fig. 7. 23 Variation of average Al and Ca contents with cooling rate in the primary α -Mg grains of the as-cast AC52 series alloys.

Fig. 7.23 presents the change of Al and Ca contents in the primary α -Mg grains of the AC52 alloys. It is evident that increasing cooling rates results in an increase Al and Ca contents. The experimental observation implies that the creep of the as-cast AC52 series

alloys is influenced by the Al and Ca contents in the primary α -Mg grains. This is because the total primary strain and the total creep strain including both the primary and secondary stages decrease with an increase in Al and Ca contents in the primary α -Mg grains resulting from high cooling rates.

The variation of creep properties with the different contents of Ca and Al in the interdendritic regions has been associated with a distinct change in the rate-controlling process. Either the generation and glide of dislocations or the rearrangement and annihilation of dislocations determine the creep rate in the power law mechanism. The slowest of these necessary processes then controls the creep rate. Dislocation glide becomes the slowest process for the as-cast AC52 series alloys since the mobile dislocations were viscously dragged by the surrounding solute atmosphere. Weertman [199] proposed a glide-controlled model for creep by assuming that the creep rate depends on the mobile dislocation density, ρ , as:

$$\dot{\epsilon} = \rho b \bar{v} \quad (7-12)$$

where \bar{v} is the average dislocation velocity which is determined by the rate at which the solute atoms can move along with the dislocations. The velocity, \bar{v} , would vary linearly with stress and ρ would increase as the square of the applied stress. This model is consistent with the experimental creep results observed in the primary stage for the as-cast AC52 alloys. Although the TEM results showed that there were almost no dislocations in the matrix of the PM AC52 alloy before the indentation testing, the dislocation density dramatically increased up to a very high value when a Berkovich indenter with a very sharp tip just contacted the surface of the sample after loading. Moreover, the stresses built up in the zone beneath the indenter are also large. Therefore, with an extremely high dislocation density beneath the

indenter and with the dislocation velocity controlled by the rate of solute drag, a high plastic penetration depth had been found on the penetration depth vs. creep time curve in the primary stage after loading. A gradual increase in dislocation density with increasing Ca and Al contents remaining in the interdendritic regions leads to a decrease in penetration depth in the primary stage of creep. On the other hand, if there was a low dislocation density in the matrix of the sample in the primary stage, a low or negligible plastic strain would be expected at the beginning of a creep test [200].

After the primary stage, the creep process reaches the secondary stage, and the low and high stress exponent regimes were observed, as shown in Fig. 7.22. The low stress exponent regime, in which the calculated values of n were around 3.0, includes strain rates lower than about $6.8 \times 10^{-5} \text{ s}^{-1}$, $5.2 \times 10^{-5} \text{ s}^{-1}$, $7.5 \times 10^{-5} \text{ s}^{-1}$ and $8.1 \times 10^{-5} \text{ s}^{-1}$ for the AC52 alloys cast at 30 °C/s, 20 °C/s, 9.2 °C/s and 0.5, °C/s respectively. The high stress exponent regime is located after the primary stage of an indentation creep test. The calculated values of n in the regime are ~ 7.0 . In all cases, irrespective of the volume fraction and average size of the precipitates, the strain rates vs. normalized average stress curve showed that the stress exponent decreases with decreasing applied stress from ~ 7.0 at high stresses to ~ 3.0 at low stresses. Although the change in stress exponent exhibited as a sudden transition at a critical stress, the variation of creep strain rate with stress appears to change in a gradual manner.

The directions for easy crystallographic slip in hcp single crystals are the three $\langle 11\bar{2}0 \rangle$ or $\langle a \rangle$ closed-packed directions. At low temperatures, the three dominant sets of planes which contain this slip direction are (i) the (0001) basal plane, (ii) the three $\{10\bar{1}0\}$ prismatic planes, and (iii) the six $\{10\bar{1}1\}$ pyramidal planes. Crystallographic slip in hcp single crystals is commonly observed to occur on the basal- $\langle a \rangle$ or prismatic- $\langle a \rangle$ systems.

Driven by the applied stress, the mobile dislocations can cut through or bow between the precipitates, or by-pass them by climb and cross-slip. Slip begins when the shear stress on the slip plane in the slip direction reaches a required level called the critical resolved shear stress. Essentially, this value is equivalent to the yield stress of a polycrystalline metal or alloy determined by a stress-strain tensile test curve. The critical stresses obtained at the intersection by drawing tangents for $n \approx 7$ and $n \approx 3$ appear to be approximately equal to the yield stress of the as-cast AC52 alloys [7]. A similar conclusion has been reached for other two-phase alloys [55] suggesting that the high value of n is observed at stresses exceeding the macroscopic yield stress. Therefore, slip bands would be formed at stresses above the macroscopic yield stress so as to relax the concentration of the stress as a result of the pile-up dislocations. Under these conditions, dislocations produced a source which can either cut through, or bow between, the precipitates. However, it can also be seen in Fig. 7.20 that the amount of overall creep deformation that can be produced in the high stress exponent regime is small. In the low stress exponent regime, not only slip but also twinning may occur within the primary α -Mg grains. At high penetration depths, more multiple slip systems were required to relieve the stress concentration caused by the pinning of dislocations by the solute or the precipitates within the matrix of the as-cast AC52 alloys. Thus, twinning could nucleate at the local stress concentration regions to place new slip systems into a favorable orientation with respect to the shear stress. Additionally, rearrangement and annihilation of dislocations could be more rapid in regions near the existing twin boundaries. Therefore, the transition of creep behavior from the high stress exponent regime to the low stress exponent regime may be attributable either to power law breakdown or to the dislocations breaking free from their solute atmospheres at the critical stresses.

7.4 Summary

- (1). Microporosity, the primary α -Mg and the eutectic phases in the DC AM50 alloys are the three main features which influence the hardness and composite modulus. The high Vickers hardness values of the DC AM50 alloy result primarily from fine primary α -Mg grains which contain high contents of alloying elements, and massive eutectic phase at grain boundaries compared to the PM AM50 alloy. The low Vickers hardness values at some local positions are related to distinctive bands of concentrated micro porosity beneath the surface of the DC AM50 alloys.
- (2). The step-shaped $(Al, Mg)_2Ca$ phase, which is present along the grain boundaries in the Ca-containing AC51 and AC52 alloys, is capable of effectively blocking the movement of the dislocations and the sliding of the grain boundaries. As a result of Ca addition, the nano-scale mechanical properties of the as-cast AC51 and AC52 alloys are superior to those of the as-cast AM50 alloys.
- (3). Linear relationships between the contact stiffness and penetration depth have been developed for the four tested magnesium alloys based on regression analysis which was used to calculate the dynamic hardness and composite modulus as the CSM technique was not available. A good agreement between the experimental and calculated results implies that the developed relations are applicable to the as-cast Mg alloys.
- (4). Both the experimental and calculated data show that the hardness values exhibit an indentation size effect (ISE) for all the tested Mg alloys, while the composite modulus is only slightly affected by the penetration depth.

- (5). The fine secondary phases, and the high amount of Ca solute atoms, within the primary α -Mg grains of the AC52 alloy improve the nanoscale creep resistance of AC52 alloy compared to that of AC51 alloy.
- (6). The nanoscale creep resistance of the as-cast AC52 alloys increases with an increase in cooling rates during solidification due to the high content of Ca and Al solutes present in the primary α -Mg solid solution.
- (7). A experimentally observed high plastic penetration depth in the primary stage of indentation creep was explained in terms of the existing of extremely high dislocation density and the dislocation velocity controlled by the rate of solute drag. Both low and high stress exponent regimes were observed on the indentation strain rate vs. normalized average stress curves. The creep behavior of the as-cast AC alloys changed from the high stress exponent regime ($n \approx 7$) to the low stress exponent regime ($n \approx 3$) at a critical stress (~ 140 MPa) and the corresponding creep behavior could be explained by the main dislocation-controlled glide mechanism accommodated by twinning in the secondary stage.

CHAPTER 8

CONCLUSIONS

The work described in this thesis attempted to develop scientific understanding of the micro- and nano-mechanical behaviours of die cast and permanent mold cast Mg-Al and Mg-Al-Ca alloys by investigating the relationships between the microstructures and micro- and nano-mechanical properties of these alloys. This is because calcium additions in Mg-Al alloys usually result in alloy strengthening through the formation of fine Ca-containing precipitates which are thermally stable and distributed in the primary α -Mg matrix and at grain boundaries. The main conclusions are summarized as follows:

- (1) The intergranular β -Mg₁₇Al₁₂ phase, along with the Al₈Mn₅ phase, are observed in the PM and DC AM50 alloys, and the β -Mg₁₇Al₁₂ phase is surrounded by the Al-rich eutectic α -Mg phase. Due to the different cooling rates in the DC and PM alloys, the β -Mg₁₇Al₁₂ phase in the PM AM50 alloy is much coarser than that in the DC AM50 alloy. There are differences between the morphologies of the Al-rich regions in the DC and PM AM50 alloys. The Al-rich regions in the PM alloy are coarser than those in the DC alloy, but are discontinuous rather than continuous.
- (2) A relatively higher aluminum content was observed within primary the α -Mg grains of the DC AM50 alloy. As a result, the DC AM50 alloy exhibited enhanced solid solution strengthening compared to the PM AM50 alloy.
- (3) The microstructures of the PM Mg-Al-Ca alloys are highly dependent on the Ca content. Quantitative analysis shows that with increasing Ca content, the average secondary dendrite arm spacing decreases, while the volume fraction of the eutectic

phases increases. The eutectic phases tend to form a continuous network with increasing Ca content instead of being distributed in the form of completely divorced phases at low Ca contents. When the Ca content reaches 1.5 wt.% or higher in the Mg-Al-Ca alloy, the β - $\text{Mg}_{17}\text{Al}_{12}$ phase was completely replaced by the $(\text{Al}, \text{Mg})_2\text{Ca}$ phase. Also, the Ca-containing eutectic phases in all PM Al-Mg-Ca alloys are only the $(\text{Al}, \text{Mg})_2\text{Ca}$ phase as confirmed by TEM.

- (4) The $(\text{Al}, \text{Mg})_2\text{Ca}$ phase present along the grain boundaries in the Ca-containing AC series alloys has a step-like shape. The step-shaped $(\text{Al}, \text{Mg})_2\text{Ca}$ phase is capable of effectively blocking the movement of the dislocations and the sliding of the grain boundaries.
- (5) The measurement of the average SDAS in the as-cast AC52 alloys shows refinement of the dendritic microstructure with increasing cooling rates, and the measured volume fraction of the eutectic phases in the PM AC52 alloys also increases with an increase in cooling rates.
- (6) The dimension and morphology of the Al_8Mn_5 phase in the as-cast AC52 alloys are dependent on the cooling rates. The Al_8Mn_5 particles are smaller at the higher cooling rates than at the lower cooling rates, and the majority of Al_8Mn_5 particles are found to be attached to the eutectic phases. This is due probably to nucleation of the eutectic phase on the Al_8Mn_5 particles present in the melt.
- (7) Two types of $\text{Mg}_{17}\text{Al}_{12}$ precipitation (discontinuous $\text{Mg}_{17}\text{Al}_{12}$ particles at grain boundaries and continuous $\text{Mg}_{17}\text{Al}_{12}$ particles within the primary α -Mg grains) occurred in the matrix of the PM AM50 alloy after solution treatment plus aging.

Spheroidisation and coarsening of the discontinuous $Mg_{17}Al_{12}$ phase in the PM AM50, AC505 and AC51 alloys and the discontinuous $(Al, Mg)_2Ca$ phase in the PM AC515 and AC52 alloys, occurred with increasing aging temperatures.

- (8) DSC curves of the DC AM50 alloy show two endothermic peaks, A & B, and one exothermic peak, C, at heating rates from 10 to 50 °C/min. Peak A is possibly related to the dissolution of B2 ordered phase, and peak B corresponds to the dissolution of the eutectic $Mg_{17}Al_{12}$ phase in the DC AM50 alloy during heating. Peak C is related to the rapid oxidation of the molten eutectic phases at higher temperatures.
- (9) The activation energy for peak A, calculated using a Kissinger-type isoconversion method, was 83.8 kJ mol⁻¹, which is similar to the grain boundary self-diffusion activation energy 90 kJ mol⁻¹. The activation energy for peak B was 141.4 kJ mol⁻¹, which was slightly higher than the self-diffusion activation energy 136 kJ mol⁻¹. The redistribution of the main alloy elements such Al and Mn in the matrix of the DC AM50 during the DSC runs also contributes to the higher activation energy for peak B.
- (10) DSC curves of the PM AC series alloys at a heating rate of 30 °C/min show that two endothermic peaks P1 (the dissolution of β - $Mg_{17}Al_{12}$) and P2 (the dissolution of $(Al, Mg)_2Ca$) are present in the DSC curves of the AC505 and AC51 alloys while only one large and sharp peak P2 is observed in the DSC curves of the AC515 and AC52 alloys, which indicates that when the Ca content reaches 1.5 wt.% or higher, the β - $Mg_{17}Al_{12}$ phase is completely replaced by the $(Al, Mg)_2Ca$ phase.
- (11) The activation energy calculated for peak P2 is 224.5 kJ mol⁻¹, which is significantly higher than the self-diffusion activation energy of Mg alloys. The larger atomic size of

calcium and dispersed ultrafine β -Mg₁₇Al₁₂ phase may result in a high activation energy for peak P2.

- (12) The heating/cooling rates during DSC runs play an important role in both the redistribution of alloying elements and the dissolution or precipitation of the eutectic phases in the as-cast Mg alloys. The average Al content in the DC AM50 alloy increases with increasing heating rates, indicating that a low heating rates result in the progressive removal of coring effects that characterize the die-cast microstructure. The peak temperature of these eutectic transformations decreases with increasing cooling rates and increases with increasing heating rates for both the DC AM50 and the PM AC52 alloy.
- (13) For the AC alloys with lower Ca concentrations after heating and air quenching, the discontinuous needle-like β -Mg₁₇Al₁₂ and (Al, Mg)₂Ca particles are distributed along the grain boundaries. As the Ca content is increased to 1.5 wt.% or higher, the eutectic phases gradually form the eutectic network in the microstructure of the alloys. In the case of the AC52 alloy, a large amount of fine (Al, Mg)₂Ca plates are present within the primary α -Mg grains, while coarse (Al, Mg)₂Ca plates are mainly distributed along the grain boundaries. Additionally, it is observed that these fine (Al, Mg)₂Ca plates are parallel within individual α -Mg grains, which suggests that there are preferred crystallographic relationships between the fine (Al, Mg)₂Ca plates and the matrix of the alloy.
- (14) The grain size decreases with increasing heating rates for the AC52 alloys after DSC runs at various heating rates and air quenching. Three morphologies of the (Al, Mg)₂Ca phase were observed in the alloy, and these are controlled by the redistribution of Ca

through diffusion. Coarse $(Al, Mg)_2Ca$ plates are often present at the grain boundaries while a large amount of fine needle-like $(Al, Mg)_2Ca$ plates precipitate within the primary α -Mg grains. Additionally, round $(Al, Mg)_2Ca$ islands with the shape of Chinese Script also form within the primary α -Mg grains when the heating rates become high.

- (15) Microporosity, the primary α -Mg and the eutectic phases in the DC AM50 alloys are the three main features which influence the hardness and composite modulus. The high Vickers hardness values of the DC AM50 alloy result primarily from fine primary α -Mg grains which contain high contents of alloying elements, and massive eutectic phase at grain boundaries compared to the PM AM50 alloy. The low Vickers hardness values at some local positions are related to distinctive bands of concentrated micro porosity beneath the surface of the DC AM50 alloys.
- (16) Linear relationships between the contact stiffness and penetration depth have been developed for the four tested magnesium alloys based on regression analysis which was used to calculate the dynamic hardness and composite modulus as the CSM technique was not available. A good agreement between the experimental and calculated results implies that the developed relations are applicable to the as-cast Mg alloys.
- (17) Both the experimental and calculated data show that the hardness values exhibit an indentation size effect (ISE) for all the tested Mg alloys, while the composite modulus is only slightly affected by the penetration depth.

- (18) The nanoscale creep resistance of the as-cast AC52 alloys increases with an increase in cooling rates during solidification due to the high content of Ca and Al solutes present in the primary α -Mg solid solution.
- (19) An experimentally observed high plastic penetration depth in the primary stage was explained in terms of the existing of extremely high dislocation density and the dislocation velocity controlled by the rate of solute drag. Both low and high stress exponent regimes were observed on the indentation strain rate vs. normalized average stress curves. The creep behavior of the as-cast AC alloys changed from the high stress exponent regime ($n \approx 7$) to the low stress exponent regime ($n \approx 3$) at a critical stress (~ 140 MPa) and the corresponding creep behavior could be explained by the main dislocation-controlled glide mechanism accommodated by twinning in the secondary stage.

CHAPTER 9

SUGGESTIONS FOR FUTURE WORK

Based on the observations of microstructure, and the investigation of the micro-and nano-mechanical properties of as-cast Mg-Al and Mg-Al-Ca alloys, the following areas are suggested for future work:

- (1) Further investigation into the significant difference in the mechanical properties and the microstructures including the amount and morphology of the precipitates in the permanent mold cast and die cast Mg-Al alloys.
- (2) Studying the effect of casting parameters including casting temperature and holding time on the precipitation of the eutectic phases in the Mg-Al-Ca alloys through use of the HTOU equipment.
- (3) Characterizing the crystallographic orientation between the primary α -Mg matrix and the eutectic phases formed during DSC runs through TEM observation.
- (4) Further investigation into the effect of the mechanical and thermal treatments, the size of indenter and tip rounding, surface-active media and sample preparation on the ISE behavior of the as-cast Mg alloys.
- (5) Further evaluation of the effects of the morphology and volume fraction and distribution of eutectic phases and casting defects on the micro mechanical properties of the Mg-Al and Mg-Al-Ca alloys, and relating the macro mechanical properties to micro-and nano-indentation behaviour of these Mg alloys.

CHAPTER 10

STATEMENT OF ORIGINALITY

Aspects of this work constitute, in the author's opinion, new and distinct contributions to the technical knowledge in the public domain. These include:

- (1). Establishment of the precipitation mechanisms of the eutectic phases during permanent mold casting and die casting of the Mg-Al alloys, and the refinement of the microstructure and the elimination of the segregation like Al-rich eutectic α -Mg by a calcium addition to the Mg-Al alloys.
- (2). The evolution of the microstructure of the Mg-Al alloys with the addition of different Ca levels, and the correlation of the as-cast microstructure development with cooling rate, and the characterization of the phase transformations for permanent mold cast Mg-Al-Ca alloys.
- (3). Calorimetric analysis of the dissolution and precipitation of the eutectic phases in the Mg-Al and Mg-Al-Ca alloys during heating and cooling through the DSC technique.
- (4). A correlation relationship between hardness, modulus and penetration depth along with a small amount of experimental indentation data obtained at low and high loads has been established to predict the continuous change of hardness and composite modulus with penetration depth during indentation tests.
- (5). The investigation of the microscale and nanoscale mechanical behaviours of the as-cast Mg-Al and Mg-Al-Ca alloys, and the exploration and explanation of the mechanism of ISE taking place during indentation tests.

REFERENCES

1. H. Hu, A. Yu, N. Li and J. E. Allison. "Potential magnesium alloys for high temperature die cast automotive applications: a review", *Materials and Manufacturing Processes*, 18(5), 2003, p 687- 717.
2. G.S. Cole. "Issues that influence magnesium use in the automotive industry", *Materials Science Forum*, 419-422, 2003, p 43-50.
3. K. Pettersen, H. Westengen, J.I. Skar, M. Videm, and L.Y. Wei. "Magnesium Alloys and Their Applications (Ed: K.L. Kainer)", *Digitalen Geländemodelle(DGM)*, Wiley-VCH, Weinheim, 2000, p 29-34.
4. S.L. Couling. "New magnesium alloys", *Metals Engineering Quarterly*, 12(2), 1972, p 7-13.
5. L.Y. Wei, G.L. Dunlop and H. Westengen. "Development of microstructure in cast Mg-Al-rare earth alloys", *Materials Science and Technology*, 12(9), 1996, p 741-750.
6. H. Hu, R. Shang and N. Li. "Effect of Ca addition on grain microstructure development of Mg alloy AM60," *AFS Transactions*, 111, 2003, p1019-1029.
7. A. Luo and R. Powell. "Tensile and compressive creep of magnesium-aluminum-calcium based alloys", *Magnesium Technology 2001, TMS Annual Meeting, 2001*, p 137-144.
8. A. Suzuki, N.D. Saddock, J.W. Jones and T.M. Pollock. "Structure and transition of eutectic (Mg, Al)₂Ca Laves phase in a die-cast Mg-Al-Ca base alloy", *Scripta Materialia*, 51(10), 2004, p 1005-1010.

9. C.S. Roberts. "Magnesium and Its Alloys", Wiley, New York, 1960, p128.
10. M.M. Avedesian, H. Baker, Eds., "Magnesium & Magnesium Alloys", ASM International, Materials Park, OH, 1999.
11. M.E. Drits, L.L. Rokhlin, A.A. Oreshkina, and N.I. Nikitina. "Principles of alloying magnesium-based heat-resistant alloys", Russian Metallurgy, 5, 1982, p 83-87.
12. Norman Woldman, "Magnesium Casting", Magnesium, ASM International, 1946.
13. W.E. Mercer II. "Magnesium die cast alloys for elevated temperature applications", SAE paper, 1990, paper no. 900788.
14. D.H. StJohn, A.K. Dahle, T. Abbott, M.D. Nave and M. Qian. "Solidification of cast magnesium alloys", Magnesium Technology 2003, TMS, 2003, p 95-100.
15. J.E. Hillis and S.O. Shook. "Composition and performance of an improved magnesium AS41 alloy" SAE paper, 1989, paper No. 890205.
16. T.K. Aune and H. Westengen, "Property update on magnesium die casting alloys", SAE paper, 1995, paper No. 950424.
17. G.S. Foerster, "Designing alloys for die casting", Metals Engineering Quarterly, 13(1), 1973, p 19-22.
18. K. Pettersen and M. Siedersleben. "Castability and mechanical properties of magnesium-based alloys, related to the production of automotive industry", 15th International Pressure Die casting Conference, Montreux, Switzerland, 21-22 May, 1996.

19. ASM Handbook Committee, Alloy Phase Diagrams, Vol.3, ASM International, 1992, p 169-171.
20. M. Dargusch, M. Hisa, C. Caceres and G.L. Dunlop. "Elevated temperature deformation of die cast Mg alloy AZ91D", Proceedings of 3rd International Magnesium Conference, Institute of Materials, London, 1997, p 153-166.
21. D.J. Sakkinen. "Physical metallurgy of magnesium die casting alloys", SAE paper, 1994, paper No. 940779.
22. E.F. Emley. "Principles of Magnesium Technology", Pergamon Press, Oxford, 1966, p126-156.
23. J.B. Clark. "Age hardening in Mg-9 wt.% Al alloy", Acta Metallurgica, 16(2), 1968, p 141-152.
24. J. Zhang, Z. Guo, F. Pan, Z. Li and X. Luo. "Effect of composition on the microstructure and mechanical properties of Mg-Zn-Al alloys", Materials Science and Engineering A, 456(1-2), 2007, p 43-51.
25. E. Aghion and B. Bronfin, Proceedings of 3rd International Magnesium Conference, Institute of Materials, London, 1997, p 313-325.
26. O. Holta, H. Westengen and D.L. Albright. "High purity creep resistant magnesium alloys" Trans. NADCA 18th Int. Die Casting Congress and Exposition, Indianapolis, 1995.
27. A. Luo and M.O. Pekguleryuz. "Cast magnesium alloys for elevated temperature application", Journal of Materials Science, 29(20), 1994, p 5259-5271.

28. G. Raynor. "The Physical Metallurgy of Magnesium and its Alloys", Pergamon Press, London, 1959.
29. J.S. Waltrip. "Fresh look at some old Mg die casting alloys for elevated temperature applications", Proc. 47th Ann. World of Magnesium Conf., Cannes, May 1990, International Magnesium Association, p 124-129.
30. F. Hollrigl-Rosta, E. Just, J. Kohler and H.J. Meltzer. "Magnesium in Volkswagen", Proceedings 37th Ann. World of Magnesium Conference, International Magnesium Association, Dayton, USA, 1980, p 38-45.
31. Metals Handbook, 9th edition, ASM, 2, 1979, p 574.
32. L. Čížek, M. Greger, L. Pawlica, L.A. Dobrzański and T. Tański. "Study of selected properties of magnesium alloy AZ91 after heat treatment and forming", Journal of Materials Processing Technology, 157-158, 2004, p 466-471.
33. Hydro Magnesium Technical Brochures and Internal Reports. Hydro Magnesium, Avenue Marcel Thiry 83, B-1200 Brussels, Belgium.
34. T.K. Aune. "Magnesium die casting – alloys and properties", IMA Automotive Seminar, Frankfurt, October 1995.
35. T.K. Aune, H. Westengen and T. Ruden. "Mechanical properties of energy absorbing magnesium alloys", SAE paper 930418, Warrendale PA, USA, 1993.
36. H. Westengen, L. Wei, T. Aune and D. Albright. "Effect of intermediate temperature aging on mechanical properties and microstructure of die cast AM alloys", In Mordike BL, Kainer KU (eds), Magnesium Alloys and their Applications, Werkstoff-Informationsgesellschaft mbH, Frankfurt, Germany, 1998, p 209-214.

37. T.G. Basner, M. Evans and D.J. Sakkinen. "The effect of extended time aging on the mechanical properties of vertical vacuum cast aluminium-manganese and aluminium-rare earth magnesium alloys", SAE Paper, 1993, paper no. 930419.
38. A. Finkel, M. Regev, E. Aghion, M. Bamberger and A. Rosen. "Aging study of AZ91D casts", In Aghion E, Eliezer D (eds) Magnesium 1997, Proceedings of the Dead Sea Magnesium Conference, p 121-126.
39. D.J. Sakkinen and M. Evans. "The effect of aging on magnesium die casting alloys", NADCA document T93-112, Cleveland, October 1993, p 305-313.
40. C. Suman. "The effects on direct aging on mechanical properties and corrosion resistance of die-cast magnesium alloys AZ91D and AM60B", SAE Paper, 1990, paper no. 900794.
41. R.W. Evans and B. Wilshire. "Creep of Metal and Alloys", The Institute of Metals, London, 1985.
42. A.H. Cottrell. "Dislocations and Plastic Flow in Crystals", Oxford Univ. Press, London, 1953.
43. H. Suzuki. "Dislocations and Mechanical Properties of Crystals", Oxford Univ. Press, London, 1953.
44. F.R.N. Nabarro and H.L. deVilliers. "The Physics of Creep", London, Taylor and Francis, 1995, p 15.
45. R.W. Evans. "Introduction to Creep", The Institute of Materials, London, 1993.
46. R.L. Bell and T.G. Langdon. "Grain boundary sliding", Interfaces Conference, Melbourne, ed. R.C. Gifkins, Butterworths, Melbourne, 1970, p 115-137.

47. H. Berns, C. Broeckmann and D. Weichert. "The effect of coarse second phase particles on the creep behaviour of hard metallic alloys", *Key Engineering Materials*, 118-119, 1996, p 163-170.
48. Norsk Hydro Magnesium Database, Norsk Hydro a.s., Porsgrunn, Norway, 1996.
49. T.K. Aune and T. Ruden. "High temperature properties of magnesium die casting alloys", SAE paper, 1992, paper No. 920070.
50. A.A. Nayeb-Hashemi and J.B. Clark. *Bulletin of Alloy Phase Diagrams*, 5, 1984, p 584.
51. R. Ninomiya, T. Ojiro and K. Kubota. "Improved heat resistance of Mg-Al alloys by the Ca addition", *Acta Metallurgica et Materialia*, 43(2), 1995, p 669-674.
52. Y. Terada, R. Sota, Ishimatsu N, Sato T and Ohori K. "A thousandfold creep strengthening by Ca addition in die-cast AM50 magnesium alloy", *Metallurgical and Materials Transactions A*, 35A(9), 2004, p 3029-3032.
53. B.R. Powell, A. Luo, V. Rezhets, B.L. Tiwari. "Development of creep-resistant magnesium alloys for powertrain applications: Part 1 of 2", SAE Paper, 2001, paper no. 2001-01-0422.
54. A. Luo, M.P. Balogh, J.J. Bommarito and B.R. Powell. "Tensile creep and microstructure of magnesium-aluminum-calcium based alloys for powertrain applications-Part 2 of 2", *SAE Trans: J Mater Manufacturing*, 110, 2001, p 414-422.
55. A.A. Luo, M.P. Balogh and B.R. Powell. "Creep and microstructure of magnesium-aluminum-calcium based alloys", *Metallurgical and Materials Transactions A*, 33A(3), 2002, p 567-574.

56. K. Ozturk, Y. Zhong, A. Luo and Z. Liu. "Creep resistant Mg-Al-Ca alloys: Computational thermodynamics and experimental investigation", JOM, 55(11), 2003, p 40-44.
57. Y. Zhong, A. Luo, J.O. Sofu and Z. Liu. "Laves phases in Mg-Al-Ca alloys", Magnesium Technology 2004, TMS Annual Meeting, 2004, p 317-323.
58. R. Ninomiya, T. Ojiro and K. Kubota. "Improved heat resistance of Mg-Al alloys by the Ca addition", Acta Metallurgica et Materialia, 43(2), 1995, p 669-674.
59. B.R. Powell, V. Rezhets, A.A. Luo, and B.L. Tiwari. "Low-cost, creep-resistant magnesium alloy for powertrain components", US Patent No. 6,264,764 dated July 24, 2001.
60. G.S. Foerster. The 7th SDCE Conf., Chicago, USA, October 1972, Paper No. 9372.
61. M. Videm. Norsk Hydro Internal Report, Norsk Hydro Research Center Porsgrunn Doc. No. 94QF29Doc, 1994.
62. L. Wei and G.L. Dunlop. "The solidification behavior of Mg-Al-rare earth alloys", Journal of Alloys and Compounds, 232, 1996, p 264-268.
63. L. Wei. "Development of Microstructure in Cast Magnesium Alloys", PhD Thesis, Chalmers University of Technology, 1990.
64. Y.C. Lee, A.K. Dahle and D.H. StJohn. "The role of solute in grain refinement of magnesium", Metallurgical and Materials Transactions A, 31A(11) (2000), p 2895-2905.

65. F. Sauerwald. "Effect of zirconium on solidification of magnesium alloys, and properties of cast magnesium zirconium alloys", *Zeitschrift fuer Metallkunde*, 40(2), 1949, p 41-46.
66. Y. Tamura, N. Kono, T. Moteqi and E. Sato. "Grain refining mechanism and casting structure of Mg-Zr alloy", *Journal of Japan Institute of Light Metals*, 47(12), 1997, p 679-684.
67. M. Qian, L. Zheng, D. Graham, M.T. Frost and D.H. St. John. "Settling of undissolved zirconium particles in pure magnesium melts", *Journal of Light Metals*, 1(3), 2001, p 157-165.
68. B. Bronfin, M. Katsir, O. Bar-Yosef, F. Moll and S.Schumann. "Metallurgical background to the development of creep resistant gravity casting magnesium alloys", *Magnesium Technology 2005*, TMS annual meeting, 2005, p 395-401.
69. EfunDa Engineering Fundamentals, Die casting process, http://www.efunda.com/processes/metal_processing/die_casting.cfm, accessed September 06, 2005.
70. Jinan Emerson Manufacturing Inc, Permanent Mold Casting, <http://www.china-aluminumcasting.com/permanent.htm>, accessed January 18, 2006.
71. A. Wahlberg. "Brinell's method of determining the hardness and other properties of iron and steel", *Journal of the Iron and Steel Institute*, 59, 1901, p 243.
72. D. Tabor. "The Hardness of Metals", Clarendon Press, Oxford, 1951.
73. B.W. Mott. "Microindentation Hardness Testing", Butterworths, London, 1956.
74. J.B. Pethica, R. Hutchings and W.C. Oliver. "Hardness measurement at penetration depths as small as 20 nm", *Philosophical Magazine A*, 48(4), 1983, p 593-606.

75. W.C. Oliver and G.M. Pharr. "Improved technique for determining hardness and elastic modulus using load and displacement sensing indentation experiments", *Journal of Materials Research*, 7(6), 1992, p 1564-1580.
76. J. P. Weiler, J. T. Wood, R. J. Klassen, R. Berkmortel and G. Wang. "The effect of grain size on the flow stress determined from spherical microindentation of die-cast magnesium AM60B alloy", *Journal of Materials Science*, 40(22), 2005, p 5999-6005.
77. L.Y. Huang, J.W. Zhao, K.W. Xu and J. Lu. "A new method for evaluating the scratch resistance of diamond-like carbon films by the nano-scratch technique", *Diamond and Related Materials*, 11(7), 2002, p 1454-1459.
78. W.R. Lafontaine, C.A. Paszkiet, M.A. Korhonen, and C.Y. Li. "Residual stress measurements of thin aluminum metallizations by continuous indentation and x-ray stress measurement techniques", *Journal of Materials Research*, 6(10), 1991, p 2084-2090.
79. S.N.G. Chu and J.C.M. Li. "Impression creep; a new creep test", *Journal of Materials Science*, 12(11), 1977, p 2200-2208.
80. R.M. Hooper and C.A. Brookes. "Incubation periods and indentation creep in lead", *Journal of Materials Science*, 19(12), 1984, p 4057-4060.
81. W.B. Li, J.L. Henshall, R.M. Hooper and K.E. Easterling. "The mechanisms of indentation creep", *Acta Metallurgica et Materialia*, 39(12), 1991, p 3099-3110.

82. B. Bhushan, A.V. Kulkarni, W. Bonin and J.T. Wyrobek. "Nanoindentation and picoindentation measurements using a capacitive transducer system in atomic force microscopy", *Philosophical Magazine A*, 74(5), 1996, p 1117-1128.
83. V. Raman and R. Berriche. "An investigation of the creep processes in tin and aluminium using a depth-sensing indentation technique", *Journal of Materials Research*, 7(3), 1992, p 627-638.
84. X. Li, D. Diao and B. Bhushan. "Fracture mechanisms of thin amorphous carbon films in nanoindentation", *Acta Materialia*, 45(11), 1997, p 4453-4461.
85. X. Li and B. Bhushan. "Nanofatigue studies of ultrathin hard carbon overcoats used in magnetic storage devices", *Journal of Applied Physics*, 91(10), 2002, p 8334-8336.
86. S.A. Syed Asif and J.B. Pethica. "Nano scale creep and the role of defects", *Thin films: Stresses and Mechanical Properties: VI*, Materials Research Society Symposium Proceedings, 436, 1997, p 201-206.
87. H. Hertz, *J. Reine, Angew, Math.* 92, 156 (1881), Translated and reprinted in English in Hertz's miscellaneous papers (Maxmillan & Co., London, U.K., 1896), Chap 5.
88. I.N. Sneddon. "J. Boussinesq's problem for rigid cone", *Cambridge Philosophical Society -- Proceedings*, 44(4), 1948, p 492-507.
89. A. Bolshakov and G.M. Pharr, "Understanding nanoindentation unloading curves", *Journal of Materials Research*, 17(10), 2002, p 2660-2671.

90. INSPEC. "Properties of silicon", EMIS Data Reviews Series no. 4, INSPEC, The Institution of Electrical Engineers, London, 1988.
91. B. Bhushan and V.N. Koinkar. "Nanoindentation hardness measurements using atomic force microscopy", *Applied Physics Letters*, 64(13), 1994, p 1653-1655.
92. N. Gane and J.M. Cox. "The micro-hardness of metals at very low loads", *Philosophical Magazine*, 22(179), 1970, p 881-891.
93. N.A. Fleck, G.M. Muller, M.F. Ashby and J.W. Hutchinson. "Strain gradient plasticity: theory and experiment", *Acta Metallurgica et Materialia*, 42(2), 1994, p 475-487.
94. B.K. Gupta and B. Bhushan. "Micromechanical properties of amorphous carbon coatings deposited by different deposition techniques", *Thin Solid Films*, 270(1-2), 1995, p 391-398.
95. X. Li and B. Bhushan. "Micro/nanomechanical characterization of ceramic films for microdevices", *Thin Solid Films*, 340(1-2), p 210-217.
96. B. Bhushan. "Introduction to Tribology", Wiley, New York, 2002.
97. K.L. Johnson. "Contact Mechanics", Cambridge University Press, Cambridge, 1985.
98. A.G. Atkins, A. Silverio and D. Tabor. "Indentation hardness and creep of solids", *Institute of Metals -- Journal*, 94(11), 1966, p 369-378.
99. J.C.M. Li. "Impression creep and other localized tests", *Materials Science and Engineering A*, 322 (1-2), 2002, p 23-42.

100. P. Grau, G. Berg, H. Meinhard and S. Mosch. "Strain rate dependence of the hardness of Glass and Meyer's law", *Journal of the American Ceramic Society*, 81(6), 1998, p 1557-1564.
101. J. Larsson and B. Storakers. "On oblique contact of creeping solids", *Journal of the Mechanics and Physics of Solids*, 50 (10), 2002, p 2029-2055.
102. B. Storakers, S. Biwa and P.L. Larsson. "Similarity analysis of inelastic contact", *International Journal of Solids and Structures*, 34 (24), 1997, p 3061-3083.
103. X. Li and B. Bhushan. "A review of nanoindentation continuous stiffness measurement technique and its applications", *Materials Characterization*, 48(1), 2002, p 11-36.
104. G. Feng and A.H.W. Ngan. "Effect of creep and thermal drift on modulus measurement using depth-sensing indentation", *Journal of Materials Research*, 17(3), 2002, p 660-668.
105. A.C. Fischer-Cripps. "Nanoindentation", Springer-Verlag, New York, 2004.
106. K. Herrmann, N.M. Jennett, W. Wegener, J. Meneve, K. Hasche and R. Seemann. "Progress in determination of the area function of indenters used for nanoindentation", *Thin Solid Films*, 377, 2000, p 394- 400.
107. J.A. Greenwood and J.H. Tripp. "The contact of two nominally rough surfaces", *Proceedings of the Institution of Mechanical Engineers*, 185, 1971, p 625-633.
108. G. Fu. "Effects of tip rounding on the fundamental relations used in the analysis of nanoindentation data", *Materials Letters*, 60(29-30), 2006, p 3855-3856.

109. J.H. Underwood. "Residual stress measurement using surface displacement around an indentation", *Experimental Mechanics*, 30, 1973, p 373-380.
110. A. Bolshakov and G.M. Pharr. "Influences of pileup on the measurement of mechanical properties by load and depth sensing indentation techniques", *Journal of Materials Research*, 13(4), 1998, p 1049-1058.
111. N.X. Randall and C. Julia-Schmutz. "Evolution of contact area and pile-up during the nanoindentation of soft coating on hard substrates", *Materials Research Society Symposium - Proceedings*, 522, 1998, p 21-26.
112. K.W. McElhaney, J.J. Vlassak and W.D. Nix. "Determination of indenter tip geometry and indentation contact area for depth-sensing indentation experiments", *Journal of Materials Research*, 13(5), 1998, p 1300-1306.
113. J.L. Hay, W.C. Oliver, A. Bolshakov and G.M. Pharr. "Using the ratio of loading slope and elastic stiffness to predict pile-up and constraint factor during indentation", *Materials Research Society Symposium - Proceedings*, 522, 1998, p 101-106.
114. M. Zhao, W.S. Slaughter, M. Li and S.X. Mao. "Material-length-scale-controlled nanoindentation size effects due to strain-gradient plasticity", *Acta Materialia*, 51(15), 2003, p 4461-4469.
115. Y.M. Soifer, A. Verdyan and L. Rapoport. "Nanoindentation size effect in alkali-halide single crystals", *Materials Letters*, 56(3), 2002, p 127-130.

116. G.P. Upit and S.A. Varchenya. In: Westbrook JH, Conrad H, editors. The science of hardness testing and its research applications. Metals Park (OH): ASM, 1974, p. 135-146.
117. H. Gao, Y. Huang, W.D. Nix and J.W. Hutchinson. "Mechanism-based strain gradient plasticity. I. Theory", Journal of the Mechanics and Physics of Solids, 47(6), 1999, p 1239-1263.
118. N. Gane and J.M. Cox. "Micro- hardness of metals at very low loads" Philosophical Magazine, 22(179), 1970, p 881-891.
119. O.N. Grigor'ev, Y.V. Milman, V.N. Skvortsov, A.P. Ternovskij, V.I. Trefilov and S.I. Chugunova. Poroshkovaya Metall, 8, 1977, p 72-79.
120. H. Li, A. Ghosh, Y.N. Han and R.C. Bradt. "The frictional component of the indentation size effect in low load microhardness testing", Journal of Materials Research, 8(5), 1993, p 1028-1032.
121. G. Hohne, W. Hemminger and H.J. Flammersheim. "Differential Scanning Calorimetry", Springer-Verlag, Berlin, 1996.
122. R. Sabbah, A.M. Zahra, R. Castanet and G. Bardon. de Segonzac: personal communications, CTM-CNRS, Marseille, France, 1996.
123. J. H. Reardon and R. V. Peterson. "Systematic Materials Analysis", academic press, New York 1978.
124. C. Michaelsen, K. Barmak and T. P. Weihs. "Investigating the thermodynamics and kinetics of thin film reactions by differential scanning calorimetry", Journal of Physics D, 30(23), 1997, p 3167-3186.

125. M. J. Richardson and E. L. Charsley. "Handbook of Thermal Analysis and Calorimetry (ed. M. E. Brown)", Amsterdam, Elsevier, 1, 1998, p 547.
126. W. Lacom. "Calorimetric investigations in a dispersion strengthened 7075 alloy", *Thermochimica Acta*, 271, 1996, p 93-100.
127. A. Charai, T. Walther, C. Alfonso, A.M. Zahra and C. Y. Zahra. "Coexistence of clusters, GPB zones S"-, S'- and S-phases in an Al-0.9% Cu-1.4% Mg alloy", *Acta Materialia*, 48(10), 2000, p 2751-2764.
128. G. W. Smith. "A method for determination of Avrami parameters directly from isothermal calorimetry data", *Thermochimica Acta*, 291(1-2), 1997, p 59-64.
129. L.F. Mondolfo. "Aluminium Alloys: Structure and Properties", Butterworths, London, 1976.
130. I. J. Polmear. "Light Alloys, the Metallurgy of the Light Metals", 3rd edn, Arnold, London, 1995.
131. T. Sato. "Early stage phenomena and role of microalloying elements in phase decomposition of aluminum alloys", *Materials Science Forum*, 331-337(1), 2000, p 85-96.
132. M. J. Starink. "Kinetic equations for diffusion-controlled precipitation reactions", *Journal of Materials Science*, 32(15), 1997, p 4061-4070.
133. M.E. Brown, D. Dollimore and A.K. Galwey. "Reactions in the Solid State. Comprehensive Chemical Kinetics", Amsterdam, Oxford, New York, 22, 1980, p 340.
134. J. Sestak. "Thermophysical Properties of Solids. Comprehensive Analytical Chemistry", Vol. 12D. Elsevier, Amsterdam, 12D, 1984, p 440.
135. C. D. Doyle. "Series approximations to the equation of thermogravimetric data", *Nature*, 207(4994), 1965, p 290-291.
136. M. J. Starink. "The determination of activation energy from linear heating rate experiments: a comparison of the accuracy of isoconversion methods", *Thermochimica Acta*, 404, 2003, p 163-176.

137. H. E. Kissinger. "Variation of peak temperature with heating rate in differential thermal analysis", United States Bureau of Standards -- Journal of Research, 57(4), 1956, p 217-221.
138. T. Ozawa. "Estimation of activation energy by isoconversion methods", Thermochemica Acta, 203, 1992, p 159-165.
139. C.R. Li and T. B. Tang. "A new method for analysing non-isothermal thermoanalytical data from solid-state reactions", Thermochemica Acta, 325(1), 1999, p 43-46.
140. A. Ortega. "The kinetics of solid-state reactions toward consensus, Part 2: Fitting kinetics data in dynamic conventional thermal analysis", International Journal of Chemical Kinetics, 34(3), 2002, p 193-208.
141. T. Akahira and T. Sunose. Trans. Joint Convention of Four Electrical Institutes, 3, 1969, p 246.
142. P. Murray and J. White. "Kinetics of thermal dehydration of clays -- 3", British Ceramic Society -- Transactions, 54(4), 1955, p 189-238.
143. R.D. Sa Lisboa and C.S. Kiminami. "Primary crystallization in amorphous $\text{Al}_{84}\text{Ni}_8\text{Co}_4\text{Y}_3\text{Zr}_1$ alloy", Journal of Non-Crystalline Solids, 304(1-3), 2002, p 36-43.
144. S. Ikeno, H. Matsui, K. Matsuda, K. Terayama and Y. Uetani. "DSC measurement and HRTEM observation of precipitates in an Al-1.6 mass%Mg₂Si alloy", Journal of the Japan Institute of Metals, 65(5), 2001, p 404-408.
145. Y. Ohmori, L. C. Doan, Y. Matsuura, S. Kobayashi and K. Nakai. "Morphology and crystallography of β -Mg₂Si precipitation in Al-Mg-Si alloys", Materials Transactions, 42(12), 2001, p 2576-2583.
146. M.Y. Zheng, K. Wu, S. Kamado and Y. Kojima. "Aging behavior of squeeze cast SiCw/AZ91 magnesium matrix composite", Materials Science and Engineering A, 348(1-2), 2003, p 67-75.
147. T. Raghu, O. Sivakesavam, and G.G. Saha. "Friction characteristics of magnesium alloy ZM-21", Journal of Materials Processing Technology, 42(3), 1994, p 349-360.

148. P. Bassani, E. Gariboldi and A. Tuissi. "Calorimetric analysis of AM60 magnesium alloy", *Journal of Thermal Analysis and Calorimetry*, 80, 2005, p 739-747.
149. G. Riontino, D. Lussana, M. Massazza and A. Zanada. "DSC investigation on WE43 and Elektron 21 Mg alloys" *Journal of Materials Science*, 41(10), 2006, p 3167-3169.
150. G. Garces, J.M. Antoranz, P. Perez, J.M. Badia, S.B. Dodd, S. Morris and P. Adeva. "Microstructural characterisation and thermal stability of a metastable Mg-8.6 wt.% Zr alloy produced by physical vapour deposition", *Zeitschrift fuer Metallkunde/Materials Research and Advanced Techniques*, 94 (8), 2003, p 880-885.
151. F. Sommer, F. Hehmann and H. Jones. "Transformation behaviour of the rapidly solidified solid solution of yttrium in magnesium", *Journal of the Less-Common Metals*, 159, 1990, p 237-259.
152. Y.X. Wang, S.K. Guan, X.Q. Zeng and W.J. Ding. "Effects of RE on the microstructure and mechanical properties of Mg-8Zn-4Al magnesium alloy" *Materials Science and Engineering A*, 416 (1-2), 2006, p 109-118.
153. N.G. Ma, C.J. Deng, P. Yu, W.Y. Kwok, M. Aravind, D.H.L. Ng and S.L.I. Chan. "Formation of Mg-Mg₂Cu nanostructured eutectic in Mg-based metal matrix composite", *Journal of Materials Research*, 18(8), 2003, p 1934-1942.
154. P.M. Jardim, G. Solórzano and J.B. Vander Sande. "Second phase formation in melt-spun Mg-Ca-Zn alloys" *Materials Science and Engineering A*, 381 (1-2), 2004, p 196-205.
155. P. Liang, T. Tarfa, J.A. Robinson and S. Wagner. "Experimental investigation and thermodynamic calculation of the Al-Mg-Zn system", *Thermochimica Acta*, 314 (1), 1998, p 87-110.
156. M. Ohno, D. Mirkovic and R. Schmid-Fetzer. "Phase equilibria and solidification of Mg-rich Mg-Al-Zn alloys" *Materials Science and Engineering A*, 421 (1-2), 2006, p 328-337.

157. M. Zhou, "An experimental study of die and squeeze cast magnesium alloy AM50", Master thesis, Department of Mechanical Engineering, University of Windsor, 2004.
158. F. Czerwinski, A. Zielinska-Lipiec, P. J. Pinet and J. Overbeeke. "Correlating the microstructure and tensile properties of a thixomolded AZ91D magnesium alloy", *Acta Materialia*, 49(7), 2001, p 1225-1235.
159. M.S. Dargusch and G.L. Dunlop. "Magnesium Alloys and their Applications," edited by B. L. Mordike and K. U. Kainer, Wolfsburg, Germany, 1998, p 277-284.
160. V.Y. Gertsman, L. Jian, X. Su, J.P. Thomson and S. Mahi. "Microstructure and second-phase particles in low- and high-pressure die-cast magnesium alloy AM50", *Metallurgical and Materials Transactions A*, 36A(8), 2005, p 1989-1997.
161. L.D. Marks. "Surface structure and energetics of multiply twinned particles", *Philosophical Magazine A*, 49(1), 1984, p 81-93.
162. C.V. Kopecky, A.V. Andreeva and G.D. Sukhomlin. "Multiple twinning and specific properties of $\Sigma = 3$ boundaries in f.c.c. crystals", *Acta Metallurgica et Materialia*, 39(7), 1991, p 1603-1615.
163. G.L. Nord Jr. "Transformation-induced twin boundaries in minerals", *Phase Transitions B*, 48 (1-3), 1994, p 107-134.
164. J. Ma. "Nanoscale study of cyclic deformation behaviour and mechanism of annealing twin", *Materials Science and Engineering A*, 427(1-2), 2006, p 282-288.
165. K.P.D. Lagerlof, J. Castaing, P. Pirouz and A.H. Heuer. "Nucleation and growth of deformation twins: a perspective based on the double-cross-slip mechanism of deformation twinning", *Philosophical Magazine A*, 82(15), 2002, p 2841-2854.

166. S.G. Lee, G.R. Patel and A.M. Gokhale. "Macro-segregation in high-pressure die-cast AM60 alloy", TMS annual meeting, 2005, p 377-380.
167. J. Yao and Z. Liu. "Influence of AZ91 die-casting on its microstructure and mechanical properties", Rare Metals, 21(SUPPL.), 2002, p 69-74.
168. M. Zhou, N. Li and H. Hu. "Effect of section thicknesses on tensile behavior and microstructure of high pressure die cast magnesium alloy AM50", Materials Science Forum, 475-479, 2005, p 463-468.
169. I.Y. Mukhina, M.A. Timonova and G.I. Spiriyakina. "Influence of phase composition on corrosion-resistance of magnesium alloys", Russian Metallurgy, 6, 1973, p 123-126.
170. C.J. Simensen, B.C. Oberlander, J. Svalestuen and A. Thorvaldsen. "The phase diagram for magnesium-aluminium-manganese above 650 °C", Zeitschrift Fur Metallkunde, 79, 1988, p 537-540 and 696-699.
171. M.A. Parvez, X. Wang, E. Essadiqi and M. Medraj. "Experimental investigation of the equilibria in Mg-Al-(Ca, Sr) systems", Magnesium Technology 2005, TMS, 2005, p 179-184.
172. W. Kurtz and D.J. Fischer. "Fundamentals of Solidification", Trans Tech Publications, Aedermansdorf, Switzerland, 1992.
173. D. Duly, J.P. Simon and Y. Brechet. "Competition between continuous and discontinuous precipitations in binary Mg-Al alloys", Acta Metallurgica et Materialia, 43(1), 1995, p 101-106.

174. S. Celotto. "TEM study of continuous precipitation in Mg-9 wt%Al-1 wt%Zn alloy", *Acta Materialia*, 48(8), 2000, p 1775-1787.
175. M.J. Starink. "A new method for the derivation of activation energies from experiments performed at constant heating rate", *Thermochimica Acta*, 288(1-2), 1996, p 97-104.
176. E.J. Mittemeijer. "Analysis of the kinetics of phase transformations", *Journal of Materials Science*, 27(15), 1992, p 3977-3987.
177. H.J. Frost and M.F. Ashby. "Deformation-mechanism Maps", Pergamon Press, Oxford, UK 1982.
178. M. J. Starink. "Analysis of aluminum based alloys by calorimetry: Quantitative analysis of reactions and reaction kinetics", *International Materials Reviews*, 49 (3-4), 2004, p 191-226.
179. X.J. Liu, I. Ohnuma, R. Kainuma and K. Ishida. "Thermodynamic assessment of the aluminum-manganese (Al-Mn) binary phase diagram", *Journal of Phase Equilibria*, 20(1), 1999, p 45-56.
180. M. Ohno and R. Schmid-Fetzer. "Thermodynamic assessment of Mg-Al-Mn phase equilibria, focusing on Mg-rich alloys", *Zeitschrift für Metallkunde*, 96(8), 2005, p 857-869.
181. J. Malzbender, G. de With and J. den Toonder. "The $P-h^2$ relationship in indentation", *Journal of Materials Research*, 15(5), 2000, p 1209-1212.
182. M. Atkinson. "Origin of size effect in indentation of metals", *International Journal of Mechanical Sciences*, 33(10), 1991, p 843-850.

183. H. Pelletier, J. Krier, A. Cornet and P. Mille. "Limits of using bilinear stress-strain curve for finite element modeling of nanoindentation response on bulk materials", *Thin Solid Films*, 379 (1-2), 2000, p 147-155.
184. H. Li, A. Chosh, Y.H. Han and R.C. Bradt. "The frictional component of the indentation size effect in low load microhardness testing", *Journal of Materials Research*, 8(5), 1993, p 1028-1032.
185. X.S. Wang and J.H. Fan. "SEM online investigation of fatigue crack initiation and propagation in cast magnesium alloy", *Journal of Materials Science*, 39(7), 2004, p 2617-2620.
186. J.P. Weiler, J.T. Wood, R.J. Klassen, R. Berkmortel and G.Wang. "Variability of skin thickness in an AM60B magnesium alloy die-casting", *Materials Science and Engineering A*, 419(1-2), 2006, p 297-305.
187. A. Kelly and R.B. Nicholson. "Precipitation hardening", *Progress in Materials Science*, 10, 1963, p 151-391.
188. J.D. Baird and A. Jamieson. "Effect of manganese and nitrogen on the tensile properties of iron in the range 20 - 600 °C", *Journal of the Iron and Steel Institute*, 204, 1966, p 793-803.
189. I. Manika and J. Maniks. "Size effects in micro- and nanoscale indentation", *Acta Materialia*, 54(8), 2006, p 2049-2056.
190. Z. Zhong, J. Lou, O.O. Adewoye, A.A. Elmustafa, F. Hammad and W.O. Soboyejo. "Indentation size effects in the nano- and micro-hardness of fcc single crystal metals", *Materials Science and Engineering A*, 434(1-2), 2006, p 178-187.

191. J.R. Greer and W.D. Nix. "Size dependence of mechanical properties of gold at the sub-micron scale", *Applied Physics A*, 80(8), 2005, p 1625-1629.
192. A. Gouldstone, H.J.Koh, K.Y. Zeng, A.E. Giannakopoulos and S. Suresh. "Discrete and continuous deformation during nanoindentation of thin films", *Acta Materialia*, 48(9), 2000, p 2277-2295.
193. Z. Zong and W.O. Soboyejo. "Indentation size effects in face centered cubic single crystal thin films", *Materials Science and Engineering A*, 404(1-2), 2005, p 281-290.
194. M. Fujiwara and M. Otsuka. "Characterization of micro-indentation creep in β -Sn single crystals at elevated temperatures", *Journal of the Japan Institute of Metals*, 63(6), 1999, p 760-769.
195. A. Bolshakov and G.M. Pharr. "Influences of pileup on the measurement of mechanical properties by load and depth sensing indentation techniques", *Journal of Materials Research*, 13(4), 1998, p 1049-1058.
196. S. Asif and J.B. Pethica. "Nanoindentation creep of single-crystal tungsten and gallium arsenide", *Philosophical Magazine A*, 76(6), 1997, p 1105-1118.
197. M. Wollgarten, M. Beyss, K. Urban, H. Liebertz and U. Koster. "Direct evidence for plastic deformation of quasicrystals by means of a dislocation mechanism", *Physical Review Letters*, 71(4), 1993, p 549-552.
198. H.J. Kaufmann, A. Luft and D. Schulze. "Deformation mechanism and dislocation structure of high-purity molybdenum single crystals at low temperatures", *Crystal Research and Technology*, 19(3), 1984, p 357-372.

199. J. Weertman. "Creep of indium, lead, and some of their alloys with various metals", Metallurgical Society of American Institute of Mining, Metallurgical and Petroleum Engineers -- Transactions, 218 (2), 1960, p 207-218.
200. O.D. Sherby and P.M. Burke. "Mechanical behavior of crystalline solids at elevated temperature", Progress in Materials Science, 13 (7), 1967, p 325-386.

PUBLICATIONS RESULTING FROM THIS WORK

1. Lihong Han, Derek Northwood and Henry Hu. "Observation of the microstructure and characterization of local mechanical properties of AM50 using micro-Berkovich indenter", Magnesium Technology 2005, TMS Annual Meeting & Exhibition, February 13-17, 2005, San Francisco, California, 2005, p 197-202.
2. Lihong Han, Henry Hu, Derek Northwood and Naiyi Li. "A calorimetric analysis of dissolution of second phases in as-cast AM50 alloys", Magnesium Technology 2007, TMS Annual Meeting & Exhibition, February 25-March 1, Orlando, Florida, 2007, p 369-374.
3. Lihong Han, Derek Northwood and Henry Hu. "Influence of solute content and secondary phases on the nano-creep behavior of Mg-Al-Ca alloys", Key Engineering Materials, 345-346, 2007, p 605-608.
4. Lihong Han, Henry Hu, Derek Northwood and Naiyi Li. "Microstructure and nano-scale mechanical behavior of Mg-Al and Mg-Al-Ca alloys", Materials Science and Engineering A, 473(1-2), 2008, p 16-27.
5. Lihong Han, Henry Hu and Derek Northwood. "Effect of Ca additions on microstructure and microhardness of an as-cast Mg-5.0 wt.% Al alloy", Materials Letters, 62(3), 2008, p 381-384.
6. Lihong Han, Henry Hu and Derek Northwood. "Effect of the cooling rates on the microstructure evolution and eutectic formation of as-cast Mg-Al-Ca alloys", Metallurgical and Materials Transactions A, 2007. (Submitted).
7. Lihong Han, Henry Hu and Derek Northwood. " A Comparative Study on the Solution Treatment of Mg-Al and Mg-Al-Ca Alloys ", Magnesium Technology 2008, TMS Annual Meeting & Exhibition, 2008. (Submitted).

VITA AUCTORIS

NAME	Lihong Han
PLACE OF BIRTH	Songjianghe, Jilin Province, P.R.China
YEAR OF BIRTH	1972
EDUCATION	Jilin Institute of Technology, Changchun, China 1990 - 1994 Bachelor of Engineering in Materials Engineering
	Harbin Institute of Technology, Harbin, China 1995 - 1997 Master of Science in Materials Engineering
	Harbin Institute of Technology, Harbin, China 1997 - 2001 Ph.D in Materials Engineering
	University of Windsor, Windsor, Ontario 2002 - 2007 Ph.D in Materials Engineering